

See discussions, stats, and author profiles for this publication at: <https://www.researchgate.net/publication/373879998>

An ethnobotanical survey of plants used by the people of the Hmar tribe of Dima Hasao district, Assam, North East India

Article in *Exploratory Animal and Medical Research* · September 2023

DOI: 10.52635/eamr/13(S)141-147

CITATIONS

0

READS

666

5 authors, including:



Aparajita Das
Tripura University

15 PUBLICATIONS 9 CITATIONS

SEE PROFILE



Panchatapa Bhattacharya
Tripura University

9 PUBLICATIONS 0 CITATIONS

SEE PROFILE



Somnath Kar
Tripura University

35 PUBLICATIONS 45 CITATIONS

SEE PROFILE



B K Datta
Tripura University

166 PUBLICATIONS 1,090 CITATIONS

SEE PROFILE

Research Article

AN ETHNOBOTANICAL SURVEY OF PLANTS USED BY THE PEOPLE OF THE HMAR TRIBE OF DIMA HASAO DISTRICT, ASSAM, NORTH EAST INDIA

Aparajita Das^{1*}, Nancy Neivarmawi Ngente¹, Panchatapa Bhattacharya¹, Somnath Kar², B. K. Datta¹

Received 12 January 2023, revised 08 August 2023

ABSTRACT: The present ethnobotanical study was undertaken to assess the uses of the local plants of Dima Hasao district, diversity, and conservation concerns of medicinal plants used in the traditional herbal care system of *Hmar* tribes in Dima Hasao district of Assam in northeastern India. Since ancient times, *Hmar* tribes have used local plants as medicines to treat many human diseases. Such information has a lot of potential for developing new medications and managing future healthcare.

Key words: *Hmar* tribe, Ethnomedicine, Dima Hasao, Northeastern India.

INTRODUCTION

The term ethno derives from the Greek word ethnos, which means nation, tribe, or race. The qualities and functions of the plants in their environment are well known to the native population. People depend on forest resources for a variety of things, such as food, medicine, wood, and non-timber forest products (Pushpangadan 1995). Different plant parts are used to solve health-related issues from some ancient days and the ethnic people living in remote areas are still practicing many of such uses (Abu-Rabia 2005, Pattanayak 2021a, Pradhan *et al.* 2021). Documentation of such uses, validation of their reported efficacies, and efforts to use them in mankind is a continuous process (Patel *et al.* 2022, Paul and Sujatha 2022). It has been observed that the treatment cost of modern medicine is becoming very high and due to various reasons, even the availability of laboratory derived effective antimicrobial medicines is decreasing rapidly (Pattanayak 2022a, Srinivas *et al.* 2023, Mondal *et al.* 2023). So, the importance of evaluation and use of cheap herb-derived medicines is increasing.

In many parts of the developing world, traditional medicine has maintained its appeal, and its usage is expanding quickly in developed nations. According to the World Health Organization, traditional medicine and healing methods represent the major source of care for almost 80% of people worldwide. Approximately 6500 plant species are utilized as DIY

(do it yourself) treatments in Asia (Karki and Williams 1999). Plants have long been used by humans as a source of medicine and for many other purposes.

India is a large country with many different landscapes, weather, plant communities, and human populations. Small-town and rural-area residents, on the one hand, and tribal residents of far-flung villages make up the bulk of India's ethnobotanical samples. More than 130 of India's 427 tribal clans are based in the region's eight northeastern states. Assam is home to 14 distinct hill tribes or 12.8% of India's total tribal population. Among these are the Khasi, Jaintia, Garo, Naga, and a scattering of Mizo and related peoples. The Lushais, Pawis, Paithes, Raltes, Pang, Hmars, Kukis, Lakhers, and others are all members of the Mizo people. An indigenous people known as the Lushai migrated to India around the turn of the nineteenth century. The Lushai tribe accounts for the vast majority of Mizos (the Lushai hills are a southern extension of the Himalayas, hence the name of the region). They have learned a great deal over time about how to employ plants and plant products to treat a wide range of illnesses. They put a lot of faith in the treatments of their indigenous folklore medicine and use only their herbal therapy. Even though there is a plethora of published information from throughout India detailing how various indigenous communities employ various medicinal herbs (Abu-Rabia 2005, Albert and Gosai 2006).

¹Plant Taxonomy and Biodiversity Laboratory, Department of Botany, ²Department of Botany, Holy Cross College, Jubatara, Lembucherra, Tripura University, Suryamaninagar -799022, Tripura, India.

*Corresponding author. e-mail: dasaparajita0210@gmail.com

STUDY AREA

Dima Hasao district is the third largest after KarbiAnglong and Sonitpur district in Assam. Towards the north-east, it shares a border with Karbi Anglong district and Nagaland; to the east, it borders Manipur; to the north, Hojai district; to the west, Meghalaya; and to the south, it shares a border with the Cachar district. The quiet, peaceful towns provide a haven for the locals, who live in homes as charming and unique as the region itself. Kachari, Zeme Naga, Hmar, Kuki, Biata, and Hrangkhoh are some of the local peoples (Fig. 1).

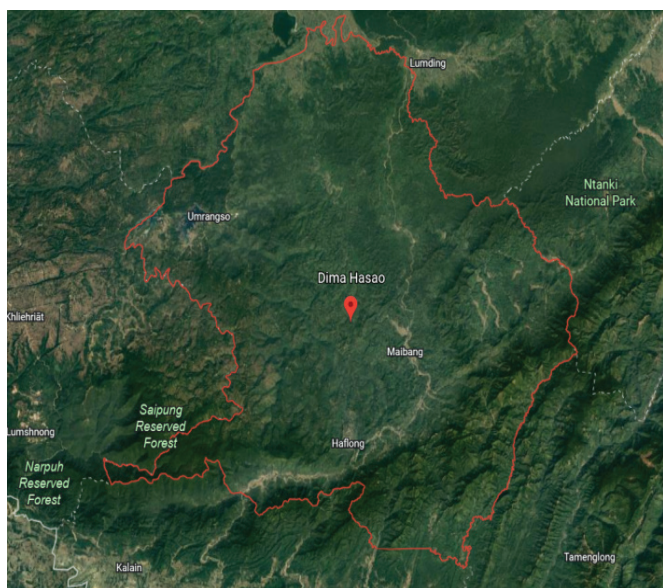


Fig. 1. Map Showing the study area Dima Hasao district, Assam, India.

THE FIELD SURVEY

From January 2020 to November 2021 researchers visited a variety of communities in the Mahur subdistrict of Assam's Dima Hasao district. The Hmar people were interviewed to compile basic information about native flora and their usage. These plants were gathered with the help of neighborhood experts and afterward photographed and identified in the herbarium. Saron, Suongbung, Garden, Khawlzang, Daudung, Gaidain Raji, Baozen, Chotorongmailai, Zoar, and Mahur market were the locations that were analyzed.

RESULTS AND DISCUSSION

There has been research done on the significant ethnobotanical plants used by the Hmar tribe in the Dima Hasao district. During the present observation and interaction with villagers, the herbal medicines practitioners, and other traditional healers of Hmar tribes, Dima Hasao. 22 species of vegetables, 22 species of edible fruits, and 61 species of medicinal

plants have been collected and listed with their correct names, vernacular names, parts used, and uses.

During a field survey, it was discovered that the Hmar population frequently suffers from many diseases, like piles, high blood pressure, cancer, dysentery, high blood sugar, jaundice, skin conditions, asthma, rheumatism, and more. Out of the 61 plants found, one plant is used to treat piles and cancer, three plants are used to treat blood sugar, five plants are used to treat skin conditions, two plants are used to treat asthma and rheumatism, eight plants are used to treat diarrhea, etc. It has been noted that they use most of the medicinal plants directly or get extracts of their succulent parts. But during validation of such ancient wisdom, this point is not given proper importance and generally only extracts of the dry plant parts are considered for all related research, though the succulent parts of the plants contain the highest number and quantity of phytoconstituents (Pattanayak *et al.* 2016, Pattanayak 2020).

The Hmar tribe uses four different species from the major families Solanaceae and Euphorbiaceae as medicine. It is interesting to note that different diseases have been treated using 48% of leaf samples, 16% of seeds, and 7% of bark. The Hmar tribe consumes 22 species of 15 family vegetables and 22 species of 17 family fruits. Alagesaboopathi (2009), Hossan *et al.* (2012) and Ojha *et al.* (2020) noted various important ethnomedicinal uses of plants of different tribal communities.

It is stressed that the flora should be encouraged to grow these ethnobotanical plants on a wide scale to optimize the economic situation. There are some reports of the use of such plants directly as some effective

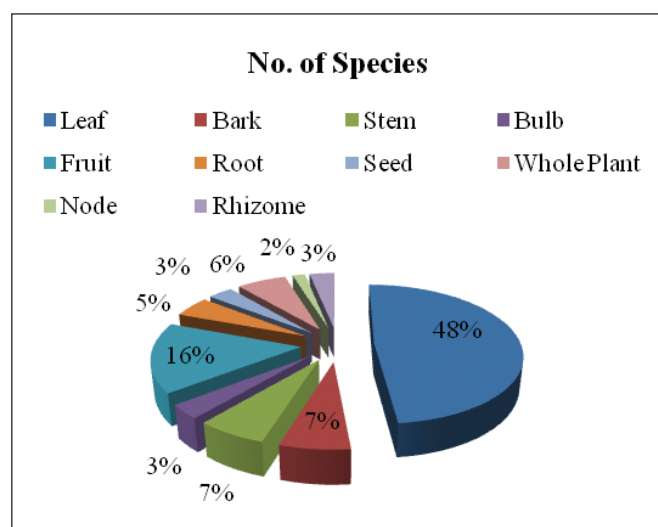


Fig. 2. Plant parts contributing no. of medicinal plant species.

An ethnobotanical survey of plants used by the people of the hmar tribe of dima hasao district ...

medicines to control many important diseases after their cultivation and encapsulation for global use (Pattanayak 2018, 2021b, 2022b) Thus, these

ethnobotanical plants may supply crude pharmaceuticals of economic importance for which they may become a very good economic source of the tribal people.

Table 1. List of ethnomedicinal plants by the Hmar tribes of Dima Hasao, Assam, India.

Plant name (Family)	Vernacular name	Parts used	Purpose of use	Mode of use
<i>Adhatoda vasica</i> Nees. [Acanthaceae]	Basok	Leaf	M	Drinking leaf juice can treat dysentery and cough.
<i>Aegle marmelos</i> L. [Rutaceae]	Belthei	Fruit	F, M	Drinking fruit juice to treat dysentery.
<i>Albizia lebbek</i> (L.) Benth [Meliaceae]	Kamatrak	Bark	M	Bark powder is strewn across the still stream as fish poison to catch fish.
<i>Allium cepa</i> L. [Liliaceae]	Purunsen	Bulb	V, M	Warm bulb juice is administered twice daily to treat menstrual irregularities.
<i>Allium sativum</i> L. [Liliaceae]	Purunvar	Bulb	V, M	One bulb piece is taken for getting relief from gastrointestinal issues.
<i>Aloe vera</i> (L.) Burm. [Liliaceae]	Elongera	Leaf	M	For relief from stomach pain and to treat black spots on the face, leaf juice is applied mixed with cow's milk and alcohol: leaf paste is used to cure wounds and reduce itching.
<i>Alstonia scholaris</i> (L.) R.Br. [Apocynaceae]	Chawngpereng	Stem	M	Localized applications of stem latex are made over the affected area of the skin as well as on all sides of the boils. To treat snakebites, the body is injected with leaf juice.
<i>Ananas comosus</i> L. [Bromeliaceae]	Rengtheite dawng	Fruit	M	Unripe fruit juice is used to induce abortions and regular menstruation.
<i>Andrographis paniculata</i> (Burm.f.) Wall. [Gentianaceae]	Chirata hna	Leaf	M	To treat stomachaches and fever, a leaf is soaked in water overnight and then taken the next morning. It is also used to eliminate tapeworms.
<i>Averrhoa carambola</i> L. [Oxalidaceae]	Thaiherot	Fruit	M	Fruit juice is consumed to treat liver issues. To treat redness or other issues with the eyes, a few drops of fruit juice are applied. Jaundice is treated with ripe fruit juice.
<i>Azadirachta indica</i> A. Juss [Meliaceae]	Neem	Leaf	M	To treat Pox, consumption of leaves or application of leaf juice and bathing in a solution made from boiled leaves.
<i>Cajanus cajan</i> L. [Leguminaceae]	Betlineng	Leaf	V,M	Jaundice is treated with leaf juice.
<i>Calotropis procera</i> (Air.) R. Br. [Asclepiadaceae]	Akanhna	Stem	M	The stem's latex is applied to the abscess.
<i>Cannabis sativa</i> L. [Cannabinaceae]	Nganja	Leaf	M	Hens and dogs are given leaf juice to treat weakness.
<i>Carica papaya</i> L. [Caricaceae]	Thingfenghna	Fruit	F, M	Dog bites can be treated using fruit sap. Jaundice is treated with leaf juice.
<i>Centella asiatica</i> L. [Apiaceae]	Lambak	Leaf	M	Dysentery can be treated with leaf juice.
<i>Chromolaena odorata</i> (L.) R.King. [Asteraceae]	Thlobuong	Leaf	M	Applying leaf juice to the area to be cut
<i>Cinnamomum tamala</i> (Buch-Ham) [Lauraceae]	Tejpata	Leaf	S, M	To control blood sugar, leaves are soaked in water overnight and then consumed the next morning.

Plant name (Family)	Vernacular name	Parts used	Purpose of use	Mode of use
<i>Citrus aurantifolia</i> (Christr.) Sw. [Rutaceae]	Serhna hring	Fruit, Leaf	F, M	To stop bleeding, leaf juice is applied inside the nose. Once the boil becomes suppured, prickle is applied.
<i>Clausena heptaphylla</i> (Roxb.) [Rutaceae]	Champara	Fruit	M	Fruit juice is taken to dissolve kidney stones and treat kidney problems.
<i>Clerodendrum viscosum</i> Vent. [Verbenaceae]	Phuibimhna	Leaf	M	Cuts and wounds are treated with leaf paste for quick healing.
<i>Clerodendrum colebrookianum</i> Walp. [Verbenaceae]	Anphui	Leaf	M	After heating, leaf juice is used to treat high blood pressure.
<i>Curcuma domestica</i> Salisb. [Zingiberaceae]	Aieng	Rhizome	M	To treat liver problems, rhizome powder, and water are taken orally.
<i>Cynodon dactylon</i> L. [Graminaceae]	Thlo	Leaf	M	Leaf juice is applied as an antiseptic to cuts.
<i>Datura metel</i> L. [Solanaceae]	Invetpar	Seed , Leaf	M	Joint pain is treated with seed and leaf paste.
<i>Datura stramonium</i> L. [Solanaceae]	Invetpar	Leaf	M	To treat asthma, boiled leaves are smoked. On rheumatism, leaf paste is externally applied.
<i>Dillenia indica</i> L. [Dilleniaceae]	Ailang	Fruit	M	Fruit juice is consumed to treat the dysentery condition.
<i>Emblica officinalis</i> Gaertn. [Euphorbiaceae]	Sunhlu	Fruit	M	To treat digestive issues and a propensity to vomit, one can consume boiling fruit juice. The fruit extract is also used topically to stop hair loss.
<i>Euphorbia niruri</i> (L.) [Euphorbiaceae]	Sunlunoith-um	Whole plant	M	When the liver is extended and in jaundice, whole plant decoction is taken.
<i>Hibiscus rosa-sinensis</i> L. [Malvaceae]	Reibalsen	Leaf	M	Cuts and abscesses are treated externally with leaf juice. To treat scurf, flower paste is applied to the hands.
<i>Jatropha curcas</i> L. [Euphorbiaceae]	Mutmaleng	Stem	M	For treating toothaches, stem latex is applied to the teeth. To relieve burning pain, charred areas are covered with leaf paste.
<i>Justicia gendarussa</i> Burm.f. [Acanthaceae]	Hlothing	Leaf	M	On cuts, leaf paste is externally applied.
<i>Kalanchoe pinnata</i> (Lam.) Pers. [Crassulaceae]	Meikang par	Leaf	M	To treat coughs, the leaves are frequently burned, consumed, and applied to body parts that are burning. Leaf paste is fed to treat diarrhea, and applied on burns.
<i>Lawsonia inermis</i> L. [Lythraceae]	Mehendi	Leaf	M	Leaf juice is used to treat wounds and remove dandruff from the head.
<i>Leucas aspera</i> L. [Lamiaceae]	Sairam	Leaf	M	Dandruff is removed by using leaf paste.
<i>Mangifera indica</i> L. [Anacardiaceae]	Theihai kung	Bark	F, M	Dysentery is treated by taking a decoction of dried bark.
<i>Melastoma malabathrium</i> L. [Melastomaceae]	Hmurkuong	Leaf	M	For diabetes, boiling leaf juice is consumed. Roots, bark, and stem are also edible.
<i>Mentha arvensis</i> L. [Lamiaceae]	Pudina	Leaf	M	Leaf juice is used as an ear drop as well as a remedy for stomachaches.

An ethnobotanical survey of plants used by the people of the hmar tribe of dima hasao district ...

Plant name (Family)	Vernacular name	Parts used	Purpose of use	Mode of use
<i>Mikania micrantha</i> Kunth. [Asteraceae]	Japanrang	Leaf	M	Leaf juice is consumed to treat piles as well as cuts and allergies.
<i>Mimosa pudica</i> L. [Mimosaceae]	Nuorhlo/Hlonuor zung	Root	M	To treat toothaches, root paste is applied to the teeth.
<i>Momordica charantia</i> L. [Cucurbitaceae]	Chankha	Leaf	M	Leaf decoction is fed to lower high blood pressure.
<i>Moringa oleifera</i> Lam. [Moringaceae]	Daingul	Bark	M	To relieve bone pain and fracture, bark paste is put on the affected area of the bone and tightly tied with the aid of a cloth. For stomach aches, a tender stem is used.
<i>Opuntia dillenii</i> Haw. [Cactaceae]	Kata kung	Whole plant	M	Plant aerial parts are warmed to use in bites of insects and snakes.
<i>Oxalis corniculata</i> L. [Oxalidaceae]	Inrainuthei	Root	M	To treat toothaches, powdered root is placed on the teeth.
<i>Piper betle</i> L. [Piperaceae]	Pan	Leaf	M	Leaf juice is applied in cuts to reduce pain due to scorpion stings
<i>Piper nigrum</i> L. [Piperaceae]	Hmarcha-inhlum	Fruit	M	Fruit powder is used for cough, sore throat, and other throat issues.
<i>Polygonum orientale</i> L. [Polygoniaceae]	Mirongru	Whole plant	M	Fish can be caught with ease by sprinkling whole plant powder on water.
<i>Psidium guajava</i> L. [Myrtaceae]	Kawlthuzik	Leaf	M	Dysentery is treated with leaf juice, abdominal pain is treated with tender leaf juice.
<i>Punica granatum</i> L. [Punicaceae]	Thaebufai	Leaf	M	For the treatment of dysentery and gastric issues, leaf twig extract is taken.
<i>Ricinus communis</i> L. [Euphorbiaceae]	Muthi	Leaf	M	Leaf juice is consumed to treat stool issues like constipation.
<i>Saccharum officinarum</i> L. [Poaceae]	Mafu	Stem	M	Jaundice and liver issues are treated with stem juice.
<i>Scoparia dulcis</i> L. [Scrophulariaceae]	Khuongabaihlo	Whole plant	M	In diabetes, extract of the aerial parts is consumed with water.
<i>Solanum indicum</i> L. [Solanaceae]	Tawkrakur	Fruit	M	To treat toothaches, fruit is boiled in mustard oil and tightly tied with a piece of cloth just below the ear or cheek.
<i>Solanum torvum</i> Sw. [Solanaceae]	Samtawkte	Fruit	M	On an abscess, fruit paste is applied locally.
<i>Spilanthes paniculata</i> wall.ex.Dc [Asteraceae]	Ansate	Leaf	M	A leaf decoction is consumed to treat pinworms
<i>Tabernaemontana divaricata</i> (L) Br. [Apocynaceae]	Pararsi	Juice	M	Juice made from leaf twigs is ingested in an early stage of cancer.
<i>Tamarindus indica</i> L. [Ceasalpinaceae]	Simkerlet	Seed & Leaf	M	Half of a warmed seed placed above a fire is applied to the area of snake and dog bites.
<i>Terminalia arjuna</i> (Roxb.) Wight. [Combretaceae]	Arjun	Bark	M	Bark has been soaked in water for one night and extract fed in digestive upset.
<i>Thunbergia grandiflora</i> (Roxb.ex Rottl.) Roxb. [Thunbergiaceae]	Vaakhrui	Node	M	Watery juice made from the node inter-node is applied locally to the eyes in conjunctivitis.

Plant name (Family)	Vernacular name	Parts used	Purpose of use	Mode of use
<i>Urena lobata</i> L. [Malvaceae]	Vawkpuihner-kawl	Root	M	Dysentery and hyperacidity are treated with root powder diluted in rice water or plain water. Also used as a toothbrush is the stem.
<i>Zingiber officinale</i> Rosc. [Zingiberaceae]	Aithing	Rhizome	S, M	Coughs are treated by taking rhizome juice. Inflammation is reduced by applying leaf paste.

[Abbreviation used: F = edible fruit, V = Vegetable, M = Medicinal, S = Spices].

CONCLUSION

This study has uncovered important details on the edible plants, vegetables, and fruit that the Hmar tribe in the area uses for ethnomedicine. It is vital that locals are made aware of the medical benefits of these native plants and properly networked, as well as formulate plans to safeguard and conserve these species. To have such a reliable system, input from diverse societal sectors, professions, and strata will be necessary. However, because ethnic or tribal people used to sell these plants on the market for high rates, many of the ethnomedicinal plants are now becoming scarce. The overuse of many useful therapeutic plants in nature demonstrates how uncommonly they are found in rural areas. To preserve the genetic resources of the plants and their long-term uses, an immediate effort must be made to safeguard these ethnomedicinal plants by mass propagation and the cessation of overexploitation of local medicinal plants from other regions of the Dima Hasao district. Additionally, comparable research must be started in other tribes as well.

ACKNOWLEDGEMENT

The authors are thankful to all informers for supporting the Field survey and to the Head, Department of Botany, Tripura University for providing the all facilities. The first author is grateful to Tripura University for financial assistance.

REFERENCES

Abu-Rabia A (2005) Urinary diseases and ethnobotany among pastoral nomads in the Middle East. *J Ethnobiol Ethnomedic* 1: 4, <https://doi.org/10.1186/1746-4269-1-4>.

Alagesaboopathi C (2009) Ethnomedicinal plants and their utilization by villagers in Kumaragiri hills of Salem district of Tamilnadu, India. *African J Tradition Complement Alternat Medic* 6(3): 222-227.

Albert LS, Gosai K (2006) Traditional use of medicinal plants by the Jaintia tribes in North Cachar Hills district of Assam, northeast India. *J Ethnobiol Ethnomedic* 2: 33, <https://doi.org/10.1186/1746-4269-2-33>.

Hossan M, Roy P, Seraj S, Sadia MM, Mirza NM *et al.* (2012) Ethnomedicinal knowledge among the Tonchongya tribal community of Roangchaari Upazila of Bandarban district, Bangladesh. *Americ-Euras J Sustainab Agricult* 6(4): 349-359.

Karki M, Williams JT (1999) Priority species of medicinal plants in South Asia. Medicinal and Aromatic Plants Programme in Asia (MAPPA), IDRC/SARO, New Delhi, India.

Mondal T, Dey S, Isore DP, Samanta S, Banerjee A *et al.* (2023) Detection of drug-resistant extended-spectrum and AmpC β -lactamases producing *Escherichia coli* from poultry faecal samples in West Bengal, India. *Explor Anim Med Res* 13(1): 31-38, DOI: 10.52635/eamr/13.1.31-38.

Ojha SN, Tiwari S, Anand S, Sundriyal RC (2020) Ethnomedicinal knowledge of a marginal hill community of Central Himalaya: diversity, usage pattern, and conservation concerns. *J Ethnobiol Ethnomedic* 16:29.

Pattanayak S, Mandal TK, Bandyopadhyay SK (2016) Validation and therapeutic use of succulent plant parts - opening of a new horizon of alternative medicine. *Explor Anim Med Res* 6(1): 8-14.

Pattanayak S (2018) Alternative to antibiotics from herbal origin - outline of a comprehensive research project. *Current Pharmacogenom Personali Medic* 16: 09-62, DOI: 10.2174/1875692116666180419154033.

Pattanayak S (2020) Succulent biomedicines - an effective way of getting protection against diseases through immunomodulation. *Explor Anim Med Res* 10(2): 112-123.

Pattanayak S (2021a) Plants in healthcare: past, present and future. *Explor Anim Med Res* 11(2): 140-144, DOI: 10.52635/eamr/11.2.140-144.

An ethnobotanical survey of plants used by the people of the hmar tribe of dima hasao district ...

Pattanayak S (2021b) Anti-COVID-19 biomedicines - a layout proposal for production, storage and transportation. *The Open Covid J* 1: 166-188, DOI: 10.2174/2666958702101010166.

Pattanayak S (2022a) Research targeting business profits: impacts on health and environment. *Explor Anim Med Res* 12 (1): 1-7, DOI: 10.52635/eamr/ 12.1.1-7.

Pattanayak S (2022b) Prevention and control of diabetes by intake of succulent biomedicines and following of designed lifestyle: A ready plan for execution. *Internati J Scientific Res Updates* 3(2): 081-103. <https://doi.org/10.53430/ijrsru.2022.3.2.0047>.

Pradhan DK, Ghosh J, Lepcha N, Nandi A, Banerjee D *et al.* (2021) New ethnomedicinal information from Lepcha community of Dzongu, Sikkim. *Explor Anim Med Res* 11(2): 179- 187, DOI : 10.52635/eamr/11.2.179-187.

Patel A, Shah H, Gandhi T (2022) Saponin rich fraction of *Bauhinia variegata* Linn. ameliorates kidney stone

formation in Rats. *Explor Anim Med Res* 12(1): 74-84. DOI: 10.52635/eamr/ 12.1.74-84.

Paul A, Sujatha K (2022) Concurrent effect of *Linum usitatissimum* and *Emblica officinalis* on lead induced oxidative stress and histomorphological changes in uterus of female Wistar rats. *Explor Anim Med Res* 12(2): 264-272, DOI: 10.52635/eamr/12.2.264-272.

Pushpangadan P (1995) Ethnobotany in India: A Status Report. All India Co-ordinated Research project Ministry of Environment and Forests. New Delhi: Government of India.

Srinivas K, Ghatak S, Angappan M, Milton AAP, Das S *et al.* (2023) Occurrence of antimicrobial resistance genes prior to approval of antibiotics for clinical use: evidences from comparative resistome analysis of *Salmonella enterica* spanning four decades. *Explor Anim Med Res* 13(1): 71-84, DOI: 10.52635/eamr/13.1.71-84.

***Cite this article as:** Das A, Ngente NN, Bhattacharya P, Kar S, Datta BK (2023) An ethnobotanical survey of plants used by the people of the *Hmar* tribe of Dima Hasao district, Assam, North East India. *Explor Anim Med Res* 13(Ethnomed. Spl.): 141-147, DOI: 10.52635/eamr/13(S)141-147.

See discussions, stats, and author profiles for this publication at: <https://www.researchgate.net/publication/376032417>

PSEUDELEPHANTOPUS (ASTERACEAE: VERNONIOIDEAE), A NEW GENERIC RECORD FOR TRIPURA, INDIA

Article · September 2023

DOI: 10.61080/JETB/V47/I3/2023/121-123

CITATIONS

0

READS

39

6 authors, including:



Panchatapa Bhattacharya

Tripura University

9 PUBLICATIONS 0 CITATIONS

SEE PROFILE



Aparajita Das

Tripura University

15 PUBLICATIONS 9 CITATIONS

SEE PROFILE



Somnath Kar

Tripura University

35 PUBLICATIONS 45 CITATIONS

SEE PROFILE



Dixit Bora

Tripura University

12 PUBLICATIONS 3 CITATIONS

SEE PROFILE

PSEUDELEPHANTOPUS (ASTERACEAE: VERNONIOIDEAE), A NEW GENERIC RECORD FOR TRIPURA, INDIA

Panchatapa Bhattacharya*, Aparajita Das, Somnath Kar¹, Dixit Bora, Sani Das and Badal Kumar Datta

Plant Taxonomy and Biodiversity Laboratory, Department of Botany, Tripura University, Suryamaninagar–799 022, Tripura, India

¹Department of Botany, Holy Cross College, Jubatara, Lembucherra, Tripura, India

*Email (Corresponding author): panchabhat96@gmail.com

Introduction

Tripura (22°56'– 24°32' N; 91°09'–92°20' E) is the second smallest state in North-eastern India. It is located at the biogeographical convergence of the Indo-Burma zone (Rao, 1994) and constitutes a part of the IUCN recognized Indo-Burma biodiversity hotspot (Mittermeier *et al.*, 2004). The environment of Tripura was greatly influenced by its undulating topography, high terrain and rainfall (Kar & Datta, 2015).

During the field surveys (Feb. 2022 to March 2023) in Tripura state, specimens of an interesting Compositae/Asteraceae were gathered from Suryamaninagar of West Tripura and Bishalgarh of Sipahijala districts. On careful observation, coupled with scrutiny of pertinent literature (Deb, 1981–1983; Bunwong & Chantaranonthai, 2010; Das, 2014), the specimens were identified as of *Pseudelephantopus* Rohr, a genus of Compositae so far not been recorded from Tripura state by Deb (1981–1983) or later workers on its flora.

The genus *Pseudelephantopus* Rohr (Asteraceae: Vernonioideae: Vernonieae) is native to the New World, from Mexico to tropical America, with two accepted species, namely *P. spicatus* (B.Juss. ex Aubl.) Rohr ex C.F.Baker and *P. spiralis* (Less.) Cronquist (POWO, 2023). The present collection is identified as of *P. spicatus* which is the only species known from India, as an introduction. Hitherto it was reported from Assam, Uttar Pradesh and West Bengal. Therefore, the present discovery of the genus constitutes a new generic record for Tripura state, India. The voucher specimen is deposited in the herbarium of the Department of Botany, Tripura University.

Taxonomic treatment

Pseudelephantopus spicatus (B.Juss. ex Aubl.) Rohr ex C.F.Baker, Trans. Acad. Sci. St. Louis 12(5): 56. 1902; N.M. Dutta & D.Mitra, Indian Forester 87(5): 308. 1961. *Elephantopus spicatus* B. Juss. ex Aubl., Hist. Pl. Guiane 2: 808. 1775. (Plate 1).

Description: Perennial herb, 12–65 cm high. *Stem* erect, branched, puberulous. *Leaves* rosulate or spiral at base, sub-sessile; basal leaves spatulate; distal ones elliptic, 5–18×1.5–6.5 cm, abaxially hirtellous, especially on veins, densely glandular, adaxially scabrous, or sub-glabrous, glandular; lateral veins 7–12 pairs; petioles up to 2 cm long; base attenuate, margin entire or remotely serrate, apex obtuse or shortly acute; upper leaves much shorter, linear-lanceolate, 4–12×0.2–1.5 cm, attenuate at ends; petioles 1.5–1.8 cm long. *Inflorescence* of several spicate-glomerate leafy branches, 1–7 head, supported by narrowly linear foliaceous bracts. *Capitula* tubular or oblong, 1.2–1.9 cm long; receptacle flat, 0.8–1.6 mm in diam., glabrous; phyllaries 8, light or dark green, 5–12 mm long, entire or filiferous, pilose, eglandular; the outer ones lanceolate, apex acute; the inner ones obovate-lanceolate or oblong, apex acute. *Florets* 4, salverform, white, zygomorphic, glabrous; corolla tube 4.5–9.5 mm long, 5-lobed; lobes lanceolate, 2.2–3.5 mm long. *Stamens* 5; anthers 1.2–2.5 mm long, apical appendages acute, bases acute. *Ovary* unilocular, style white, 5.4–9.5 mm long, pubescent, lobes 2. *Achnes* linear oblong, 5.5– 6.2 cm long pappus of 8–10, persistent; 2 of these twice-folded at apex (plicate), 2.2–7 mm long.

Flowering and fruiting: February–June.

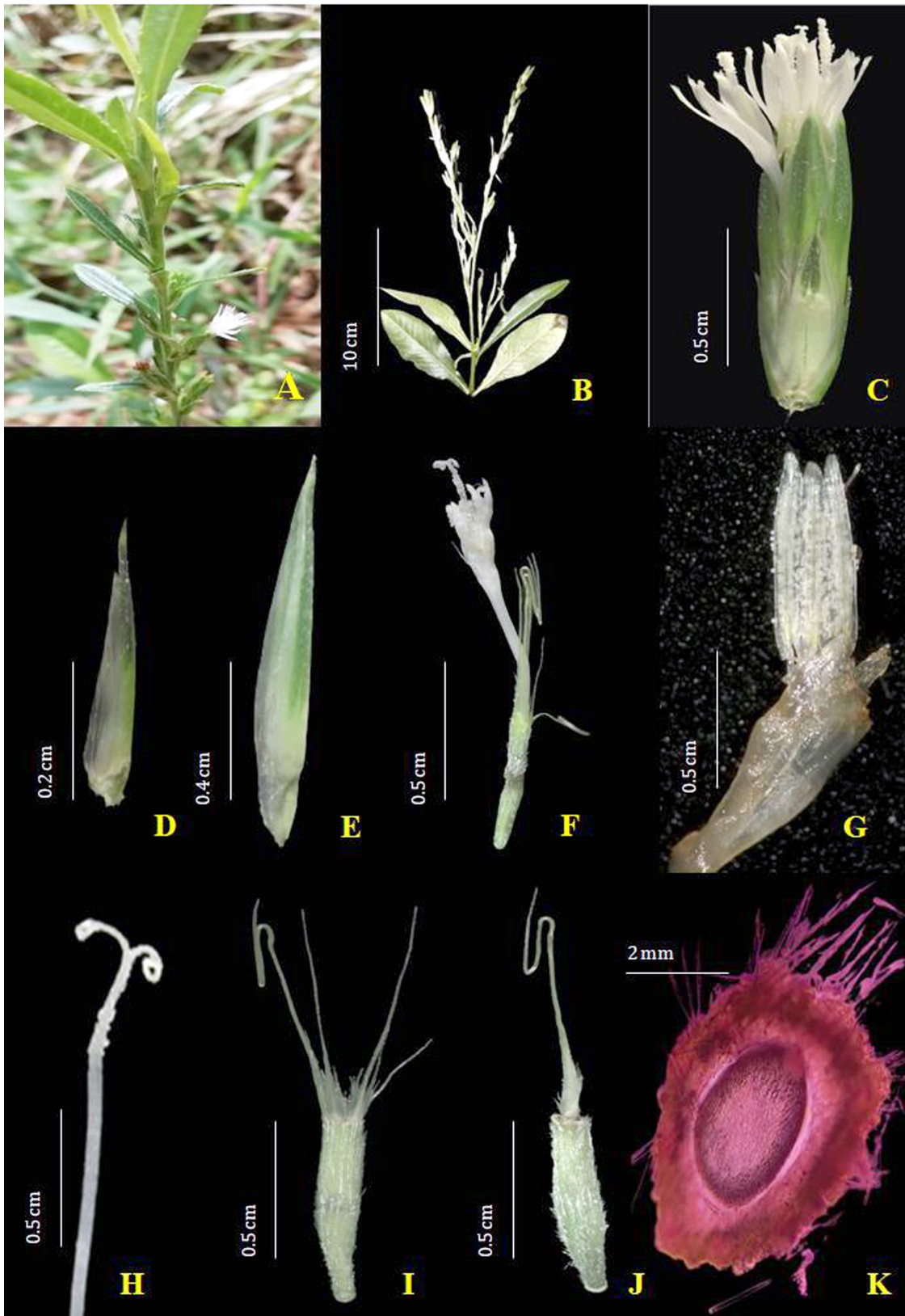


Plate 1. *Pseudelephantopus spicatus*: A–Habit in its habitat; B–Flowering twig; C–Capitulum; D, E –Dimorphic bracts; F–Single floret; G–Androecium; H–Style with re-curved stylar branches; I & J–Pappus; K–V.S. of ovary. [inverted with the placenta up]

Distribution: China, Philippines, Jamaica, Mexico, Malay Archipelago, Thailand, Taiwan, Africa and India: Assam, Tripura [present record], Uttar Pradesh and West Bengal.

Specimen examined: INDIA, Tripura: West Tripura distr., Suryamaninagar (23°45.00'50.40" N; 91°15'38.20" E; 24 m AMSL; 12.02.2022, *Bhattacharya & Datta* TUH-4307; Sipahijala distr., Bishalgarh: 23°33'57.8" N; 91°25'22.9" E; 33 m AMSL: 23.03.2022, *Bhattacharya & Datta* TUH-4359.

Note: The genus *Pseudelphantopus* has superficial semblance to *Elephantopus* of the same family wherein the capitula are usually terminal and more than 10, not spicate and the achenes bear pappus of many straight, scabrid-barbellate and basally widened awns. On the other, *P. spiralis*, the second species known of *Pseudelphantopus* is distinct being a stoloniferous herb, with achenes being resin-dotted, bearing single series of pappus of 5–10 bristle of more or less equal length (WFO, 2023).

Acknowledgements

The authors are thankful to the Head, Department of Botany, Tripura University, Tripura, for providing necessary facilities and the reviewer for his constructive suggestions and the Editor-in-Chief, JETB, for his valuable inputs.

References

- Bunwong, S. & Chantaranonthai, P. 2010. A new record of *Pseudelephantopus spicatus* (Juss. ex Aubl.) C.F.Baker (Asteraceae) from Thailand. *Thai Forest Bulletin, Botany* **38**: 124–127.
- Das, K.K. 2014. *Pseudelephantopus* J.P. Rohr (Asteraceae) – a new generic record for North-East India from Assam, India. *Pleione* **8**(1): 210–213.
- Deb, D.B. 1981–1983. *The Flora of Tripura State*. Vols. **1 & 2**. Today & Tomorrow's Printers and Publishers, New Delhi.
- Kar, S. & Datta, B.K. 2015. A glimpse of the traditional uses of plants by Kolois subtribe of Tripura. *Journal of the Botanical Society of Bengal* **69**(2): 147–152.
- Mittermeier, R.A., Robles-Gil, P., Hoffmann, M., Pilgrim, J., Brooks, T., Mittermeier, C.G., Lamoreux, J & Fonseca, G.A.B. da 2004. *Hotspots Revisited: Earth's Biologically Richest and Most Endangered Ecoregions*. CEMEX, Mexico City.
- POWO 2023. Plants of the World Online. Facilitated by the Royal Botanic Gardens, Kew. Published on the Internet (Accessed: 10 July 2023)
- Rao, R.R. 1994. *Biodiversity in India: Floristic Aspects*. Bishen Singh Mahendra Pal Singh, Dehra Dun.
- WFO, 2023. <https://www.worldfloraonline.org/taxon/wfo-0000084717> (Accessed: 10 July 2023).

Received: 21.03.2023 Revised: 11.08.2023 Published: 31.08.2023

See discussions, stats, and author profiles for this publication at: <https://www.researchgate.net/publication/374540738>

Floral biology and phenological studies of *Datura metel* L. in Tripura, Northeast India, with special reference to floral morphotypes

Article in *Plant Science Today* · October 2023

DOI: 10.14719/pst.2517

CITATIONS

0

READS

188

6 authors, including:



Aparajita Das
Tripura University

15 PUBLICATIONS 9 CITATIONS

[SEE PROFILE](#)



Somnath Kar
Tripura University

35 PUBLICATIONS 45 CITATIONS

[SEE PROFILE](#)



Panchatapa Bhattacharya
Tripura University

9 PUBLICATIONS 0 CITATIONS

[SEE PROFILE](#)



Sani Das
Tripura University

10 PUBLICATIONS 1 CITATION

[SEE PROFILE](#)



RESEARCH ARTICLE

Floral biology and phenological studies of *Datura metel* L. in Tripura, Northeast India, with special reference to floral morphotypes

Aparajita Das^{1*}, Somnath Kar², Panchatapa Bhattacharya¹, Sani Das¹, Dixit Bora¹ & B.K. Datta¹

¹Plant Taxonomy and Biodiversity Laboratory, Department of Botany, Tripura University, Suryamaninagar -799022, Tripura, India

²Department of Botany, Holy Cross College, Jubatara, Lembucherra, Tripura, India

*Email: dasaparajita0210@gmail.com



ARTICLE HISTORY

Received: 20 March 2023
Accepted: 23 July 2023

Available online
Version 1.0 : 07 October 2023
Version 1.1: 15 October 2023



Additional information

Peer review: Publisher thanks Sectional Editor and the other anonymous reviewers for their contribution to the peer review of this work.

Reprints & permissions information is available at https://horizonepublishing.com/journals/index.php/PST/open_access_policy

Publisher's Note: Horizon e-Publishing Group remains neutral with regard to jurisdictional claims in published maps and institutional affiliations.

Indexing: Plant Science Today, published by Horizon e-Publishing Group, is covered by Scopus, Web of Science, BIOSIS Previews, Clarivate Analytics, NAAS, UGC Care etc. See https://horizonepublishing.com/journals/index.php/PST/indexing_abstracting

Copyright: © The Author(s). This is an open-access article distributed under the terms of the Creative Commons Attribution License, which permits unrestricted use, distribution and reproduction in any medium, provided the original author and source are credited (<https://creativecommons.org/licenses/by/4.0/>)

CITE THIS ARTICLE

Das A, Kar S, Bhattacharya P, Das S, Bora D, Datta B K. Floral biology and phenological studies of *Datura metel* L. in Tripura, Northeast India, with special reference to floral morphotypes. Plant Science Today (Early Access). <https://doi.org/10.14719/pst.2517>

Abstract

Datura metel L. is an important medicinal plants of Tripura. There are four floral morpho-types found throughout India. The floral biology of four morpho-types of *D. metel* collected from different places of Tripura state have been investigated based on their morphological and palynological study. Initiation of the floral bud, anthesis, pollen viability, pollen germination, and pollen production are the topics covered in the present study. The present study includes photographic representations and UPGMA dendrogram for quick identification, as well as a detailed explanation of four morpho-types of the species.

Keywords

Floral morphs, Floral visitors, Pollen germination, Reproductive success

Introduction

Datura is an important genus of the *Solanaceae* family and comprises approximately 15 species. In India, five species of *Datura*, *Datura metel* L., *D. stramonium* L., *D. ferox* L., *D. innoxia* Mill. and *D. quercifolia* Kunth were recorded. As the name "Datur" is derived from the Indian word for the seed capsule "Dhatura", the term "Dhatura" commonly refers to *Datura metel* (1). However, any species belonging to the entire genus may also be referred to as "Dhatura" (2). *Datura metel* is a perennial herbaceous plant that can grow to a height of 1.5 metres. The leaves of the plant are dark green, glabrous, simple, alternate, broadly ovate, and shallowly lobed. Flowers are huge, solitary, trumpet-shaped, and have a sweet aroma that is typically savoured in the mornings and nights. Colour of the flowers vary from white to yellow and light to dark purple and pollination is through insects. Different colours of corolla and sweet fragrances of *D. metel* attract the insects. The fruit is a capsule and it is covered by tiny spines. The plant is typically found growing in waste areas and along roadsides. This plant tolerates mediocre soil but prefers rich, moist soil. Since 16th century, the use of the genus *Datura* has been established in traditional medicine, associated with its psychotropic, anticholinergic, and anti-inflammatory effects (3). Night-blooming *Datura* species, such as *D. innoxia*, *D. metel*, *D. stramonium* and *D. wrightii* are grown for their attractive, funnel-shaped and scented blooms (4).

Studies of reproductive biology or floral biology are essential for the successful cultivation, conservation and genetic improvement of plants (5-7). Knowledge of the floral structure and breeding systems is important for the controlled pollination and crossing of any species. Inflorescence structure influences the foraging efficiency of insects, the degree of outcrossing and other aspects of plant reproductive success (8). There has been no previous

record of published studies on reproductive biology, including the floral structure, floral morphs and development of *D. metel*.

Materials and Methods

Six populations of *D. metel* were selected for the present investigation in the natural conditions. The selected places were Damdamia (N 23°53 '48.9" and E 091°18'27.6"), Mohanpur (N 23°58'15.0" and E 091°22'20.5"); Khowai (N 24° 04 '03.5" and E 091°36'15.2"); Bishalgarh (N 23°33 '57.8" and E 091°25'22.9"); Dhalai (N 24°11 '48.7" and E 091°49'42.5") and Udaipur (N 23°33 '02.2" and E 091°27'48.9").

As per the field investigation, the species exhibited four different floral morphs (morphs 1, 2, 3, and 4) that could be distinguished by the colour of the corolla and shape of the capsules. The first morph type (morph 1) had an entirely purple corolla; the second morph (morph 2) displayed a completely purplish white corolla; the third morph (morph 3) had white corolla; and the fourth morph (morph 4) had yellow corolla. The shape of fruit capsules is an important character of *Datura* for proper identifications. Here, round to ovoid shape capsule were present in morph 1, oval shape capsule in morph 2, broad-ovoid capsule in morph 3 and ovoid-ellipsoid capsule in morph 4. The samples were collected when they were in full bloom and images of the flowers were taken with a Nikon (D5600) camera, and some fresh specimens were collected from the field for further taxonomic authentication. Morphological and morphometric analysis were performed using a stereo microscope (Stimi508, Carl ZEISS), binocular microscope (OLYMPUS CX23), and a scanning electron microscope (Sigma 300, Carl ZEISS) at the Central Instrument Centre, Tripura University, India. Various important characteristics of four floral morphs of *D. metel* L., UPGMA dendrograms (Fig. 4) were created based on the floral morphometric properties. The processed specimens (9) were placed in the Tripura University Herbarium (TUH).

Five healthy plants were chosen from each population and the phenological characters were observed periodically in the natural habitat. Habit of the plant, the time of anthesis, floral bud initiation and blooming were noted during systematic observational study. Morphological and morphometric studies of flowers were carried out using a hand lens and a dissecting microscope. The process and the pollinating agents of the flowers were noticed and documented (Plate 1 and 2). The morphology and morphometric analysis of acetolysed pollen, mounted in glycerine jelly was performed under oil-immersion (10, 11). *In-vitro* pollen germination and pollen tube germination was carried out following the standard methods (12, 13). Acetocarmine (2%) and 2, 3, 5-triphenyl tetrazolium chloride (TTC; 1%) solutions were used to examine pollen fertility and pollen viability respectively (14, 15). The pollen germination study was conducted using various concentrations of sucrose solution (2%, 5%, 10%, 15%, 20%, 25%, 30%, 35%, and 40%) and 10% sucrose solution combined with various concentrations of boric acid. Stigmas of various ages were fixed in Carnoy's fixative for 3 to 4 hours, stained with aniline blue-lactophenol, and then

examined under a microscope to determine the stigma receptivity (16). The stigmas with the developing pollen grains were regarded to be receptive and the pollen-ovule ratio was determined using Dafni's method (17).

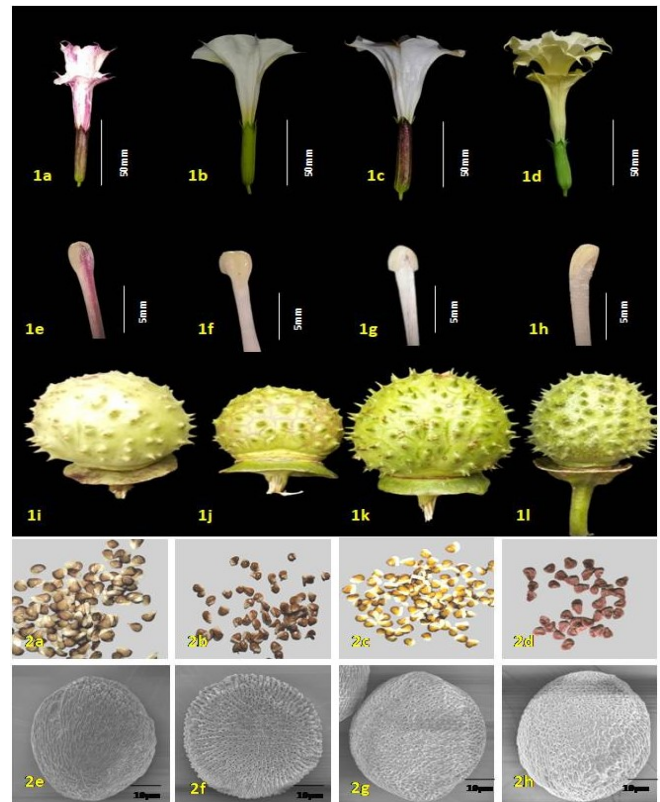


Plate 1: 1a) Flower, 1e) Stigma, 1i) Fruit, 2a) Seeds and 2e) Pollen of Morph 1; 1b) Flower, 1f) Stigma, 1j) Fruit, 2b) Seeds and 2f) Pollen of Morph 2; 1c) Flower, 1g) Stigma, 1k) Fruit, 2c) Seeds and 2g) Pollen of Morph 3 and 1d) Flower, 1h) Stigma, 1l) Fruit, 2d) Seeds and 2h) Pollen of Morph 4 of *Datura metel*.

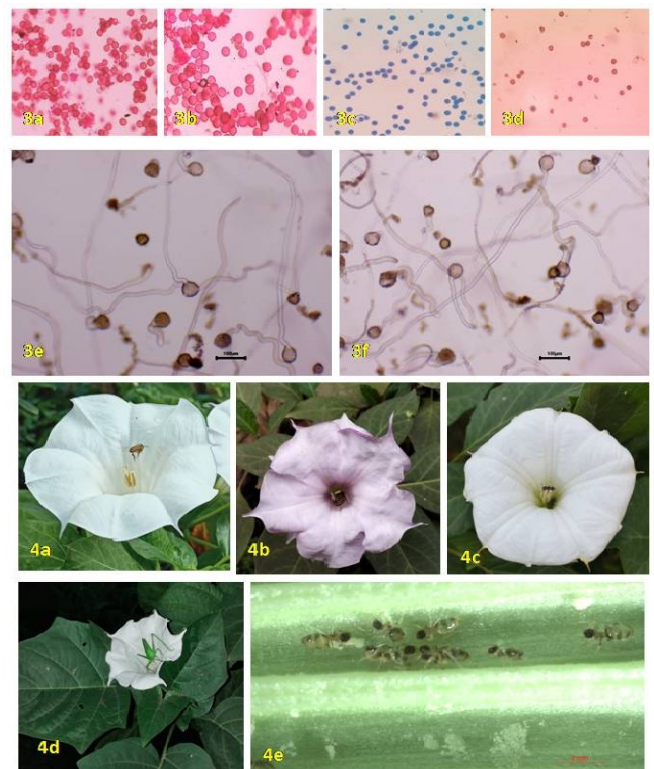


Plate 2: 3a) Muntzing's mixture, 3b) 2% Aceto-carmine, 3c) Lactophenol cotton blue, 3d) TTC pollen viability slides of *Datura metel* L.; 3e) Pollen germination in 10% sucrose of *Datura metel* L., 3f) Pollen germination in 10% sucrose with 500 ppm Boric acid solution of *Datura metel* L.; 4a), 4b), 4c), 4d) and 4e) Different pollinators of *Datura metel* L.

Results

Floral Phenology

All of the plant phenotypes were observed from April 2019 to October 2020, and then again from May 2021 to April 2022. The blooming period of all the plants were lasted for 2-3 months; however in *D. metel* it was throughout the year, but its prime flowering time was from the end of March to the middle of December. It took 18-20 days for vegetative shoots to produce floral buds, however, it took only 12-15 days for the buds to bloom. The ovary produces ripe fruits after 15-25 days of pollination. It was discovered that on rainy days, the process of anthesis, when the flower emerges from its bud, is delayed by an hour. Between 4 and 5 O'clock, anthesis occurred, and between 5 and 6 O'clock, the bloom unfolds. The average lifespan of a flower was 37.1 ± 0.75 hours with a range of 35 - 40 hours.

Floral Morphology

Inflorescence is solitary, in fork of branches; pedicel 5-6 mm in length, pedicel indumentums densely hairy. Calyx 60-90 mm in length, 34-55 mm in width, calyx indumentums densely hairy, purple or green in colour, calyx teeth 5, 10-16 mm in length, unequal, apex acuminate. Corolla infundibuliform, lobes 5-10, purple/yellow/white/purplish white in colour, 150-200 mm in length, 60-130 mm in width. Lobes 20-26 mm in length, apex acuminate. Stamens 5-7, filament 100-150 mm in length, hairy at adnate region, anther 13- 15 mm in length, 0.2-3.2 mm in width, yellowish white in colour, anther indumentums sparsely hairy. Ovary ovoid, carpel 2, 4-8 mm in length, 3-6 mm in width, style 118-150 mm in length, stigma 3-4 mm in length, 2-3 mm in width.

Pollinating agents

There were a total 10 genera of floral visitors out of which *Apis* sp., *Alphitobius diapernus*, and *Tapinoma melanocephelum* were the significant floral visitors. Pollination activity was most conveniently operated during 6 am to 12 pm, and it slowly declined later. It was found that *Apis* sp. regularly visited the flowers during the day time for pollination. It has been recorded that *Alphitobius diapernus* visited during the pollination one to three flowers per spell. The duration of the visit was 10 to 30 seconds per flower. *Tetragonula* sp. were significant floral visitor in Morph 1, 2 & 3; *Alphitobius diapernus* were in Morph 2 & 4 and *Camponotus compressus* were in Morph

1, 2 & 3. Bees would visit one to six blooms at a time, staying for four to sixty seconds each time. The pollination method, which was determined to be most useful, involved *Apis* sp. visiting the flowers to gather pollen and nectar. They frequently move from one flower to another, which may facilitate pollen transport. After the flowers are opened, the visitors to the blooms begin their activities. During cloudy days, there is less insect activity. Flowers with morph 1 and morph 2 had the highest frequency of floral visitors, whereas flowers with morph 4 (entirely yellow) had the lowest frequency (Table 2).

Stigma receptivity

In *D. metel*, the stigma became receptive between 15 and 17 hours before flowering, and the flowers bloomed between 17 and 18 hours. During the second day of blossoming, the stigma was still open. The stigma was glossy and yellowish when in the receptive condition and turned blackish red when the receptivity is lost. In *D. metel*, the stigma receptivity lasted anywhere from a few hours to a few days. The time of day and the existence or absence of stigmatic exudates may have an impact on the susceptibility to stigma. Environmental elements like temperature and humidity have an impact on the receptivity period. Typically, the stigma's receptive period lasted until the third day of flowering on overcast and wet days. Also correlated with the shift in blossom colour is stigma receptivity. According to the findings, the stigma of morph 1 was more receptive than those of the other three morphs.

Pollen Viability

Pollen viability is the ability to successfully complete fertilisation on a suitable, receptive stigma and carry out the post-pollination activities. Pollen viability also known as pollen stainability as it depends on the staining method (18). In order to discriminate between viable and nonviable pollen grains as well as fertile and sterile pollen grains, all of the colours used in this experiment demonstrated good colour contrast.

A high likelihood of fertilisation may be ensured by the pollens of *D. metel*, which demonstrated great viability and fertility rates. The pollens of morph 2 showed higher percentages i.e. 95% than the other floral morphs in all tests for viability and fertility (Fig. 1).

Table 1. Comparison of different essential characters of four floral of morphs of *Datura metel* L.

Parameters	Morph 1	Morph 2	Morph 3	Morph 4
Calyx size	60 mm (<70mm)	69 mm (<70mm)	78mm (<100mm)	82mm (<100mm)
Calyx teeth no.	5 (2+1+2)	5 (2+3)	5 (2+1+1+1)	5 (2+1+1+1)
Corolla size	177mm(<200mm)	182mm(<200mm)	192mm(<200mm)	203mm (>200mm)
Stamen size	13 to 14 mm	15mm	15mm	14mm
Pollen size	P	50.71 ± 0.91	44.70 ± 0.63	47.66 ± 0.85
	E	48.60 ± 1.14	47.92 ± 0.52	43.23 ± 0.95
Style length	119 mm	126mm	124mm	148mm
Ovule number (Mean±SE)	205.4 ± 1.99	210.6 ± 2.85	208.8 ± 2.03	197.6 ± 1.46
Fruit size (Mean±SE)	43.8 ± 0.95	52.8 ± 1.37	50.3 ± 1.00	39.1 ± 0.86
Seed weight (Mean±SE)	0.0167 ± 0.00	0.0182 ± 0.00	0.0189 ± 0.00	0.0160± 0.00

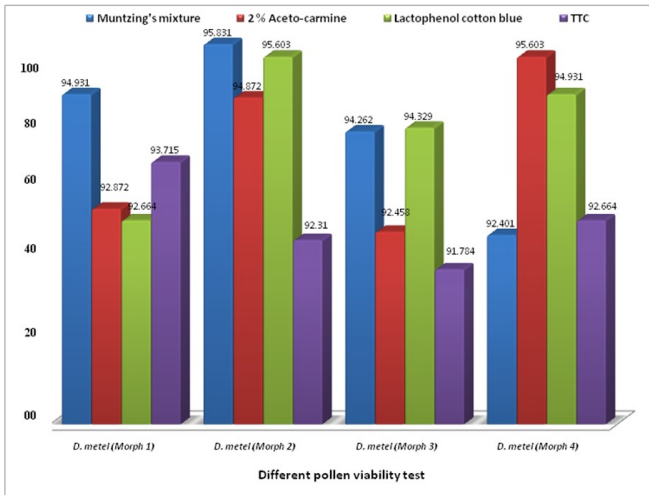


Figure 1: Pollen viability of four floral morphs of *Datura metel*.

Pollen germination

In this study, the pollen grains displayed the highest rates of germination (81.18% by *D. metel* morphs 1 respectively) and pollen tube formation ($705.433 \pm 61.376 \mu\text{m}$, $785.42 \pm 18.95 \mu\text{m}$ by the morphs 1, 2 respectively) in 10% sucrose solution. The maximum pollen germination rate (80.01 ± 1.16) by morph 1 in *D. metel* and the largest pollen tube development ($814.37 \pm 25.67 \mu\text{m}$) by morph 3 were seen in 500 ppm Boric acid +10% sugar solution, which was one of several concentrations of boric acid and 10% sucrose solution (Fig. 2, 3).

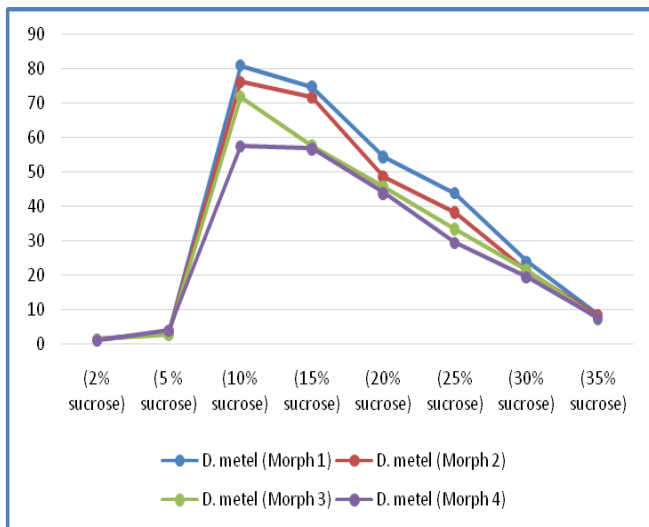


Figure 2: Extent of pollen germination in four floral morphs of *Datura metel* in different concentration of sucrose solution.

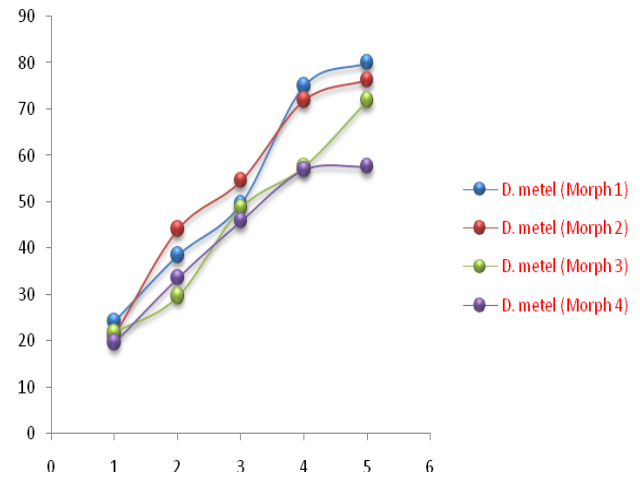


Figure 3: Extent of pollen germination in four floral morphs of *Datura metel* in different concentrations of boric acid along with 10% sucrose solution.

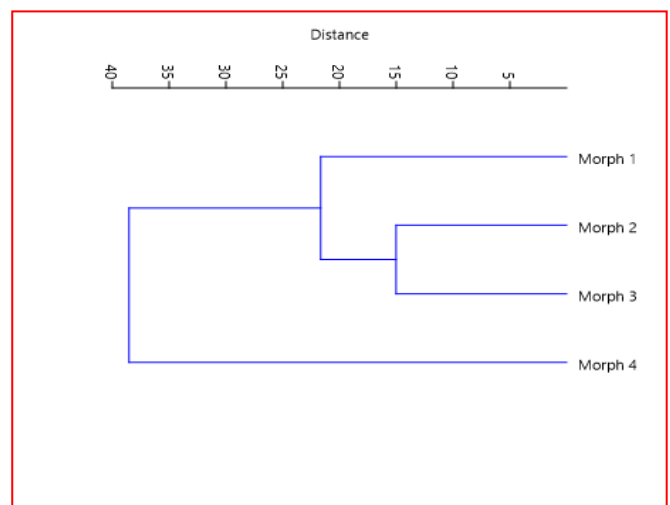


Figure 4: UPGMA dendrogram based on floral morphometric characters by Comparison of different essential characters of four floral of morphs of *Datura metel*.

Pollen: ovule ratio

According to Shivanna et al. (19), the pollen: ovule ratio is a more reliable indicator of reproductive success than the total amount of pollen in each flower or plant. During the present investigation estimated pollen: ovule ratio was found to be 8259.72 ± 153.50 in morph 1, 1994.25 ± 73.64 in morph 2, 2820.21 ± 175.922 in Morph-3 and 5251.4 ± 535.751 in morph 4 (Table 3). According to Cruden (20), xenogamous flowers had pollen: ovule ratios that ranged from 2108 to 19523. According to Cruden's findings and

Table 2. Floral visitors of four floral morphs of *Datura metel* L.

Sl. no.	Name of floral visitors	Family	Visiting time	Frequency of visitation			
				Morph 1	Morph 2	Morph 3	Morph 4
1.	<i>Tetragonula sp.</i>	Apidae	Day (8 am to 11am)	++	++	++	--
2.	<i>Alphitobius diaperinus</i>	Tenebrionidae	Evening (5 pm) to Night (1 am), Day (7 am to 10 am)	--	++	--	++
3.	<i>Forficula auricularisa</i>	Forficulidae	Day (2pm to 4pm)	++	--	++	++
4.	<i>Maladera sp.</i>	Scarabaeidae	Day (9 am to 11am)	++	++	++	--
5.	<i>Eunconocephalus thunbergi</i>	Tettigoniidae	Evening (5pm to 7pm)	++	++	--	--
6.	<i>Apis sp.</i>	Apidae	Day (6am to 11 am and 3pm to 5pm)	++	++	++	++
7.	<i>Tapinoma melanocephelum</i>	Formicidae	Night (9 pm) to Day (10 am)	--	++	--	++
8.	<i>Camponotus compressus</i>	Formicidae	Night (7 pm to 1am)	++	++	++	--
9.	<i>Aulacophora nigripennis</i>	Chrysomelidae	Day (6 am to 12pm)	++	--	++	++
10.	<i>Megacopta sp.</i>	Plastuspididae	Day (4 am to 11am)	--	--	++	++

the pollen-to-ovule ratio statistics for *D. metel*, the species is obligately xenogamous. Xenogamous flowers had pollen: ovule ratios that ranged from 2108 to 19523. According to Cruden's findings and the pollen-ovule ratio statistics for *D. metel*, the species is obligately xenogamous.

Reproductive Success

Morph 2 was able to produce the largest number of inflorescence per plant of 53 to 101 (mean \pm SD, 53.4 \pm 2.30, n = 50) and lowest in morph 4 varied between 34 and 84 (mean \pm SD, 34.4 \pm 4.602, n = 50), respectively. Whereas fruit set/inflorescence showed highest and lowest values in morph 4 (mean \pm SD, 125.82 \pm 4.91, n = 50) and morph 2 (mean \pm SD = 108.212 \pm 1.09, n = 50). The *D. metel* plant has the absolute/maximum reproductive potential (Rm) to produce 11320.6 \pm 378.97, 10703.6 \pm 579.82, 10857.8 \pm 699.07 and 7242.6 \pm 1013.99 seeds, respectively (Table 4). Morph 1 showed the highest value of maximum reproductive potential (Rm) and Ecological reproductive potential (Re) i.e. 11320.6 \pm 378.97 and 11270.4 \pm 400.92 (Table 4). This could be as a result of some significant ecological constraints.

Discussion

The four investigated floral morphs of *D. metel* of the family Solanaceae were characterized by some important floral morphological features which can serve as marker characters for the identified different morphs of this species (Plate. 1, 2). In previous studies morph 1 was considered as *D. metel* (21). But the present study clears the doubts abouts floral morphotypes of *D. metel*. It was observed that all studied floral morphs of *D. metel* showed that the initiation timing of floral buds takes 18 to 20 days to develop from vegetative shoots. Whereas, floral buds take 12-15 days to bloom. After pollination, the ovary takes 15-25 days to produce a mature fruit and the period of anthesis was 4.00 to 5.00 pm and the flower opens from 5.30 to 6.30 pm. In Table 1, there are comparisons of different essential

characters (calyx size, calyx teeth, corolla size, pollen size, stamen size, style length, ovule no., fruit size and seeds weight) of four floral morphs of *D. metel*. A total of 10 genera of floral pollinators were recorded. The important floral pollinators were *Apis* sp., *Alphitobius diapernus* and *Tapinoma melanocephelum*. From 6 am to 12 pm, there was a spike in the pollinator's activity. In the late afternoon and at night, there were fewer floral pollinators. The *Apis* sp. frequently visited the flowers during the day, whereas Thrips did so both during the day and at night. Almost one to three flowers were visited in a single spell by *A. diapernus* (Table 2). Flowers begin to bloom between 17.00 and 18.00 hours before the stigma became receptive. One to three flowers were visited in a single spell by *Alphitobius diapernus* (Table 2). Flowers begin to bloom between 17.00 and 18.00 hours before the stigma becomes receptive. During the second day of blossoming, the stigma is still open. The stigma is glossy and yellowish when in the receptive condition and turns blackish red when the receptivity is lost. All the dyes used in the experiment for pollen viability of four morphs of *D. metel* (Fig. 1) showed good colour to differentiate between fertile and sterile pollens viz., larger percentages of Muntzing's mixture (95.83% in morph 2), Acetocarmine (95.60 % in morph 4) and Lactophenol cotton blue (95.60% in morph 2). In the TTC test the percentage of viable pollen was 93.71% in morph 1 (Fig. 1). Saha & Datta (22) also found similar results in their experiments, emphasizing that pollen grain viability assessment through the staining method seemed to express the germination potential, but not its occurrence. It may be explained by the fact that this technique overestimates the percentage of pollen tubes formed. Pollen viability is considered as an important parameter of pollen quality (23). Pollen size and viability are good markers of the course of microsporogenesis. The effect of sucrose on *in vitro* pollen germination of *D. metel* showed that the four morphs of this species required comparatively low sucrose concentration (10%) for their optimal germination (Fig. 2). It was also observed that to some extent boric acid also influences the percentages of pollen germination. However,

Table 3. Pollen production and pollen: ovule ration in four floral morphs of *Datura metel* L.

Floral Attribute	Values (Mean \pm SE)			
	Morph 1	Morph 2	Morph 3	Morph 4
Number of Pollen per anther	339582.8 \pm 9304.23	75390.2 \pm 2211.45	115087 \pm 7857.53	77107 \pm 3144.16
Number of Pollen per flower	1697914 \pm 46521.14	376951 \pm 11057.24	587437 \pm 32219.6	1034388 \pm 99804.3
Number of ovule per flower	205.4 \pm 1.99	210.6 \pm 2.85	208.8 \pm 2.03	197.6 \pm 1.46
Pollen / Ovule Ratio	8259.72 \pm 153.50	1794.25 \pm 73.64	2820.21 \pm 175.92	5251.40 \pm 535.75
Assessment	The high P/O ratio along with high pollen production attributes to its high seed set.			

Table 4. Absolute and Ecological Reproductive Potential

Floral attributes	Morph 1 (Mean \pm SE)	Morph 2 (Mean \pm SE)	Morph 3 (Mean \pm SE)	Morph 4 (Mean \pm SE)
Inflorescences / plant	53.4 \pm 2.30	48.7 \pm 1.90	45 \pm 2.93	34.4 \pm 4.60
Fruit set	124.97 \pm 9.21	108.21 \pm 1.09	113.59 \pm 5.99	125.82 \pm 4.91
Seeds per fruit	202.5 \pm 5.15	191.5 \pm 2.50	179.5 \pm 5.43	125 \pm 5.51
Absolute / maximum reproductive potential (Rm)	11320.6 \pm 378.97	10703.6 \pm 579.82	10857.8 \pm 699.07	7242.6 \pm 1013.99
Ecological/realized reproductive potential (Re)	11270.4 \pm 400.92	10650.6 \pm 572.28	10776.2 \pm 701.02	7104 \pm 1020.75

the best result was obtained in 10% sucrose solution supplemented with 500 ppm boric acid (Fig. 2, 3). Lower concentrations than 300 ppm were shown to be toxic and to have the lowest germination rates in the four morphs of *D. metel*. Similarly, concentrations of boric acid, higher than 300 ppm showed larger pollen tubes and maximum germination percentages. Boron may increase the uptake of sucrose and induce germination because it is known to interact with sugar to form a sugar-borate complex, which is more easily transported than non-borate sugar molecules (19). Saha & Datta (24) and Kar & Datta (25) have also recorded similar results. The pollen: ovule ratio is 2108 to 19523. According to Cruden's findings and the pollen-ovule ratio statistics for *D. metel*, the species is represented obligately xenogamous. The present study represented the values of ecological reproductive potential (Re) i.e. 11320.6 ± 378.97 and 11270.4 ± 400.92 (Table 4). This could be as a result of some significant ecological constraints.

Conclusion

This article is the first to include full information on the floral biology and phenological investigations on floral morphotypes of *D. metel* L. This species has night blooming flowers and the floral opening occurs between 05:00 h to 06:00 h. Funnel shaped with different coloured corolla and are the main attractive structure to pollinating insects. The shape of fruit capsules is an important character to properly identify the four morphs of *D. metel*. The field experiment indicated classification *D. metel* as xenogamous flower according to the P/O ratio. The different concentrations of sucrose (2%, 5%, 10%, 15%, 20%, 25%, 30%, 35%) and boric acid (100ppm, 200ppm, 300ppm, 400ppm, 500ppm) used in the study of *in vitro* pollen germination. This study has to be expanded to include more *Datura* species in order to find cross-promoters for future crosses that will result in hybrids with the potential to be useful in agriculture, pharmacological, and ornamentation. This present work discusses that the floral biology and phenological studies of *D. metel* is valuable for understanding the reproductive biology and pollination ecology of other *Datura* species in addition to its critical implications for the preservation and management of this important plant.

Acknowledgements

Authors are grateful to Department of Botany and Central Instruments Centre (CIC) of Tripura University for providing necessary and FE SEM (Field Emission Scanning Electron Microscope) facilities during work.

Authors' contributions

AD and PB carried out the field survey and collected the specimens. SK and BD identified the specimens and conceived the study. AD carried out the field data analysis. SD and DB participated in design and coordination the manuscript. All authors read and approved the final manuscript.

Compliance with ethical standards

Conflict of interest: The authors do not have any competing interests to declare.

Ethical issues : None

References

1. Bouziri A, Hamdi A, Borgi A, Hadj SB, Fitouri Z, Menif K, Jaballah NB. *Datura stramonium* L. poisoning in a geophagous child: A case report. *Int J Emerg Med*. 2011; <https://doi.org/10.1186/1865-1380-4-31>.
2. Freye E. Pharmacology and abuse of cocaine, amphetamines, ecstasy and related designer drugs. Springer Dordrecht Heidelberg London New York. 2010; Pp: 215-18. <http://dx.doi.org/10.1007/978-90-481-2448-0>.
3. Benítez G, March-Salasb M, Villa-Kamelc A, Cháves-Jiménez U, Hernández J, Montes-Osunad N, Moreno-Chocanoa J, Cariñanos P. The genus *Datura* L. (Solanaceae) in Mexico and Spain – Ethnobotanical perspective at the interface of medical and illicit uses. *J Ethnopharmacol*. 2018;219:133-51. <http://dx.doi.org/10.1016/j.jep.2018.03.007>.
4. DeWolf GP. Notes on cultivated Solanaceae 2 *Datura*. *Baileya*. 1956;4:12-13.
5. Baskorowati L. Controlled pollination methods for *Melaleuca alternifolia* (Maiden & Betche) Cheel. ACIAR Technical Reports Series, Issue 63. (Australian Centre for International Agricultural Research: Canberra, ACT). 2006.
6. Moza MK, Bhatnagar AK. Plant reproductive biology studies crucial for conversation. *Curr Sci*. 2007; 92:1207.
7. Baskorowati L, Moncur MW, Doran JC, Kanowski PJ. Reproductive biology of *Melaleuca alternifolia* (Myrtaceae) 1. Floral biology. *Austral J Bot*. 2010;58:373-83. <http://dx.doi.org/10.1071/BT10035>.
8. Wyatt R. Inflorescence architecture – howflower number, arrangement and phenology affect pollination and fruit-set. *Amer J Bot*. 1982;69:585-94. <https://doi.org/10.2307/2443068>.
9. Jain SK, Rao RR. A handbook of field and herbarium methods. Today and Tomorrow Printers and Publishers, New Delhi. 1977; p.157.
10. Erdtman G. Pollen morphology and plant taxonomy-Angiosperms. Almqvist and Wiksell, Stockholm, Sweden. 1952;p.539. <https://doi.org/10.1080/11035895209453507>
11. Wodehouse RP. Pollen grains. McGraw-Hill Book Co., New York and London. 1935.
12. Taylor LP, Hepler PK. Pollen germination and tube growth. *Plant Physiol Plant Mol Biol*. 1997;48:461-91. <https://doi.org/10.1146/annurev.arplant.48.1.461>.
13. Nair PK, Rastogi K. Pollen production in some allergenic plants. *Curr Sci*. 1963;32:566-67.
14. Radford AE, Dickinson WC, Massey JR, Bell CR. Vascular plant systematics. New York, Harper and Row. 1974.
15. Norton JD. Testing of plum pollen viability with tetrazolium salts. *Am Soc Hort Sci*. 1966;89:132-34.
16. Hauser EJP, Morrison JH. The cytochemical reduction of nitroblue tetrazolium as an index of pollen viability. *Amer J Bot*. 1964;51:748-52. <https://doi.org/10.1002/j.1537-2197.1964.tb06696.x>.
17. Dafni A. Pollination ecology. Oxford University Press, New York. 1992; Pp.1- 57.
18. Bhowmik S, Datta BK. *In vitro* pollen germination in *Eichhornia Crassipes* (Mart.) Solms: An insight into its preferred mode of clonal reproduction. *Notul Sci Biol*. 2012;4 (2):65-71. <http://dx.doi.org/10.15835/nsb.4.2.7419>.

19. Shivanna KR, Johri BM. The angiosperm pollen structure and function. Wiley Eastern Ltd. Publisher, New Delhi. 1985;Pp.5-83.
20. Cruden RW. Pollen-ovule ratios: A conservative indicator of breeding systems in flowering plants. *Evolution*. 1977;31:32-46. <https://doi.org/10.2307/2407542>.
21. Das A, Kar S, Datta BK. Phenological and micro-morphological study on two *Datura* species of Tripura, North East India. *Biosystematics and Bioresources: The proceedings of the International conference on "Algae, Fungi and Plants: Systematics to Applications"*. Chapter-8. 2022; pp.129-13.
22. Saha M, Datta BK. Reproductive biology of *Solanum viarum* Dunal (Solanaceae) in Northeast India. *Pleione*. 2014;8(2):258-66.
23. Dafni A, Firmage D. Pollen viability and longevity practical, ecological and evolutionary implications. *Plant Syst Evol*. 2000;222:113-32. <https://www.jstor.org/stable/23644330>. https://doi.org/10.1007/978-3-7091-6306-1_6
24. Saha M, Datta BK. Reproductive biology of *Solanum sisymbriifolium* Lamk. (Solanaceae) in Tripura, North-East India. *Int J Plant Reprod Biol*. 2017;9(1):59-62.
25. Kar S, Datta BK. Floral biology of *Cajanus cajan* (L.) Millsp. (Leguminosae) in Tripura (India). *Pleione*. 2017;11(1):104-15.



General De Novo Programming Problem Under Type-2 Fuzzy Environment

Susanta Banik¹ · Debasish Bhattacharya¹

Received: 28 February 2022 / Revised: 23 August 2023 / Accepted: 9 November 2023
© The Author(s), under exclusive licence to The National Academy of Sciences, India 2023

Abstract The de novo programming technique is used to design an optimal system when the objectives and constraints are linear. It was initially introduced with crisp parameters. Later, de novo programming with fuzzy parameters has been studied to make it more flexible. But the fuzzy set has its limitations too. On the other hand, type-2 fuzzy sets are capable of embracing even those uncertainties that have not been covered or addressed by fuzzy sets. So the general de novo programming problem with interval type-2 fuzzy parameters has been introduced and studied here to make the system more reliable by removing the shortcomings of the human thinking process. This makes de novo programming better for modelling real-life problems than a fuzzy (type-1 fuzzy) logic-based system. The solution procedures for the proposed problem have been illustrated by a solid transportation problem.

Keywords De novo programming · Interval type-2 fuzzy set · Defuzzification · Multi-objective optimization · Min–max goal programming

Significance Statement: In this article, we have introduced general de novo programming problems in a type-2 fuzzy environment and developed a model with its solution procedure. This model can be used in managerial, portfolio selection, etc. problems. One application of this developed model is illustrated by a solid transportation problem. Now it is drawing the attention of researchers, and this article will motivate further investigation and application.

✉ Debasish Bhattacharya
debasish.math2021@gmail.com
Susanta Banik
susanta.banik580@gmail.com

¹ Department of Mathematics, National Institute of Technology Agartala, Agartala, Tripura 799046, India

MSC Classification 90C29 · 90C90 · 90C70

1 Introduction

The De Novo Programming concept was first proposed by Zeleny [1], to design an optimal system by extending existing resources if necessary instead of finding an optimum in a given system with fixed resources. This method was first designed for single-criteria decision making [1, 2], later, it was extended to multi-criteria decision making, containing the maximizing type of objectives only [3–5]. In real-life situations, the decision-maker often has to consider several objectives, like high quality of product, maximization of profit, employment stability, minimizing cost, etc., due to some social and other requirements. So the concept of the general de Novo programming problem (GDNPP) involving both maximizing and minimizing types of objectives came into the literature [6–8]. In GDNPP, the objectives are often conflicting in nature too. In multi-objective optimisations, due to the conflicting nature of the objectives, the decision-maker has to settle for some sort of compromise or trade-off solution. The main target of multi-objective de Novo programming (MODNP) is to obtain a trade-off free solution and full utilization of scarce resources. Thus, through MODNP, the decision maker can optimize the objectives simultaneously or obtain objective values that are close to their respective optimum values under a given budgetary provision using path ratios [9]. One salient feature of de Novo programming formulation is the introduction of budget constraints. Combining this budget constraint with the given structural and technological constraints, we can get a single constraint. The set of basic feasible solutions to the single constraint problem and that of the given problem are the same. A budget is expended to harness resources. With the

increase in budget allocation, more and more resources can be made available to the system, and thereby the feasible region of the solution gets extended. In the extended feasible region, one may find a point that simultaneously optimizes all the objectives. But no general method exists for the solution of GDNPP involving both maximizing and minimizing types of objectives [6–8].

In real-world problems, it is only rarely possible to determine the coefficients of the variables appearing in the de Novo programme or other linear and non-linear programmes with accuracy. So the decision-maker has to deal with inaccurate data, which adversely affects the solution obtained. Fuzzy sets address the uncertainty inherent in the human thinking process to some extent. In fuzzy sets, for each member of the universe of discourse or primary domain, a real number in $[0, 1]$ is assigned as a membership grade of the element. But such an assignment of a unique or crisp membership grade may not always be possible. So there are some uncertainties that remain unaddressed. This is a limitation of fuzzy sets. On the other hand, in type-2 fuzzy sets introduced by Zadeh [10] the membership functions are themselves fuzzy and hence are able to incorporate the uncertainties not being tackled by fuzzy sets. Thus, to encompass the uncertainty of a system more aptly in such situations, type-2 fuzzy sets (T2FSs) are preferred. T2FSs allow us to handle linguistic uncertainties as well as numerical uncertainties. A system described by a higher type (e.g., type-2) of fuzzy sets is regarded as one way to increase the fuzziness of the system [11]. Also according to Hisdal, increased fuzziness in a description means increased ability to handle inexact information in a logical manner [12]. Therefore, to make the construction of GDNPP more efficient and realistic in real-world applications, type-2 fuzziness in the parameters of GDNPP has been proposed in this paper.

But it is very difficult to manipulate T2FSs in numerical applications. However, the problem can be considerably simplified if the secondary membership grades of the T2FS are all taken as one. The resulting T2FS is called the interval type-2 fuzzy set (IT2FS), and it has the capacity to reflect uncertainties more than that of a fuzzy set or type-1 fuzzy set (T1FS). It has been shown that IT2FSs can outperform their T1FS counterparts in a variety of fields, including data and image processing and decision-making [13]. In the proposed model of GDNPP, the parameters of costs, technological coefficients, and unit prices of the resources used are all taken as IT2FS.

Again, to get the output of a decision process involving IT2FSs as parameters in crisp form (which is needed in practical applications), type reduction is a standard process adopted for the purpose. Using type reduction, a T2FS is first converted into a T1FS, and it is then defuzzified to get a crisp value. In both processes, the centroid of the respective

fuzzy sets is calculated, which is capable of capturing more about their uncertainties and thereby avoiding the chance of information loss. The defuzzified value is thus representative of the fuzziness involved in the corresponding parameter. The type reduction and consequent defuzzification of the interval type-2 fuzzy parameters have been accomplished by the KM Algorithm method [11, 13] and a new defuzzification method proposed in this paper. Thus, the GDNPP with interval type-2 fuzzy parameters (IT2FPs) has been converted to a crisp programme that retains the uncertainties of the original problem. It is then solved by the Min-max GP approach [14] in one-step.

2 Literature Survey

In the case of group decision-making problems, Wan et al. [15–17] developed new methods and also illustrated them with suitable examples. In the realm of multi-objective fuzzy linear programming, Dong and Wan [18, 19] developed new methods using trapezoidal fuzzy numbers. Further, a new two-state method for fuzzy multi-objective linear programmes was developed by Dong and Wan in [20] and the method was applied to solve the engineering portfolio selection problem.

Li and Lee [6] first introduced a two-phase fuzzy approach based on the ideal and negative ideal values of the objectives to solve a crisply defined GDNPP. Chen and Hsieh [7] introduced an innovative fuzzy approach for the solution of a multi-stage GDNPP using the fuzzy dynamic programming concept. Umarusman [8] employed the min-max goal programming (GP) technique for the solution of GDNPP in two steps and examined the closeness of the optimal objective values to the ideal values of the objectives. Chakraborty and Bhattacharya in [21, 22] further studied GDNPP and proposed a method for the solution of the problem in one step by fuzzy-fying the objectives using Zimmermann's technique [23]. Zhaung et al. [24] introduce the Meta-GP approach for solving GDNPP. Banik and Bhattacharya [25] further introduced a modified approach of min-max GP for solving GDNPP in one-step. Shi [26] applied MODNP to formulate and solve problems of system design that involved multiple decision-makers and a possible debt. Saeedi et al. [27] utilized de Novo programming techniques to determine the capacity of a closed-loop supply chain network when a queueing system is established at each recovery centre in the reverse flow. Helena Brozova [28] introduced optimal design of production systems with a generalized de Novo programming approach incorporating two more constraints, viz., requirement and balance constraints, other than the usual budget constraints. Also, Babic and Pavic [29], Huang et al. [30], and Chen and Tzeng [31] have contributed de novo programming literature with their studies.

Miao, D.Y. et al. [32] considered the interval fuzzy de Novo programming method for planning water resources systems under uncertainty. Zhang et. al [33] introduced the concept of inexact de Novo programming and used this concept to solve MODNP with inexact numbers as coefficients of objectives and constraints. Banik and Bhattacharya [34] introduced a one-step approach for solving GDNPP involving fuzzy parameters.

3 General De Novo Programming Problem

In this section, we will discuss the basic concept of the de Novo programming problem suggested by Zeleny [1]. The GDNPP with crisp parameters can be represented as

$$\begin{aligned} \text{Max } Z &= C^1 \mathbf{x} \\ \text{Min } W &= C^2 \mathbf{x} \end{aligned}$$

Subject to

$$\begin{aligned} \mathbf{Ax} &\leq \mathbf{b} \\ \sum_{i=1}^m p_i b_i &\leq B; \quad \mathbf{x} \geq 0 \end{aligned} \tag{1}$$

where $C^1 = [c_{kj}]_{r \times n}$; $C^2 = [c_{(l+r)j}]_{s \times n}$; $\mathbf{A} = [a_{ij}]_{m \times n}$; $\mathbf{b}^T = [b_1, b_2, \dots, b_m]$; $\mathbf{x}^T = [x_1, x_2, \dots, x_n]$; $\mathbf{Z}^T = [z_1, z_2, \dots, z_r]$; and $\mathbf{W}^T = [w_1, w_2, \dots, w_s]$.

Here, \mathbf{x} is the vector of decision variables for products; \mathbf{b} is the vector of the resource components (b_i); p_i is the cost per unit of i^{th} resources, which are known; $i = 1, 2, 3, \dots, m$; and B is the total available budget to harness the resources. The parameter $v_j = \sum_{i=1}^m p_i a_{ij}$ then denotes the per-unit cost of producing the j^{th} product. The de novo programme (1) can be re-written as,

$$\begin{aligned} \text{Max } Z &= C^1 \mathbf{x} \\ \text{Min } W &= C^2 \mathbf{x} \end{aligned}$$

Subject to

$$\begin{aligned} \sum_{j=1}^n v_j x_j &\leq B \\ x_j &\geq 0, \quad j = 1, 2, \dots, n \end{aligned} \tag{2}$$

The problem has been reduced to an equivalent problem containing only one constraint involving n arguments. It can be proved that every solution of the system (1) is also a solution of the system (2) and conversely, Zeleny [1]. Thus, with this restructuring, the generality of the system is not disturbed. In this paper, we have proposed type-2 fuzziness in the above system and designed a problem in which all the parameters, c_{kj} , $c_{(l+r)j}$, p_i , a_{ij} , B , are interval type-2 fuzzy numbers.

4 Type-2 Fuzzy Sets and its Defuzzification

Type-2 fuzzy sets were introduced by Zadeh [10] to provide additional design degrees of freedom for making the system more realistic, especially in situations where uncertainty manifests in many forms.

Definition 1 [10] A type-2 fuzzy set \tilde{A} in the universe of discourse X can be represented by a type-2 membership function $\mu_{\tilde{A}}$ shown as follows:

$$\begin{aligned} \tilde{A} &= \{((x, u), \mu_{\tilde{A}}(x, u)) \mid \forall x \in X, \\ &u \in J_x \subseteq [0, 1]; 0 \leq \mu_{\tilde{A}}(x, u) \leq 1\} \end{aligned}$$

where, $J_x = \{u \in [0, 1] : \mu_{\tilde{A}}(x, u) > 0\}$.

The T2FS \tilde{A} defined above can also be represented as follows:

$$\tilde{A} = \int_{x \in X} \int_{u \in J_x} \mu_{\tilde{A}}(x, u) / (x, u),$$

where $J_x \subseteq [0, 1]$ and $\int \int$ denotes the union over all admissible values of $x \in X$ and $u \in J_x$.

For the above definition one may refer to [35, 36].

4.1 Interval Type-2 Fuzzy Sets

Type-2 fuzzy sets are difficult to understand, and their type reduction, i.e., reduction from a T2FS to a T1FS, and consequent defuzzification procedures are also complicated. But as a particular case of T2FS, if we restrict the secondary membership function $\mu_{\tilde{A}}(x, u)$ values to either zero or one, i.e., to interval type set $\{0, 1\}$, the resulting T2FSs are called IT2FSs: [35–37]. IT2FSs are the most widely used T2FSs because of their simplicity in handling and, at the same time, their capacity to capture uncertainties better than a T1FS.

Definition 2 Let \tilde{A} be a T2FS in the universe of discourse X , which is represented by a type-2 membership function $\mu_{\tilde{A}}$. If $\mu_{\tilde{A}}(x, u) = 1, \forall x \in X, u \in J_x \subseteq [0, 1]$ then \tilde{A} is called an interval type-2 fuzzy set (IT2FS). An IT2FS \tilde{A} can be considered as a special case of T2FS, where the secondary membership function is the constant function 1 which is represented as follows:

$$\tilde{A} = \int_{x \in X} \int_{u \in J_x} 1 / (x, u)$$

where $J_x \subseteq [0, 1]$.

One can represent an IT2FS in a 2D plane graphically. The graph will look like a bounded region enclosed between two curves $u = u_x^L$ and $u = u_x^U$ of lower and upper primary membership values of u at each $x \in X$. The bounded region is called the Footprint of Uncertainty (FOU) [35].

Utilizing this concept, the notion of trapezoidal and triangular fuzzy numbers can easily be generalized in the realm of IT2FSs. In this paper, we considered the interval type-2 trapezoidal fuzzy set (IT2TrFS) for our study, which includes the interval type-2 triangular fuzzy set as a special case.

Definition 3 [38] An interval type-2 trapezoidal fuzzy set [IT2TrFS] \tilde{A} over the universe of discourse R (the set of all real numbers) can be represented by

$$\begin{aligned}\tilde{A} &= (A^U, A^L) \\ &= ((a^U, b^U, c^U, d^U; h_1(A^U), h_2(A^U)), \\ &\quad (a^L, b^L, c^L, d^L; h_1(A^L), h_2(A^L)))\end{aligned}$$

where A^U (resp. A^L) denotes the upper membership function (UMF) (resp. the lower membership function (LMF)) of the IT2TrFS \tilde{A} . Here $h_1(A^U)$, $h_2(A^U)$ respectively denote the upper membership function values at the point $x = b^U$ and $x = c^U$. Similarly, $h_1(A^L)$, $h_2(A^L)$ respectively denote the lower membership function values at $x = b^L$ and $x = c^L$.

Definition 4 [39] Fuzzy numbers are a special kind of fuzzy sets that are bounded, convex and its universe of discourse is the set of real numbers R . Trapezoidal fuzzy numbers are the most widely used fuzzy numbers.

The general arithmetic operation between Interval Type-2 Trapezoidal Fuzzy Numbers (IT2TrFNs) and its multiplication by real number has been studied in [40].

4.2 Type Reduction and Defuzzification

The process of type reduction of an IT2FS and subsequent defuzzification of the type-reduced T1FS have been accomplished here by two schemes.

- (i) In the first scheme, type reduction and defuzzification of IT2FS have been accomplished using the Karnik–Mendel Iterative Procedure (KMIP). This method is based on the centroid calculation of the given IT2FS.
- (ii) In the second scheme, a new method of type reduction for an IT2TrFS has been proposed, followed by defuzzification based on centroid calculation.

4.2.1 Karnik–Mendel Algorithm Method

The widely adopted method for type-reducing an interval type-2 fuzzy set (IT2FS) is the Karnik–Mendel Iterative Procedure (KMIP) [11]. The result of type reduction of an interval type-2 fuzzy set is an interval set (which is a particular case of type-1 fuzzy set) called the centroid of the considered IT2FS with a defuzzified value located at the midpoint of the interval set. The iterative procedure for finding the end points of the interval is accomplished by the efficient KM Algorithm.

Now we discuss the centroid computation technique of an IT2FS with the KM Algorithm.

Let $x_i (i = 1, 2, \dots, N)$ represent a discretization of the universe of discourse X of an IT2FS \tilde{A} . The centroid of IT2FS \tilde{A} , i.e., $c_{\tilde{A}} = [c_l, c_r]$ can be computed as the optimal solution of the following interval weighted average problems [11]:

$$\begin{aligned}c_l &= \min_{\theta_i} \left[\frac{\sum_{i=1}^n x_i \theta_i}{\sum_{i=1}^n \theta_i} \right], \quad c_r = \max_{\theta_i} \left[\frac{\sum_{i=1}^n x_i \theta_i}{\sum_{i=1}^n \theta_i} \right], \quad \forall \theta_i \\ &\in [\underline{\mu}_{\tilde{A}}(x_i), \bar{\mu}_{\tilde{A}}(x_i)]\end{aligned}$$

where, $\underline{\mu}_{\tilde{A}}(x_i)$, $\bar{\mu}_{\tilde{A}}(x_i)$ respectively denotes the lower and upper membership functions of the given IT2FS. Again c_l and c_r can be expressed as follows

$$\begin{aligned}c_l &= \frac{\sum_{i=1}^L x_i \bar{\mu}_{\tilde{A}}(x_i) + \sum_{i=L+1}^N x_i \underline{\mu}_{\tilde{A}}(x_i)}{\sum_{i=1}^L \bar{\mu}_{\tilde{A}}(x_i) + \sum_{i=L+1}^N \underline{\mu}_{\tilde{A}}(x_i)}; \\ c_r &= \frac{\sum_{i=1}^R x_i \underline{\mu}_{\tilde{A}}(x_i) + \sum_{i=R+1}^N x_i \bar{\mu}_{\tilde{A}}(x_i)}{\sum_{i=1}^R \underline{\mu}_{\tilde{A}}(x_i) + \sum_{i=R+1}^N \bar{\mu}_{\tilde{A}}(x_i)}\end{aligned}$$

where L and R called switch points with $x_L \leq c_l \leq x_{L+1}$ and $x_R \leq c_r \leq x_{R+1}$. The determination of L and R can be performed by using the KM algorithms [11, 36, 37] which are summarized in Table 1. In this Table the defuzzified value of the IT2FS \tilde{A} is then given by $x_c = \frac{c_l + c_r}{2}$.

A Matlab program (Matlab 2015a) has been developed based on the KM Algorithm and it is utilized in this paper for defuzzification of IT2FSs in the numerical example.

Table 1 KM algorithm to compute centroid end points of an IT2FS

Step	KM algorithm for c_l	KM algorithm for c_r
1.	Initializing $\theta_i = [\underline{\mu}_{\tilde{A}}(x_i) + \bar{\mu}_{\tilde{A}}(x_i)]/2, i = 1, 2, \dots, N$	
2.	$\bar{c} = c(\theta_1, \theta_2, \dots, \theta_N) = \frac{\sum_{i=1}^N x_i \theta_i}{\sum_{i=1}^N \theta_i}$	
	Compute	
3.	Find $k(1 \leq k \leq N - 1)$ such that $x_k \leq \bar{c} \leq x_{k+1}$.	
4.	$c_l(k) = \frac{\sum_{i=1}^k x_i \bar{\mu}_{\tilde{A}}(x_i) + \sum_{i=k+1}^N x_i \underline{\mu}_{\tilde{A}}(x_i)}{\sum_{i=1}^k \bar{\mu}_{\tilde{A}}(x_i) + \sum_{i=k+1}^N \underline{\mu}_{\tilde{A}}(x_i)}$	$c_r(k) = \frac{\sum_{i=1}^k x_i \underline{\mu}_{\tilde{A}}(x_i) + \sum_{i=k+1}^N x_i \bar{\mu}_{\tilde{A}}(x_i)}{\sum_{i=1}^k \underline{\mu}_{\tilde{A}}(x_i) + \sum_{i=k+1}^N \bar{\mu}_{\tilde{A}}(x_i)}$
	Compute	Compute
5.	Check if $c_l(k) = \bar{c}$. If yes stop and set $c_l(k) = c_l$ and $k = L$. If no go to step 6	Check if $c_r(k) = \bar{c}$. If yes stop and set $c_r(k) = c_r$ and $k = L$. If no go to step 6
6.	Set $\bar{c} = c_l(k)$ and go to step 3	Set $\bar{c} = c_r(k)$ and go to step 3
7.	$x_c = \frac{c_l + c_r}{2}$	

4.2.2 Proposed Method of Type Reduction and Defuzzification for IT2TrFN

Let us consider a IT2TrFN $\tilde{A} = [(r_1^L, r_2^L, r_3^L, r_4^L; h_1^L, h_2^L), (r_1^U, r_2^U, r_3^U, r_4^U; h_1^U, h_2^U)]$ where, $h_j^L, h_j^U \in [0, 1]$ and $r_i^L, r_i^U \in R, i = 1, 2, 3, 4; j = 1, 2$. We propose here three types of reduction schemes and subsequent centroid based defuzzification method of the considered IT2TrFN \tilde{A} . On the FOU of \tilde{A} . we can consider two obvious T1FNs viz. the LMF, i.e. $(r_1^L, r_2^L, r_3^L, r_4^L; h_1^L, h_2^L)$ and UMF, i.e. $(r_1^U, r_2^U, r_3^U, r_4^U; h_1^U, h_2^U)$. The membership functions of these two type reduced T1FNs are respectively denoted by $\mu_{\underline{A}}(x)$ and $\mu_{\bar{A}}(x)$. Hence,

$$\mu_{\underline{A}}(x) = \begin{cases} \frac{h_1^L(x-r_1^L)}{r_2^L-r_1^L} & \text{if } r_1^L \leq x \leq r_2^L \\ h_1^L + \frac{(h_2^L-h_1^L)(x-r_2^L)}{r_3^L-r_2^L} & \text{if } r_2^L \leq x \leq r_3^L \\ h_2^L - \frac{h_2^L(x-r_3^L)}{r_4^L-r_3^L} & \text{if } r_3^L \leq x \leq r_4^L \\ 0 & \text{otherwise} \end{cases} \quad (3)$$

$$\mu_{\bar{A}}(x) = \begin{cases} \frac{h_1^U(x-r_1^U)}{r_2^U-r_1^U} & \text{if } r_1^U \leq x \leq r_2^U \\ h_1^U + \frac{(h_2^U-h_1^U)(x-r_2^U)}{r_3^U-r_2^U} & \text{if } r_2^U \leq x \leq r_3^U \\ h_2^U - \frac{h_2^U(x-r_3^U)}{r_4^U-r_3^U} & \text{if } r_3^U \leq x \leq r_4^U \\ 0 & \text{otherwise} \end{cases} \quad (4)$$

Apart from the above mentioned two type reduced T1FNs, we can construct infinite number of intermediate T1FNs also. Next we discuss the process of obtaining a typical intermediate reduced T1TrFN $[r_1, r_2, r_3, r_4; h_1, h_2]$ between

LMF and UMF whose membership functions are given in (3) and (4) respectively. Let us denote the membership function of an intermediate T1TrFN by $\mu_A(x)$. The values of r_i 's and h_j 's are to be determined from the parameters of the given IT2TrFN \tilde{A} .

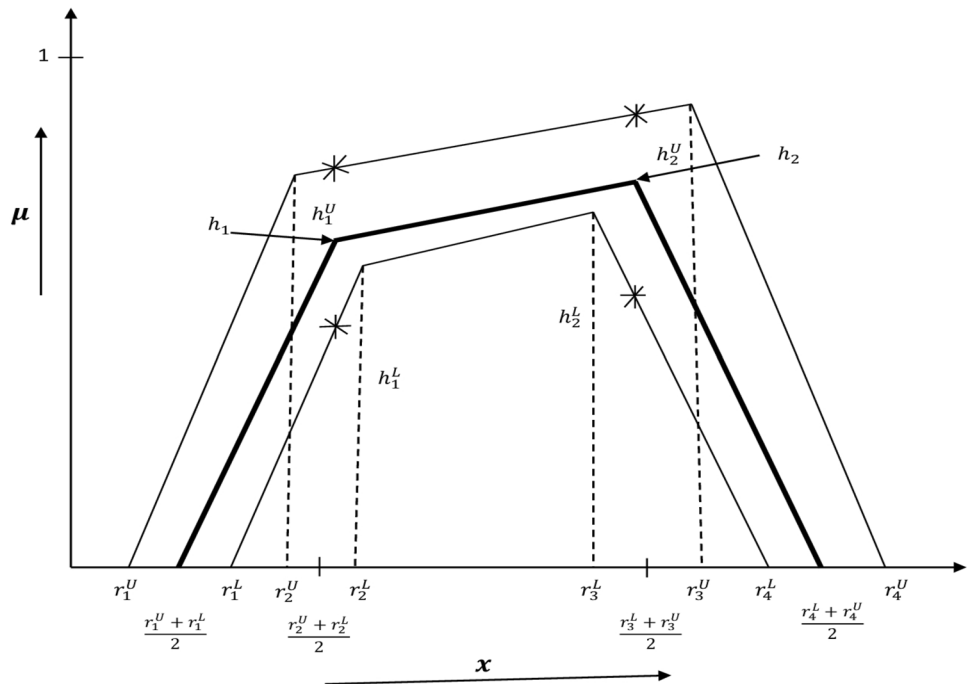
The values of r_i 's and h_j 's are calculated as follows. We take $r_i = \frac{r_i^L+r_i^U}{2}, i = 1, 2, 3, 4$ and $h_j =$ ordinate dividing the membership values of LMF and UMF at $\frac{r_2^U+r_2^L}{2}$ (resp. $\frac{r_3^U+r_3^L}{2}$) in the ratio $k : 1, k > 0$ for $j = 1$ (resp. $j = 2$), i.e. $h_1 = \frac{A+kB}{1+k}$ and $h_2 = \frac{C+kD}{1+k}$.

Here, A and B are respectively the LMF and UMF values at $\frac{r_2^U+r_2^L}{2}$; C and D are respectively the LMF and UMF values at $\frac{r_3^U+r_3^L}{2}$.

As $k \rightarrow 0$, then $\mu_A(x) \rightarrow \mu_{\underline{A}}(x)$ and as $k \rightarrow \infty$ then $\mu_A(x) \rightarrow \mu_{\bar{A}}(x)$. Thus varying k between 0 and ∞ we can scan the entire FOU. In particular choosing $k = 1$ we get the mid way T1TrFS. In our numerical calculation $h_1 = \frac{A+B}{2}$ and $h_2 = \frac{C+D}{2}$ have been taken, i.e., the mid way T1TrFS between LMF and UMF has been considered which corresponds to $k = 1$. The explicit expressions of $A, B; C, D$ are given below:

$$\left. \begin{aligned} A &= \frac{h_1^L(r_2^U+r_2^L-2r_1^L)}{2(r_2^U-r_1^L)} \\ B &= \frac{2h_1^U r_3^U - r_2^U (h_1^U + h_2^U) + r_2^L (h_2^U - h_1^U)}{2(r_3^U - r_2^U)} \\ C &= \frac{r_3^U (h_1^U + h_2^U) + r_3^L ((h_2^U - h_1^U) - 2h_2^U r_2^U)}{2(r_3^U - r_2^U)} \\ D &= \frac{h_2^L (2r_4^L - r_3^L - r_3^U)}{2(r_4^L - r_3^L)} \end{aligned} \right\} \quad (5)$$

Fig. 1 Interval type-2 trapezoidal fuzzy set



The bold line graph in Fig. 1 depicts the mid way T1TrFN $(r_1, r_2, r_3, r_4; h_1, h_2)$. Its membership function is given by:

$$\mu_A(x) = \begin{cases} \frac{h_1(x-r_1)}{r_2-r_1} & \text{if } r_1 \leq x \leq r_2 \\ h_1 + \frac{(h_2-h_1)(x-r_2)}{r_3-r_2} & \text{if } r_2 \leq x \leq r_3 \\ h_2 - \frac{h_2(x-r_3)}{r_4-r_3} & \text{if } r_3 \leq x \leq r_4 \\ 0 & \text{otherwise} \end{cases} \quad (6)$$

Where, $h_1 = \frac{A+B}{2}$; $h_2 = \frac{C+D}{2}$; A, B, C, D are given in Eq. (5).

In the same way one can obtain the lower and upper quartile T1TrFNs between the LMF and UMF by putting $k = \frac{1}{3}$ and $k = 3$ respectively.

These T1TrFNs are then defuzzified by centroid method. Now the centroid based defuzzification of the T1FNs Eq. (3), (4), (6) are respectively given by, $x_\alpha, x_\beta, x_\gamma$.

$$x_\alpha = \frac{\int_{r_1^L}^{r_4^L} x\mu_A(x)dx}{\int_{r_1^L}^{r_4^L} \mu_A(x)dx} = \frac{h_1^L(r_3^L - r_1^L)(r_3^L + r_1^L + r_2^L) + h_2^L(r_4^L - r_2^L)(r_4^L + r_2^L + r_3^L)}{3[h_1^L(r_3^L - r_1^L) + h_2^L(r_4^L - r_2^L)]} \quad (7)$$

$$x_\beta = \frac{\int_{r_1^U}^{r_4^U} x\mu_{\tilde{A}}(x)dx}{\int_{r_1^U}^{r_4^U} \mu_{\tilde{A}}(x)dx} = \frac{h_1^U(r_3^U - r_1^U)(r_3^U + r_1^U + r_2^U) + h_2^U(r_4^U - r_2^U)(r_4^U + r_2^U + r_3^U)}{3[h_1^U(r_3^U - r_1^U) + h_2^U(r_4^U - r_2^U)]} \quad (8)$$

$$x_\gamma = \frac{\int_{r_1^L}^{r_4^L} x\mu_A(x)dx}{\int_{r_1^L}^{r_4^L} \mu_A(x)dx} = \frac{h_1(r_3 - r_1)(r_3 + r_1 + r_2) + h_2(r_4 - r_2)(r_4 + r_2 + r_3)}{3[h_1(r_3 - r_1) + h_2(r_4 - r_2)]} \quad (9)$$

The values of x_α and x_β can easily be computed directly from the LMF and UMF respectively of the given IT2TrFNs using Matlab. The value of x_γ is also computed from the parameters of \tilde{A} and using the relation $r_i = \frac{r_i^L+r_i^U}{2}$, $i = 1, 2, 3, 4$.

5 Interval Type-2 Fuzzy De Novo Programming

To make the decision-making process using de novo programming more flexible and responsive in reflecting the uncertainties inherent in the process, we introduce the following model of a general de novo programming problem with all parameters as interval type-2 fuzzy sets.

$$\left. \begin{aligned}
 & \text{Max } \tilde{Z}_k = \sum_{j=1}^n \tilde{C}_{kj}x_j; \quad k = 1, 2, \dots, r. \\
 & \text{Min } \tilde{W}_l = \sum_{j=1}^n \tilde{C}_{(l+r)j}x_j; \quad l = 1, 2, \dots, s. \\
 & \text{Subject to} \\
 & \sum_{j=1}^n \tilde{v}_jx_j \leq \tilde{B} \\
 & \tilde{v}_j = \sum_{i=1}^m \tilde{p}_i\tilde{a}_{ij} \\
 & x_j \geq 0, \quad j = 1, 2, \dots, n
 \end{aligned} \right\} \quad (10)$$

where parameters $\tilde{C}_{kj}, \tilde{C}_{(l+r)j}, \tilde{p}, \tilde{a}_{ij}, \tilde{B}$ are interval type-2 fuzzy sets [IT2FSs] and \tilde{Z}_k and \tilde{W}_l are the corresponding type-2 fuzzy objectives.

The objectives and the constraints in the proposed model (10) are all well defined, since it is known that addition and multiplication of two IT2FSs is again an IT2FS. The same is true for multiplication of an IT2FS by a real number [40, 41].

In the discussion that follows, we consider the parameters as IT2TrFSs, i.e., type-2 fuzzy sets of the form $[(r_1^l, r_2^l, r_3^l, r_4^l; h_1^l, h_2^l), (r_1^u, r_2^u, r_3^u, r_4^u; h_1^u, h_2^u)]$.

It is very difficult to perform manipulation with type-2 fuzzy sets. One alternative way to get rid of this difficulty is type reduction. So the first step of solving the model (10) would be the type reduction of the coefficients. Through this process, the IT2TrFSs are converted into their type-1 counterparts. Finally, these type-reduced sets are defuzzified to give a single value that represents the entire imprecision of the environment. This has been done in this paper by our proposed type reduction and defuzzification method (explained in Sect. 4.2). After type reduction and defuzzification, the corresponding crisp model of the interval type-2 fuzzy de novo programme (10) is given by:

$$\left. \begin{aligned}
 & \text{Max } |\tilde{Z}_k| = \sum_{j=1}^n |\tilde{C}_{kj}|x_j \quad k = 1, 2, 3, \dots, r. \\
 & \text{Min } |\tilde{W}_l| = \sum_{j=1}^n |\tilde{C}_{(l+r)j}|x_j \quad l = 1, 2, 3, \dots, s. \\
 & \text{Subject to,} \\
 & \sum_{j=1}^n |\tilde{v}_j|x_j \leq |\tilde{B}| \\
 & x_j \geq 0
 \end{aligned} \right\} \quad (11)$$

where, $|\tilde{C}_{kj}|, |\tilde{C}_{(l+r)j}|, |\tilde{v}_j|, |\tilde{B}|$ are the defuzzified value of $\tilde{C}_{kj}, \tilde{C}_{(l+r)j}, \tilde{v}_j, \tilde{B}$ respectively obtained by the proposed defuzzification method. $|\tilde{Z}_k|$ and $|\tilde{W}_l|$ represent the crisp versions of \tilde{Z}_k and \tilde{W}_l respectively. Therefore the model (11) although crisp is a representative of all the fuzziness of model (10).

Table 2 Calculation of pessimistic values of the objectives

Solution	Objectives		
	Z_1	Z_2	W_1
x_1^*	$Z_1(x_1^*) = Z_1^*$	$Z_2(x_1^*)$	$W_1(x_1^*)$
x_2^*	$Z_1(x_2^*)$	$Z_2(x_2^*) = Z_2^*$	$W_1(x_2^*)$
x_3^*	$Z_1(x_3^*)$	$Z_2(x_3^*)$	$W_1(x_3^*) = W_3^*$

5.1 Ideal and Pessimistic Value of Objective

To solve the crisp de Novo programming problem (11) using Min-max GP technique, we need the concept of ideal value and pessimistic value of the objective, which we recall first. The ideal value of an objective in a multi-objective linear programming problem (MOLPP) is its optimal (maximum or minimum) value subject to the given constraints when considered as a single-objective optimization. In a de Novo programme, these values can be easily evaluated by following the technique as detailed below:

For this, we first find the basic feasible solutions of the system (11). Setting $(n - 1)$ variables to zero in the single constraint of the model (11) and finding the value of the remaining variable, we can find a basic feasible solution. Thus the n basic feasible solutions (BFSs) of the system (11) are,

$$\left(\frac{|\tilde{B}|}{|\tilde{v}_1|}, 0, \dots, 0 \right); \left(0, \frac{|\tilde{B}|}{|\tilde{v}_2|}, 0, \dots, 0 \right); \dots; \left(0, 0, \dots, \frac{|\tilde{B}|}{|\tilde{v}_n|} \right);$$

where, $|\tilde{B}|, |\tilde{v}_j|, j = 1, 2, \dots, n$ have the meaning as stated above.

Substituting these basic feasible solutions one by one in all objectives and calculating their values we can find the optimum values of each of the objectives.

$$\begin{aligned}
 \text{Let } Z_k^* &= \text{Max } |\tilde{Z}_k| \\
 &= \text{Max} \left(\frac{|\tilde{C}_{k1}| |\tilde{B}|}{|\tilde{v}_1|}, \frac{|\tilde{C}_{k2}| |\tilde{B}|}{|\tilde{v}_2|}, \dots, \frac{|\tilde{C}_{kn}| |\tilde{B}|}{|\tilde{v}_n|} \right), \quad k \\
 &= 1, 2, \dots, r \\
 W_l^* &= \text{Min } |\tilde{W}_l| \\
 &= \text{Min} \left(\frac{|\tilde{C}_{(l+r)1}| |\tilde{B}|}{|\tilde{v}_1|}, \frac{|\tilde{C}_{(l+r)2}| |\tilde{B}|}{|\tilde{v}_1|}, \dots, \frac{|\tilde{C}_{(l+r)n}| |\tilde{B}|}{|\tilde{v}_n|} \right) \quad l \\
 &= 1, 2, \dots, s.
 \end{aligned}$$

Thus the ideal point is, $I^* = (Z_1^*, Z_2^*, \dots, Z_r^*, W_1^*, \dots, W_s^*)$

The pessimistic values for the objective functions are determined by the Luhandjula’s comparison technique [42].

The determination of the pessimistic expectations of the objectives functions is explained by taking the following

multi-objective linear programming problem involving two maximizing objectives Z_1, Z_2 and one minimizing objective W_1 . The computation is displayed in Table 2. Further let $\mathbf{x}_1^*, \mathbf{x}_2^*, \mathbf{x}_3^*$ are three basic feasible solutions of the problem such that

$$Z_1^* = \text{Max } Z_1 = Z_1(\mathbf{x}_1^*); Z_2^* = \text{Max } Z_2 = Z_2(\mathbf{x}_2^*), W_1^* = \text{Min } W_1 = W_1(\mathbf{x}_3^*).$$

We calculate the pessimistic value of the objectives using Luhandjula’s comparison technique as follows:

$$\begin{aligned} \widehat{Z}_1 &= \begin{cases} \text{Min}\{Z_1^*, Z_1(\mathbf{x}_2^*), Z_1(\mathbf{x}_3^*)\} & \text{if } \text{Min}\{Z_1^*, Z_1(\mathbf{x}_2^*), Z_1(\mathbf{x}_3^*)\} \neq Z_1^* \\ \text{Min}\{Z_1^*, Z_1(\mathbf{x}_2^*), Z_1(\mathbf{x}_3^*)\} - \epsilon_1 & \text{if } \text{Min}\{Z_1^*, Z_1(\mathbf{x}_2^*), Z_1(\mathbf{x}_3^*)\} = Z_1^* \end{cases} \\ \widehat{Z}_2 &= \begin{cases} \text{Min}\{Z_2(\mathbf{x}_1^*), Z_2^*, Z_2(\mathbf{x}_3^*)\} & \text{if } \text{Min}\{Z_2(\mathbf{x}_1^*), Z_2^*, Z_2(\mathbf{x}_3^*)\} \neq Z_2^* \\ \text{Min}\{Z_2(\mathbf{x}_1^*), Z_2^*, Z_2(\mathbf{x}_3^*)\} - \epsilon_2 & \text{if } \text{Min}\{Z_2(\mathbf{x}_1^*), Z_2^*, Z_2(\mathbf{x}_3^*)\} = Z_2^* \end{cases} \\ \widehat{W}_1 &= \begin{cases} \text{Max}\{W_1(\mathbf{x}_1^*), W_1(\mathbf{x}_2^*), W_1^*\} & \text{if } \text{Max}\{W_1(\mathbf{x}_1^*), W_1(\mathbf{x}_2^*), W_1^*\} \neq W_1^* \\ \text{Max}\{W_1(\mathbf{x}_1^*), W_1(\mathbf{x}_2^*), W_1^*\} + \epsilon_3 & \text{if } \text{Max}\{W_1(\mathbf{x}_1^*), W_1(\mathbf{x}_2^*), W_1^*\} = W_1^* \end{cases} \end{aligned}$$

where $\epsilon_1, \epsilon_2, \epsilon_3 > 0$ are chosen by decision maker. Then the vector $\widehat{\beta} = (\widehat{Z}_1, \widehat{Z}_2, \widehat{W}_1)$ is taken as the vector of pessimistic expectation of the objective functions. The above calculation for finding pessimistic expectations could easily be extended to the more involved cases.

Let the pessimistic values of the objectives in Eq. (11) be represented by,

$$\widehat{\beta} = (\widehat{Z}_1, \widehat{Z}_2, \dots, \widehat{Z}_r, \widehat{W}_1, \widehat{W}_2, \dots, \widehat{W}_s).$$

Now our aim is to solve this crisp model (11) using min-max GP technique introduced by Flavell [14]. In the min-max GP approach, the maximum of the deviations of the objectives from their targeted values is minimized. Hence, objectives attain values that are close to their targeted values or aspiration level. It is an established method for the solution of MOLPP.

In min-max GP approaches, different types of goals must be denominated in the same unit; this requires normalization of the units of the different goals. This can be done by determining two fixed values for each objective, e.g., the optimistic (ideal) value and a pessimistic value. Ideal values will serve as the aspiration levels of the respective objectives. While the difference between the ideal and pessimistic values will be used to normalize the deviation variable. The process is detailed in Sect. 5.2.

5.2 Solution of GDNPP Using Min–Max GP

Goal Programming (GP) is one of the most important methods in the Multi-Objective Decision Making (MODM) system.

The term GP was first introduced by Charnes and Cooper [43]. There are several variants of goal programming. For our present purpose the min-max GP technique [14] has been used for the solution GDNPP.

We now proceed to solve the GDNPP (Eq. 11) using min-max GP technique. For this we first define the followings:

ω_k (or ω_l)= specified aspiration level for the objective $\max |\widetilde{Z}_k|$ (or $\min |\widetilde{W}_l|$),

n_k (or p_k) = negative (or positive) deviation from the aspiration level of the maximizing objective $|\widetilde{Z}_k|$,

n_l (or p_l) = negative (or positive) deviation from the aspiration level of the minimizing objective $|\widetilde{W}_l|$,

α_k (or β_k) = non-negative weights attached to the negative (or positive) deviations n_k (or p_k),

α_l (or β_l) = non-negative weights attached to the negative (or positive) deviations n_l (or p_l)

Then the mathematical model of min-max GP for the problem (11) is given by,

$$\left. \begin{aligned} &\text{Min } d \\ &\text{Subject to,} \\ &|\widetilde{Z}_k| + n_k - p_k = \omega_k \\ &|\widetilde{W}_l| + n_l - p_l = \omega_l \\ &\alpha_k n_k + \beta_k p_k \leq d \\ &\alpha_l n_l + \beta_l p_l \leq d \\ &\sum_{j=1}^n |\widetilde{v}_j| x_j \leq |\widetilde{B}| \\ &x_j \geq 0, k = 1, 2, \dots, r; l = 1, 2, \dots, s; j = 1, 2, \dots, n \end{aligned} \right\} \quad (12)$$

where, d is the maximum of the weighted deviations between the achievement of the objectives and their respective aspirational levels, all the weights attached to deviation variables are non-negative and their sum is taken as unity, i.e.

$$\sum_{k=1}^r (\alpha_k + \beta_k) + \sum_{l=1}^s (\alpha_l + \beta_l) = 1.$$

In the proposed model, $\omega_k = Z_k^*$, and $\omega_l = W_l^*$ have been taken. Since the ideal values have been used as aspiration levels for the objectives, so $|\tilde{Z}_k| \leq Z_k^*$, and $|\tilde{W}_l| \geq W_l^*$. Hence we must have $p_k = 0$ and $n_l = 0$. In this case, we have the goal constraint: $|\tilde{Z}_k| + n_k = Z_k^*$ and $|\tilde{W}_l| - p_l = W_l^*$. To restrict goal deviations to a single unit, we adopt the normalization procedure. This is achieved by dividing the deviation variables n_k and p_l respectively by $t_k = Z_k^* - \hat{Z}_k$ and $t_l = \hat{W}_l - W_l^*$, $k = 1, 2, \dots, r; l = 1, 2, \dots, s$, and set $\bar{d} = \max\{\frac{d}{t_k}, \frac{d}{t_l}\}$.

Therefore, the proposed modified min-max GP model of the GDNPP can be written as follows:

$$\left. \begin{array}{l} \text{Min } \bar{d} \\ \text{Subject to} \\ |\tilde{Z}_k| + n_k = Z_k^* \\ \alpha_k \frac{n_k}{t_k} \leq \bar{d} \\ |\tilde{W}_l| - p_l = W_l^* \\ \beta_l \frac{p_l}{t_l} \leq \bar{d} \\ \sum_{j=1}^n |\tilde{v}_j| x_j \leq |\tilde{B}| \\ x_j \geq 0 \end{array} \right\} \quad (13)$$

$k = 1, 2, \dots, r; l = 1, 2, \dots, s; t_k = Z_k^* - \hat{Z}_k, t_l = \hat{W}_l - W_l^*, |\tilde{Z}_k| = f_k(x)$ for the k^{th} maximizing objective and $|\tilde{W}_l| = f_l(x)$ for the l^{th} minimizing objective. Here \bar{d} is the maximum normalized weighted deviation between the achievement of the goals and their aspiration levels. This crisp linear program (13) can now be solved using Lingo. The advantage of this approach is that the interval type 2 fuzzy de Novo programming problem (10) can be solved in a single phase [25, 34].

Now we illustrate the proposed method of solving GDNPP with IT2TrFNs as parameters with the help of a real-life problem.

6 Application of Proposed Method to Solve a Solid Transportation Problem in De Novo Set Up

In this model the following notations and assumptions are used.

Notations

$t, i, j, k \rightarrow$ are the indices denoting the terminal number, source point, destination point and the vehicle type respectively.

$\tilde{C}_{ijk}, \tilde{p}_{ij}, \tilde{\xi}_{ijk} \rightarrow$ are respectively the unit transportation costs, processing charges and fixed charges, all these parameters are IT2TrFNs.

$\tilde{e}_{tik}^0, \tilde{e}_{ijk}^1 \rightarrow$ are type-2 fuzzy amount of carbon emission for an empty vehicle and a loaded one respectively.

$\tilde{a}_i \rightarrow$ is the fuzzy amount available at source i .

$\tilde{b}_j \rightarrow$ is the fuzzy demand placed at destination j .

$\tilde{e}_k \rightarrow$ is the fuzzy capacity for the vehicle k .

δ_{ti} and $\bar{\delta}_{ij} \rightarrow$ are distances (crisp) between the terminal t to source i and source i to destination j respectively. Here terminal t provide the empty vehicles.

$x_{ijk} \rightarrow$ is the unknown quantity that is to be transported from source i to destination j using the k type vehicle.

Assumptions The following assumptions are made for developing the mathematical model of the solid transportation problem. We assume that there are u terminal points, m source points, n destinations, and r different types of vehicles are available.

The problem is an unbalanced problem i.e. $\sum_{i=1}^m \tilde{a}_i \neq \sum_{j=1}^n \tilde{b}_j \neq \sum_{k=1}^r \tilde{e}_k$

Carbon emissions depends on distance travelled by the vehicle, load and vehicle type.

The fuzzy membership functions for the system parameters are defined based on the previous statistical information and following the expert's opinion about the parameters.

All the vehicles are considered as fully loaded according to their capacity, partially loaded case is not considered here.

6.1 Mathematical Model Formulation

Here a solid transportation problem in type-2 fuzzy environment is considered along with the harmful factor of carbon-dioxide emissions. For the considered problem two objectives are set: maximizing the profit and minimizing CO₂ emissions from transportation operations. The mathematical formulation of the model is defined as follows.

$$\max \tilde{Z} = \sum_{i=1}^m \sum_{j=1}^n \sum_{k=1}^r (\tilde{C}_{ijk} - \tilde{p}_{ij} - \tilde{\xi}_{ijk}) x_{ijk} \quad (14)$$

It is worthy to mention here that from the unit cost of transportation if we subtract processing charge and fixed charge of per unit of transportation, what remains is the net profit per unit of transportation.

$$\min \tilde{W} = \sum_{i=1}^m \sum_{j=1}^n \sum_{k=1}^r \sum_{t=1}^u (\delta_{it} \tilde{c}_{tik}^0 + \bar{\delta}_{ij} \tilde{c}_{ijk}^1 x_{ijk}) \tag{15}$$

Subject to,

$$\sum_{j=1}^n \sum_{k=1}^r x_{ijk} \leq \tilde{a}_i \quad (i = 1, 2, \dots, m) \tag{16}$$

$$\sum_{i=1}^m \sum_{k=1}^r x_{ijk} \geq \tilde{b}_j \quad (j = 1, 2, \dots, n) \tag{17}$$

$$\sum_{i=1}^m \sum_{j=1}^n x_{ijk} \leq \tilde{e}_k \quad (k = 1, 2, \dots, r) \tag{18}$$

$$\sum_i \tilde{a}_i P_i + \sum_j \tilde{b}_j Q_j + \sum_k \tilde{e}_k R_k \leq \tilde{B} \tag{19}$$

$$x_{ijk} \geq 0 \quad \forall i, j, k \tag{20}$$

$$\delta_{ii} \geq 0 \tag{21}$$

$$\bar{\delta}_{ij} \geq 0 \tag{22}$$

where, P_i, Q_j, R_k respectively denote per unit cost for arranging the amount available at the source i , for satisfying the demand at destination j and using k vehicle type.

Here \tilde{Z} and \tilde{W} are the profit maximizing and carbon emission minimizing objective functions respectively. Constraint (16) is the source constraint, which implies that total amount of transported goods ($\sum_{j=1}^n \sum_{k=1}^r x_{ijk}, i = 1, 2, \dots, m$) is less or equal to the amount available at the source (\tilde{a}_i). Similarly (17) and (18) are the demand and conveyance constraint respectively. (19) is budget constraint and \tilde{B} is the total given budget. The remaining constraints are the non negativity restrictions for the transportation system.

The solid transportation problem defined in Sect. 6.1 has mnr variables x_{ijk} , $(m + n + r)$ technological constraints and one budget constraints.

To solve the above solid transportation problem in type-2 fuzzy environment, firstly we defuzzify all the type-2 fuzzy parameters using the methods discussed in Sect. 4. After this defuzzification, the model is into converted into a crisp model. Then the system is converted into a single constraint problem as explained in Sect. 3. Thus the above problem becomes,

$$\max |\tilde{Z}| = \sum_{i=1}^m \sum_{j=1}^n \sum_{k=1}^r (|\tilde{C}_{ijk}| - |\tilde{p}_{ij}| - |\tilde{\xi}_{ijk}|) x_{ijk}$$

$$\min |\tilde{W}| = \sum_{i=1}^m \sum_{j=1}^n \sum_{k=1}^r \sum_{t=1}^u (\delta_{ii} |\tilde{c}_{tik}^0| + \bar{\delta}_{ij} |\tilde{c}_{ijk}^1| x_{ijk})$$

$$\text{Subject to, } |\tilde{v}_1| x_{111} + |\tilde{v}_2| x_{112} + \dots + |\tilde{v}_r| x_{11r} + |\tilde{v}_{r+1}| x_{121} + \dots + |\tilde{v}_{2r}| x_{12r} + \dots + |\tilde{v}_{nr}| x_{1nr} \tag{23}$$

$$+ |\tilde{v}_{nr+1}| x_{211} + \dots + |\tilde{v}_{2nr}| x_{2nr} + \dots + |\tilde{v}_{mnr}| x_{mnr} \leq |\tilde{B}|$$

$$x_{ijk} \geq 0 \quad \forall i, j, k$$

$$\delta_{ii} \geq 0$$

$$\bar{\delta}_{ij} \geq 0$$

The problem (23) is a crisp problem involving single constraints. Here $\mathbf{v} = \mathbf{pA}$, where \mathbf{A} is the $(m + n + r) \times mnr$ matrix of the coefficients of the variables x_{ijk} in the technological constraints, \mathbf{p} is the row vector of the unit cost of the resources of order $1 \times (m + n + r)$ and \mathbf{v} . is a row vector of order $1 \times mnr$ having components v_1, v_2, \dots, v_{mnr} .

It should be mentioned here that in the above construction the variables x_{ijk} , have been arranged in lexicographic order.

6.2 Solution Methodology

This crisp model (23) will be solved by min-max approach (as discussed in Sect. 5.2). The defuzzified model encompasses all the fuzziness of the given type-2 fuzzy parameters.

6.3 Application of Developed Model

Here a real-life numerical example is presented to illustrate the proposed model and its method of solution.

Ramkrishna Roadways, a well-known utility transport agency in Tripura, India, deals in freight transportation using different types of vehicles. Tripura is a north-eastern hilly state of India, surrounded by Bangladesh on three sides. Due to the undulating land relief, vehicles like trucks, dumpers, mini trucks, auto-rickshaws, etc. are the main mode of transportation of goods in the state. The agency mainly operates vehicles from its two branch offices, situated at Agartala, the capital of Tripura, and Dharmanagar, a northern city of the state of Tripura. From the available data of this agency, the fluctuating unit transportation cost, fixed charges, article processing or handling cost, and safety cost are represented as type-2 fuzzy numbers with the help of experts' or experienced businessmen's opinions. Also from the available data of the Bright Automobile Exhaust Testing Centre in Agartala, the Tripura State Pollution Control Board, and the vehicle supplying agency, the fluctuating carbon emissions due to empty and loaded vehicles are also represented as type-2 fuzzy numbers. For simplicity, we have considered

two origins ($m = 2$) and three destinations ($n = 3$). From their origins, the vehicles operate to deliver to three distinct demand points or destinations. For the transportation of goods, four types of vehicles ($k = 4$) are used. Also, there are two terminals ($t = 2$) available, from where the empty vehicles are sent to the source points.

Here it should be mentioned that the type-2 fuzzy parameters used in the example have been constructed on the basis of different experts' opinions. Generally, imprecise values of the system parameters are assumed on the basis of experts' opinions when sufficient past data on the system is not available. In such situations, type-2 fuzzy parameter values are more appropriate than type-1 fuzzy values because the type-2 fuzzy set gives a second-order approximation of uncertainty, whereas the type-1 fuzzy set is of the first order.

Also, it has been observed that experts' opinions on each parameter vary, and each expert's opinion on a particular parameter can be taken in the form of a trapezoidal fuzzy number. Hence, by collecting the opinions of all the experts' on a particular parameter, we get an IT2TrFN. So the collection of all experts' opinions provides us with type-2 fuzzy sets for all the parameters. The infimum and the supremum of all these membership values for a particular parameter form, respectively, the LMF and UMF of the corresponding IT2TrFN. We have taken the midway membership value as the representative of the type-2 fuzzy set of parameters.

In Tables 3, 4, 5, 6, we have placed the T2TrFNs which has been converted to type-reduced T1TrFNs by our proposed method as mid-way T1FNs in the FOU. These T1FNs are then defuzzified using the relation (9). With this

Table 3 Input for source, demand and conveyance

\tilde{a}_1	\tilde{a}_2		
(27,29,34,37;0.8,0.9)	(24,26,29,36;0.6,0.9)		
\tilde{b}_1	\tilde{b}_2	\tilde{b}_3	
(15,18,19,24;0.4,0.8)	(12,19,24,29;0.4,0.6)	(18,20,20,20;0.3,0.5)	
\tilde{e}_1	\tilde{e}_2	\tilde{e}_3	\tilde{e}_4
(16,17,19,20;0.5,0.7)	(15,17,18,19;0.5,0.6)	(14,15,17,18;0.3,0.4)	(16,18,19,21;0.4,0.6)

Table 4 Input for transportation cost

ilk	1	2	3	4	j
<i>Fuzzy unit transportation cost (\tilde{C}_{ijk})</i>					
1	(17,19,20,21;0.5,0.7)	(23,24,26,28;0.7,0.9)	(19,21,24,26;0.4,0.7)	(21,23,24,28;0.4,0.5)	1
	(14,18,19,24;0.6,0.7)	(16,18,22,25;0.2,0.6)	(12,16,18,22;0.6,0.7)	(21,23,25,28;0.3,0.5)	2
	(20,24,27,28;0.2,0.8)	(18,21,22,28;0.3,0.5)	(20,23,25,30;0.4,0.5)	(20,21,23,29;0.7,0.9)	3
2	(21,23,26,27;0.6,0.8)	(18,20,21,23;0.3,0.6)	(20,24,26,27;0.5,0.8)	(18,24,27,29;0.8,0.9)	1
	(15,17,19,21;0.7,0.8)	(17,20,23,26;0.4,0.8)	(20,24,25,29;0.5,0.7)	(18,23,26,27;0.4,0.8)	2
	(19,22,26,29;0.6,0.9)	(19,22,23,29;0.5,0.6)	(21,24,25,28;0.6,0.7)	(20,23,24,27;0.3,0.5)	3

Table 5 Input for processing and fixed charges

ilk	1	2	3	4	j
<i>Fuzzy unit processing charge (\tilde{p}_{ijk})</i>					
1	(5,6,7,9;0.5,0.6)	(3,4,5,8;0.3,0.5)	(4,5,7,8;0.6,0.7)	(2,3,4,6;0.4,0.8)	1
	(4,5,6,8;0.5,0.6)	(6,8,9,11;0.3,0.4)	(2,3,4,6;0.6,0.7)	(2,3,5,7;0.7,0.9)	2
	(3,4,5,6;0.2,0.6)	(1,4,5,7;0.4,0.5)	(3,4,5,6;0.3,0.4)	(3,4,5,6;0.6,0.8)	3
2	(2,3,6,7;0.4,0.7)	(3,4,7,8;0.5,0.8)	(2,4,6,7;0.3,0.9)	(8,9,10,11;0.2,0.7)	1
	(5,6,7,8;0.7,0.8)	(7,9,10,12;0.5,0.6)	(2,4,6,8;0.4,0.5)	(1,2,3,5;0.4,0.5)	2
	(2,4,6,7;0.6,0.9)	(2,3,4,6;0.5,0.7)	(1,2,3,4;0.2,0.3)	(3,4,6,7;0.5,0.7)	3
<i>Fuzzy unit of fixed charge (\tilde{c}_{ijk})</i>					
1	(2,0,2,5,4,5;0.5,0.7)	(2,2,5,3,3,5;0.6,0.7)	(2,5,3,3,5,4;0.1,0.3)	(0,5,1,5,3,0,4;0.3,0.4)	1
	(1,0,2,2,5,4;0.7,0.8)	(0,5,1,2,3,5;0.3,0.5)	(1,5,2,3,5,4;0.5,0.7)	(2,2,5,3,5,4,5;0.3,0.8)	2
	(2,5,3,3,5,4;0.6,0.8)	(2,0,2,5,3,4;0.3,0.7)	(1,0,1,5,2,4;0.4,0.5)	(1,5,2,0,3,0,4;0.7,0.9)	3
2	(1,0,1,5,2,3;0.2,0.3)	(1,5,2,2,5,4;0.4,0.6)	(1,2,2,5,3,5;0.5,0.7)	(2,0,2,5,3,3,5;0.4,0.6)	1
	(2,5,3,3,5,5;0.5,0.9)	(2,2,5,3,5,5;0.2,0.4)	(1,0,2,0,3,5;0.4,0.6)	(1,5,2,5,4,0,5;0.4,0.7)	2
	(1,0,2,5,0,6;0.2,0.3)	(1,5,2,0,4,6;0.5,0.6)	(2,5,3,0,4,5;0.6,0.7)	(1,0,1,5,3,0,5;0.2,0.3)	3

Table 6 Input for emission parameters of the objective functions

<i>ti</i>	1	2		<i>k</i>
<i>Carbon emission from empty vehicle (\tilde{e}_{tik}^0)</i>				
1	(0.02,0.04,0.05,0.07;0.7,0.8)	(0.05,0.06,0.08,0.09;0.2,0.5)	–	1
	(0.01,0.03,0.04,0.06;0.5,0.7)	(0.02,0.03,0.05,0.07;0.2,0.6)	–	2
	(0.02,0.03,0.05,0.08;0.4,0.7)	(0.03,0.04,0.06,0.09;0.5,0.9)	–	3
	(0.03,0.04,0.06,0.07;0.5,0.9)	(0.02,0.03,0.06,0.08;0.3,0.6)	–	4
2	(0.02,0.05,0.06,0.09;0.3,0.8)	(0.03,0.05,0.06,0.09;0.4,0.7)	–	1
	(0.01,0.04,0.05,0.07;0.3,0.5)	(0.02,0.04,0.06,0.09;0.2,0.6)	–	2
	(0.03,0.05,0.07,0.09;0.5,0.7)	(0.03,0.04,0.07,0.08;0.3,0.6)	–	3
	(0.01,0.02,0.04,0.05;0.2,0.4)	(0.02,0.05,0.08,0.09;0.3,0.7)	–	4
<i>ilj</i>	1	2	3	<i>k</i>
<i>Carbon emission from fully loaded vehicle (\tilde{e}_{ijk}^1)</i>				
1	(1.0,1.5,1.9,2.8;0.4,0.8)	(1.6,2.9,3.4,6;0.4,0.7)	(1.1,4.1,6.1,6.8;0.4,0.7)	1
	(1.2,1.9,2.7,3.2;0.2,0.7)	(4.5,8.5,9.0,10;0.4,0.8)	(5.0,8.0,9.0,9.5;0.2,0.5)	2
	(1.3,1.8,2.8,3.5;0.5,0.8)	(1.4,2.4,3.1,4.8;0.1,0.5)	(1.4,2.3,2.9,5.4;0.4,0.9)	3
	(2.1,2.6,3.2,4.1;0.3,0.6)	(1.9,4.0,8.0,9.5;0.1,0.4)	(2.7,4.1,5.7,8.9;0.4,0.9)	4
2	(2.0,2.5,3.0,4.0;0.2,0.6)	(3.0,3.6,5.0,5.9;0.2,0.9)	(2.8,3.4,5.3,6.7;0.3,0.8)	1
	(1.1,2.5,3.0,3.5;0.3,0.6)	(4.5,5.9,6.7,7.1;0.2,0.8)	(2.4,2.9,5.2,8.1;0.1,0.4)	2
	(3.5,5.0,6.0,8.6;0.2,0.4)	(1.3,2.3,3.3,4.3;0.1,0.3)	(2.3,3.6,4.9,7.8;0.2,0.7)	3
	(2.9,3.8,5.0,8.2;0.2,0.5)	(1.6,2.8,3.9,5.2;0.1,0.6)	(2.2,4.4,5.6,7.8;0.2,0.6)	4

defuzzified value, the problem is converted into a crisp problem, which is then solved by the min-max approach.

Here, the available given budget, $\tilde{B} = (145000, 155000, 163000, 172000; 0.5, 0.9)$. Also $P_1 = Rs.12, P_2 = Rs.15; Q_1 = Rs.8, Q_2 = Rs.10, Q_3 = 12;$ and $R_1 = 2500, R_2 = 2000, R_3 = 2700, R_4 = 2200$.

Hence the row vector \mathbf{p} of the unit costs of the resources is given by,

$$\mathbf{p} = [P_i \ Q_j \ R_k] = [12 \ 15 \ 8 \ 10 \ 12 \ 2500 \ 2000 \ 2700 \ 2200].$$

In the present case of solid transportation problem having $m = 2, n = 3, r = 4$, the matrix \mathbf{A} formed by the coefficients of the variables x_{ijk} in the technological constraints is an $(m + n + r) \times mnr = (9 \times 24)$ matrix formed by 0 and 1. Using the two matrices \mathbf{A} and \mathbf{p} , the row vector $\mathbf{v} = \mathbf{pA}$, a (1×24) matrix is formed. For example, The first column of matrix \mathbf{A} , say \mathbf{A}_1 is given by $(\mathbf{A}_1)^T = [1 \ 0 \ 1 \ 0 \ 0 \ 1 \ 0 \ 0 \ 0]$.

Hence, $v_1 = [12 \times 1 + 15 \times 0 + 8 \times 1 + 10 \times 0 + 12 \times 0 + 2500 \times 1 + 2000 \times 0 + 2700 \times 0 + 2200 \times 0] = 2520$. Similarly, the other v_j has been calculated.

Thus applying Zeleny’s method the problem is reduced in a single constraint problem given by $\mathbf{vx} \leq |\tilde{B}|$.

In our numerical problem, $\mathbf{v} = (v_k)_{1 \times 24}, \kappa = 1, 2, \dots, 24$; where,

$$\begin{aligned} v_1 &= 2520, v_2 = 2020, v_3 = 2720, v_4 = 2220, v_5 = 2522, \\ v_6 &= 2022, v_7 = 2722, v_8 = 2222, v_9 = 2524, v_{10} = 2024, \\ v_{11} &= 2724, v_{12} = 2224, v_{13} = 2523, v_{14} = 2023, v_{15} = 2723, \\ v_{16} &= 2223, v_{17} = 2525, v_{18} = 2025, v_{19} = 2725, v_{20} = 2225, \\ v_{21} &= 2527, v_{22} = 2027, v_{23} = 2727, v_{24} = 2227. \end{aligned}$$

Table 3 represents the type-2 fuzzy resources, demands, and conveyance capacities. Table 4 represents transportation costs. The cost of processing and the fixed charge are given in Table 5. Also, Table 6 represents the amount of carbon emissions for an empty vehicle and a loaded one. The data has been collected from the available data of the Tripura State Pollution Control Board.

The distances between the two terminals to origins and then origins to destinations are approximately considered as, $\delta_{11} = 1.2, \delta_{21} = 0.8, \delta_{12} = 1.3, \delta_{22} = 0.9$ and $\delta_{11}^- = 2.8, \delta_{12}^- = 3.1, \delta_{13}^- = 2.7, \delta_{21}^- = 2.5, \delta_{22}^- = 2.5, \delta_{23}^- = 2.5$, unit by changing the scale of measure for simplicity, respectively.

Table 7 Optimal solution of the problem using KM algorithm and proposed method

	Ideal solution	KM algorithm	Proposed method
Maximum profit	1075.49	828.5309	1074.468
Minimum carbon emission	329.1719	661.773	654.7523

For comparative analysis, the optimal solution of the given problem using KM Algorithm method and proposed method has been presented in Table 7.

7 Conclusion

In this paper, the general De Novo programming problem with interval type-2 fuzzy parameters has been introduced. For type reduction and subsequent defuzzification of the interval type-2 fuzzy parameters, a new method has been proposed. We have obtained equivalent crisp numbers for each type-2 fuzzy parameter. After that, using the Min-max goal programming technique, the problem was solved in one phase. In the proposed defuzzification method, the centroid of the given IT2TrFSs has been computed, and thereby the resulting crisp model captures all the fuzziness of the initial problem. Thus, it is a good method for applying de Novo programmes in optimal system design where fuzziness of higher order is involved. The advantage of this model is that it can reflect the inherent uncertainties in determining the coefficients more efficiently than crisp or type-1 fuzzy numbers. This makes the problem more flexible and can be efficiently used in designing optimal systems for real-life problems. As an application of the proposed defuzzification methodology, a multi-objective solid transportation problem with real-life data in the form of trapezoidal type-2 fuzzy variable has been formulated and solved. Here the two objectives are chosen as profit maximization and minimum carbon emissions from the vehicle used in transportation. A comparative solution has been shown in Table 7.

Author Contributions All the authors contributed equally.

Funding Not applicable, the research is not supported by any funding agency.

Data Availability The article does not contain any data for analysis.

Code Availability Not applicable

Declarations

Conflict of interest The authors declare that the article is free from conflicts of interest.

Consent for Publication YES

References

- Zeleny M (1980) Mathematical programming with multiple objectives (special issue). *Comput Oper Res* 7:101–107
- Zeleny M (1981) On the squandering of resources and profits via linear programming. *Interfaces* 11(5):101–107
- Zeleny M (1981) A case study in multiobjective design: de novo programming. *Oper Mult Criteria Anal* 37–51
- Zeleny M (1986) Optimal system design with multiple criteria: de novo programming approach. *Eng Costs Prod Econ* 10(2):89–94
- Zeleny M (1990) Optimizing given systems vs. designing optimal systems: the de novo programming approach. *Int J General Syst* 17(4):295–307
- Li R, Lee ES (1990) Fuzzy approaches to multicriteria de novo programs. *J Math Anal Appl* 153(1):97–111
- Chen YW, Hsieh HE (2006) Fuzzy multi-stage de-novo programming problem. *Appl Math Comput* 181(2):1139–1147
- Umarusman N (2013) Min-max goal programming approach for solving multi-objective de novo programming problems. *Int J Oper Res* 10(2):92–99
- Shi Y (1995) Studies on optimum-path ratios in multicriteria de novo programming problems. *Comput Math Appl* 29(5):43–50
- Zadeh LA (1975) The concept of a linguistic variable and its application to approximate reasoning. *Inf Sci* 8(3):199–249
- Nilesh NK, Jerry MM (2001) Centroid of a type-2 fuzzy set. *Inf Sci* 132(1):195–220
- Hisdal E (1981) The if then else statement and interval-valued fuzzy sets of higher type. *Int J Man Mach Stud* 15(4):385–455
- Liu X, Mendel JM (2011) Connect Karnik-Mendel algorithms to root-finding for computing the centroid of an interval type-2 fuzzy set. *IEEE Trans Fuzzy Syst* 19(4):652–665
- Flavell R (1976) A new goal programming formulation. *Omega* 4(6):731–732
- Wan SP, Qin YL, Dong JY (2017) A hesitant fuzzy mathematical programming method for hybrid multi-criteria group decision making with hesitant fuzzy truth degrees. *Knowl-Based Syst* 138:232–248
- Wan SP, Wang F, Xu GL, Dong JY, Tang J (2017) An intuitionistic fuzzy programming method for group decision making with interval-valued fuzzy preference relations. *Fuzzy Optim Decis Making* 16:269–295
- Wan SP, Jin Z, Dong JY (2018) Pythagorean fuzzy mathematical programming method for multi-attribute group decision making with Pythagorean fuzzy truth degrees. *Knowl Inf Syst* 55:437–466
- Dong JY, Wan SP (2018) A new trapezoidal fuzzy linear programming method considering the acceptance degree of fuzzy constraints violated. *Knowl-Based Syst* 148:100–114
- Wan SP, Dong JY (2014) Possibility linear programming with trapezoidal fuzzy numbers. *Appl Math Model* 38(5–6):1660–1672
- Dong J, Wan S (2019) A new method for solving fuzzy multi-objective linear programming problems. *Iran J Fuzzy Syst* 16(3):145–159
- Chackraborty S, Bhattacharya D (2012) A new approach for solution of multi-stage and multi-objective decision-making problem using de novo programming. *Eur J Sci Res* 79(3):393–417
- Chackraborty S, Bhattacharya D (2012) Optimal system design under multi-objective decision making using de-novo concept: a new approach. *Int J Comput Appl* 63(12):0975–8887
- Zimmermann H (1978) Fuzzy programming and linear programming with several objective functions. *Fuzzy Sets Syst* 1(1):45–55
- Zhuang ZY, Hocine A (2018) Meta goal programming approach for solving multi-criteria de novo programming problem. *Eur J Oper Res* 265(1):228–238
- Banik S, Bhattacharya D (2020) A note on min-max goal programming approach for solving multi-objective de novo programming problems. *Int J Oper Res* 37(1):32–47
- Shi Y (1999) Optimal system design with multiple decision makers and possible debt: a multicriteria de novo programming approach. *Oper Res* 47(5):723–729

27. Saeedi S, Mohammadi M, Torabi S (2015) A de novo programming approach for a robust closed-loop supply chain network design under uncertainty: an m/m/1 queueing model. *Int J Ind Eng Comput* 6(2):211–228
28. Brozová H, Vlach M (2019) Optimal design of production systems: meta optimization with generalized de novo programming. In: ICORES
29. Babic Z, Pavic I (1996) Multicriterial production planning by de novo programming approach. *Int J Prod Econ* 43(1):59–66
30. Huang JJ, Tzeng GH, Ong CS (2006) Choosing best alliance partners and allocating optimal alliance resources using the fuzzy multi-objective dummy programming model. *J Oper Res Soc* 57(10):1216–1223
31. Chen J, Tzeng GH (2009) Perspective strategic alliances and resource allocation in supply chain systems through the de novo programming approach. *Int J Sustain Strateg Manag* 1(3):320–339
32. Miao D, Huang W, Li Y, Yang Z (2014) Planning water resources systems under uncertainty using an interval-fuzzy de novo programming method. *J Environ Inf* 24(1):11–23
33. Zhang YM, Huang G, Zhang X (2009) Inexact de novo programming for water resources systems planning. *Eur J Oper Res* 199(2):531–541
34. Banik S, Bhattacharya D (2019) One-step approach for solving general multi-objective de novo programming problem involving fuzzy parameters. *Hacet J Math Stat* 48(6):1824–1837
35. Mendel JM, John RB (2002) Type-2 fuzzy sets made simple. *IEEE Trans Fuzzy Syst* 10(2):117–127
36. Mendel JM, John RI, Liu F (2006) Interval type-2 fuzzy logic systems made simple. *IEEE Trans Fuzzy Syst* 14(6):808–821
37. Liang Q, Mendel JM (2000) Interval type-2 fuzzy logic systems: theory and design. *IEEE Trans Fuzzy Syst* 8(5):535–550
38. Chen SM, Wang CY (2013) Fuzzy decision making systems based on interval type-2 fuzzy sets. *Inf Sci* 242:1–21
39. Grzegorzewski P, Mrowka E (2005) Trapezoidal approximations of fuzzy numbers. *Fuzzy Sets Syst* 153(1):115–135
40. Chen SM, Lee LW (2010) Fuzzy multiple attributes group decision-making based on the ranking values and the arithmetic operations of interval type-2 fuzzy sets. *Expert Syst Appl* 37(1):824–833
41. Chen TY (2013) A linear assignment method for multiple-criteria decision analysis with interval type-2 fuzzy sets. *Appl Soft Comput* 13(5):2735–2748
42. Luhandjula M (1982) Compensatory operators in fuzzy linear programming with multiple objectives. *Fuzzy Sets Syst* 8(3):245–252
43. Charnes A, Cooper WW (1957) Management models and industrial applications of linear programming. *Manag Sci* 4(1):38–91

Publisher's Note Springer Nature remains neutral with regard to jurisdictional claims in published maps and institutional affiliations.

Springer Nature or its licensor (e.g. a society or other partner) holds exclusive rights to this article under a publishing agreement with the author(s) or other rightsholder(s); author self-archiving of the accepted manuscript version of this article is solely governed by the terms of such publishing agreement and applicable law.

Language in India www.languageinindia.com
ISSN 1930-2940
11249 Oregon Circle, Bloomington, MN 55438 USA
languageinindiaUSA@gmail.com, 1-952-412-3583

August 31, 2023

Certificate of Publication

Title of the Article: **Negation and First Phase Syntax**

Name/s of Author/s: **Dr. Moumita Dey, M.A., Ph.D.**

Volume and Issue: Language in India www.languageinindia.com ISSN 1930-2940 Vol. 23:8 August 2023

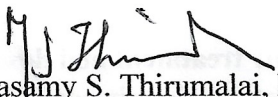
Link/s: <http://languageinindia.com/aug2023/drdeynegationsyntaxbangla.html>
<http://languageinindia.com/aug2023/drdeynegationsyntaxbangla.pdf>

Google Scholar:




https://scholar.google.com/scholar?hl=en&as_sdt=0%2C24&q=Dr.+Moumita+Dey%2C+M.A.%2C+Ph.D.+Negation+and+First+Phase+Syntax&btnG=

Full Volume: <http://languageinindia.com/aug2023/v23i8aug2023.pdf>

1. Language in India www.languageinindia.com is an international monthly online journal with its own Library of Congress ISSN Number. ISSN 1930-2940.
2. Language in India is published from the United States, Bloomington, MN.
3. Authors from many nations including those from India, Pakistan, Bangladesh, Sri Lanka, Singapore, Malaysia, Indonesia, Thailand, Vietnam, China, United States, UK, several European nations, Iran, Turkey, Jordan, Yemen, Saudi Arabia, Oman, Nigeria, Ghana, Kenya, etc. publish their research through Language in India.
4. Articles and dissertations published in Language in India are indexed in four major International databases: EBSCOHost, ProQuest (Linguistics and Language Behavior Abstracts), MLA International Bibliography, and Gale Search/Cengage Learning. The journal is also included in the Cabell's Directory, a leading directory in the USA.
5. Articles are easily accessible to scholars all around the world through the established Databases and open access Internet.
6. The journal does not charge any fee from readers or institutions to access articles, and thus the journal is freely available 24/7 to help researchers and students for personal use and not for distribution.
7. The journal has been consistently and regularly published for the last 22 years. This is our 23rd year of publication.
8. Articles published in the journal are reviewed before publication by one or more members of the Board of Editors and/or another specialist, and authors are given an opportunity to revise their papers based on such reviews.


Madasamy S. Thirumalai, Ph.D.
Managing Editor and Publisher

Targeted inhibition of colorectal cancer proliferation: The dual-modulatory role of 2,4-DTBP on anti-apoptotic Bcl-2 and Survivin proteins

Partha Saha¹ | Mangala Hegde² | Kanak Chakraborty¹ | Achinta Singha¹ |
 Nobendu Mukerjee^{3,4}  | Deepshikha Ghosh⁵ | Ajaikumar B. Kunnumakkara² |
 Mohd Shahnawaz Khan⁶ | Md Irshad Ahmad⁷ | Arabinda Ghosh⁸  | Ajoy Kumer⁹  |
 Samir Kumar Sil¹

¹Molecular Genetics and Cell Physiology Laboratory, Department of Human Physiology, Tripura University, Suryamaninagar, Tripura, India

²Cancer Biology Laboratory and DBT-AIST International Center for Translational and Environmental Research (DAICENTER), Department of Biosciences and Bioengineering, Indian Institute of Technology (IIT) Guwahati, Guwahati, Assam, India

³Center for Global Health Research, Saveetha Medical College and Hospital, Saveetha Institute of Medical and Technical Sciences, Chennai, Tamil Nadu, India

⁴Department of Health Sciences, Novel Global Community Educational Foundation, Hebersham, New South Wales, Australia

⁵Cell Biology and Physiology Division, CSIR-Indian Institute of Chemical Biology, Kolkata, West Bengal, India

⁶Department of Biochemistry, College of Science, King Saud University, Riyadh, Saudi Arabia

⁷Department of Structural Biology, School of Medicine, UTHealth Science Center, San Antonio, Texas, USA

⁸Department of Computational Biology and Biotechnology, Mahapurusha Srimanta Sankaradeva Viswavidyalaya, Guwahati, Assam, India

⁹Department of Chemistry, College of Arts and Sciences, IUBAT-International University of Business Agriculture and Technology, Dhaka, Bangladesh

Correspondence

Ajoy Kumer, Department of Chemistry, College of Arts and Sciences, IUBAT-International University of Business Agriculture and Technology, 4 Embankment Drive Road, Sector 10, Uttara Model Town, Dhaka 1230, Bangladesh.
 Email: kumarajoy.cu@gmail.com

Samir Kumar Sil, Molecular Genetics and Cell Physiology Laboratory, Department of Human Physiology, Tripura University Suryamaninagar, 799022 Tripura, India.
 Email: s_k_sil@tripurauniv.ac.in

Abstract

The anti-apoptotic proteins, Bcl-2 and Survivin, are consistently overexpressed in numerous human malignancies, notably in colorectal cancer. 2,4-Di-tert-butylphenol (2,4-DTBP) is a naturally occurring phenolic compound known for its diverse biological activities, including anti-cancer properties. The mechanism behind 2,4-DTBP-induced inhibition of cell proliferation and apoptosis in human colorectal cancer cells, specifically regarding Bcl-2 and Survivin, remains to be elucidated. In this study, we employed both in silico and in vitro methodologies to underpin this interaction at the molecular level. Molecular docking demonstrated a substantial binding affinity of 2,4-DTBP towards Bcl-2 ($\Delta G = -9.8$ kcal/mol) and Survivin ($\Delta G = -5.6$ kcal/mol), suggesting a potential inhibitory effect. Further, molecular dynamic simulations complemented by MM-GBSA calculations confirmed the significant binding of 2,4-DTBP with Bcl-2 ($dG_{\text{bind}} = -54.85 \pm 6.79$ kcal/mol) and Survivin ($dG_{\text{bind}} = -32.36 \pm 1.29$ kcal/mol). In vitro assays using HCT116 colorectal cancer cells revealed that 2,4-DTBP inhibited proliferation and promoted apoptosis in both a dose- and time-dependent manner. Fluorescence imaging and scanning electron microscopy illustrated the classical features associated with apoptosis upon 2,4-DTBP exposure. Cell cycle analysis through flow cytometry

This is an open access article under the terms of the [Creative Commons Attribution](https://creativecommons.org/licenses/by/4.0/) License, which permits use, distribution and reproduction in any medium, provided the original work is properly cited.

© 2024 The Authors. *Journal of Cellular and Molecular Medicine* published by Foundation for Cellular and Molecular Medicine and John Wiley & Sons Ltd.

highlighted a G1 phase arrest and apoptosis assay demonstrated increased apoptotic cell population. Notably, western blotting results indicated a decreased expression of Bcl-2 and Survivin post-treatment. Considering the cytoprotective roles of Bcl-2 and Survivin through the inhibition of mitochondrial dysfunction, our findings of disrupted mitochondrial bioenergetics, characterized by reduced ATP production and oxygen consumption, further accentuate the functional impairment of these proteins. Overall, the integration of *in silico* and *in vitro* data suggests that 2,4-DTBP holds promise as a therapeutic agent targeting Bcl-2 and Survivin in colorectal cancer.

KEYWORDS

2,4-Di-tert-butylphenol (PubChem CID: 71315956), apoptosis, Bcl-2, colorectal cancer, mitochondrial stress, Survivin

1 | INTRODUCTION

Colorectal cancer (CRC) has emerged as a leading oncological challenge, marking its presence as one of the most prevalent gastrointestinal cancers that significantly contributes to global morbidity and mortality.^{1,2} Recent data from GLOBOCAN 2020 elucidate a worrying trend, placing CRC at the third spot in terms of cancer incidence, encompassing 10% of all new cancer diagnoses, while it stands second in causing 9.4% of global cancer-related fatalities, irrespective of demographic divisions such as age and gender.³ The disease exhibits significant variability, influenced by both genetic and environmental factors.⁴ Numerous studies have demonstrated that dietary patterns and inflammation induced by various factors can contribute to the development of CRC.^{5,6} Despite the leaps in oncological diagnostic technologies, the late-stage diagnosis of CRC remains a persistent issue, leading to complex clinical manifestations.⁷

With an increasing understanding of the cellular and molecular mechanisms underpinning CRC, apoptotic pathways, specifically the targeting of antiapoptotic proteins such as Bcl-2 and Survivin, have garnered immense attention in therapeutic research.^{8,9} These proteins often showcase elevated expression levels in chemo-resistant cancer cell subtypes, creating a formidable barrier against the apoptotic potential of many chemotherapeutics.^{10,11} Delving into the specificity of their expression, Bcl-2 is found to be predominantly expressed in intestinal stem cells (ISCs) across both human and rodent models.¹² Prior studies highlight the pivotal role of Bcl-2 in safeguarding ISCs from radiation-mediated injuries; intriguingly, the pharmacological inhibition of Bcl-2 manifests retardation in the proliferation of malignant cells, accentuating its potential as a chemopreventive target.¹² Parallely, Survivin, identified as the most compact member of the inhibitor of apoptosis protein (IAP) family, presents an overexpression pattern across an array of cancers, including CRC, with its presence being minimal in mature, differentiated tissues.¹³ Given these unique expression profiles, both Bcl-2 and Survivin have emerged as compelling targets for the development of innovative CRC therapeutics.

Nevertheless, the clinical management of CRC is riddled with challenges, most prominently due to inherent drug resistance

mechanisms and a myriad of other molecular complexities.¹⁴ In this therapeutic quest, nature's vast arsenal of molecules has often been the starting point for the identification of efficacious drug candidates, mainly attributed to their innate pharmacological properties and favourable safety profiles.¹⁵ In this vast natural repository, 2,4-ditert-butylphenol (2,4-DTBP), a lipophilic phytochemical,¹⁶⁻¹⁹ stands out with its plethora of biological activities that span from antioxidant,^{20,21} anti-inflammatory²² and antimicrobial²³⁻²⁷ to notable anti-cancer properties.²⁸ However, a distinct knowledge gap persists in understanding how 2,4-DTBP modulates the activities of Bcl-2 and Survivin, especially in the context of CRC cell proliferation and apoptotic responses. In addressing this lacuna, the present study embarks on a groundbreaking journey, employing rigorous methodologies to elucidate the molecular interplay between 2,4-DTBP and these pivotal antiapoptotic proteins in CRC. With a focus on uncharted territories, our research promises not only to contribute novel insights into CRC therapeutics but also to redefine the potential of naturally derived compounds in oncological applications.

2 | MATERIALS AND METHODOLOGY

2.1 | Molecular docking

In order to delve into the binding capabilities of 2,4-DTBP with target proteins Survivin (PDB ID: 1F3H) and Bcl-2 (PDB ID: 6GL8), we utilized molecular docking methodologies. The computational process was carried out using Autodock version 4.2.1, a widely accepted software known for its precision and robustness in predicting ligand-protein interactions.²⁹ To ensuring the reliability and reproducibility of the results, three independent docking runs were performed. Each run generated a total of 50 solution poses, operating within a population size of 500. The key parameters set for the docking experiments were 2,500,000 evaluations and a maximum of 27,000 generations, ensuring thorough sampling of the conformational space. The other software settings were maintained at their default values to maintain the standard protocol. Subsequent to the docking procedure, root mean square deviation (RMSD) clustering

was employed to interpret and group the obtained docking poses. The poses were re-clustered employing three distinct clustering tolerances, viz., 0.5 Å, 1 Å and 2 Å. This strategy aids in pinpointing the most favourable ligand pose cluster, gauged by the lowest energy score and maximum population.

The binding pocket for Survivin was ascertained from prior literature.³⁰ Key residues involved in ligand binding include LEU-96, PHE-93, VAL-89, LEU-98, PHE-101, LEU-104, LYS-15, PHE-86, LEU-102, LEU-6, TYR-10, LEU-14, PHE-13, ARG-18, LEU-87 and ILE-74. Accordingly, a grid box encapsulating this binding pocket was defined with centre coordinates $X=31.4487$, $Y=2.1169$, $Z=16.214$ and spanning dimensions of $X:30$, $Y:25$, $Z:24$. Conversely, the binding cavity for Bcl-2 was derived from the structural database (<https://www.rcsb.org/structure/6GL8>).³¹ The residues forming this cavity were delineated based on a 3 Å radius encompassing the co-crystallized ligand. The resultant grid box for Bcl-2 docking was positioned at $X=14.09$, $Y=15.47$, $Z=15.48$, with dimensions set at $X:3.53$, $Y:0.58$, $Z:12.41$. This rigorous and comprehensive methodology was essential for revealing the intricate details of how 2,4-DTBP interacts with both Survivin and Bcl-2, shedding light on its potential therapeutic implications.

2.2 | Molecular dynamics simulations

Molecular dynamics (MD) simulations are carried out for the complexes between Bcl-2 and Survivin with 2,4-DTBP using Desmond 2020.1 from Schrödinger, LLC. The simulation set-up utilized the reliable OPLS-2005 force field, renowned for its accuracy in modelling biological systems.^{31,32} An explicit solvent model was employed, and TIP3P water molecules filled a salvation box of dimensions $10\text{Å} \times 10\text{Å} \times 10\text{Å}$.³³ The physiological ionic environment was mimicked using a 0.15 M NaCl solution, with Na⁺ ions neutralizing any net charge. To ensure system stability and optimal conformational sampling, an NVT ensemble equilibrated the protein–ligand complexes for 10 ns. This was followed by a 12-ns NPT ensemble equilibration and minimization. The simulations incorporated the Nose-Hoover chain coupling scheme for temperature regulation³⁴ and utilized the Martyna–Tuckerman–Klein chain coupling approach for pressure control.³⁵ Key parameters like the electrostatic interactions were computed using the particle mesh Ewald method.³⁶ For accuracy in capturing dynamic interactions, bonded forces were calculated at every 2-fs time step by the RESPA integrator. The overall simulation was conducted for a substantial duration of 100 ns, and essential parameters such as RMSD, Rg, RMSF, H-bonds, salt bridges and SASA were tracked to monitor system stability and interactions.

2.3 | Cell lines and reagents

Since HCT116 cells have been used in a range of biological investigations, including colorectal cancer proliferation, therapeutic research

and drug screening, we used this colorectal cancer cell line for our research along with a normal human fibroblast cell line, GM00637. We got the colorectal cancer cell line (human; HCT116) from NCCS, India, and normal human fibroblast cell line (GM00637) from Jadavpur University, West Bengal, India. Normal and cancer cells were cultured in DMEM (HiMedia) with FBS (10%) (HiMedia) and 2% antibiotic (Penstrep; HiMedia) in a CO₂ incubator (Esco Scientific; at 37°C in a 5% CO₂ environment). SRL Pvt. Ltd., India supplied the crystal violet. The drugs 2,4-DTBP (Sigma-Aldrich; Product No.: 137731) and 5-fluorouracil (5-FU) (Sigma-Aldrich; Product No.: F6627) were used in this study.

2.4 | MTT assay

The proliferation of HCT116 and GM00637 cells after treatment with 2,4-DTBP was determined by MTT assay, as we described earlier.³⁷ Cells were treated with or without 2,4-DTBP and 5-FU and incubated for 24 h. A 0.5 mg/mL concentration of MTT solution (100 µL/well) was added following incubation. At 570 nm, the absorbance was recorded using a plate reader (Thermo Scientific, USA).

2.5 | Clonogenic assay

A total of 3×10^3 HCT116 cells in each well of a six-well plate were seeded, and the clonogenicity assay was performed according to the standard protocol.³⁸ 2,4-DTBP-treated and vehicle-controlled colonies were stained for 30 min with 0.5% crystal violet (SRL Pvt. Ltd., India) and washed with double distilled water. Images of each well were taken, and ImageJ software was used to count the colonies.

2.6 | Cell migration assay

A uniform monolayer of HCT116 cells in 35 mm culture plates was scratched with a 10 µL microtip, treated with/without the IC₅₀ concentration of 2,4-DTBP and kept in the incubator for 24 h. The bright field images (0 and 24 h) of the same treated and vehicle-controlled scratched area were taken by an inverted microscope (ZEISS Axio).³⁹

2.7 | AO/PI and DAPI fluorescent staining assay

The AO/EB (AO:EB = 1:1) and DAPI fluorescent staining procedures were performed to investigate the 2,4-DTBP-induced chromatin condensation in HCT116 colorectal cancer cells according to the standard protocols.^{40,41}

2.8 | DNA fragmentation assay

The nuclear DNA damage caused by 2,4-DTBP was studied using a DNA fragmentation assay.⁴² DNA isolated from the vehicle-controlled

and 2,4-DTBP-treated HCT116 cells was electrophoresed on a 1.5% agarose gel to separate the bands. The ChemiDoc™ MP imaging system (Bio-Rad, USA) was used to capture images of the gel.

2.9 | Scanning electron microscopic (SEM) study

HCT116 cells cultured on glass coverslips were treated with or without the IC₅₀ dose of 2,4-DTBP for 3 h. Following treatment, the cells were washed in PBS and fixed at room temperature for 30 min in 2.5% glutaraldehyde (HiMedia; diluted in PBS). Postfixation, the cells were rinsed three times for 10 min with PBS. For lipid fixing, 1% osmium tetroxide (OSO₄) was applied to the fixed cells for 1 h.⁴³ After washing, graded ethanol was used to dry the cells (20%, 30%, 40%, 50%, 60%, 70%, 80% and 90%, once for each and twice in 100% for 10 min each). After being dehydrated with graded alcohol, the cells were then placed in tetramethylsilane [Si(CH₃)₄] overnight to complete the drying process. The next day, the samples were prepared for imaging by SEM (Carl ZEISS Sigma 300 VP).

2.10 | Annexin V/PI flow cytometric assay

Treated (IC₅₀ concentration of 2,4-DTBP) and untreated (vehicle-controlled) HCT116 cells were fixed at room temperature for 10–15 min with formaldehyde (4%). After fixation, the cells were kept on ice for 5–10 min. The cells were incubated for 10 min in a solution containing 5 mg/mL BSA in PBS after they had been washed and resuspended in the same solution. The exposed phosphatidylserine residues of cells were tracked using FITC-Annexin V staining using the protocol outlined in the 'Apoptosis kit' (Molecular Probes). Flow cytometry was used to figure out how many cells were positive for Annexin V and PI alone or together. For dot blot analysis, Cell Quest Pro software (BD BioSciences, USA) was used.⁴⁴

2.11 | Cell-cycle assay

HCT116 cells (50 × 10³ cells/35 mm culture plate) were seeded, and the following day, cells were treated with or without the IC₅₀ concentration of 2,4-DTBP for 24 h, trypsinized, and washed three times with cold PBS. After discarding the PBS, 70% ethanol was added drop by drop with moderate vortexing of the tube containing the cell palate to fix the cells and stored overnight at 4°C. The alcohol was discarded from each vial after centrifugation (3000 rpm) for 15 min at 4°C. Following a PBS wash, cells were stained for 30 min in the dark with a PI/RNAase solution. FACS Celesta (Becton-Dickinson, Franklin Lakes, NJ) was used to detect cell cycle distribution, and FCS Express software was used to evaluate the resulting data. The intensity of the labelled cells' fluorescence is proportional to the amount of DNA they have.⁴⁵

2.12 | Western blot analysis

The western blot study was performed according to the standard protocol.⁴⁵ SDS-PAGE separated equal amounts of protein from 2,4-DTBP-treated and vehicle-controlled HCT116 cells, which were transferred to a nitrocellulose membrane, and subsequently processed to detect the target protein. Primary antibodies against Bcl-2 (CST 15071; Cell Signaling Technology, USA), Survivin (CST 2808; Cell Signaling Technology, USA), Caspase-3 (BB-AB0243; Bio Bharati Life Science Pvt. Ltd., India) and α -tubulin (CST 2144; Cell Signaling Technology, USA; used as a loading control) were used to incubate the membranes. A secondary antibody coupled with horseradish peroxidase (Abcam, USA) was used to incubate the blots for 2 h at room temperature. The bands representing the individual proteins were seen using a ChemiDoc XRS System.

2.13 | Cellular bioenergetics study

After counting the HCT116 cells with a TC-10 cell counter (Bio-Rad, Hercules, CA, USA), 1 × 10⁴ cells were seeded in each well and incubated for 24 h in a CO₂ incubator. Following attachment, the cells were treated with/without the IC₅₀ concentration of 2,4-DTBP for 3 h. The same treatment was repeated three times. The bioenergetics study was performed by an Agilent Seahorse extracellular flux analyzer (XFe24; Seahorse Bioscience, Billerica, MA, USA) according to the standard protocol.^{44,46}

2.14 | ProTox study

The OSIRIS Property Explorer was used to analyse pharmaceutically essential aspects of a natural chemical (2,4-DTBP) swiftly; it predicts all-natural compounds' Absorption, Distribution, Metabolism and Elimination (ADME) properties (https://www.cheminfo.org/Chemistry/Cheminformatics/Property_explorer/index.html). ProTox-II (https://tox-new.charite.de/protox_II/), a free in silico toxicity prediction web server, projected 2,4-DTBP's toxicity profile. The PubChem Name of the drug was entered into the ProTox-II graphical user interface for toxicity computation using machine learning algorithms-based models that comprised acute (oral) and organ (liver) toxicities, toxicological endpoints, pathways and targets. The webserver's prediction types, training/test set compounds, cross-validation, descriptors, and techniques were used without modification.^{47,48}

2.15 | Statistical analysis

Graphs were made using GraphPad Prism-8.2.1 (GraphPad Prism, RRID: SCR_002798) as well as Excel software (Microsoft Excel-2019). Experiments were conducted three times, and the results of these experiments were reported as the mean ± SD of

three data sets. A two-tailed paired *t*-test was performed when the number of groups was two to calculate the *p*-value using the SPSS (IBM SPSS Statistics 25) software, which reflects the significance of differences between distinct sets of experimental data. $p < 0.05$, $p < 0.01$ and $p < 0.001$ are denoted by *, ** and ***, respectively.

3 | RESULTS AND ANALYSIS

3.1 | Molecular Docking

In molecular docking analysis, the X-ray crystal structures of proteins Bcl-2 and Survivin have interacted with 2,4-DTBP. During docking analysis, the highest population of ligand 2,4-DTBP poses with Bcl-2 belongs to the 0.25 Å RMSD cluster having the lowest binding energy $\Delta G = -9.8$ kcal/mol has been considered for further analysis. Out of 50, 31 generated ligand pose populations fall within this cluster, ranging from 9.1 to 9.8 kcal/mol binding energies. The complex with the lowest binding energy exhibited pi-pi stacking with Phe104 and Phe112

residues of the binding cavity of Bcl-2, while Ala149 was involved in pi-alkyl interaction with the ligand (Figure 1A). Met115, Val133, Arg146, Glu152 and Phe153 residues are involved in van der Waal's interaction (Figure 1A). Survivin interaction with 2,4-DTBP exhibited the lowest binding energy $\Delta G = -5.6$ kcal/mol and formed a pi-alkyl interaction with Phe86 residue (Figure 1B). This complex is further analysed for molecular dynamics simulation studies in order to analyse the complex's stability. The negative score of docking output signifies the free energy of binding (ΔG). The more negative ΔG indicates more efficient binding of the ligand with the respective proteins.

3.2 | Molecular dynamics simulation

To assess the convergence and stability of Bcl-2 + 2,4-DTBP and Survivin + 2,4-DTBP, molecular dynamics and simulation (MD) investigations were performed. Comparing the root mean square deviation (RMSD) values for simulations of 100 ns revealed stable conformation. The C α -backbone of Bcl-2 that was bound to 2,4-DTBP-ligand displayed an RMSD of 1.9 Å (Figure 2A).

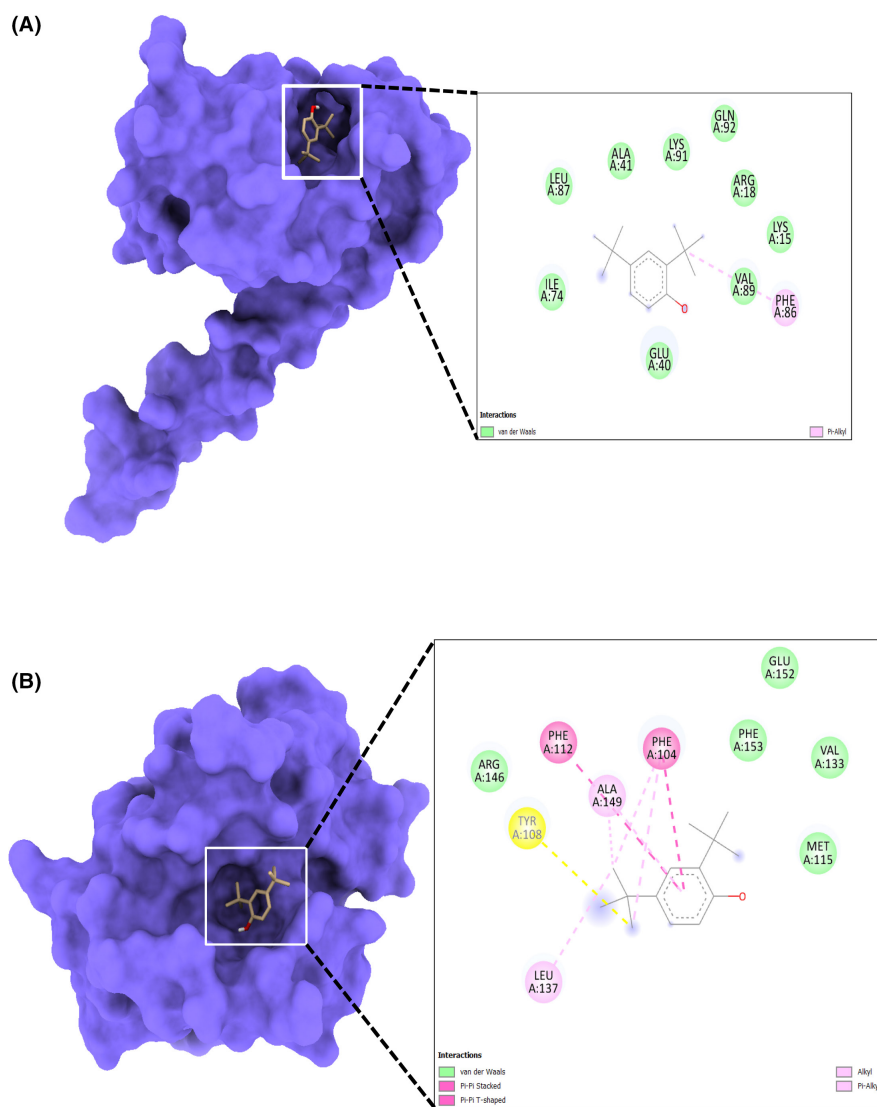


FIGURE 1 Molecular docking study: Surface view of the best pose of (A) Bcl-2 + 2,4-Di-tert-butylphenol and (B) Survivin + 2,4-Di-tert-butylphenol complexes displaying the surface view on the left panel and 2D interaction profile of the ligand with binding cavity residues.

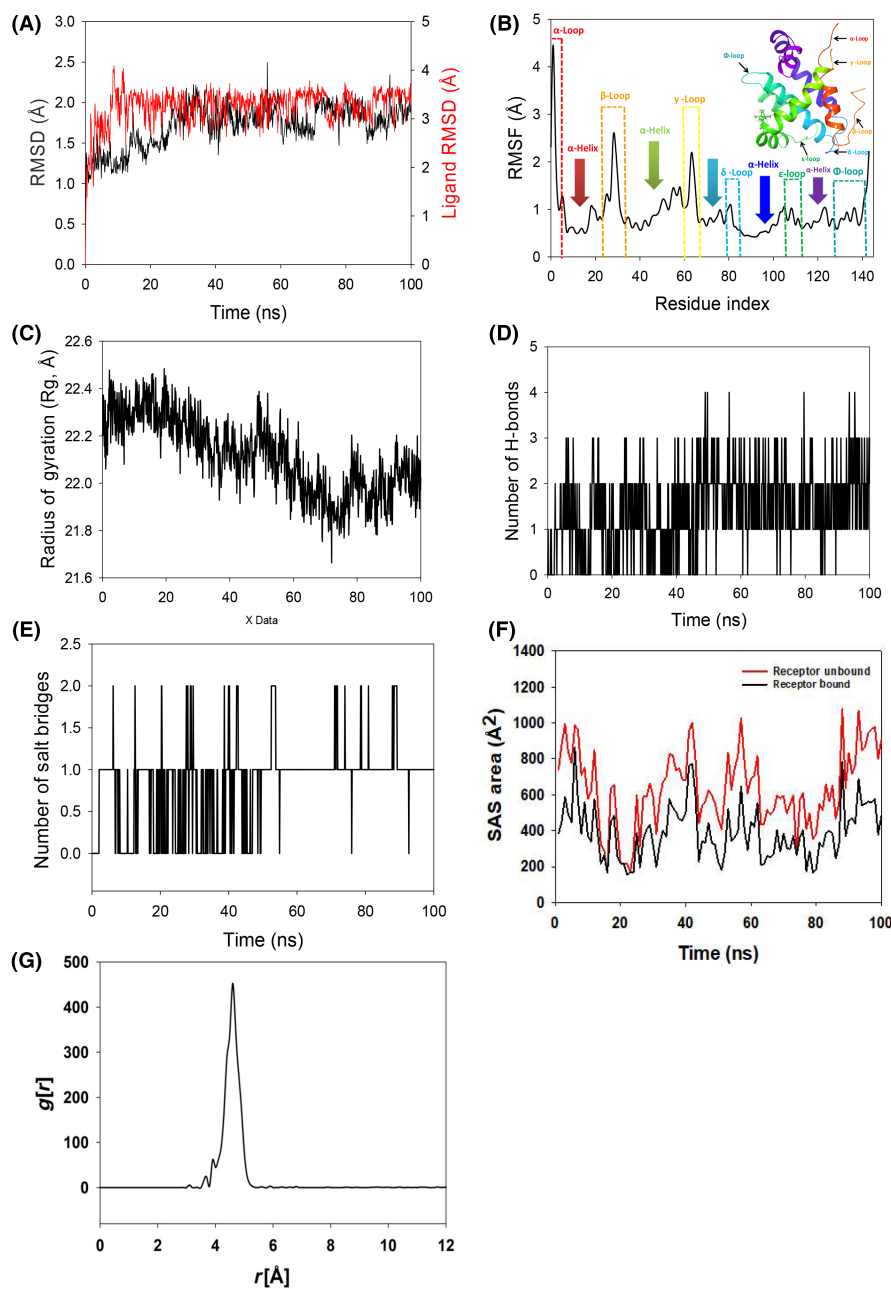


FIGURE 2 Molecular dynamics simulation analysis of 100ns trajectories and radial distribution function of Bcl-2 bound with 2,4-DTBP complex: (A) α -backbone of Bcl-2 + 2,4-DTBP-ligand, (B) RMSF of α -backbone of Bcl-2 bound with 2,4-DTBP-ligand, (C) Radius of gyration (R_g) of α -backbone of Bcl-2 bound with 2,4-DTBP (D) Formation of hydrogen bonds in Bcl-2 bound with 2,4-DTBP complex, (E) Numbers of salt bridge formation between and 2,4-DTBP, (F) Solvent accessible surface area of Bcl-2 bound with 2,4-DTBP complex and (G) Radial distribution function (RDF) indicating the distance $g[r]$ of 2,4-DTBP-ligand from binding cavity residues of Bcl-2.

While the ligand RMSD of 2,4-DTBP-ligand is depicted as 2.0 Å (Figure 2A). Stable RMSD plots during simulation indicate convergence and stability. So, it can be hypothesized that 2,4-DTBP bound to Bcl-2 is quite stable due to the ligand's high affinity. The plot for root mean square fluctuations (RMSF) indicates the residual fluctuations due to conformational variations into different secondary structures. Here, the RMSF plot displayed six distinct loops formed due to fluctuating residues, while high fluctuations were observed among 1–5, 23–35 and 60–67 residual positions (Figure 2B). The highest fluctuating peak comprised of 4.5 Å coined as α -loop, β -loop 3.2 Å and γ -loop 3.1 Å, respectively (Figure 2B). Other three loops formed between 79–84 residues (δ -loop), 106–112 residues (ϵ -loop) and 134–143 residues (ϕ -loops) (Figure 2B). Rest small spikes conformed into α -helices. Therefore, the protein Bcl-2 has significant flexibility to conform to specific secondary

structures in order to accommodate the ligand. The radius of gyration (R_g) quantifies the protein's compactness. Bcl-2 α -backbone bound to 2,4-DTBP-ligand demonstrated a decrease in radius of gyration (R_g) from 22.3 to 22.01 Å (Figure 2C). A significantly decreasing gyration (R_g) indicates that the ligand-bound protein is in a highly compact orientation. The high number of hydrogen bonds between the protein and ligand is indicative of strong engagement and high complex stability. During the 100ns simulation, the number of hydrogen bonds between Bcl-2 and 2,4-DTBP was significant (Figure 2D). Bcl-2 and 2,4-DTBP-ligand exhibit an average number of consistent hydrogen bonds (average three numbers) (Figure 2D). Salt bridges are generated between nearby oppositely charged residues and serve a crucial role in protein stability.⁴⁹ The average number of salt bridges formed between Bcl-2 and 2,4-DTBP-ligand in this study (Figure 2E). Similar patterns

were observed in both ligand-bound and unbound states of solvent accessible surface area (SASA) after Rg analysis. Figure 2F clearly shows that in the unbound state of the 2,4-DTBP-ligand to the receptor, the protein Bcl-2 displayed a large solvent accessible surface area (Figure 2F, red). The SASA value decreased when attached to the 2,4-DTBP-ligand compared to the unbound condition (Figure 2F, black). Overall, the Rg study shows that when ligands bind to proteins, they become more compact and less flexible. The interaction between the ligand and active site amino acid residues centre of mass is analysed by studying the radial density function (RDF). RDF finds the probability of distances between two particles from their centres. In this study, the distance of the ligand 2,4-DTBP from the key binding residues of Bcl-2 was detected after a pro-simulation study, as shown in Figure 2G. The significance $g[r]$ values indicated in the plot signify good interaction of the 2,4-DTBP-ligand with the residues, where the highest probability of finding the ligand near the residues was measured to be 4.5 Å (Figure 2G).

The RMSD of C α -backbone of Survivin bound to 2,4-DTBP-ligand exhibited a deviation of 2.1 Å (Figure 3A). The ligand RMSD of 2,4-DTBP-ligand is depicted as 5.2 Å (Figure 3A). Stable RMSD plots during simulation indicate convergence and stability. Therefore, it can be hypothesized that 2,4-DTBP bound to Survivin is quite stable due to the ligand's high affinity. The

plot for root mean square fluctuations (RMSF) indicates the residual fluctuations due to conformational variations into different secondary structures. Here, the RMSF plot displayed 1 distinct loop and 2 helices formed due to fluctuating residues, while high fluctuations were observed among the 15–20 (H1-helix), 38–56 (L1-loop) and 115–125 (H2-helix) residual positions (Figure 3B). The highest fluctuating peak comprised 5.8 Å for L1 loop, 3.8 Å for H1 helix and 6 Å for H2 helix, respectively (Figure 3B). Rest small spikes conformed into α -helices. Therefore, the protein Survivin has significant flexibility to conform to specific secondary structures in order to accommodate the ligand. The radius of gyration (Rg) quantifies the protein's compactness. Survivin C α -backbone bound to 2,4-DTBP-ligand demonstrated a decrease in radius of gyration (Rg) from 18.85 to 18.4 Å (Figure 3C). Significantly decreasing gyration (Rg) indicates that the ligand-bound protein is in a highly compact orientation. The high number of hydrogen bonds between the protein and ligand is indicative of strong engagement and high complex stability. During the 100 ns simulation, the number of hydrogen bonds between Survivin and 2,4-DTBP was significant (Figure 3D). Survivin and 2,4-DTBP-ligand exhibit an average number of consistent hydrogen bonds (Average 1 numbers) (Figure 3D). Similar patterns were observed in both ligand-bound and unbound states of solvent accessible surface area (SASA) after Rg analysis. Figure 3E clearly shows that in the unbound state of

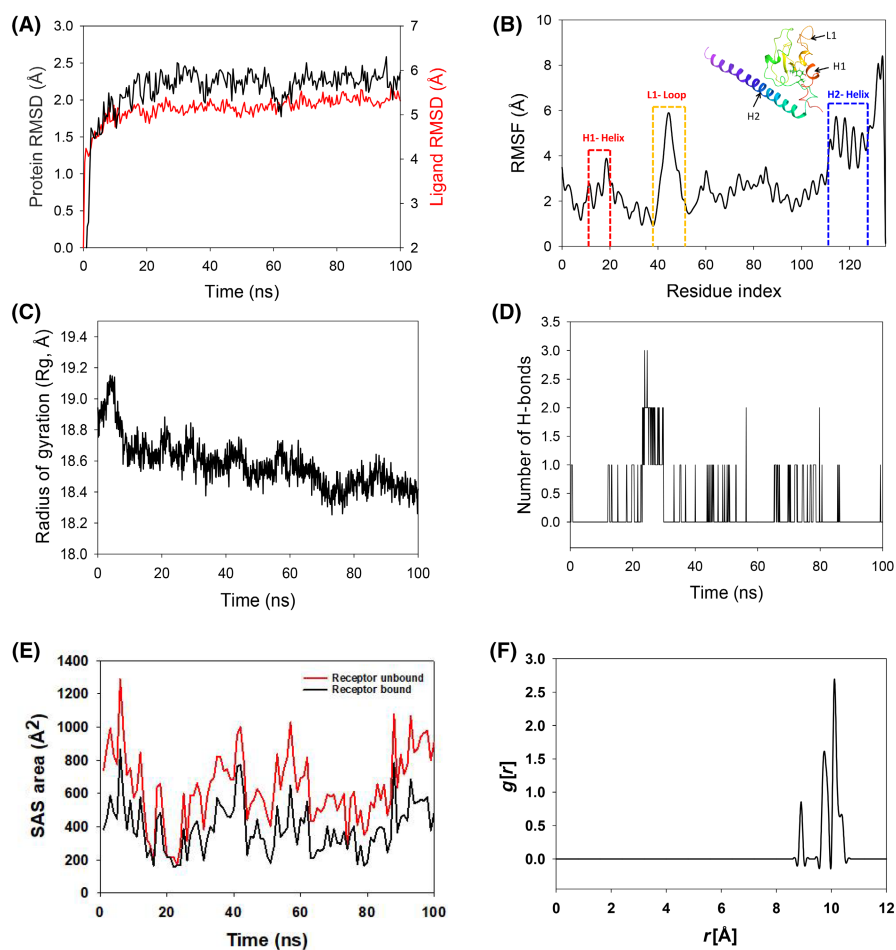


FIGURE 3 Molecular dynamics simulation analysis of 100 ns trajectories and radial distribution function of Survivin bound with 2,4-DTBP complex: (A) C α -backbone of Survivin+2,4-DTBP-ligand, (B) RMSF of C α -backbone of Survivin bound with 2,4-DTBP-ligand, (C) radius of gyration (Rg) of C α -backbone of Survivin bound with 2,4-DTBP, (D) formation of hydrogen bonds in Survivin bound with 2,4-DTBP complex, (E) solvent accessible surface area of Survivin bound with 2,4-DTBP complex and (F) radial distribution function (RDF) indicating the distance $g[r]$ of 2,4-DTBP-ligand from binding cavity residues of Survivin.

2,4-DTBP-ligand to the receptor, the protein Survivin displayed a large solvent accessible surface area (Figure 3E, red). The SASA value decreased when attached to the 2,4-DTBP-ligand compared to the unbound condition (Figure 3E, black). Overall, the Rg study shows that when ligands bind to proteins, they become more compact and less flexible.

Usually, water bridges play a significant role in the presence of water as a solvent to hold the ligand in proper proximity to the binding residues of proteins, as confirmed by the RDF study. In the 2,4-DTBP–Survivin interaction, the ligand distance from the key residues of Survivin exhibited much lesser (Figure 3F) compared to Bcl-2. The lesser distance indicates less interaction, which might be due to the absence of salt bridges between Survivin and 2,4-DTBP.

3.3 | Molecular mechanics generalized born surface area (MM-GBSA) calculations

Using the MD simulation trajectory, the binding free energy and other contributing energy in the form of MM-GBSA are determined for the Bcl-2+2,4-DTBP and Survivin+2,4-DTBP complexes. The results (Table 1) suggested that the maximum contribution to ΔG_{bind} in the stability of the simulated complexes was due to $\Delta G_{\text{bindCoulomb}}$, $\Delta G_{\text{bindvdW}}$, $\Delta G_{\text{bindHbond}}$ and $\Delta G_{\text{bindLipo}}$, while $\Delta G_{\text{bindCovalent}}$ and $\Delta G_{\text{bindSolvGB}}$ contributed to the instability of the corresponding complexes. Bcl-2+2,4-DTBP complex has comparatively higher binding free energies $dG_{\text{bind}} = -54.85 \pm 6.79$ kcal/mol higher than Survivin+2,4-DTBP complex $dG_{\text{bind}} = -32.36 \pm 1.29$ kcal/mol (Table 1). These results demonstrated that Bcl-2+2,4-DTBP and Survivin+2,4-DTBP have the potential to form stable protein-ligand complexes with a high affinity for binding to the protein, efficacy in binding to the target protein and the ability to efficiently attach to the target protein.

3.4 | Time series analysis of Bcl-2+2,4-DTBP and Survivin+2,4-DTBP complex

Time series analysis of MD simulation frames of Bcl-2+2,4-DTBP from the beginning of simulation (0ns), 20, 40, 60, 80 and 100ns

TABLE 1 Binding free energy components for the Bcl-2+2,4-DTBP and Survivin+2,4-DTBP complex calculated by MM-GBSA.

Energies (kcal/mol)	Bcl-2+2,4-DTBP	Survivin+2,4-DTBP
ΔG_{bind}	-54.85 ± 6.79	-32.36 ± 1.29
$\Delta G_{\text{bindLipo}}$	-16.18 ± 1.04	-12.02 ± 2.94
$\Delta G_{\text{bindvdW}}$	-46.19 ± 2.18	-26.91 ± 2.28
$\Delta G_{\text{bindCoulomb}}$	-25.27 ± 6.20	-15.71 ± 2.10
$\Delta G_{\text{bindHbond}}$	-1.93 ± 0.34	-1.53 ± 2.34
$\Delta G_{\text{bindSolvGB}}$	32.34 ± 3.34	41.56 ± 1.14
$\Delta G_{\text{bindCovalent}}$	5.83 ± 4.51	7.31 ± 2.21

was recorded and represented in Figure 4. At the beginning of the simulation, the ligand 2,4-DTBP exhibited a linear arrangement (Figure 4A, arrow), while at 20ns, 2,4-DTBP moved and bent a little from its initial pose. These angular movements were observed through the simulation to orient the ligand 2,4-DTBP for better accommodation within the binding pocket (Figure 4A). Time series analysis of MD simulation frames of Survivin+2,4-DTBP from the beginning of simulation (0ns), 20, 40, 60, 80 and 100ns was recorded and represented in Figure 4B. At the beginning of simulation, the ligand 2,4-DTBP exhibited a linear tilted arrangement (Figure 4B, arrow), while at 20ns 2,4-DTBP moved outward linearly from its initial pose. At 40–100ns, the pose of the ligand is arranged to occupy different dimensions. These angular movements were observed through the simulation to orient the ligand 2,4-DTBP for better accommodation within the binding pocket (Figure 4B).

3.5 | 2,4-DTBP-induced cytotoxicity

The antiproliferative effect of 2,4-DTBP in HCT116 (human colorectal cancer) cells and GM00637 (human normal fibroblast) cells was determined by exposing both cell lines to a series of 2,4-DTBP concentrations for 24h (Figure 5A,B). HCT116 cells were also treated with the conventional anti-cancer drug 5-FU (used as a positive control). An in vitro cytotoxicity assay (MTT) was used for 24h to measure the percentage of cell viability with or without (vehicle control) the drugs. The estimated IC_{50} value of 2,4-DTBP in HCT116 cells was $57.044 \pm 0.32 \mu\text{M}$. However, it showed lower toxicity on the GM00637 cells ($90.84 \mu\text{M} \pm 4.28 \mu\text{M}$) compared to the colorectal cancer cells. 5-FU exhibited a higher IC_{50} ($>100 \mu\text{M}$) than 2,4-DTBP in colorectal cancer cells (Figure 5A).

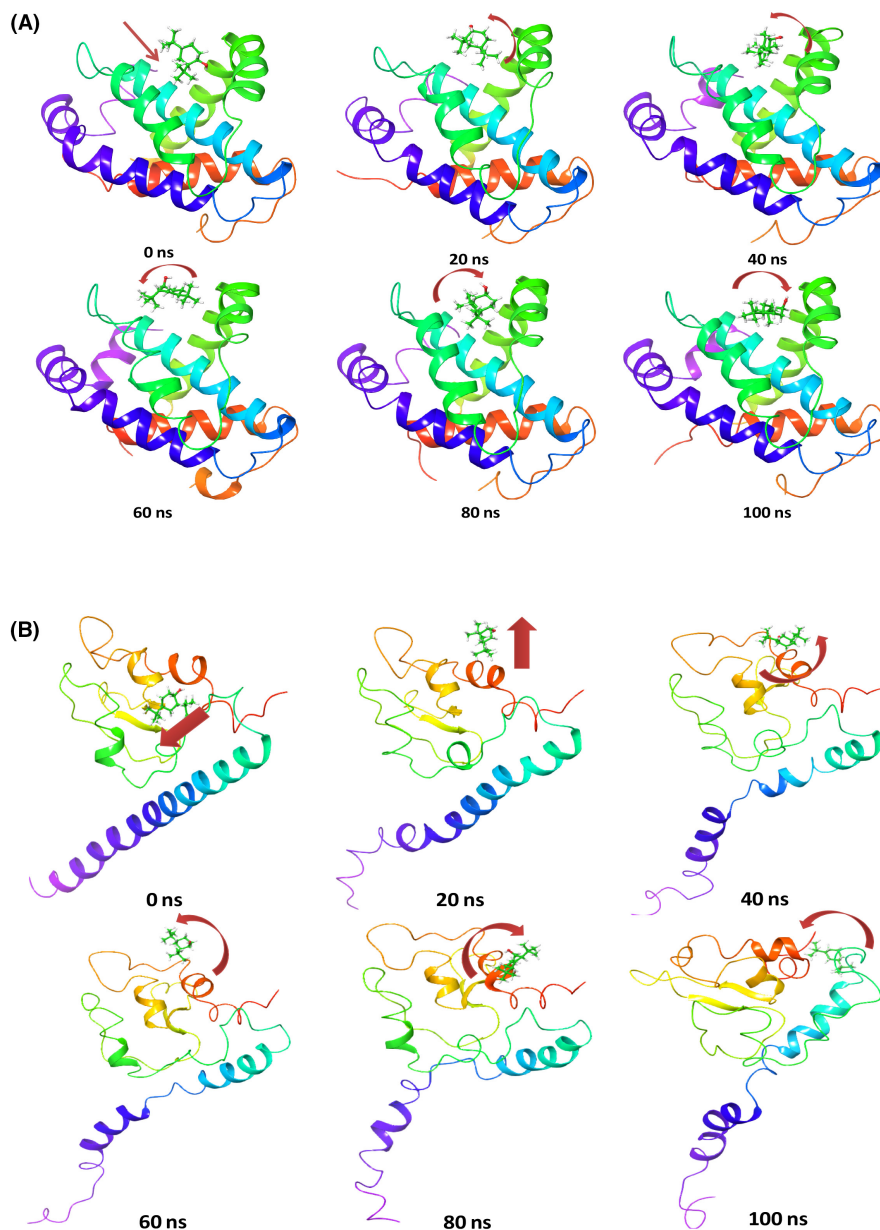
3.6 | 2,4-DTBP inhibited the clonogenic potential

Using a clonogenic test, we validated the impact of 2,4-DTBP on the ability of each HCT116 cell to form colonies. When 2,4-DTBP was used at the IC_{50} concentration for 24h, the number of colonies was significantly reduced in the experimental group compared to the untreated vehicle control group (Figure 5C).

3.7 | 2,4-DTBP inhibited the cell migration

The impact of 2,4-DTBP on cell migration was evaluated by a migration assay. Once a scratch was made using a $10 \mu\text{L}$ microtip into a monolayer of HCT116 cells, the cells were incubated with the IC_{50} concentration of 2,4-DTBP for 24h, and images of the scratched site were captured between 0 and 24h. Comparing the gap size of treated and untreated (vehicle-controlled) wounds (0 and 24h), it was revealed that the gap size of the untreated scratch reduced after 24h, whereas, in case of treated scratch,

FIGURE 4 Time series analysis of Bcl-2+2,4-DTBP and Survivin+2,4-DTBP complex: Time series analysis of the MD trajectory in order to understand the behaviour of the (A) Bcl-2+2,4-DTBP complex and (B) Survivin+2,4-DTBP complex.



2,4-DTBP prevented the cell migration after 24h of treatment (Figure 5D). So, the results suggest that 2,4-DTBP is a potential anti-migrating agent.

3.8 | 2,4-DTBP-induced morphological changes indicating apoptosis

The acridine orange/ethidium bromide (AO/EB) (AO:EB=1:1) fluorescent staining procedure was used to find out if alterations caused by apoptosis took place in the nucleus of HCT116 colorectal cancer cells. Results were seen after 24h of incubation. After 24h, the majority of the HCT116 cells in the vehicle-controlled group fluoresce a light-green colour due to AO nuclear staining (Figure 6A), but cells treated with the IC_{50} concentration of 2,4-DTBP for 24h fluoresce a yellow-green or orange-coloured condensed chromatin, which

represents early and late apoptosis, respectively (Figure 6A).⁴⁰ DAPI (4',6-diamidino-2-phenylindole) may also be used to detect apoptosis by observing nuclear alterations as it binds specifically and firmly to the minor groove of the adenine-thymine sections of DNA. The distinct nuclear morphology of apoptotic cells, such as chromosome condensation and disintegration, aids in the detection of DAPI-stained apoptotic cells.⁴¹ In response to 2,4-DTBP (treated with the IC_{50} concentration for 24h) treatment, chromatin condensation in HCT116 cells was observed using DAPI staining, which is a hallmark of apoptosis, whereas vehicle-controlled cells had a uniformly blue-stained nucleus (Figure 6B). Plasma membrane blebbing is also a morphological sign of cells going through late-stage apoptosis. A bleb is an unusual bulge in a cell's plasma membrane brought on by localized cytoskeleton-to-plasma membrane dissociation. An apoptotic cell's plasma membrane is severely degraded and lacks the integrity needed to maintain crucial transmembrane gradients.^{50,51}

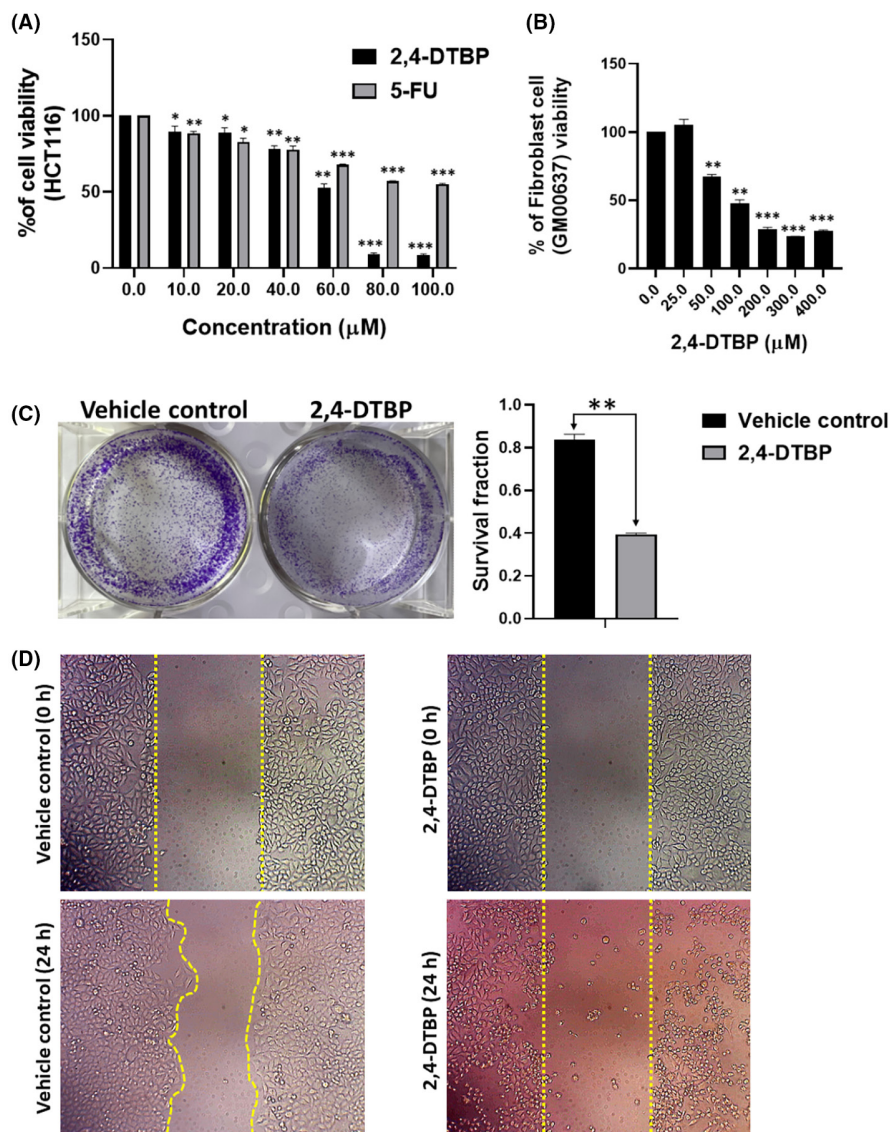


FIGURE 5 Cytotoxic, anti-clonogenic and anti-migrating potential of 2,4-DTBP. (A, B) Cell viability assay (MTT assay). (A) The bar graph demonstrates the percentage of viability of HCT116 colon cancer cells at different concentrations of 2,4-DTBP and the positive control, 5-FU. (B) The bar graph demonstrates the percentage of viability of human fibroblast cells (GM00637) at different concentrations of 2,4-DTBP. (C) HCT116 cells treated with (IC_{50}) or without (vehicle control) 2,4-DTBP. The treated group of cells shows significant anti-clonogenic potential compared to the vehicle-controlled group of cells. (D) Scratched areas of untreated (vehicle-controlled) and 2,4-DTBP-treated HCT116 colon cancer cells at 0 and 24 h, indicating inhibition of migration of HCT116 cells upon treatment. Data are presented as mean \pm SD (A, B and C graphs). * $p < 0.05$, ** $p < 0.01$ and *** $p < 0.001$ vs. vehicle control, which was determined by a two-tailed paired t-test.

Under a scanning electron microscope, treated HCT116 colorectal cancer cells (with the IC_{50} concentration of 2,4-DTBP) showed prominent membrane blebbing that indicates late apoptosis, whereas the vehicle-controlled cells did not show any such feature (Figure 6C). Fragmentation of DNA is another characteristic of late-stage apoptotic cells.^{52,53} To see whether 2,4-DTBP may cause DNA fragmentation and consequently apoptosis, HCT116 cells exposed to 2,4-DTBP (IC_{50} concentration for 24 h), tested for DNA laddering and observed using agarose gel electrophoresis, which exhibited a DNA fragmentation profile (Figure 6D) characteristic of apoptosis. However, untreated (vehicle-controlled) cells showed no signs of nucleic acid fragmentation.

3.9 | 2,4-DTBP-induced apoptosis detected by annexin V/PI double staining

After observing the apoptotic morphology from the aforementioned assays, we further examined the potential of 2,4-DTBP in inducing

apoptosis in HCT116 colorectal cancer cells by using a flowcytometric assay with Annexin V and PI. An increase in the Annexin V and PI both positive cells from 3.1% ($\pm 0.17\%$) to 19.27% ($\pm 1.62\%$) was observed after 3h of 2,4-DTBP treatment with the IC_{50} concentration for 24 h (Figure 7A). So, ultimately, the flow cytometric assay results confirm the potential of 2,4-DTBP to induce apoptosis in HCT116 cells.

3.10 | 2,4-DTBP-induced cell cycle arrest

Disruption of normal cell cycle progression is the most often recognized event in the emergence of cancer. Cell cycle arrest is a mechanism through which some phytochemicals have been shown to prevent the development of cancer cells.⁵⁴ To better comprehend the mechanism of action of 2,4-DTBP on HCT116 cells, the cell cycle distribution of HCT116 cells was assessed using flow cytometry. Comparing untreated (vehicle-controlled) cells to those treated with the IC_{50} concentration for 24h, we found that most of the treated

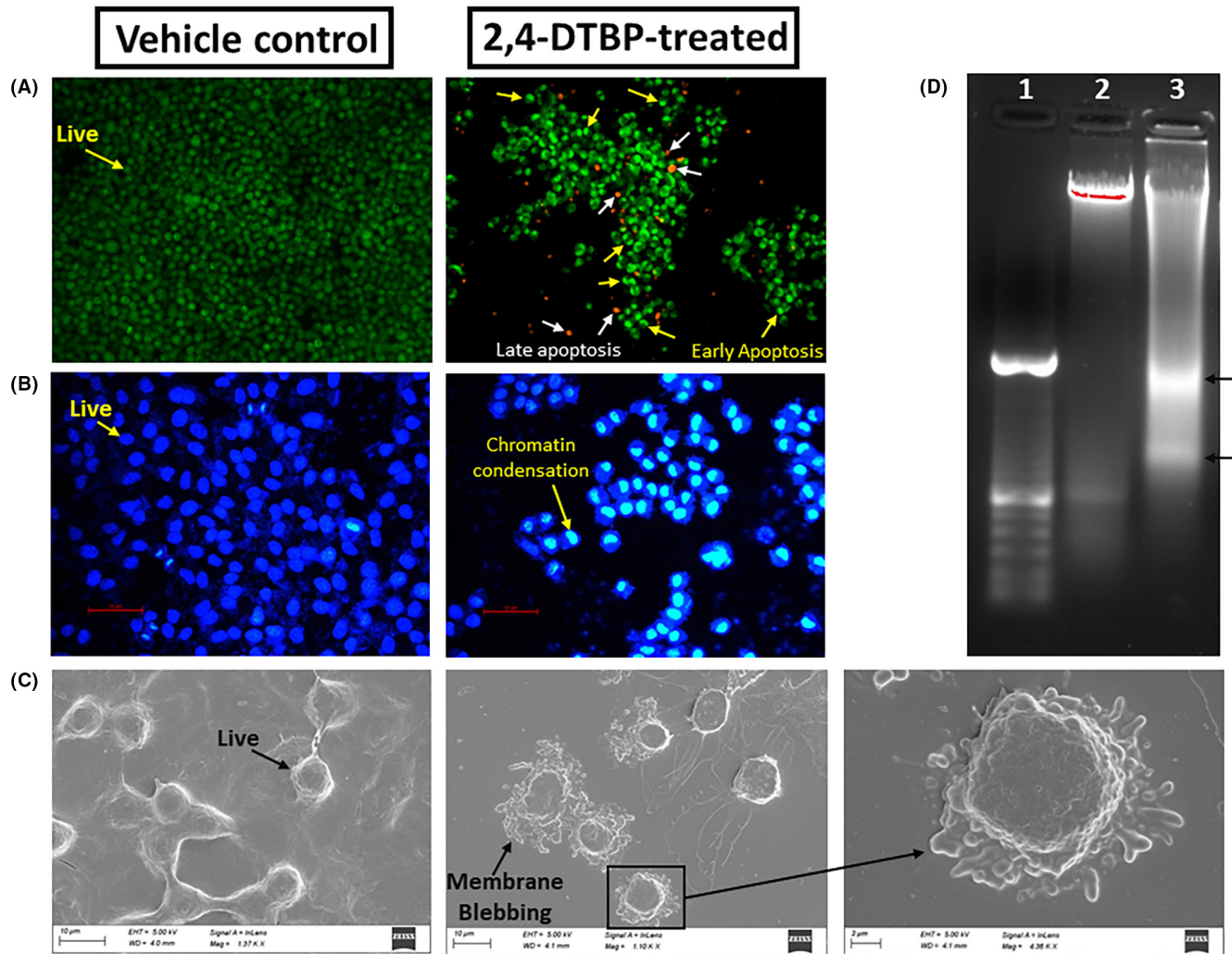


FIGURE 6 Apoptotic morphological changes induced by 2,4-DTBP in HCT116 cells. (A) Acridine orange/Ethidium bromide (AO/EB) fluorescent staining shows a group of untreated (vehicle-controlled), uniformly green-stained live HCT116 colon cancer cells and a group of 2,4-DTBP-treated HCT116 cells with yellow-green (early apoptosis) or orange (late apoptosis) coloured condensed chromatin. (B) DAPI fluorescent staining represents an untreated (vehicle-controlled) uniformly blue-stained live cell population and a group of 2,4-DTBP-treated HCT116 cells with a condensed nucleus, indicating apoptosis. (C) Scanning electron microscopic images show normal morphology of the vehicle-controlled (untreated) HCT116 cells, whereas, 2,4-DTBP-treated HCT116 cells show prominent membrane blebbing, indicating apoptosis. (D) Represents the agarose gel image of a DNA fragmentation assay. Lane: 1 represents the DNA ladder (100bp), Lane: 2 represents the isolated DNA of untreated HCT116 cells and Lane: 3 represents the isolated DNA of HCT116 cells treated with 2,4-DTBP.

cells underwent an arrest in the cell cycle's G1 phase compared to the untreated group. This data suggest that the reduction in cell proliferation and viability of 2,4-DTBP-treated HCT116 cells may have been caused by the triggering of cell cycle arrest at distinct stages of the cell cycle (Figure 7B).

3.11 | 2,4-DTBP-induced alteration of protein expression

Results of western blot showed that in treated (IC_{50} concentration for 24h) HCT116 cells, anti-apoptotic proteins Survivin and Bcl-2 had lower levels of expression compared to vehicle control. 2,4-DTBP

also activated the pro-Caspase-3 into active Caspase-3. Here, α -tubulin is used as a loading control (Figure 7C).

3.12 | 2,4-DTBP-induced mitochondrial stress

Mitochondria play a key role in deciding whether a cell will continue to live or die (apoptosis).⁵⁵ Therefore, we concentrated on cellular bioenergetics to comprehend the survival strategies of treated (IC_{50} concentration of 2,4-DTBP for 3h) and untreated HCT116 colorectal cancer cells. An investigation of metabolic activity was done by the Agilent Seahorse extracellular flux analyzer (XFe24). The Extracellular Flux Analyzer is capable of

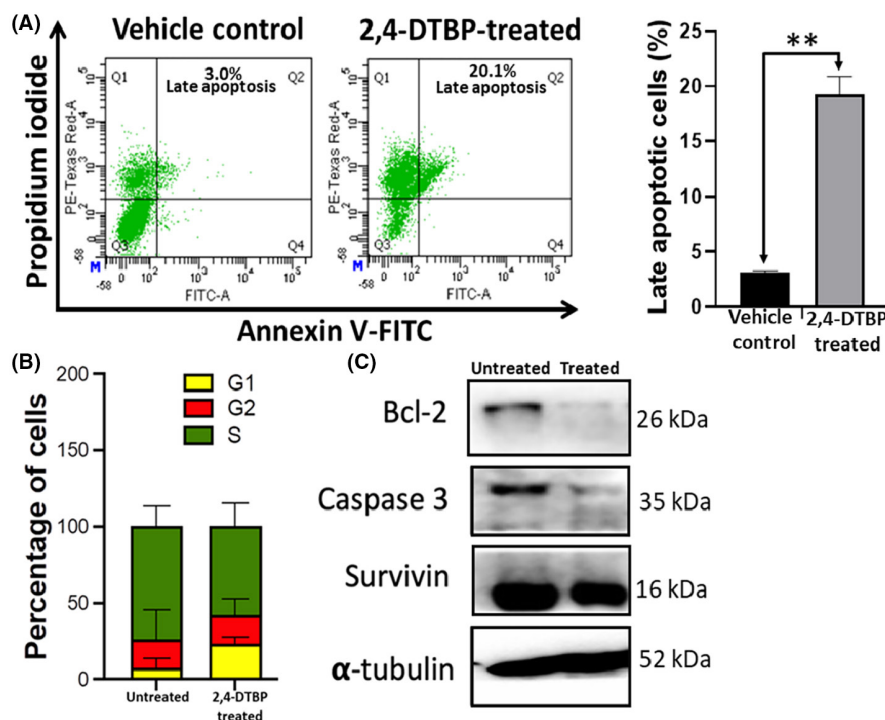


FIGURE 7 Detection of apoptosis by annexin V-FITC/PI flow cytometric assay. (A) The effect of 2,4-DTBP on apoptosis induction was determined by Annexin V-FITC/PI flow cytometric assay. The bar graph represents the % of apoptotic cells in the experimental groups compared to vehicle-controlled groups (an average of three sets). In this representative experimental group, 20.1% of treated cells showed late apoptosis (Annexin V+, PI+), compared to the vehicle-controlled (untreated) cells (3.0% of cells showed late apoptosis). Cells were classified as healthy cells (Annexin V-, PI-), early apoptotic cells (Annexin V+, PI-), late apoptotic cells (Annexin V+, PI+) and damaged cells (Annexin V-, PI+). The error bar demonstrates the mean \pm SD of three independent experiments; ** p < 0.01 vs. vehicle control. (B) Induction of cell cycle arrest in HCT116 cells by 2,4-DTBP. The bar graph represents the percentage of each phase of the cell cycle arrest in HCT116 cells, treated with or without 2,4-DTBP. The percentage of each phase of the cell cycle was obtained using FCS Express software. (C) Western blot results show the expression of anti-apoptotic Bcl-2 and Survivin proteins along with Caspase-3. α -tubulin represents a loading control.

measuring both the oxygen consumption rate (OCR), an indicator of mitochondrial respiration and the extracellular acidification rate (ECAR), an indicator of net proton loss during glycolysis, in a living cell at the same time.⁵⁶ Many bioenergetic characteristics can be determined by monitoring the ECAR and OCR in response to 2,4-DTBP.^{56,57} The ECAR and OCR readings in each well were normalized to the total protein concentration (BCA protein assay, Pierce). A percentage of basal OCR is used for the ATP synthesis of the cells.⁵⁸ The cell mitostress assay showed reduced ECAR (Figure 8A), mitochondrial OCR (Figure 8B), basal mitochondrial respiration (Figure 8C), maximal mitochondrial respiration (Figure 8C) and mitochondrial ATP production (Figure 8C) in 2,4-DTBP-treated HCT116 cells than in untreated vehicle-controlled cells.

3.13 | In silico prediction of ADME and toxicity of 2,4-DTBP

The ligand structure was retrieved from the PubChem database. OSIRIS Property Explorer assessed the recruited natural

chemical based on its ADME properties and toxicity profile. The synthesized compound was run through a drug-likeness filter. The filter's requirements were molecular weight in the range of 160–480, number of hydrogen bond donors in the field of 0–7 and obeying Lipinski's rule indicating drug-like properties of 2,4-DTBP (Table 2).

Regarding acute oral toxicity, based on the ProTox results, Compound 2,4-DTBP had an LD50 value of 700mg/kg BW.⁵⁹ Its predicted toxicity score is 4 (toxicity class: 4).⁶⁰ So, it is much less toxic in nature. It shows activity on Tox21-Stress response pathways, that is, on Mitochondrial Membrane Potential (MMP), which signifies induction of mitostress (Figure 9).

4 | DISCUSSION

In maintaining the delicate equilibrium of cellular homeostasis, especially within the colorectal region, the balance between proliferation and apoptosis is pivotal.⁶¹ Disruption of this balance can be a driving force behind the evolution and progression of colorectal cancer (CRC).⁶¹ The presence of Survivin in CRC is strongly associated

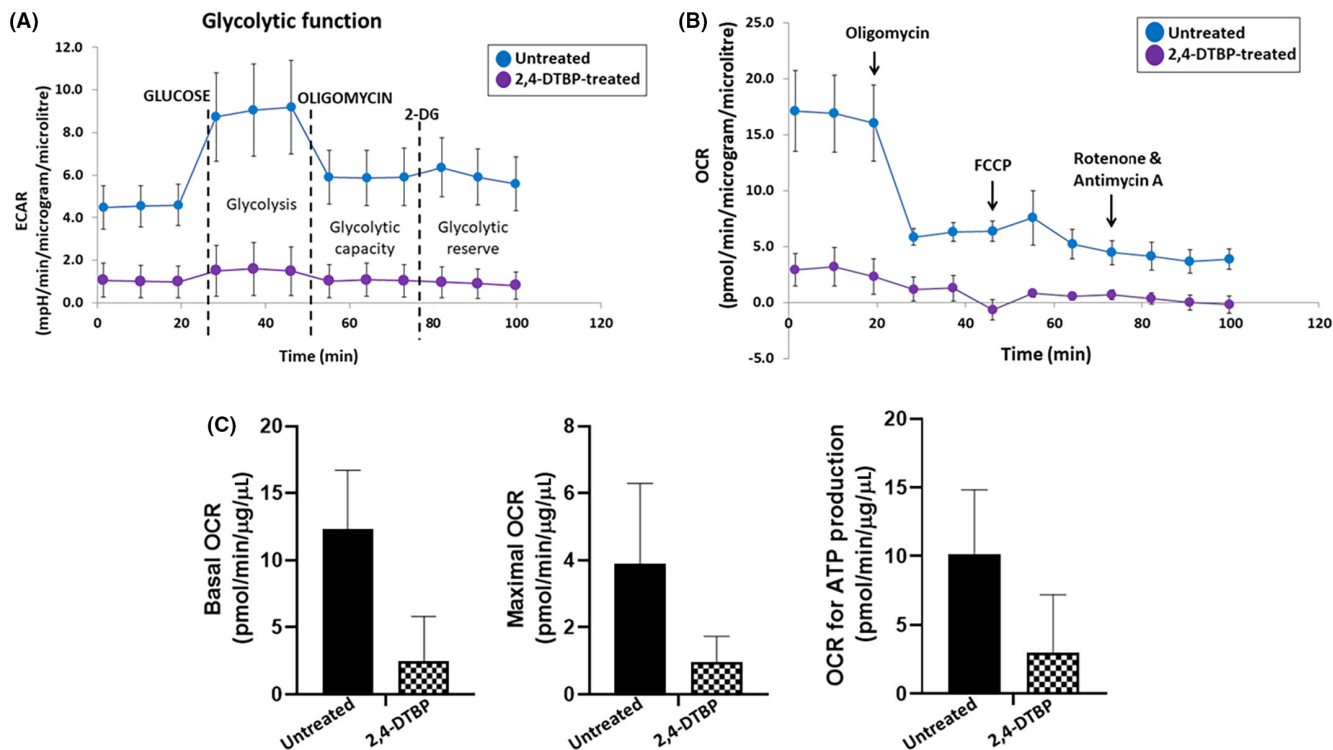


FIGURE 8 Cell Mitostress assay. (A) The extracellular acidification rate (ECAR) of untreated (vehicle-controlled) and 2,4-DTBP-treated HCT116 cells, (B) mitochondrial oxygen consumption rate (OCR), (C) basal respiration, maximal respiration and ATP production.

with the expression of Bcl-2, though they exert different and non-overlapping anti-apoptosis mechanisms.^{62,63} The membrane protein Bcl-2, primarily located on the mitochondrial outer membrane, effectively prevents the release of cytochrome c, thus hindering apoptosis initiation.⁶⁴ In contrast, Survivin blocks apoptosis by targeting the terminal effector caspase-3.⁶⁵ By inhibiting both Bcl-2 and Survivin, there is an observed enhancement in radiosensitivity and chemoresistance in tumour cells, ultimately amplifying the therapeutic response against CRC.⁶² Given the reliance of CRC tumours on these anti-apoptotic proteins throughout the disease's different stages, these proteins present themselves as potential therapeutic targets.⁶¹ As a result, a number of research groups have developed several inhibitors targeting Bcl-2 and Survivin, however, compounds concurrently targeting both proteins remain scarce.^{66–68} Therefore, the present study primarily focused on examining the inhibitory capacities of 2,4-DTBP against both Bcl-2 and Survivin. Molecular docking and molecular dynamics simulations firmly established the significant binding potential of 2,4-DTBP with survivin and Bcl-2. To strengthen this molecular evidence, a series of *in vitro* assays were conducted.

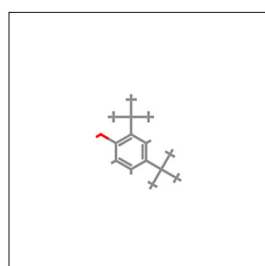
Through cytotoxicity assays, it was ascertained that 2,4-DTBP could limit HCT116 colorectal cancer cell proliferation in both time- and dose-dependent fashions, demonstrating its heightened efficacy compared to 5-FU, the conventional control. The capability of 2,4-DTBP to impair the cell migration and colony-forming ability of

HCT116 cells was corroborated further by the cell migration assay and the clonogenic assay, respectively.

Morphological assessments of 2,4-DTBP-treated HCT116 cells showcased classical apoptotic features such as nuclear shrinkage, chromatin condensation and membrane blebbing. These observations were further fortified by DNA fragmentation patterns consistent with apoptosis.

The apoptosis-inducing potential of 2,4-DTBP in HCT116 cells was further confirmed by using Annexin V and propidium iodide (PI) staining (flowcytometric assay), which revealed a significant increase in apoptotic cells.

Furthermore, cell cycle analysis identified a predominant arrest at the G1 phase, pointing towards the influence of 2,4-DTBP on CRC cell cycle dynamics. A comprehensive western blot analysis elucidated the decline in Bcl-2 and Survivin levels post-2,4-DTBP treatment, alongside the activation of pro-Caspase-3, suggesting the involvement of mitochondrial pathway of apoptosis. This pathway's functionality is closely intertwined with mitochondrial ATP production and membrane stability. Assessments of mitochondrial bioenergetics in treated cells revealed decreased OCR and ECAR, indicative of attenuated mitochondrial respiration and net proton loss during glycolysis, respectively, potentially leading to mitochondrial stress. In light of its potent anti-CRC activities, 2,4-DTBP's toxicity profile was investigated *in silico*, revealing its non-toxic nature across several crucial parameters, marking it as a promising candidate for future CRC therapeutic applications.



Predicted LD50: 700mg/kg

Predicted Toxicity Class: 4

1 2 3 4 5 6

Average similarity: 100%

Prediction accuracy: 100%



Name	2,4-Di-tert-butylphenol
Molweight	206.32
Number of hydrogen bond acceptors	23
Number of hydrogen bond donors	1
Number of atoms	37
Number of bonds	37
Number of rotatable bonds	2
Molecular refractivity	67.01
Topological Polar Surface Area	20.23
octanol/water partition coefficient(logP)	3.99

Toxicity Model Report

Classification	Target	Shorthand	Prediction	Probability
Organ toxicity	Hepatotoxicity	dili	Inactive	0.78
Toxicity end points	Carcinogenicity	carcino	Inactive	0.52
Toxicity end points	Immunotoxicity	immuno	Inactive	0.93
Toxicity end points	Mutagenicity	mutagen	Inactive	0.99
Toxicity end points	Cytotoxicity	cyto	Inactive	0.91
Tox21-Nuclear receptor signalling pathways	Aryl hydrocarbon Receptor (AhR)	nr_ahr	Inactive	1.0
Tox21-Nuclear receptor signalling pathways	Androgen Receptor (AR)	nr_ar	Inactive	1.0
Tox21-Nuclear receptor signalling pathways	Androgen Receptor Ligand Binding Domain (AR-LBD)	nr_ar_lbd	Inactive	1.0
Tox21-Nuclear receptor signalling pathways	Aromatase	nr_aromatase	Inactive	0.99
Tox21-Nuclear receptor signalling pathways	Estrogen Receptor Alpha (ER)	nr_er	Inactive	1.0
Tox21-Nuclear receptor signalling pathways	Estrogen Receptor Ligand Binding Domain (ER-LBD)	nr_er_lbd	Inactive	1.0
Tox21-Nuclear receptor signalling pathways	Peroxisome Proliferator Activated Receptor Gamma (PPAR-Gamma)	nr_ppar_gamma	Inactive	1.0
Tox21-Stress response pathways	Nuclear factor (erythroid-derived 2)-like 2/antioxidant responsive element (nrf2/ARE)	sr_are	Inactive	1.0
Tox21-Stress response pathways	Heat shock factor response element (HSE)	sr_hse	Inactive	1.0
Tox21-Stress response pathways	Mitochondrial Membrane Potential (MMP)	sr_mmp	Active	0.96
Tox21-Stress response pathways	Phosphoprotein (Tumor Suppressor) p53	sr_p53	Inactive	0.99
Tox21-Stress response pathways	ATPase family AAA domain-containing protein 5 (ATAD5)	sr_atad5	Inactive	1.0



FIGURE 9 In silico evaluation of the toxicity of 2,4-DTBP. (A) Oral toxicity prediction results; (B) Toxicity Model Report; (C) The toxicity radar chart. Evaluation processed by ProTox-II server (https://tox-new.charite.de/protox_II/).

TABLE 2 Predicted toxicity risks and predicted properties from OSIRIS Property Explorer.

Predicted toxicity risks	
Mutagenic	No
Tumorigenic	No
Irritant	No
Reproductive effective	No
Predicted ADME properties	
cLogP	4.48
Solubility	-3.64
Molweight	206.33
TPSA	20.23
Drug-likeness	-5.83
H bond acceptor	1
H bond donor	1
Nb stereocenters	0
Nb rotatable bonds	2
Drug-Score	0.40

5 | CONCLUSION AND FUTURE DIRECTIONS

The compound 2,4-DTBP stands out in this research for its remarkable inhibitory potential against both Bcl-2 and Survivin. Through rigorous molecular docking and in vitro assays, 2,4-DTBP illustrated not just commendable binding efficacy but also an ability to impede CRC cell proliferation significantly. Its consequential impact on cell cycle dynamics, primarily inducing an arrest at the G1 phase, and its role in triggering apoptosis via the mitochondrial pathway, accentuate its therapeutic prospects. Given that Survivin and Bcl-2 constitute two pivotal pro-survival mechanisms fostering therapeutic resistance in cancer cells, our revelation that 2,4-DTBP concurrently downregulates both proteins becomes particularly consequential. This discovery positions 2,4-DTBP as a potential agent to enhance drug sensitivity in CRC cases that inherently resist or develop resistance to cancer therapeutics.

Furthermore, with the burgeoning interest in proteolysis-targeting chimeras (PROTACs) in the realm of precision therapeutics, the future might see an amalgamation of PROTAC principles with compounds like 2,4-DTBP. By leveraging PROTACs' inherent capacity for selective protein degradation, we can potentially refine the specificity and potency of agents like 2,4-DTBP, furthering their therapeutic response against CRC. In addition, chemical modification of the compound may generate derivatives with higher efficacy. Ultimately, this study uncovers the promising role of 2,4-DTBP as a potent therapeutic contender for CRC management, alluding to a future where precision and efficacy in treatment paradigms for CRC are further enhanced.

AUTHOR CONTRIBUTIONS

Partha Saha: Conceptualization (equal); formal analysis (equal); software (equal); writing – original draft (equal). **Mangala Hegde:** Data

curation (equal); formal analysis (equal); methodology (equal); visualization (equal); writing – original draft (equal). **Kanak Chakraborty:** Data curation (supporting); formal analysis (supporting); methodology (supporting); validation (supporting); visualization (supporting); writing – original draft (supporting). **Achinta Singha:** Formal analysis (supporting); methodology (supporting); visualization (supporting); writing – review and editing (supporting). **Nobendu Mukerjee:** Data curation (equal); formal analysis (equal); methodology (equal); software (equal); validation (equal); visualization (equal); writing – original draft (equal). **Deepshikha Ghosh:** Formal analysis (equal); supervision (equal); validation (equal). **Ajaikumar B. Kunnumakkara:** Data curation (equal); validation (equal); writing – review and editing (equal). **Mohd Shahnawaz Khan:** Methodology (equal); software (equal); validation (equal); writing – original draft (equal). **Md Irshad Ahmad:** Formal analysis (equal); investigation (equal); visualization (equal). **Arabinda Ghosh:** Conceptualization (equal); formal analysis (equal); supervision (equal); writing – review and editing (equal). **Ajoy Kumar:** Formal analysis (equal); methodology (equal); writing – original draft (equal). **Samir Kumar Sil:** Conceptualization (equal); project administration (equal); software (equal); writing – review and editing (equal).

ACKNOWLEDGEMENTS

M.S.K. acknowledges the generous support from the Research Supporting Project (RSP2024R352) by the King Saud University, Riyadh, Kingdom of Saudi Arabia.

CONFLICT OF INTEREST STATEMENT

The authors declare no conflict of interest.

DATA AVAILABILITY STATEMENT

The data used to support the findings of this study are available from the corresponding author upon request.

ORCID

Nobendu Mukerjee  <https://orcid.org/0000-0002-7129-7003>

Arabinda Ghosh  <https://orcid.org/0000-0002-3891-5949>

Ajoy Kumar  <https://orcid.org/0000-0001-5136-6166>

REFERENCES

- Haggar FA, Boushey RP. Colorectal cancer epidemiology: incidence, mortality, survival, and risk factors. *Clin Colon Rectal Surg.* 2009;22(4):191-197. doi:10.1055/s-0029-1242458
- Xi Y, Xu P. Global colorectal cancer burden in 2020 and projections to 2040. *Transl Oncol.* 2021;14(10):101174.
- Sung H, Ferlay J, Siegel RL, et al. Global cancer statistics 2020: GLOBOCAN estimates of incidence and mortality worldwide for 36 cancers in 185 countries. *CA Cancer J Clin.* 2021;71(3):209-249. doi:10.3322/caac.21660
- Zhang Y, Yin C, Wei C, et al. Exosomal miR-625-3p secreted by cancer-associated fibroblasts in colorectal cancer promotes EMT and chemotherapeutic resistance by blocking the CELF2/WWOX pathway. *Pharmacol Res.* 2022;186:106534. doi:10.1016/j.phrs.2022.106534
- Deng Y, Wei B, Zhai Z, et al. Dietary risk-related colorectal cancer burden: estimates from 1990 to 2019. *Front Nutr.* 2021;8:690663.

6. Long AG, Lundsmith ET, Hamilton KE. Inflammation and colorectal cancer. *Curr Colorectal Cancer Rep.* 2017;13(4):341-351. doi:[10.1007/s11888-017-0373-6](https://doi.org/10.1007/s11888-017-0373-6)
7. Wu Z, Lu Z, Li L, et al. Identification and validation of ferroptosis-related lncRNA signatures as a novel prognostic model for colon cancer. *Front Immunol.* 2022;12:783362. doi:[10.3389/fimmu.2021.783362](https://doi.org/10.3389/fimmu.2021.783362)
8. Koehler BC, Scherr AL, Lorenz S, et al. Beyond cell death—antiapoptotic Bcl-2 proteins regulate migration and invasion of colorectal cancer cells in vitro. *PLoS One.* 2013;8(10):e76446. doi:[10.1371/journal.pone.0076446](https://doi.org/10.1371/journal.pone.0076446)
9. Or CHR, Huang CW, Chang CC, Lai YC, Chen YJ, Chang CC. Obatoclox, a Pan-BCL-2 inhibitor, downregulates survivin to induce apoptosis in human colorectal carcinoma cells via suppressing WNT/ β -catenin signaling. *Int J Mol Sci.* 2020;21(5):1773. doi:[10.3390/ijms21051773](https://doi.org/10.3390/ijms21051773)
10. Maji S, Panda S, Samal SK, et al. Bcl-2 antiapoptotic family proteins and chemoresistance in cancer. *Adv Cancer Res.* 2018;137:37-75. doi:[10.1016/bs.acr.2017.11.001](https://doi.org/10.1016/bs.acr.2017.11.001)
11. Virrey JJ, Guan S, Li W, Schönthal AH, Chen TC, Hofman FM. Increased survivin expression confers chemoresistance to tumor-associated endothelial cells. *Am J Pathol.* 2008;173(2):575-585. doi:[10.2353/ajpath.2008.071079](https://doi.org/10.2353/ajpath.2008.071079)
12. Van Der Heijden M, Zimmerlin CD, Nicholson AM, et al. Bcl-2 is a critical mediator of intestinal transformation. *Nat Commun.* 2016;7(1):10916. doi:[10.1038/ncomms10916](https://doi.org/10.1038/ncomms10916)
13. Fang W, Che X, Li G, et al. Sur-X, a novel peptide, kills colorectal cancer cells by targeting survivin-XIAP complex. *J Exp Clin Cancer Res.* 2020;39(1):1-18. doi:[10.1186/s13046-020-01581-3](https://doi.org/10.1186/s13046-020-01581-3)
14. Yan J, Duan W, Gao Q, et al. ENPP2 inhibitor improves proliferation in AOM/DSS-induced colorectal cancer mice via remodeling the gut barrier function and gut microbiota composition. *Pharmacol Res.* 2023;195:106877.
15. Sun X, Zhang Y, Zhou Y, et al. NPCDR: natural product-based drug combination and its disease-specific molecular regulation. *Nucleic Acids Res.* 2022;50(D1):D1324-D1333. doi:[10.1093/nar/gkab913](https://doi.org/10.1093/nar/gkab913)
16. Malek SNA, Shin SK, Wahab NA, Yaacob H. Cytotoxic components of *Pereskia bleo* (Kunth) DC.(Cactaceae) leaves. *Molecules.* 2009;14(5):1713-1724.
17. Rana VS, Blazquez MA. Chemical constituents of *Gynura cusimbua* aerial parts. *J Essential Oil Res.* 2007;19(1):21-22.
18. Kavisri M, Malathy BR, Lavanya G, et al. Molecular structure and bioactivities of 2, 4-Ditert butyl phenol extracted from *Plumbago zeylanica*, investigated using HPLC and NMR. *Biomass Convers Biorefinery.* 2023;1-11. doi:[10.1007/s13399-023-04514-0](https://doi.org/10.1007/s13399-023-04514-0)
19. Saha P, Sharma D, Dash S, Dey KS, Sil SK. Identification of 2, 4-Di-tert-butylphenol (2, 4-DTBP) as the major contributor of anti-colon cancer activity of active chromatographic fraction of *Parkia javanica* (Lamk.) Merr. Bark Extract. *Biomed Pharmacol J.* 2023;16(1):275-288. doi:[10.13005/bpj/2609](https://doi.org/10.13005/bpj/2609)
20. Yoon MA, Jeong TS, Park DS, et al. Antioxidant effects of quinoline alkaloids and 2, 4-di-tert-butylphenol isolated from *Scolopendra subspinipes*. *Biol Pharm Bull.* 2006;29(4):735-739. doi:[10.1248/bpb.29.735](https://doi.org/10.1248/bpb.29.735)
21. Choi SJ, Kim JK, Kim HK, et al. 2, 4-Di-tert-butylphenol from sweet potato protects against oxidative stress in PC12 cells and in mice. *J Med Food.* 2013;16(11):977-983. doi:[10.1089/jmf.2012.2739](https://doi.org/10.1089/jmf.2012.2739)
22. Nair RV, Jayasree DV, Biju PG, Baby S. Anti-inflammatory and anticancer activities of erythrodiol-3-acetate and 2, 4-di-tert-butylphenol isolated from *Humboldtia unijuga*. *Nat Prod Res.* 2020;34(16):2319-2322. doi:[10.1080/14786419.2018.1531406](https://doi.org/10.1080/14786419.2018.1531406)
23. Padmavathi AR, Abinaya B, Pandian SK. Phenol, 2, 4-bis (1, 1-dimethylethyl) of marine bacterial origin inhibits quorum sensing mediated biofilm formation in the uropathogen *Serratia marcescens*. *Biofouling.* 2014;30(9):1111-1122. doi:[10.1080/08927014.2014.972386](https://doi.org/10.1080/08927014.2014.972386)
24. Viswapiya D, Prithika U, Deebika S, Balamurugan K, Pandian SK. In vitro and in vivo antibiofilm potential of 2, 4-Di-tert-butylphenol from seaweed surface associated bacterium *Bacillus subtilis* against group A streptococcus. *Microbiol Res.* 2016;191:19-31. doi:[10.1016/j.micres.2016.05.010](https://doi.org/10.1016/j.micres.2016.05.010)
25. Aissaoui N, Mahjoubi M, Nas F, et al. Antibacterial potential of 2, 4-di-tert-butylphenol and calixarene-based prodrugs from thermophilic *Bacillus licheniformis* isolated in Algerian hot spring. *Geomicrobiol J.* 2019;36(1):53-62. doi:[10.1080/01490451.2018.1503377](https://doi.org/10.1080/01490451.2018.1503377)
26. Leila A, Lamjed B, Roudaina B, et al. Isolation of an antiviral compound from Tunisian olive twig cultivars. *Microb Pathog.* 2019;128:245-249. doi:[10.1016/j.micpath.2019.01.012](https://doi.org/10.1016/j.micpath.2019.01.012)
27. Padmavathi AR, Bakkiyaraj D, Thajuddin N, Pandian SK. Effect of 2, 4-di-tert-butylphenol on growth and biofilm formation by an opportunistic fungus *Candida albicans*. *Biofouling.* 2015;31(7):565-574. doi:[10.1080/08927014.2015.1077383](https://doi.org/10.1080/08927014.2015.1077383)
28. Song YW, Lim Y, Cho SK. 2, 4-Di-tert-butylphenol, a potential HDAC6 inhibitor, induces senescence and mitotic catastrophe in human gastric adenocarcinoma AGS cells. *Biochim Biophys Acta Mol Cell Res.* 2018;1865(5):675-683. doi:[10.1016/j.bbamcr.2018.02.003](https://doi.org/10.1016/j.bbamcr.2018.02.003)
29. Bowers KJ, Chow E, Xu H, et al. Scalable algorithms for molecular dynamics simulations on commodity clusters. In: Proceedings of the 2006 ACM/IEEE Conference on Supercomputing Tampa, FL, USA, 43. 2006. doi:[10.1145/1188455.1188544](https://doi.org/10.1145/1188455.1188544)
30. Wendt MD, Sun C, Kunzer A, et al. Discovery of a novel small molecule binding site of human survivin. *Bioorg Med Chem Lett.* 2007;17(11):3122-3129. doi:[10.1016/j.bmcl.2007.03.042](https://doi.org/10.1016/j.bmcl.2007.03.042)
31. Chow E, Rendleman CA, Bowers KJ, et al. Desmond performance on a cluster of multicore processors. 2008. DE Shaw Research Technical Report DESRES/TR-2008-01.
32. Shivakumar D, Williams J, Wu Y, Damm W, Shelley J, Sherman W. Prediction of absolute solvation free energies using molecular dynamics free energy perturbation and the OPLS force field. *J Chem Theory Comput.* 2010;6(5):1509-1519. doi:[10.1021/ct900587b](https://doi.org/10.1021/ct900587b)
33. Jorgensen WL, Chandrasekhar J, Madura JD, Impey RW, Klein ML. Comparison of simple potential functions for simulating liquid water. *J Chem Phys.* 1983;79(2):926-935. doi:[10.1063/1.445869](https://doi.org/10.1063/1.445869)
34. Martyna GJ, Tobias DJ, Klein ML. Constant pressure molecular dynamics algorithms. *J Chem Phys.* 1994;101:4177-4189. doi:[10.1063/1.467468](https://doi.org/10.1063/1.467468)
35. Martyna GJ, Klein ML, Tuckerman M. Nose-Hoover chains: The canonical ensemble via continuous dynamics. *J Chem Phys.* 1992;97(4):2635-2643. doi:[10.1063/1.463940](https://doi.org/10.1063/1.463940)
36. Toukmaji AY, Board JA Jr. Ewald summation techniques in perspective: a survey. *Comput Phys Commun.* 1996;95:73-92. doi:[10.1016/0010-4655\(96\)00016-1](https://doi.org/10.1016/0010-4655(96)00016-1)
37. Saha P, Saha S, Sil SK. Anti-colon cancer activity of *Parkia javanica* (Lamk.) Merr. Bark extract: an in-vitro study. *Int J Pharm Sci Drug Res.* 2021;13(5):536-542. doi:[10.25004/IJPSDR.2021.130511](https://doi.org/10.25004/IJPSDR.2021.130511)
38. Prasad S, Yadav VR, Sung B, et al. Ursolic acid inhibits growth and metastasis of human colorectal cancer in an orthotopic nude mouse model by targeting multiple cell signaling pathways: chemosensitization with capecitabine. *Clin Cancer Res.* 2012;18(18):4942-4953. doi:[10.1158/1078-0432.CCR-11-2805](https://doi.org/10.1158/1078-0432.CCR-11-2805)
39. Ebeling S, Naumann K, Pollok S, et al. From a traditional medicinal plant to a rational drug: understanding the clinically proven wound healing efficacy of birch bark extract. *PLoS One.* 2014;9(1):e86147. doi:[10.1371/journal.pone.0086147](https://doi.org/10.1371/journal.pone.0086147)
40. Liu K, Liu PC, Liu R, Wu X. Dual AO/EB staining to detect apoptosis in osteosarcoma cells compared with flow cytometry. *Med Sci Monit Basic Res.* 2015;21:15-20. doi:[10.12659/MSMBR.893327](https://doi.org/10.12659/MSMBR.893327)
41. Kntayya SB, Ibrahim MD, Mohd Ain N, Iori R, Ioannides C, Abdull Razis AF. Induction of apoptosis and cytotoxicity by isothiocyanate

- sulforaphene in human hepatocarcinoma HepG2 cells. *Nutrients*. 2018;10(6):718. doi:[10.3390/nu10060718](https://doi.org/10.3390/nu10060718)
42. Saadat YR, Saeidi N, Vahed SZ, Barzegari A, Barar J. An update to DNA ladder assay for apoptosis detection. *Bioimpacts*. 2015;5(1):25-28. doi:[10.15171/bi.2015.01](https://doi.org/10.15171/bi.2015.01)
 43. Hossain S, Yamamoto H, Chowdhury EH, et al. Fabrication and intracellular delivery of doxorubicin/carbonate apatite nanocomposites: effect on growth retardation of established colon tumor. *PLoS One*. 2013;8(4):e60428. doi:[10.1371/journal.pone.0060428](https://doi.org/10.1371/journal.pone.0060428)
 44. Chowdhury SR, Ray U, Chatterjee BP, Roy SS. Targeted apoptosis in ovarian cancer cells through mitochondrial dysfunction in response to *Sambucus nigra* agglutinin. *Cell Death Dis*. 2017;8(5):e2762. doi:[10.1038/cddis.2017.77](https://doi.org/10.1038/cddis.2017.77)
 45. Aswathy M, Banik K, Parama D, et al. Exploring the cytotoxic effects of the extracts and bioactive triterpenoids from dillenia indica against oral squamous cell carcinoma: a scientific interpretation and validation of indigenous knowledge. *ACS Pharmacol Transl Sci*. 2021;4(2):834-847. doi:[10.1021/acscptsci.1c00011](https://doi.org/10.1021/acscptsci.1c00011)
 46. Mitra T, Prasad P, Mukherjee P, Chaudhuri SR, Chatterji U, Roy SS. Stemness and chemoresistance are imparted to the OC cells through TGF β 1 driven EMT. *J Cell Biochem*. 2018;119(7):5775-5787. doi:[10.1002/jcb.26753](https://doi.org/10.1002/jcb.26753)
 47. Banerjee P, Eckert AO, Schrey AK, Preissner R. ProTox-II: a web-server for the prediction of toxicity of chemicals. *Nucleic Acids Res*. 2018;46:W257-W263. doi:[10.1093/nar/gky318](https://doi.org/10.1093/nar/gky318)
 48. Lin L, Lin K, Wu X, et al. Potential inhibitors of fascin from a database of marine natural products: a virtual screening and molecular dynamics study. *Front Chem*. 2021;9:719949. doi:[10.3389/fchem.2021.719949](https://doi.org/10.3389/fchem.2021.719949)
 49. Bosshard HR, Marti DN, Jelesarov I. Protein stabilization by salt bridges: concepts, experimental approaches and clarification of some misunderstandings. *J Mol Recognit*. 2004;17(1):1-16. doi:[10.1002/jmr.657](https://doi.org/10.1002/jmr.657)
 50. Coleman ML, Sahai EA, Yeo M, Bosch M, Dewar A, Olson MF. Membrane blebbing during apoptosis results from caspase-mediated activation of ROCK I. *Nat Cell Biol*. 2001;3(4):339-345. doi:[10.1038/35070009](https://doi.org/10.1038/35070009)
 51. Wyllie AH. Apoptosis: cell death under homeostatic control. In: Chambers CM, Chambers PL, Davies DS, eds. *Archives of Toxicology: Supplement. Mechanisms and Models in Toxicology*. Vol 11. Springer; 1987:3-10. doi:[10.1007/978-3-642-72558-6_1](https://doi.org/10.1007/978-3-642-72558-6_1)
 52. Gencheva G, Tsekova D, Gochev G, et al. Synthesis, structural characterization, and cytotoxic activity of novel paramagnetic platinum hematoporphyrin IX complexes: potent antitumor agents. *Metal-Based Drugs*. 2007;2007:67376. doi:[10.1155/2007/67376](https://doi.org/10.1155/2007/67376)
 53. Wyllie AH, Morris RG, Smith AL, Dunlop D. Chromatin cleavage in apoptosis: association with condensed chromatin morphology and dependence on macromolecular synthesis. *J Pathol*. 1984;142(1):67-77. doi:[10.1002/path.1711420112](https://doi.org/10.1002/path.1711420112)
 54. Chen C, Kong ANT. Dietary cancer-chemopreventive compounds: from signaling and gene expression to pharmacological effects. *Trends Pharmacol Sci*. 2005;26(6):318-326. doi:[10.1016/j.tips.2005.04.004](https://doi.org/10.1016/j.tips.2005.04.004)
 55. Youle RJ, Karbowski M. Mitochondrial fission in apoptosis. *Nat Rev Mol Cell Biol*. 2005;6(8):657-663. doi:[10.1038/nrm1697](https://doi.org/10.1038/nrm1697)
 56. Dier U, Shin DH, Hemachandra LMP, Uusitalo LM, Hempel N. Bioenergetic analysis of ovarian cancer cell lines: profiling of histological subtypes and identification of a mitochondria-defective cell line. *PLoS One*. 2014;9(5):e98479. doi:[10.1371/journal.pone.0098479](https://doi.org/10.1371/journal.pone.0098479)
 57. Hill BG, Benavides GA, Lancaster JR Jr, et al. Integration of cellular bioenergetics with mitochondrial quality control and autophagy. *Biol Chem*. 2012;393(12):1485-1512. doi:[10.1515/hsz-2012-0198](https://doi.org/10.1515/hsz-2012-0198)
 58. Prasad P, Ghosh S, Roy SS. Glutamine deficiency promotes stemness and chemoresistance in tumor cells through DRP1-induced mitochondrial fragmentation. *Cell Mol Life Sci*. 2021;78(10):4821-4845. doi:[10.1007/s00018-021-03818-6](https://doi.org/10.1007/s00018-021-03818-6)
 59. Drwal MN, Banerjee P, Dunkel M, Wettig MR, Preissner R. ProTox: a web server for the in-silico prediction of rodent oral toxicity. *Nucleic Acids Res*. 2014;42(W1, Web Server Issue):W53-W58. doi:[10.1093/nar/gku401](https://doi.org/10.1093/nar/gku401)
 60. Hodge A, Sterner B. *Toxicity Classes*. Canadian Center for Occupational Health and Safety; 2005. <http://www.ccohs.ca/oshanswers/chemicals/id50.htm>
 61. Ramesh P, Medema JP. BCL-2 family deregulation in colorectal cancer: potential for BH3 mimetics in therapy. *Apoptosis*. 2020;25(5-6):305-320. doi:[10.1007/s10495-020-01601-9](https://doi.org/10.1007/s10495-020-01601-9)
 62. Kawasaki H, Altieri DC, Lu CD, Toyoda M, Tenjo T, Tanigawa N. Inhibition of apoptosis by survivin predicts shorter survival rates in colorectal cancer. *Cancer Res*. 1998;58(22):5071-5074.
 63. Cai Y, Ma W, Huang X, et al. Effect of survivin on tumor growth of colorectal cancer in vivo. *Int J Clin Exp Pathol*. 2015;8(10):13267-13272.
 64. Yang J, Liu X, Bhalla K, et al. Prevention of apoptosis by Bcl-2: release of cytochrome c from mitochondria blocked. *Science*. 1997;275(5303):1129-1132. doi:[10.1126/science.275.5303.1129](https://doi.org/10.1126/science.275.5303.1129)
 65. Ambrosini G, Adida C, Altieri DC. A novel anti-apoptosis gene, survivin, expressed in cancer and lymphoma. *Nat Med*. 1997;3(8):917-921. doi:[10.1038/nm0897-917](https://doi.org/10.1038/nm0897-917)
 66. Trudel S, Li ZH, Rauw J, Tiedemann RE, Wen XY, Stewart AK. Preclinical studies of the pan-Bcl inhibitor obatoclax (GX015-070) in multiple myeloma. *Blood*. 2007;109(12):5430-5438. doi:[10.1182/blood-2006-10-047951](https://doi.org/10.1182/blood-2006-10-047951)
 67. Park CM, Bruncko M, Adickes J, et al. Discovery of an orally bioavailable small molecule inhibitor of prosurvival B-cell lymphoma 2 proteins. *J Med Chem*. 2008;51(21):6902-6915. doi:[10.1021/jm800669s](https://doi.org/10.1021/jm800669s)
 68. Albadari N, Li W. Survivin small molecules inhibitors: recent advances and challenges. *Molecules*. 2023;28(3):1376. doi:[10.3390/molecules28031376](https://doi.org/10.3390/molecules28031376)

How to cite this article: Saha P, Hegde M, Chakraborty K, et al. Targeted inhibition of colorectal cancer proliferation: The dual-modulatory role of 2,4-DTBP on anti-apoptotic Bcl-2 and Survivin proteins. *J Cell Mol Med*. 2024;28:e18150. doi:[10.1111/jcmm.18150](https://doi.org/10.1111/jcmm.18150)

VMHdm/c^{SF-1} neuronal circuits regulate skeletal muscle PGC1- α via the sympathoadrenal drive



Takuya Yoshida^{1,2,7}, Mina Fujitani^{3,4}, Scottlynn Farmer¹, Ami Harada^{1,5}, Zhen Shi^{1,6}, Jenny J. Lee³, Arely Tinajero³, Ashish K. Singha¹, Tepei Fujikawa^{1,3,*}

ABSTRACT

Objective: To adapt to metabolically challenging environments, the central nervous system (CNS) orchestrates metabolism of peripheral organs including skeletal muscle. The organ-communication between the CNS and skeletal muscle has been investigated, yet our understanding of the neuronal pathway from the CNS to skeletal muscle is still limited. Neurons in the dorsomedial and central parts of the ventromedial hypothalamic nucleus (VMHdm/c) expressing steroidogenic factor-1 (VMHdm/c^{SF-1} neurons) are key for metabolic adaptations to exercise, including increased basal metabolic rate and skeletal muscle mass in mice. However, the mechanisms by which VMHdm/c^{SF-1} neurons regulate skeletal muscle function remain unclear. Here, we show that VMHdm/c^{SF-1} neurons increase the sympathoadrenal activity and regulate skeletal muscle peroxisome proliferator-activated receptor gamma coactivator 1 alpha (PGC-1 α) in mice via multiple downstream nodes.

Methods: Optogenetics was used to specifically manipulate VMHdm/c^{SF-1} neurons combined with genetically-engineered mice and surgical manipulation of the sympathoadrenal activity.

Results: Optogenetic activation of VMHdm/c^{SF-1} neurons dramatically elevates mRNA levels of skeletal muscle *Pgc-1 α* , which regulates a spectrum of skeletal muscle function including protein synthesis and metabolism. Mechanistically, the sympathoadrenal drive coupled with β 2 adrenergic receptor (β 2AdR) is essential for VMHdm/c^{SF-1} neurons-mediated increases in skeletal muscle PGC1- α . Specifically, both adrenalectomy and β 2AdR knockout block augmented skeletal muscle PGC1- α by VMHdm/c^{SF-1} neuronal activation. Optogenetic functional mapping reveals that downstream nodes of VMHdm/c^{SF-1} neurons are functionally redundant to increase circulating epinephrine and skeletal muscle PGC1- α .

Conclusions: Collectively, we propose that VMHdm/c^{SF-1} neurons-skeletal muscle pathway, VMHdm/c^{SF-1} neurons \rightarrow multiple downstream nodes \rightarrow the adrenal gland \rightarrow skeletal muscle β 2AdR, underlies augmented skeletal muscle function for metabolic adaptations.

© 2023 Published by Elsevier GmbH. This is an open access article under the CC BY-NC-ND license (<http://creativecommons.org/licenses/by-nc-nd/4.0/>).

Keywords Hypothalamus; VMH; Sympathetic nervous system; Skeletal muscle

1. INTRODUCTION

The central nervous system (CNS) orchestrates the whole-body metabolism [1,2]. Within the CNS, the hypothalamus plays a dominant role in the regulation of metabolic homeostasis in response to dynamic challenges such as hypoglycemia [3], cold-exposure [4], and exercise [5]. Our previous work articulates that neurons in the dorsomedial and central parts of ventromedial hypothalamic nucleus (VMHdm/c neurons) substantially contribute to metabolic adaptations to exercise training including augmented skeletal muscle mass and basal metabolic rate in mice [6]. Knockdown of steroidogenic factor-1 (SF-1) [7,8] in VMHdm/c neurons hampers exercise-induced mRNA expression of *peroxisome proliferator-activated receptor gamma coactivator 1 alpha* (*Pgc-1 α*) in skeletal muscle [6]. PGC-1 α is a key transcriptional regulator that

controls a broad range of genes related to glucose and fat metabolism, mitochondrial function, angiogenesis, and protein synthesis [9,10]. Loss- or gain-of-function of PGC-1 α in skeletal muscle dramatically changes skeletal muscle physiology as well as whole-body metabolism [11,12]. These data suggest that VMHdm/c neurons expressing SF-1 (VMHdm/c^{SF-1} neurons) mediate metabolic responses of skeletal muscle to exercise, thereby contributing to metabolic benefits of exercise. However, the mechanisms by which VMHdm/c^{SF-1} neurons mediate exercise-induced augmented skeletal muscle PGC-1 α expression remains unclear. In particular, the pathway from VMHdm/c^{SF-1} neurons to skeletal muscle has yet to be unraveled. PGC-1 α expression in skeletal muscle is augmented by a variety of physiological stimuli [9,13]. For example, *ex vivo* muscle contraction is sufficient to increase mRNA levels of *Pgc-1 α* by activation of calcium

¹Department of Cellular and Integrative Physiology, Long School of Medicine, University of Texas Health San Antonio, San Antonio, USA ²Department of Clinical Nutrition School of Food and Nutritional Sciences, University of Shizuoka, Shizuoka, Japan ³Center for Hypothalamic Research, Department of Internal Medicine, UT Southwestern Medical Center, Dallas, USA ⁴Laboratory of Nutrition Science, Department of Bioscience, Graduate School of Agriculture, Ehime University, Matsuyama, Japan ⁵Nara Medical University, Nara, Japan ⁶Department of Plastic Surgery, Hospital Zhejiang University School of Medicine, Zhejiang, China

⁷ Current address: Laboratory of Clinical Nutrition, Division of Food and Health Environmental Sciences, Prefectural University of Kumamoto, Kumamoto, Japan.

*Corresponding author. Center for Hypothalamic Research, Department of Internal Medicine, UT Southwestern Medical Center, Dallas, USA. E-mail: tepei.fujikawa@utsouthwestern.edu (T. Fujikawa).

Received August 10, 2023 • Accepted August 14, 2023 • Available online 24 August 2023

<https://doi.org/10.1016/j.molmet.2023.101792>

signaling pathways [14,15]. Notably, the adrenergic activation such as epinephrine, norepinephrine, and β -2 adrenergic receptors (β 2AdR) agonist can dramatically increase mRNA levels of *Pgc-1 α* in skeletal muscle [16,17]. In contrast, blocking the adrenergic signaling by a systemic injection of β 2AdR antagonist significantly hampers exercise-induced *Pgc-1 α* mRNA in skeletal muscle [18]. Numerous studies have indicated that VMH neurons affect the sympathetic nervous system (SNS) activity [19,20]. Knockdown of SF-1 in VMHdm/c neurons suppresses exercise-induced epinephrine release [6]. These data indicate that VMHdm/c^{SF-1} neurons regulate skeletal muscle PGC-1 α via the SNS. However, the functional neurocircuits underlying VMHdm/c^{SF-1} neuronal regulation of the SNS are still unclear. A genetic labeling study using *Sf-1-Cre* mice, which express Cre-recombinase in VMHdm/c in adults, portrays that VMHdm/c neurons highly innervate to several areas that regulate the SNS activity, including the anterior bed nucleus of the stria terminalis (aBNST), preoptic area (POA), anterior hypothalamus area (AH), paraventricular hypothalamic nucleus (PVH), and periaqueductal gray (PAG) [21]. Although studies using optogenetics have identified that distinct downstream sites of VMHdm/c^{SF-1} neurons regulate blood glucose [22], defensive behaviors [23], and food intake [24], the vital downstream node of VMHdm/c^{SF-1} neurons regulating the SNS is unknown.

In this study, we used optogenetics and genetically-engineered mice to determine the key downstream nodes of VMHdm/c^{SF-1} neurons that regulate skeletal muscle PGC-1 α via the SNS. We found that epinephrine release by the sympathoadrenal activity coupled with β 2AdR is essential for VMHdm/c^{SF-1} neuronal-induced skeletal muscle PGC-1 α . Furthermore, our results demonstrated that VMHdm/c^{SF-1} neurons regulate the SNS through functionally redundant circuits with the PVH and PAG acting as the main downstream nodes.

2. MATERIAL AND METHODS

2.1. Genetically-engineered mice

Sf-1-Cre mice were obtained from the Jackson Laboratory (US; Strain# 012462, RRID:IMSR_JAX:012462). *Abrb2* KO mice (RRID:IMSR_JAX:031496) were derived from β -null mice [25], which was kindly provided by Dr. Bradford Lowell (Harvard Medical School). The sequences of genotyping primers are followings; for *Sf-1-Cre*, aggaagcagccctggaac, aggcaaatgttggtacgg, agaaactgctccgcttcc with expected bands sizes of 627 bp for internal control and 236 bp for *Sf-1-Cre*; for *Abrb2* knockout (KO), cagcagactagtgagacgtg, accaagaa-taaggcccgagt, ccgggaatagacaagacca with expected bands sizes of 225 bp for the wild-type allele and 410 bp for the knockout allele. *Sf-1-Cre* and *Abrb2* KO mice were bred to generate *Sf-1-Cre::Abrb2*^{KO/KO} and *Sf-1-Cre::Abrb2*^{WT/WT} mice. *Sf-1-Cre* mice were on a C57BL/J6 background and other mice are on a mixed background (C57BL/J6 and FVB.129). We used 3-6 month-old male mice whose body weights were above approximately 25–30 g. Mice were housed at room temperature (22–24) with a 12 h light/dark cycle (lights on at 6am, and 7am during daylight saving time) and fed a normal chow diet (2016 Teklad global 16% protein rodent diets, Envigo, US). Mice were maintained in groups and singly housed after adeno-associated virus (AAV) injections and optic fiber probes insertions. Animal care was according to established NIH guidelines, and all procedures were approved by the Institutional Animal Care and Use Committee of the University of Texas Southwestern Medical Center and University of Texas Health San Antonio.

2.2. AAV injections and optic fiber probe insertions

Recombinant AAVs were purchased from the Vector Core at the University of North Carolina at Chapel Hill, US or Addgene Inc (US). rAAV5-

EF1 α -DIO-mCherry (3.3×10^{12} VM/mL), rAAV5-EF1 α -DIO-channelrhodopsin2(ChR2)(H134R)-mCherry (3.4×10^{12} VM/mL), and rAAV5-EF1 α -DIO-ChR2(H134R)-EYFP (3.2×10^{12} VM/mL) were unilaterally administered into the right side of the VMH of mice using a UMP3 UltraMicroPump (WPI, US) with 10 μ L NanoFil microsyringe (WPI) and 35G NanoFil beveled needle (WPI; Catalog# NF35BV-2). The volume of AAVs was 500–1000 nL at the rate 50–100 nL per minute, and the needle was left for another 5 min after the injection was finished. The face of beveled needle was placed towards the center of the brain. The coordinates of VMH-microinjection were AP; -1.4 L +0.5, and D -5.5 (from Bregma). The optic fiber probe was inserted as following coordinates; the VMH (AP; -1.4, L +0.5, and D -5.0), aBNST (AP; 0.3, L +0.5, and D -3.75), POA (AP; 0.4, L +0.25, and D -4.5), AH (AP; -0.9, L +0.5, and D -4.75), PVH/AH (AP; -0.8, L +0.25, and D -4.5), and PAG (AP; -4.3, L +0.2, and D -2.0). The configuration of the probe for the VMH stimulation was 400 μ m Core, 0.5NA, \varnothing 2.5 mm ceramic ferrule, and 6 mm length (RWD Life science Inc, US and Doric Lenses, Canada) for the LED input. The configuration of probe for other sites and the VMH (S Figure 4) was 200 μ m Core diameter, 0.39NA, \varnothing 2.5 mm Ceramic Ferrule diameter, and with varied length varied (3–6 mm depending on the place) (RWD Life science Inc, US and Doric Lenses, Canada). The fiber probe was secured by adhesion bond (Loctite 454, Loctite Inc, US). Mice were allowed to recover for at least three weeks after the AAV injections to fully express recombinant proteins.

2.3. Optogenetics

The light emitting diode (LED) driver (Thorlabs, US; DC4104) with fiber-coupled LED (Thorlabs; Catalog# M470F3) was used for the VMH stimulation, and the laser unit (Opto engine LLC, US; Catalog# MDL-III-470) was used for the terminal of VMHdm/c^{SF-1} neuronal stimulations. The power of tips was set to ~ 1 mW/mm² for the VMH stimulation and ~ 10 mW/mm² for the terminal stimulations. The customized transistor–transistor logic generator was built based on the design by the University of Colorado Optogenetics and Neural Engineering Core. Rotary joint patch cable (Thorlabs; Catalog# RJPSF4 for LED and RJPPF4 for the laser) was used to connect either fiber-coupled LED or the laser unit. The quick-release interconnect (Thorlabs; Catalog# ADAF2) was used to connect the rotary joint patch cable to the fiber probe attached to mouse head. The stimulation was set to; 5 ms duration, 20 Hz, 2 s activation and 2 s rest cycle, 30 min (Figure 1B) otherwise specified.

2.4. Chemogenetics

Gi-Designer Receptors Exclusively Activated by Designer Drugs (DREADDs)-AAV (Gi-DREADD), rAAV8-hSyn-DIO-hM4D(Gi)-mCherry (Addgene Inc, Catalog# 44362-AAV8, 3.2×10^{12} VM/mL), was used for inhibition of VMHdm/c^{SF-1} neuronal activity induced by optogenetics. rAAV8-hSyn-DIO-hM4D(Gi)-mCherry and rAAV5-EF1 α -DIO-ChR2(H134R)-EYFP (250 nL each, total 500 nL) were injected into the right side of the VMH of *Sf-1-Cre* mice as described above. Control for rAAV5-EF1 α -DIO-ChR2(H134R)-EYFP was rAAV5-EF1 α -DIO-EYFP. The optic cannula was inserted the VMH, PVH/AH or PAG as described above. Clozapine-N-Oxide (CNO, catlog# HB6149, Hello Bio Inc, NJ, USA) was injected intraperitoneally (i.p.) 10 min before optogenetic stimulation begun (2.5 mg/kg per BW). Sterile saline was used as vehicle and control.

2.5. Adrenalectomy (ADX)

Skin and muscle incisions (approximately 1 cm) were made close to the abdominal area where kidney was located. Both the adrenal glands

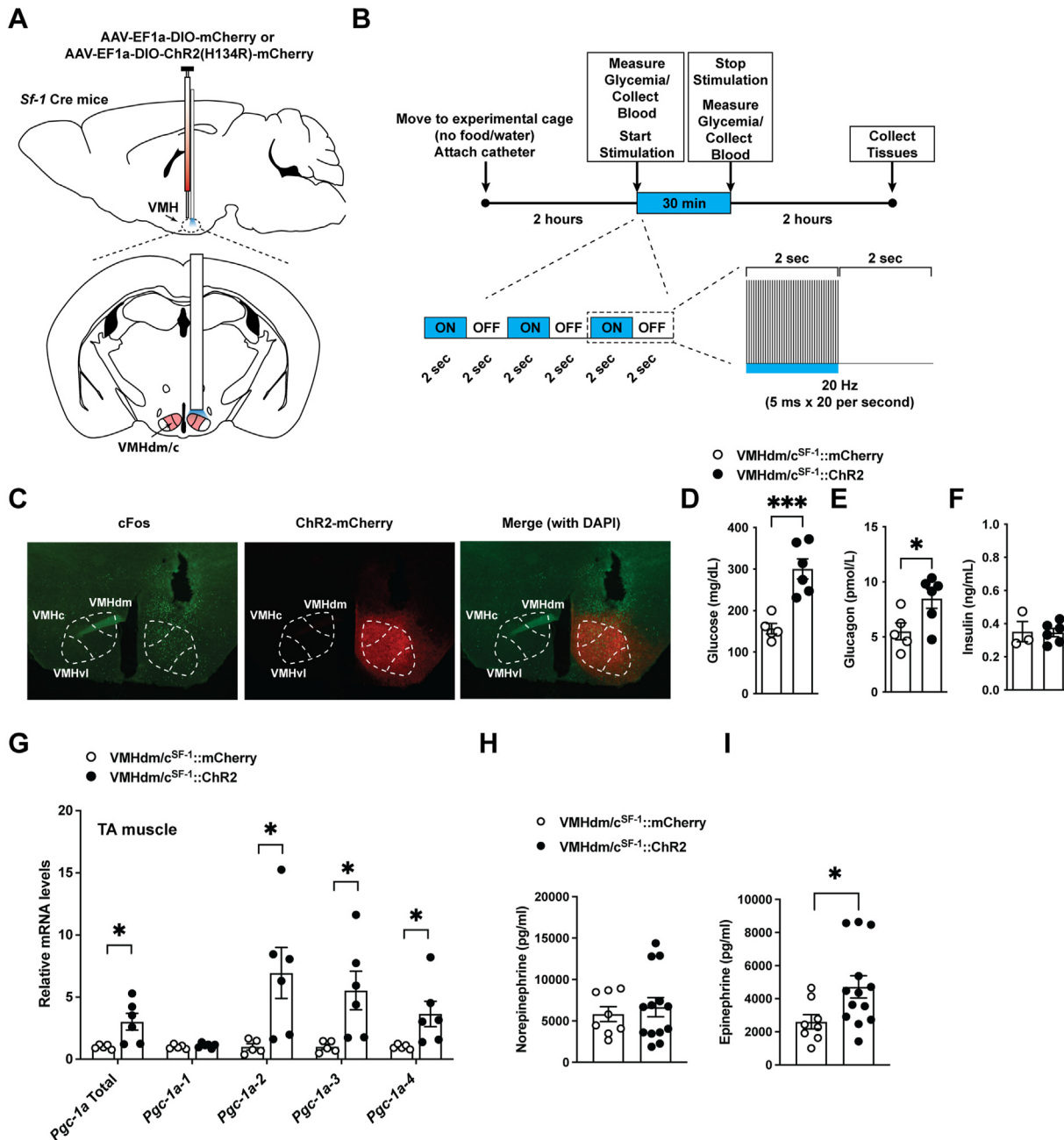


Figure 1: Optogenetic activation of VMHdm/c^{SF-1} neurons increases mRNA levels of skeletal muscle *Pgc1-α* (A) Schematic figure of targeting site of VMHdm/c^{SF-1} neurons. (B) Experimental design and stimulus setting of optogenetics. (C) Representative figures of Fos expression pattern in the hypothalamus of mice expressing ChR2 in SF-1 expression neurons in VMHdm/c (VMHdm/c^{SF-1}::ChR2) after VMHdm/c^{SF-1} neuronal stimulation. Control group is composed of mice expressing mCherry in VMHdm/c^{SF-1} neurons (VMHdm/c^{SF-1}::mCherry). (D) Blood glucose, (E) plasma glucagon, (F) plasma insulin in mice after VMHdm/c^{SF-1} neuronal stimulation. (G) mRNA expression levels of *Pgc1-α* isoform in skeletal muscle of VMHdm/c^{SF-1}::ChR2 mice after optogenetic stimulation. (H) Plasma norepinephrine and (I) epinephrine in VMHdm/c^{SF-1}::ChR2 mice after optogenetic stimulation. Values are mean ± S.E.M. ***p < 0.001, *p < 0.05.

were removed by tying with sterile suture. The sham operation was performed as same as ADX surgery except for removing the adrenal glands. The corticosterone water (75 µg/mL, vehicle was sterile 1% ethanol/0.9% NaCl water) was provided with ADX mice, and vehicle was provided with sham mice.

2.6. Immunohistochemistry and Fos counting

Mouse brains were prepared as previously described [26,27]. Anti-cFos (Sigma, US; Catalog# F7799, batch #0000102540,

RRID:AB_259739) and secondary fluorescent antibodies (Thermofisher Inc, US; Catalog# A-21202, Lot#WF320931, and RRID:AB_141607; A-21203, Lot#WD319534, and RRID:AB_141633; A10523, Lot#, and RRID:AB_1500679) were used. Dilution rates for antibodies were 1:1000 for first antibody and 1:200 for second antibodies. Images were captured by fluorescence microscopies (Keyence US, US; Model: BZ-X710, Leica Inc, US; Model DM6 B). Exposure of captured images was adjusted, and each area (aBNST, POA, AH, PVH, VMH, and PAG) was clipped by Photoshop based on the mouse brain atlas [28].

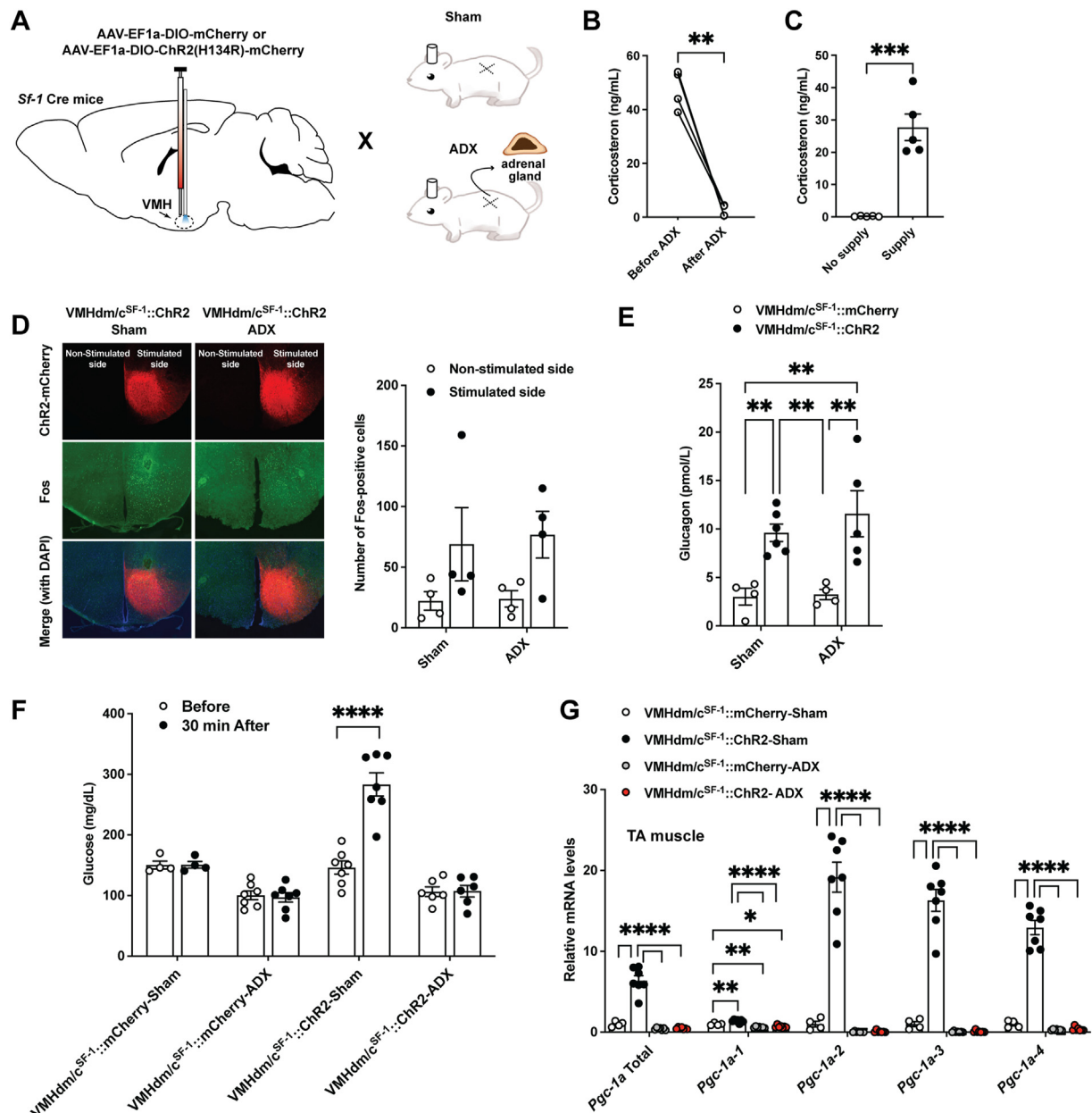


Figure 2: Adrenalectomy (ADX) completely blocks VMHdm/c^{SF-1} neurons-induced blood glucose and skeletal muscle *Pgc1-α* expression (A) Schematic of ADX experimental design. (B) Blood corticosterone levels before and after ADX in mice. (C) Blood corticosterone levels in ADX mice with and without corticosterone supplementation. (D) Representative figures of Fos expression pattern in the hypothalamus of ADX mice expressing ChR2 in SF-1 expression neurons in VMHdm/c (VMHdm/c^{SF-1}::ChR2-ADX) and the number of Fos positive cells in the VMH of VMHdm/c^{SF-1}::ChR2-ADX and sham VMHdm/c^{SF-1}::ChR2 (VMHdm/c^{SF-1}::ChR2-sham). (E) Blood glucose, (F) plasma glucagon, and (G) mRNA expression levels of *Pgc1-α* isoform in skeletal muscle of VMHdm/c^{SF-1}::ChR2-ADX after optogenetic stimulation. Values are mean \pm S.E.M. **** p < 0.0001, *** p < 0.001, ** p < 0.01, * p < 0.05.

Clipped images were exported to Fiji, and the number of cells expressing Fos was counted by particle measurement function (Figure 5B).

2.7. Assessment of glucose, catecholamines, and hormone levels in the blood

Blood glucose was measured by a glucose meter as previously described [6,27,29]. Plasma catecholamines and hormones levels were measured as previously described [6,27]. Briefly, the plasma catecholamines were analyzed by the Vanderbilt Hormone Assay &

Analytical Services Core. Plasma Glucagon (Merckodia Inc, US; Catalog#10-1281-01), insulin (Crystal Chem Inc, US; Catalog# 90080), and corticosterone (Cayman Chemical, US; Catalog #501320) levels were determined by commercially available ELISA kits.

2.8. Assessment of mRNA

mRNA levels in the tibialis anterior (TA) muscle were determined as previously described [30]. The sequences of the deoxy-oligonucleotides primers are: *Ppargc1a* total (5' tgatgtgaatgacttgatagaca, and 5' gctcatgtgtgactgttgatg), *Ppargc1a-1* (5' ggacatgtgcagccaagactct,

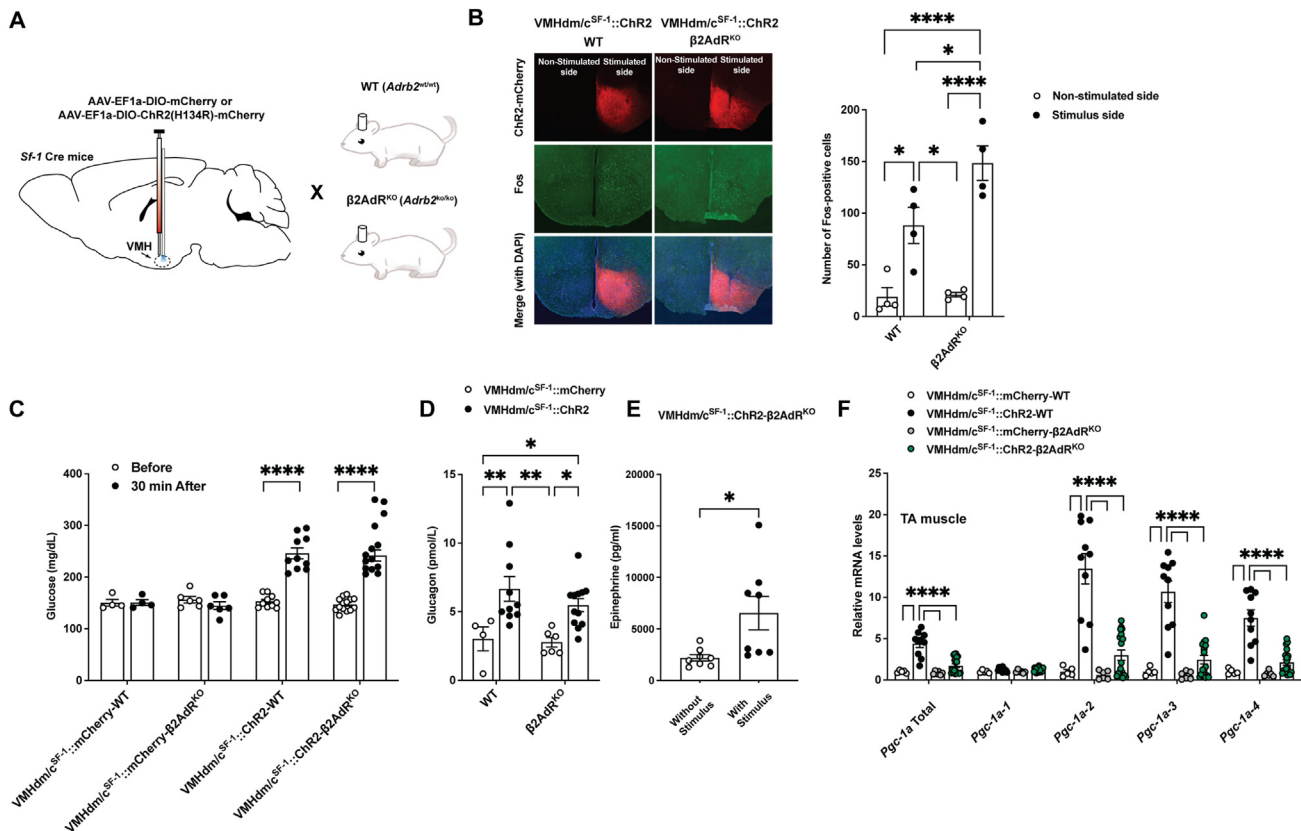


Figure 3: Ablation of $\beta 2\text{AdR}$ hampers VMHdm/c^{SF-1} neurons-induced skeletal muscle *Pgc1- α* (A) Schematic of experimental design. (B) Representative figures of Fos expression pattern in the hypothalamus of VMHdm/c^{SF-1}::ChR2 mice lacking $\beta 2\text{AdR}$ (VMHdm/c^{SF-1}::ChR2- $\beta 2\text{AdR}^{\text{KO}}$), and the number of Fos positive cells in the VMH of VMHdm/c^{SF-1}::ChR2- $\beta 2\text{AdR}^{\text{KO}}$ and wild-type control (WT) (VMHdm/c^{SF-1}::ChR2-WT). (C) Blood glucose and (D) plasma glucagon levels in VMHdm/c^{SF-1}::ChR2- $\beta 2\text{AdR}^{\text{KO}}$ mice after optogenetic stimulation. (E) Plasma epinephrine levels in VMHdm/c^{SF-1}::ChR2- $\beta 2\text{AdR}^{\text{KO}}$ mice with and without optogenetic stimulation. (F) mRNA expression levels of *Pgc1- α* isoform in skeletal muscle of ChR2- $\beta 2\text{AdR}^{\text{KO}}$ mice after optogenetic stimulation. Values are mean \pm S.E.M. **** $p < 0.0001$, ** $p < 0.01$, * $p < 0.05$.

and 5' cacttcaatccaccagaagct), *Ppargc1a-2* (5' ccaccagaatgagtcacatgga, and 5' gttcgaagaatctggcaaa), *Ppargc1a-3* (5' aagtgagtaaccggaggcattc, and 5' tcaggaagaatctggcaaa), *Ppargc1a-4* (5' tcacacaaaccacagaaa, and 5' ctggaagaatggcacat), and *18S* (5' catcgagaccaccagacagta and 5' cctcagcagctgtgtctca).

2.9. Data analysis and statistical design

The data are represented as means \pm S.E.M. GraphPad PRISM version 9 (GraphPad, US) was used for the statistical analyses and $P < 0.05$ was considered as a statistically significant difference. A detailed analysis was described in Supplemental Table 1. The sample size was decided based on previous publications [6,26,27,29–34], and no power analysis was used. Experiments were biologically replicated in Figures 1–4. Experiments for qPCR were technically replicated. We did not carry out replicate experiments for data shown in Figures 4C–H and 5. Figures were generated by PRISM version 9, Illustrator 2021–23, and Photoshop 2021–23 (Adobe Inc, US).

3. RESULTS

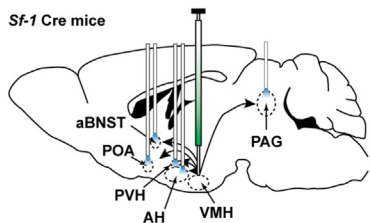
3.1. Optogenetic VMHdm/c^{SF-1} neuronal activation induces skeletal muscle *Pgc1- α* mRNA expression

To determine the neuronal mechanism by which VMHdm/c^{SF-1} neurons regulate skeletal muscle function via the SNS, we

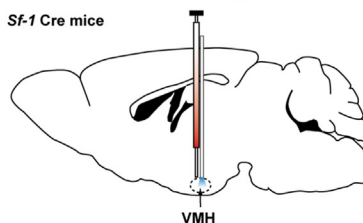
generated mice expressing ChR2(H134R) [35] specifically in VMHdm/c^{SF-1} neurons by microinjection of AAV bearing Cre-dependent ChR2 fused with fluorescent reporters (AAV-DIO-ChR2) into *Sf-1* Cre mice [36] (VMHdm/c^{SF-1}::ChR2, Figure 1A). We used AAV containing Cre-dependent mCherry for control (VMHdm/c^{SF-1}::mCherry). We used the following stimulation configurations; 5 ms duration, 20 Hz, 2 s activation/2 s resting cycle for 30 min (Figure 1B). We confirmed that our optogenetic configuration significantly induced Fos protein expression, a neuronal activation marker, in the stimulated side of the VMHdm/c, but not in the non-stimulated side (Figure 1C). Similar to previous studies [22,37,38], VMHdm/c^{SF-1} neuronal activation increased blood glucose (Figure 1D). In addition, we observed that VMHdm/c^{SF-1} neuronal activation induced increases in plasma glucagon without changing plasma insulin levels (Figure 1E and F). Next, we determined whether VMHdm/c^{SF-1} neuronal activation can induce transcriptional changes in skeletal muscle. PGC-1 α is a key transcriptional regulator for a spectrum of genes governing glucose and fat metabolism, oxidative capacity, protein synthesis and degradation, and vascularization [9,10,13]. Importantly, *Pgc1- α* mRNA induction can be used as a readout of exercise-related skeletal muscle transcriptional changes because a single exercise training dramatically increases mRNA levels of *Pgc1- α* [6,13]. PGC-1 α has several isoforms such as PGC1 α -1, -2, -3 and -4 [39]. We found that 30 min of VMHdm/c

A

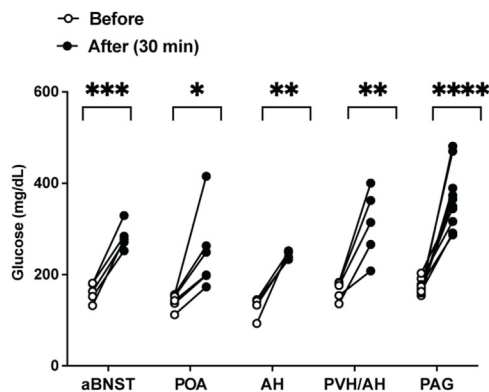
AAV-EF1a-DIO-ChR2(H134R)-mCherry for PA, PVH/AH stimulation or AAV-EF1a-DIO-ChR2(H134R)-EYFP for aBNST, AH, PAG stimulation



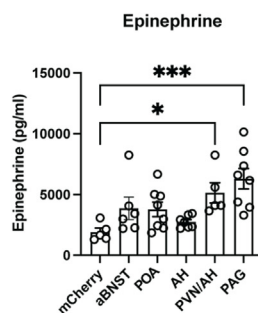
AAV-EF1a-DIO-mCherry into the VMH



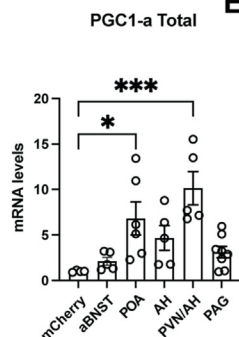
B



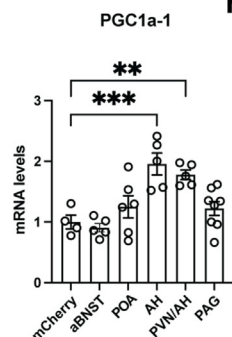
C



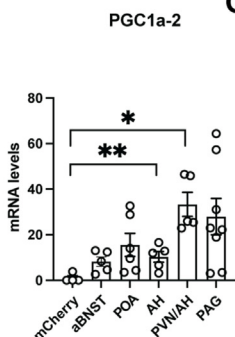
D



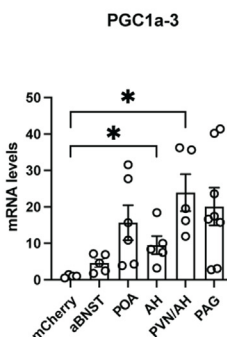
E



F



G



H

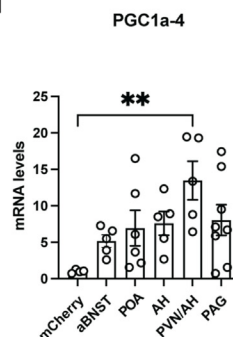


Figure 4: Downstream nodes of VMHdm/c^{SF-1} neurons are functionally redundant to regulate the sympathoadrenal activity. (A) Schematic figure of experimental design. (B) Blood glucose levels in VMHdm/c^{SF-1}::ChR2 mice before and after the terminal stimulation of the anterior bed nucleus of the stria terminalis (aBNST), preoptic area (POA), anterior hypothalamus area (AH), paraventricular hypothalamic nucleus (PVH) and AH, and periaqueductal gray (PAG). Control group is VMHdm/c^{SF-1}::mCherry mice after the VMH stimulation. (C) Plasma epinephrine levels in VMHdm/c^{SF-1}::ChR2 mice after the terminal stimulation of aBNST, POA, AH, PVH/AH, and PAG. (D) mRNA expression levels of *Pgc1- α -Total*, (E) *Pgc1- α -1*, (F) *Pgc1- α -2*, (G) *Pgc1- α -3*, and (H) *Pgc1- α -4*, skeletal muscle of VMHdm/c^{SF-1}::ChR2 mice after the terminal stimulation of aBNST, POA, AH, PVH/AH, and PAG. Values are mean \pm S.E.M. ****p < 0.0001, ***p < 0.001, **p < 0.01, *p < 0.05.

c^{SF-1} neuronal activation is sufficient to induce *Pgc-1 α -2*, -3, and -4 mRNA levels in TA skeletal muscle (Figure 1G). We then measured plasma catecholamines levels after VMHdm/c^{SF-1} neuronal activation. Interestingly, plasma epinephrine levels were significantly increased by VMHdm/c^{SF-1} neuronal activation, but norepinephrine levels in VMHdm/c^{SF-1} neuronal activated mice were not significantly different from control group (Figure 1H and I). The increased epinephrine likely caused suppression of insulin secretion while mice showed hyperglycemia. Previous studies have shown that optogenetic VMHdm/c^{SF-1} neuronal activation elicits behavioral changes such as freeze and burst activity (combination of freeze,

jump, and run) [23,40]. In line with that, we found that VMHdm/c^{SF-1} neuronal activation induced freeze or burst activity (17 cases of freeze (55%), 14 cases of burst activity (45%); total 31 trials). However, we did not observe any differences of skeletal muscle *Pgc-1 α* mRNA levels between mice showed freeze and burst activity (S Figure 1), suggesting that the burst activity is unlikely to contribute to VMHdm/c^{SF-1} neurons-induced *Pgc-1 α* expression. Collectively, these data indicate that VMHdm/c^{SF-1} neurons regulate skeletal muscle function via sympathoadrenal activity, as the adrenal gland is the only organ able to secrete epinephrine into circulation.

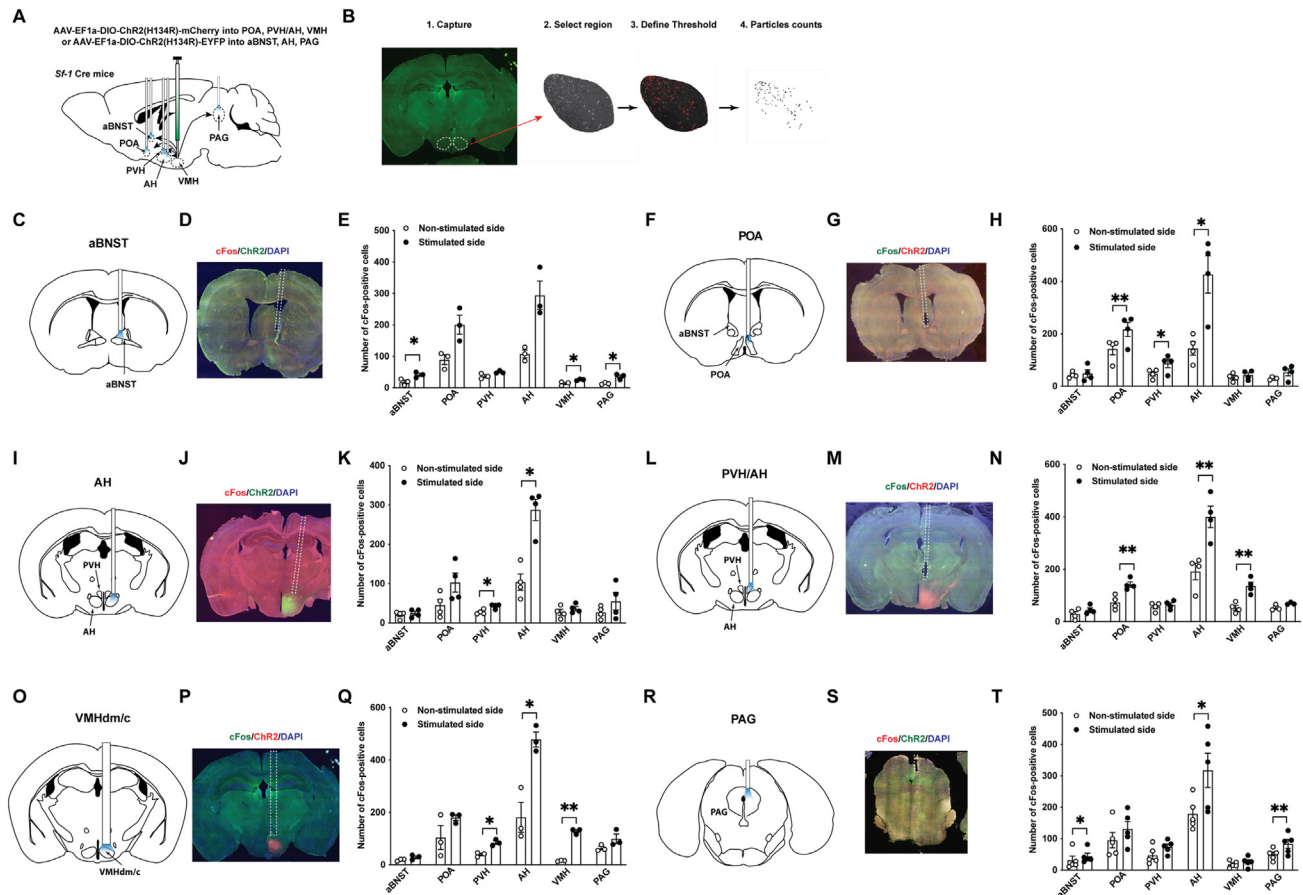


Figure 5: The terminal activation of VMHdm/c^{SF-1} neurons evokes Fos expression in the proximal terminal sites. (A) Schematic figure of experimental design. (B) Schematic of Fos expression counts in the nucleus. The brain maps of optic fiber insertion sites of (C), aBNST, (F) POA (I), AH (L), PVH/AH, (O), VMH, and (R) PAG. Representative figures of Fos expression at the terminal sites or soma of VMHdm/c^{SF-1} neurons; (D) aBNST, (G) POA, (J) AH, (M) PVH/AH, (P), VMHdm/c, and (S) PAG. The number of Fos expression cells at the aBNST, POA, AH, PVH/AH, and PAG of VMHdm/c^{SF-1}:ChR2 mice after the terminal stimulation of (E) aBNST, (H) POA, (K) AH, (N) PVH/AH, (Q) VMHdm/c and (T) PAG. Values are mean \pm S.E.M. *****p* < 0.0001, ****p* < 0.001, ***p* < 0.01, **p* < 0.05.

3.2. The adrenal gland is essential for VMHdm/c^{SF-1} neuronal regulation of skeletal muscle

Next, to determine whether epinephrine release from the adrenal gland is required for VMHdm/c^{SF-1} neurons-induced skeletal muscle *Pgc-1 α* , we surgically removed the adrenal gland, and then stimulated VMHdm/c^{SF-1} neurons. Sham surgery were used as surgical controls. As we expected, the ADX eliminated blood corticosterone (Figure 2B). ADX mice were supplied with corticosterone in the drinking water to maintain the physiological levels of blood corticosterone (Figure 2C). We carried out optogenetic stimulation five days after ADX. ADX appeared not to affect Fos induction in the VMH (Figure 2D), suggesting ADX does not affect the ability of VMHdm/c^{SF-1} neuronal activation. Indeed, plasma glucagon levels were significantly higher in ADX mice after VMHdm/c^{SF-1} neuronal activation (Figure 2E). The removal of the adrenal medulla in rats blocks hyperglycemia induced by microinjection of a cholinergic agonist into the VMH [41]. In line with the report, VMHdm/c^{SF-1} neuronal activation could not increase blood glucose levels in ADX mice at all (Figure 2F). Stunningly, ADX also completely blocked the effects of VMHdm/c^{SF-1} neuronal activation on skeletal muscle *Pgc-1 α* expression (Figure 2G), suggesting that the sympathoadrenal drive, specifically the epinephrine release, is essential for VMHdm/c^{SF-1}

neuronal regulation of skeletal muscle function. In addition, these data suggest that glucagon release unlikely contributes to VMHdm/c^{SF-1} neuronal-induced blood glucose levels.

3.3. β 2AdR is required for VMHdm/c^{SF-1} neuronal-induced skeletal muscle *Pgc-1 α*

We assessed the contribution of β 2AdR in VMHdm/c^{SF-1} neuronal-induced skeletal muscle *Pgc-1 α* expression. β 2AdR is the major form of adrenergic receptors in skeletal muscle [42]. β 2AdR agonist injection increases skeletal muscle *Pgc-1 α* -2, -3, and -4 mRNA levels [16], suggesting that the sympathetic input coupled with β 2AdR is key for skeletal muscle physiology. We tested whether β 2AdR global KO can diminish VMHdm/c^{SF-1} neuronal-induced skeletal muscle *Pgc-1 α* expression (Figure 3A). We first determined whether β 2AdR KO affects the ability of ChR2 to activate VMHdm/c^{SF-1} neurons. Optogenetic stimulation induced equal levels of Fos expression in the VMH of wild-type and β 2AdR KO mice (VMHdm/c^{SF-1}::ChR2-WT and VMHdm/c^{SF-1}::ChR2- β 2AdR^{KO}, Figure 3B), suggesting β 2AdR KO does not affect the capacity for optogenetic activation of VMHdm/c^{SF-1} neurons. Blood glucose and plasma glucagon in VMHdm/c^{SF-1}::ChR2- β 2AdR^{KO} were significantly higher than that of control group (VMHdm/c^{SF-1}::mCherry- β 2AdR^{KO}) (Figure 3C and D). In addition, optogenetic stimulation of

VMHdm/c^{SF-1} neurons significantly increased plasma epinephrine in β 2AdR KO compared to non-stimulation control (Figure 3E). VMHdm/c^{SF-1}::ChrR2- β 2AdR^{KO} showed significantly lower mRNA levels of skeletal muscle *Pgc-1 α -2*, *-3*, and *-4* compared to VMHdm/c^{SF-1}::ChrR2-WT (Figure 3F). Collectively, these results demonstrate that β 2AdR is essential for VMHdm/c^{SF-1} neuronal-induced skeletal muscle transcriptional regulation, but not blood glucose levels.

3.4. Redundant functionality of downstream nodes of VMHdm/c^{SF-1} neurons

VMHdm/c^{SF-1} neurons project to a broad range of the CNS sites that regulate the SNS including presympathetic nodes [21]. Among these areas, we examined the contributions of the aBNST, POA, AH, PVH/AH, and PAG to VMHdm/c^{SF-1} neuronal-induced augmentations in plasma epinephrine, and skeletal muscle *Pgc-1 α* expression. As the PVH and AH are located in close proximity to each other (the AH is located at ventral side of the PVH), thus the light source can reach to both areas based on the theoretical irradiance value calculation (<https://web.stanford.edu/group/dlab/cgi-bin/graph/chart.php>), it is possible that the PVH stimulation also affects the AH. Therefore, going forward, we will refer to optogenetic stimulation in this region as the PVH/AH stimulation instead of the PVH stimulation. We injected AAV-DIO-ChR2 into the VMH of *Sf-1* Cre mice followed by the insertion of the optic fiber probe into each area (Figure 4A). Intriguingly, all terminal stimulations of VMHdm/c^{SF-1} neurons significantly increased blood glucose (Figure 4B). While stimulation in each area also increased plasma epinephrine (mean values \pm SEM; 1919 \pm 324, 3869 \pm 922, 3782 \pm 594, 2759 \pm 188, 5145 \pm 841, and 6311 \pm 836 pg/mL for mCherry, aBNST, POA, AH, PVH/AH, and PAG, respectively), the most striking differences were observed after terminal stimulation of VMHdm/c^{SF-1} neurons in the PVH/AH and PAG (Figure 4C). We found that *Pgc-1 α* total mRNA expression levels were significantly increased in the terminal stimulation of the POA and PVH/AH (Figure 4D). *Pgc-1 α -1* mRNA expression levels were significantly increased in the terminal stimulation in the AH and PVH/AH (Figure 4E). *Pgc-1 α -2* and *-3* mRNA expression levels were significantly increased in the terminal stimulation in the PVH/AH and PAG (Figure 4G). Finally, *Pgc-1 α -4* mRNA expression levels were significantly increased in the terminal stimulation in the PVH/AH. Of note, although the terminal stimulation in the aBNST, POA, and AH did not statistically increase RNA levels of skeletal muscle *Pgc-1 α -2*, *-3*, and *-4*, the mean values were higher than those in the control group. Collectively, we conclude that VMHdm/c^{SF-1} neuronal projections to the PVH/AH and PAG have greater contributions to the regulation of skeletal muscle *Pgc-1 α* mRNA expression and plasma epinephrine. However, other projection sites likely contribute as well, indicating that VMHdm/c^{SF-1} neurons use neurocircuits that are functionally redundant to regulate the sympathoadrenal activity. A previous study found that VMHdm/c^{SF-1} neurons project to downstream sites collaterally [23]. For example, VMHdm/c^{SF-1} neurons projecting to the PAG also send axons to the AH [40]. Each VMHdm/c^{SF-1} neuron likely projects to multiple sites, especially to the areas that are topographically adjacent, such as aBNST and POA or the AH and PVH. In other words, when the terminal activation of VMHdm/c^{SF-1} neurons at one downstream area occurs, back-propagated neuronal activation could happen in other non-stimulated areas. To determine whether it is the case, we assessed Fos expression after the terminal activation of VMHdm/c^{SF-1} neurons in the aBNST, POA, AH, PVH/AH, and PAG as well as the soma stimulation of VMHdm/c^{SF-1} neurons (Figure 5A and B). We compared the stimulated side (right hemisphere) and the non-stimulated side (left hemisphere). As shown (Figure 1C), the optogenetic stimulation of the soma of VMHdm/c^{SF-1} neurons (Figure 5O

and P, SFigure 2E) significantly increased Fos expression in the stimulated side of the VMH (Figure 5Q). Mice received the control AAV did not show any difference between stimulated and non-stimulated sides after the VMH stimulation (S Figure 3). Intriguingly, the soma activation of VMHdm/c^{SF-1} neurons significantly increased Fos expression only in the PVH and AH (Figure 5Q). We did not find distal neuronal propagations by the terminal activation in the POA, PVH/AH, AH, and PAG (Figure 5H, K, N, Q, and T, S Figure 2A–F). The terminal stimulation in the aBNST increased Fos expression in distal site PAG (Figure 5E). However, it is unclear that Fos expression in the PAG was induced by the distal propagation as Fos expression in the VMH was not changed after aBNST stimulation (Figure 5E). We frequently observed Fos-expression in the sites proximal to the stimulated site. For instance, the aBNST stimulation induced Fos-expression in the POA (Figure 5E). Likewise, the AH stimulation induced Fos-expression in the PVH (Figure 5K), and the PVH/AH stimulation induced Fos-expression in the POA and VMH (Figure 5N). Fos expression in the stimulated hemisphere of AH was significantly higher of all the stimulation sites (Figure 5E, H, K, N, Q, and T), suggesting that these Fos-inductions in the AH may be the secondary rather than direct propagated activation.

To further investigate the redundant roles of downstream sites of VMHdm/c^{SF-1} neurons regulating the SNS, we stimulated the terminal of VMHdm/c^{SF-1} neurons in the PVH/AH or PAG while suppressing the soma of VMHdm/c^{SF-1} neurons to eliminate back-propagations, at least, between the PVH/AH and PAG. We selected these two sites as our data (Figure 4) showed that stimulation of those two sites led to the most prominent the SNS activation. We confirmed that Gi-DREADD hampers hyperglycemia, skeletal muscle *Pgc-1 α* mRNA expression, and Fos activation induced by optogenetics (S Figure 4). The terminal stimulation of PVH/AH or PAG still induced hyperglycemia (S Figure 5A) and skeletal muscle *Pgc-1 α* mRNA expression (S Figure 5B and C) while Gi-DREADD inhibited VMHdm/c^{SF-1} neurons. However, Gi-DREADD significantly suppressed *Pgc-1 α* mRNA expression compared to control injection group (S Figure 5B and C). Gi-DREADD suppressed Fos activation in the VMH by the terminal stimulation of PVH/AH or PAG of VMHdm/c^{SF-1} neurons (S Figure 5D and F). As described above, we observed prominent Fos activation in the AH by any conditions, further confirming that these Fos expression in the AH may not be reflected to direct activation of VMHdm/c^{SF-1} neurons. The terminal stimulation of PVH/AH with Gi-DREADD did not induce Fos in the PAG, while the terminal stimulation of PAG with Gi-DREADD did not induce Fos in the VMH (S Figure 6D and E). In these conditions, the readouts of the SNS activity (glucose and skeletal *Pgc-1 α* mRNA expression) were still increased (S Figure 6A–C), suggesting that at least these two distal projection sites of VMHdm/c^{SF-1} neurons, PVH/AH and PAG projections, are functionally redundant. Collectively, Fos expression data indicated that each single VMHdm/c^{SF-1} neuronal axon projects many downstream sites collaterally, strengthening the idea of functionally redundant VMHdm/c^{SF-1} neuronal circuits that regulate the SNS.

4. DISCUSSION

Here we demonstrate that VMHdm/c^{SF-1} neuronal circuits regulate skeletal muscle *Pgc-1 α* mRNA via the sympathoadrenal-released epinephrine coupled with β 2AdR. Our data further predict that VMHdm/c^{SF-1} neurons collaterally project multiple presympathetic nodes in the CNS that possess redundant functions to regulate the sympathoadrenal activation. The VMH facilitates glucose uptake in skeletal muscle and brown adipose tissue (BAT) and fatty acid

mobilization from white adipose tissues (WAT) by direct sympathetic innervation rather than the sympathoadrenal drive [43–47]. Intriguingly, these studies have demonstrated that direct sympathetic innervation is key for VMH-induced glucose uptake and lipolysis in BAT and skeletal muscle rather than the sympathoadrenal activity [43,44,46,47]. Contrary to these previous findings, results in this study highlight the importance of the sympathoadrenal activity for VMHdm/c^{SF-1} neurons-induced skeletal muscle *Pgc-1α* expression. Because VMH neurons are genetically heterogeneous [48,49], it is possible that VMHdm/c^{SF-1} neurons regulate skeletal muscle function primarily via sympathoadrenal activity, while other subtypes of neurons in the VMH mediate skeletal muscle glucose uptake via the direct sympathetic innervation. Optogenetic activation of leptin receptors-expressing neurons in the VMHdm/c does not affect blood glucose, plasma glucagon, and plasma insulin levels [22], supporting the notion that functional segregation may exist within the VMHdm/c neuronal subgroups. Further studies are warranted to reveal the mechanistic differences among the genetically distinctive neuronal groups within the VMHdm/c that regulate skeletal muscle function.

PGC-1α is one of the key molecules regulating a wide range of skeletal muscle physiology [50]. PGC-1α-1 is “classic” PGC-1α, and regulates mitochondrial function, glucose and fat metabolism [14,39]. PGC-1α-4 regulates the protein synthesis [14,39]. The physiological role of PGC-1α-2 and -3 are still not clear. It is predicted that they contribute to angiogenesis, epithelial function, chromosomal maintenance, and cholesterol metabolism [16]. PGC-1α-1 is derived from the proximal promoter region of PGC-1α locus, and PGC-1α-2, -3, and -4 are derived from the distal promoter region [10]. Intriguingly, running wheel activity and treadmill exercise activate the distal promoter region but not the proximal promoter region [18,51]. Furthermore, β2AdR agonist also only initiates the transcription of PGC-1α exclusively at the proximal promoter region [18,51], leading to increased mRNA levels of PGC-1α-2, -3, and -4, but not PGC-1α-1 [16]. These data indicate the importance of the CNS → the SNS → skeletal muscle β2AdR axis for the regulation of skeletal muscle PGC-1α in response to exercise. Our data demonstrate that VMHdm/c^{SF-1} neurons can regulate PGC-1α-2, -3, and -4, but not -1, further strengthening the idea that these neurons are important for exercise-induced augmentation of skeletal muscle function.

VMHdm/c^{SF-1} neuronal activation increases circulating epinephrine, and ADX completely blocks VMHdm/c^{SF-1} neuronal-induced skeletal muscle *Pgc-1α* expression (Figure 2), suggesting that epinephrine secretion from the adrenal gland is essential for VMHdm/c^{SF-1} neuronal regulation of skeletal muscle function. Because the adrenal gland secretes many endocrine hormones, we must consider the contribution of non-catecholamines hormones to VMHdm/c^{SF-1} neuronal-induced skeletal muscle *Pgc-1α* expression. For instance, optogenetic activation of VMHdm/c^{SF-1} neurons increases blood corticosterone [22]. Thus, it is possible that the surge of corticosterone from the adrenal gland also contributes to VMHdm/c^{SF-1} neuronal-induced skeletal muscle *Pgc-1α*. Corticosterone supplement (Figure 2B) can only provide physiologically stable corticosterone levels but can not imitate endogenous dynamics of corticosterone releases. However, dexamethasone (DEX) treatments suppress PGC-1α in skeletal muscle cell lines [52], and in the testis of *in vivo* mouse model [53]. Glucocorticoid receptors (GRs) are expressed in skeletal muscle, and skeletal muscle-specific GR-KO mice show increased lean mass [54], which is in line with the fact that DEX can induce atrophy [55]. Therefore, we conclude that corticosterone unlikely contributes to the induction of skeletal muscle PGC-1α after VMHdm/c^{SF-1} neuronal

activation. However, further studies are necessary to determine that epinephrine is the only factor in the adrenal gland that contributes to VMHdm/c^{SF-1} neuronal-induced skeletal muscle *Pgc-1α*.

A large body of literature has concluded that β2AdR signaling is key to the regulation of skeletal muscle PGC-1α expression [42], and ultimately orchestrating protein synthesis/degradation, glucose and fat metabolism, and angiogenesis [9,10,51]. Our study extends these findings to show that the sympathoadrenal activity coupled with β2AdR is essential for VMHdm/c^{SF-1} neuronal-induced skeletal muscle *Pgc-1α* expression (Figure 3). β2AdR is expressed throughout the body [18], and even within the skeletal muscle, β2AdR is expressed in a variety of cell types including skeletal muscle cells, smooth muscle cells (blood vessels), and endothelial cells [42,56]. In addition, recent studies highlight the key role of β2AdR at the neuromuscular junctions (NMJs) to regulate acetylcholine and acetylcholine receptors [57,58]. As we used global β2 AdR KO mice, we can not formally exclude the possibility that β2AdR in the non-skeletal muscle organs are actually essential. Further studies using tissue specific β2AdR manipulation (e.g., deletion of β2AdR in specifically skeletal or smooth muscle cells) are necessary to decipher the precise targets of VMHdm/c^{SF-1} neurons and the sympathoadrenal axis.

The terminal activation of VMHdm/c^{SF-1} neurons in the PVH/AH and PAG significantly increases blood epinephrine and skeletal muscle *Pgc-1α-2* and -3 mRNA (Figure 4). Because the PVH and PAG directly project to the sympathoadrenal preganglionic neurons in the intermediolateral nucleus of the spinal cord [59–62], it is predicted that activation of these areas can have more profound effects on the sympathoadrenal activity. By comparing the results of the PVH/AH and AH stimulation (Figure 4), it is likely that VMHdm/c^{SF-1} neurons projecting to the PVH substantially contribute to the regulation of the SNS activity than that to the AH. Because ADX completely diminishes augmented blood glucose by VMHdm/c^{SF-1} neuronal stimulation (Figure 2), epinephrine release by the SNS activation is likely required for the augmented blood glucose levels. Interestingly, the terminal activation in all sites we investigated significantly increased blood glucose (Figure 4). Taken together, blood glucose data (Figure 4) indicate that all sites we investigated can activate the sympathoadrenal activity, although the degree of the sympathoadrenal activation may vary. In fact, the mean value of blood epinephrine, skeletal muscle *Pgc-1* mRNA levels in all the sites are higher than control group (Figure 4), suggesting that all sites we investigated contribute to VMHdm/c^{SF-1}-neuronal regulation of the sympathoadrenal activity at some extent of degree. Collectively, these data suggest that the downstream sites of VMHdm/c^{SF-1} neurons have redundant functions regarding the augmented sympathoadrenal activity.

The Fos expression data (Figure 5) indicate that VMHdm/c^{SF-1} neuronal axon projections are collaterals rather than one-to-one projections [63] as terminal stimulations can induce back-propagated activation in the proximal projected sites of VMHdm/c^{SF-1} neuronal (Figure 5). A previous study using the retrograde tracing method supports this notion as they found that most of VMHdm/c^{SF-1} neurons project to the AH also collaterally send the axon to the PAG [23]. The VMH regulate essential physiological function for survival and high-energy demand situations including counterregulatory actions to hypoglycemia [3], defensive behavior [23,40], and exercise [5,64]. These survival functions have to be executed coordinately at the whole-body level. Considering that collateral VMHdm/c^{SF-1} neuronal circuits are functionally redundant, we propose that similar to monoaminergic neurons [65], VMHdm/c^{SF-1} neurons play a “broadcast” role in the regulation of physiological functions at the whole-body level during emergency or high-energy demand situations. Further studies will be necessary to delineate the

degree of contributions of each VMHdm/c^{SF-1} neuronal downstream node to the regulation of metabolism.

4.1. Limitation of this study

As many previous studies have noted, optogenetic stimulation induces firing patterns that are dissimilar to endogenous firing patterns in many neurons [66]. Therefore, we can not exclude the possibility that our data demonstrate the maximum capability of VMHdm/c^{SF-1} neurons on the regulation of skeletal muscle rather physiological roles of VMHdm/c^{SF-1} neurons. We also used a fixed optogenetic configuration throughout the terminal activations, despite the fact that each site we investigated has a different density of VMHdm/c^{SF-1} neuronal axon and terminals [21]. It is virtually possible that different terminal sites require different firing pattern to execute their function properly. Future studies to use fine-tuning configuration are necessary to test this possibility.

As we mentioned above, the inherent limitations of the ADX studies have to be considered. Although we supplied the corticosterone to maintain its physiological levels, the surgical removal of the adrenal gland can compromise many physiological functions directly and indirectly. For instance, we observed that the basal levels of skeletal muscle *Pgc-1α* were decreased in ADX mice (56%, 51%, 96%, 95%, and 72% mean reductions in *Pgc-1α total*, *Pgc-1α-1*, *Pgc-1α-2*, *Pgc-1α-3*, and *Pgc-1α-4* respectively compared to sham control, in Figure 2G). To exclude the possibility that ADX affects the sensitivity of adrenergic receptors, we investigated whether β2AdR agonist can induce skeletal muscle *Pgc-1α* in ADX mice. β2AdR agonist significantly induced skeletal muscle *Pgc-1α*, and there were no significant differences between sham and ADX mice (SFigure 6). Thus, ADX unlikely affects the sensitivity of adrenergic receptors in skeletal muscle in our experimental design. Nonetheless, we have to interpret ADX studies with careful consideration, and future experiments using sophisticated techniques (e.g., genetic-ablation of epinephrine only from the adrenal medulla) will be warranted to further confirm the role of epinephrine releases from the adrenal medulla in the regulation of skeletal muscle physiology.

Fos protein expression is used as the readout of neuronal activity. However, there are limitations we have to consider. First, we can not distinguish whether Fos activation is direct consequences of VMHdm/c^{SF-1} neuronal activation or indirect consequences of physiological changes induced by VMHdm/c^{SF-1} neuronal activation. For instance, it is well appreciated that stressors can increase Fos expressions. VMHdm/c^{SF-1} neuronal activation clearly induce fight or flight type of endocrine responses (e.g., increased epinephrine, corticosterone, glucagon, and glucose in the blood), that potentially can increase Fos expression indirectly.

5. CONCLUSION

The CNS-skeletal muscle interactions are important to maintain metabolic homeostasis. The skeletal muscle plays a critical role in the regulation of metabolic homeostasis as it substantially contributes to basal energy expenditure and glucose disposal after meal [13,67]. A large body of studies has built the foundation of neuroanatomy regarding metabolic homeostasis [62]. In the last decade, optogenetic tools have revealed detailed functional neurocircuits regulating metabolism including food intake and glucose metabolism [1,68,69]. This study using optogenetics demonstrates that VMHdm/c^{SF-1} neurons regulate skeletal muscle PGC1-α via epinephrine released from the adrenal gland coupled with β2AdR. In addition, our data suggest that

VMHdm/c^{SF-1} neuronal circuits regulating the sympathoadrenal activity are functionally redundant, yet varied contributions from each downstream node to the regulation of the SNS likely exist (SFigure 7). Our study advances the understanding of brain-skeletal muscle communications and implies the significant contributions of VMHdm/c^{SF-1} neurons → sympathoadrenal axis to beneficial effects of exercise on skeletal muscle.

CONTRIBUTION

T.Y. designed, performed and analyzed experiments, and edited the manuscript. M. F., S.F., A.H., Z.S., J.L., A.S.T., and A.K.S., performed experiments. T.F. designed, performed, supervised, and analyzed experiments, and wrote and finalized the manuscript.

DATA AVAILABILITY

Data will be made available on request.

ACKNOWLEDGEMENT

We thank Glenn Toney at UT Health San Antonio (UTHSA) for valuable advice, Nancy Gonzalez and Harun A. Khan (UTHSA), Bandy Chen, Safia Baset, and Jasmine Dushime (UTSW) for the technical assistant, Juri C. Fujikawa for providing animal illustrations, and Steven Wyler, Ryan Reynolds, Luis Leon Mercado, Syann Lee, and Joel K. Elmquist (UTSW) for valuable comments on the manuscript. This work was supported by the University of Texas System (UT Rising STARS to T.F.), and San Antonio Area Foundation (to T.F.). This manuscript has been released as a pre-print at Biorxiv (<https://www.biorxiv.org/content/10.1101/2022.04.01.486756v1>).

DECLARATION OF COMPETING INTEREST

The authors declare that they have no known competing financial interests or personal relationships that could have appeared to influence the work reported in this paper.

APPENDIX A. SUPPLEMENTARY DATA

Supplementary data to this article can be found online at <https://doi.org/10.1016/j.molmet.2023.101792>.

REFERENCES

- [1] Gautron L, Elmquist JK, Williams KW. Neural control of energy balance: translating circuits to therapies. *Cell* 2015;161(1):133–45.
- [2] Morton GJ, Meek TH, Schwartz MW. Neurobiology of food intake in health and disease. *Nat Rev Neurosci* 2014;15(6):367–78.
- [3] Stanley S, Moheet A, Seaquist ER. Central mechanisms of glucose sensing and counterregulation in defense of hypoglycemia. *Endocr Rev* 2019;40(3):768–88.
- [4] Zhang Z, Boelen A, Kalsbeek A, Fliers E. TRH neurons and thyroid hormone coordinate the hypothalamic response to cold. *Eur Thyroid J* 2018;7(6):279–88.
- [5] Fujikawa T, Castorena CM, Lee S, Elmquist JK. The hypothalamic regulation of metabolic adaptations to exercise. *J Neuroendocrinol* 2017;29(10).
- [6] Fujikawa T, Castorena CM, Pearson M, Kusminski CM, Ahmed N, Battiprolu PK, et al. SF-1 expression in the hypothalamus is required for beneficial metabolic effects of exercise. *Elife* 2016;5.
- [7] Zhao L, Bakke M, Krimkevich Y, Cushman LJ, Parlow AF, Camper SA, et al. Steroidogenic factor 1 (SF1) is essential for pituitary gonadotrope function. *Development* 2001;128(2):147–54.

- [8] Parker KL, Rice DA, Lala DS, Ikeda Y, Luo X, Wong M, et al. Steroidogenic factor 1: an essential mediator of endocrine development. *Recent Prog Horm Res* 2002;57:19–36.
- [9] Handschin C, Spiegelman BM. The role of exercise and PGC1alpha in inflammation and chronic disease. *Nature* 2008;454(7203):463–9.
- [10] Ruas JL, White JP, Rao RR, Kleiner S, Brannan KT, Harrison BC, et al. A PGC-1alpha isoform induced by resistance training regulates skeletal muscle hypertrophy. *Cell* 2012;151(6):1319–31.
- [11] Handschin C, Choi CS, Chin S, Kim S, Kawamori D, Kurpad AJ, et al. Abnormal glucose homeostasis in skeletal muscle-specific PGC-1alpha knockout mice reveals skeletal muscle-pancreatic beta cell crosstalk. *J Clin Invest* 2007;117(11):3463–74.
- [12] Benton CR, Nickerson JG, Lally J, Han XX, Holloway GP, Glatz JF, et al. Modest PGC-1alpha overexpression in muscle in vivo is sufficient to increase insulin sensitivity and palmitate oxidation in subsarcolemmal, not intermyofibrillar, mitochondria. *J Biol Chem* 2008;283(7):4228–40.
- [13] Hawley JA, Hargreaves M, Joyner MJ, Zierath JR. Integrative biology of exercise. *Cell* 2014;159(4):738–49.
- [14] Kang C, Li Ji L. Role of PGC-1alpha signaling in skeletal muscle health and disease. *Ann N Y Acad Sci* 2012;1271:110–7.
- [15] Barres R, Yan J, Egan B, Treebak JT, Rasmussen M, Fritz T, et al. Acute exercise remodels promoter methylation in human skeletal muscle. *Cell Metabol* 2012;15(3):405–11.
- [16] Martinez-Redondo V, Jannig PR, Correia JC, Ferreira DM, Cervenka I, Lindvall JM, et al. Peroxisome proliferator-activated receptor gamma coactivator-1 alpha isoforms selectively regulate multiple splicing events on target genes. *J Biol Chem* 2016;291(29):15169–84.
- [17] Miura S, Kawanaka K, Kai Y, Tamura M, Goto M, Shiuchi T, et al. An increase in murine skeletal muscle peroxisome proliferator-activated receptor-gamma coactivator-1alpha (PGC-1alpha) mRNA in response to exercise is mediated by beta-adrenergic receptor activation. *Endocrinology* 2007;148(7):3441–8.
- [18] Miura S, Kai Y, Kamei Y, Ezaki O. Isoform-specific increases in murine skeletal muscle peroxisome proliferator-activated receptor-gamma coactivator-1alpha (PGC-1alpha) mRNA in response to beta2-adrenergic receptor activation and exercise. *Endocrinology* 2008;149(9):4527–33.
- [19] Uyama N, Geerts A, Reynaert H. Neural connections between the hypothalamus and the liver. *Anat Rec A Discov Mol Cell Evol Biol* 2004;280(1):808–20.
- [20] Shimazu T, Minokoshi Y. Systemic glucoregulation by glucose-sensing neurons in the ventromedial hypothalamic nucleus (VMH). *J Endocr Soc* 2017;1(5):449–59.
- [21] Lindberg D, Chen P, Li C. Conditional viral tracing reveals that steroidogenic factor 1-positive neurons of the dorsomedial subdivision of the ventromedial hypothalamus project to autonomic centers of the hypothalamus and hind-brain. *J Comp Neurol* 2013;521(14):3167–90.
- [22] Meek TH, Nelson JT, Matsen ME, Dorfman MD, Guyenet SJ, Damian V, et al. Functional identification of a neurocircuit regulating blood glucose. *Proc Natl Acad Sci U S A* 2016;113(14):E2073–82.
- [23] Wang L, Chen IZ, Lin D. Collateral pathways from the ventromedial hypothalamus mediate defensive behaviors. *Neuron* 2015;85(6):1344–58.
- [24] Zhang J, Chen D, Sweeney P, Yang Y. An excitatory ventromedial hypothalamus to paraventricular thalamus circuit that suppresses food intake. *Nat Commun* 2020;11(1):6326.
- [25] Bachman ES, Dhillon H, Zhang CY, Cinti S, Bianco AC, Kobilka BK, et al. betaAR signaling required for diet-induced thermogenesis and obesity resistance. *Science* 2002;297(5582):843–5.
- [26] Fujikawa T, Berglund ED, Patel VR, Ramadori G, Vianna CR, Vong L, et al. Leptin engages a hypothalamic neurocircuitry to permit survival in the absence of insulin. *Cell Metabol* 2013;18(3):431–44.
- [27] Singha A, Palavicini JP, Pan M, Farmer S, Sandoval D, Han X, et al. Leptin receptors in RIP-cre(25Mgn) neurons mediate anti-dyslipidemia effects of leptin in insulin-deficient mice. *Front Endocrinol* 2020;11:588447.
- [28] Keith BJ, Franklin GP. The mouse brain in stereotaxic coordinates. Academic Press; 2008.
- [29] Singha AK, Yamaguchi J, Gonzalez NS, Ahmed N, Toney GM, Fujikawa T. Glucose-lowering by leptin in the absence of insulin does not fully rely on the central melanocortin system in male mice. *Endocrinology* 2019;160(3):651–63.
- [30] Fujikawa T, Chuang JC, Sakata I, Ramadori G, Coppari R. Leptin therapy improves insulin-deficient type 1 diabetes by CNS-dependent mechanisms in mice. *Proc Natl Acad Sci U S A* 2010;107(40):17391–6.
- [31] Miyaki T, Fujikawa T, Kitaoka R, Hirano N, Matsumura S, Fushiki T, et al. Noradrenergic projections to the ventromedial hypothalamus regulate fat metabolism during endurance exercise. *Neuroscience* 2011;190:239–50.
- [32] Asterholm IW, Rutkowski JM, Fujikawa T, Cho YR, Fukuda M, Tao C, et al. Elevated resistin levels induce central leptin resistance and increased atherosclerotic progression in mice. *Diabetologia* 2014;57(6):1209–18.
- [33] Williams KW, Liu T, Kong X, Fukuda M, Deng Y, Berglund ED, et al. Xbp1s in pomc neurons connects ER stress with energy balance and glucose homeostasis. *Cell Metabol* 2014;20(3):471–82.
- [34] Castorena CM, Caron A, Michael NJ, Ahmed NI, Arnold AG, Lee J, et al. CB1Rs in VMH neurons regulate glucose homeostasis but not body weight. *Am J Physiol Endocrinol Metab* 2021;321(1):E146–55.
- [35] Berndt A, Schoenenberger P, Mattis J, Tye KM, Deisseroth K, Hegemann P, et al. High-efficiency channelrhodopsins for fast neuronal stimulation at low light levels. *Proc Natl Acad Sci U S A* 2011;108(18):7595–600.
- [36] Dhillon H, Zigman JM, Ye C, Lee CE, McGovern RA, Tang V, et al. Leptin directly activates SF1 neurons in the VMH, and this action by leptin is required for normal body-weight homeostasis. *Neuron* 2006;49(2):191–203.
- [37] Shimazu T, Fukuda A, Ban T. Reciprocal influences of the ventromedial and lateral hypothalamic nuclei on blood glucose level and liver glycogen content. *Nature* 1966;210(5041):1178–9.
- [38] Flak JN, Goforth PB, Dell’Orco J, Sabatini PV, Li C, Bozadjieva N, et al. Ventromedial hypothalamic nucleus neuronal subset regulates blood glucose independently of insulin. *J Clin Invest* 2020;130(6):2943–52.
- [39] Martinez-Redondo V, Pettersson AT, Ruas JL. The hitchhiker’s guide to PGC-1alpha isoform structure and biological functions. *Diabetologia* 2015;58(9):1969–77.
- [40] Kunwar PS, Zelikowsky M, Remedios R, Cai H, Yilmaz M, Meister M, et al. Ventromedial hypothalamic neurons control a defensive emotion state. *Elife* 2015;4.
- [41] Brito NA, Brito MN, Kettelhut IC, Migliorini RH. Intra-ventromedial hypothalamic injection of cholinergic agents induces rapid hyperglycemia, hyperlactatemia and gluconeogenesis activation in fed, conscious rats. *Brain Res* 1993;626(1–2):339–42.
- [42] Lynch GS, Ryall JG. Role of beta-adrenoceptor signaling in skeletal muscle: implications for muscle wasting and disease. *Physiol Rev* 2008;88(2):729–67.
- [43] Takahashi A, Shimazu T. Hypothalamic regulation of lipid metabolism in the rat: effect of hypothalamic stimulation on lipolysis. *J Auton Nerv Syst* 1981;4(3):195–205.
- [44] Minokoshi Y, Saito M, Shimazu T. Sympathetic denervation impairs responses of brown adipose tissue to VMH stimulation. *Am J Physiol* 1986;251(5 Pt 2):R1005–8.
- [45] Sudo M, Minokoshi Y, Shimazu T. Ventromedial hypothalamic stimulation enhances peripheral glucose uptake in anesthetized rats. *Am J Physiol* 1991;261(3 Pt 1):E298–303.
- [46] Haque MS, Minokoshi Y, Hamai M, Iwai M, Horiuchi M, Shimazu T. Role of the sympathetic nervous system and insulin in enhancing glucose uptake in peripheral tissues after intrahypothalamic injection of leptin in rats. *Diabetes* 1999;48:1706–12.
- [47] Minokoshi Y, Haque MS, Shimazu T. Microinjection of leptin into the ventromedial hypothalamus increases glucose uptake in peripheral tissues in rats. *Diabetes* 1999;48(2):287–91.

- [48] Affinati AH, Sabatini PV, True C, Tomlinson AJ, Kirigiti M, Lindsley SR, et al. Cross-species analysis defines the conservation of anatomically segregated VMH neuron populations. *Elife* 2021;10.
- [49] van Veen JE, Kammel LG, Bunda PC, Shum M, Reid MS, Massa MG, et al. Hypothalamic estrogen receptor alpha establishes a sexually dimorphic regulatory node of energy expenditure. *Nat Metab* 2020;2(4):351–63.
- [50] Lira VA, Benton CR, Yan Z, Bonen A. PGC-1alpha regulation by exercise training and its influences on muscle function and insulin sensitivity. *Am J Physiol Endocrinol Metab* 2010;299(2):E145–61.
- [51] Chinsomboon J, Ruas J, Gupta RK, Thom R, Shoag J, Rowe GC, et al. The transcriptional coactivator PGC-1alpha mediates exercise-induced angiogenesis in skeletal muscle. *Proc Natl Acad Sci U S A* 2009;106(50):21401–6.
- [52] Rahnert JA, Zheng B, Hudson MB, Woodworth-Hobbs ME, Price SR. Glucocorticoids alter CRTC-CREB signaling in muscle cells: impact on PGC-1alpha expression and atrophy markers. *PLoS One* 2016;11(7):e0159181.
- [53] Annie L, Gurusubramanian G, Kumar Roy V. Dexamethasone mediated downregulation of PGC-1alpha and visfatin regulates testosterone synthesis and antioxidant system in mouse testis. *Acta Histochem* 2019;121(2):182–8.
- [54] Shimizu N, Maruyama T, Yoshikawa N, Matsumiya R, Ma Y, Ito N, et al. A muscle-liver-fat signalling axis is essential for central control of adaptive adipose remodelling. *Nat Commun* 2015;6:6693.
- [55] Pereira RM, Freire de Carvalho J. Glucocorticoid-induced myopathy. *Joint Bone Spine* 2011;78(1):41–4.
- [56] Conti V, Russomanno G, Corbi G, Izzo V, Vecchione C, Filippelli A. Adrenoreceptors and nitric oxide in the cardiovascular system. *Front Physiol* 2013;4:321.
- [57] Khan MM, Lustrino D, Silveira WA, Wild F, Straka T, Issop Y, et al. Sympathetic innervation controls homeostasis of neuromuscular junctions in health and disease. *Proc Natl Acad Sci U S A* 2016;113(3):746–50.
- [58] Rodrigues ACZ, Messi ML, Wang ZM, Abba MC, Pereyra A, Birbrair A, et al. The sympathetic nervous system regulates skeletal muscle motor innervation and acetylcholine receptor stability. *Acta Physiol* 2019;225(3):e13195.
- [59] Strack AM, Sawyer WB, Platt KB, Loewy AD. CNS cell groups regulating the sympathetic outflow to adrenal gland as revealed by transneuronal cell body labeling with pseudorabies virus. *Brain Res* 1989;491(2):274–96.
- [60] Jansen AS, Nguyen XV, Karpitskiy V, Mettenleiter TC, Loewy AD. Central command neurons of the sympathetic nervous system: basis of the fight-or-flight response. *Science* 1995;270(5236):644–6.
- [61] Saper CB, Loewy AD, Swanson LW, Cowan WM. Direct hypothalamo-autonomic connections. *Brain Res* 1976;117(2):305–12.
- [62] Saper CB, Stornetta RL. The rat nervous system. 4th ed. Academic Press; 2015. p. 629–73 [Chapter 23].
- [63] Betley JN, Cao ZF, Ritola KD, Sternson SM. Parallel, redundant circuit organization for homeostatic control of feeding behavior. *Cell* 2013;155(6):1337–50.
- [64] Cavalcanti-de-Albuquerque JP, Donato Jr J. Rolling out physical exercise and energy homeostasis: focus on hypothalamic circuitries. *Front Neuroendocrinol* 2021;63:100944.
- [65] Scammell TE, Arrigoni E, Lipton JO. Neural circuitry of wakefulness and sleep. *Neuron* 2017;93(4):747–65.
- [66] Guru A, Post RJ, Ho YY, Warden MR. Making sense of optogenetics. *Int J Neuropsychopharmacol* 2015;18(11):pyv079.
- [67] Egan B, Zierath JR. Exercise metabolism and the molecular regulation of skeletal muscle adaptation. *Cell Metabol* 2013;17(2):162–84.
- [68] Sternson SM, Atasoy D, Betley JN, Henry FE, Xu S. An emerging technology framework for the neurobiology of appetite. *Cell Metabol* 2016;23(2):234–53.
- [69] Zimmerman CA, Knight ZA. Layers of signals that regulate appetite. *Curr Opin Neurobiol* 2020;64:79–88.



Molecular Insights into the Interaction of Vitamin C (Ascorbic Acid) with Glutathione Peroxidase: A Comprehensive Computational Study

Bhattacharjee S^{1*}, Chakraborty S², Sharma A³, Chakraborty A⁴, Das PK⁵, Das P⁶, Lodh D⁷ and Chakraborty TR⁸

¹Department of Biological Sciences, Prachya Bharati Higher Secondary School, India

²Department of Physics, Bir Bikram Memorial College, India

³Department of Education, Henry Derozio Academy, India

⁴Department of Sports Physiology and Nutrition, National Sports University (A Central University), India

⁵Department of Physics, Prachya Bharati Higher Secondary School, India

⁶Department of Human Physiology, Dasaratha Deb Memorial College, India

⁷Department of Botany, Holy Cross College, India

⁸Department of Education, Tripura University, India

***Corresponding author:** Surajit Bhattacharjee, Department of Biological Sciences, Prachya Bharati Higher Secondary School, Agartala, Tripura (West), India, Email: surajit.hptu@gmail.com

Research Article

Volume 8 Issue 1

Received Date: November 30, 2023

Published Date: January 31, 2024

DOI: 10.23880/macij-16000188

Abstract

This research investigates the molecular interaction between vitamin C (ascorbic acid) and glutathione peroxidase (GPX), a key enzyme in the antioxidant defense system. Oxidative stress-induced damage, caused by an imbalance in reactive oxygen species (ROS) production, is implicated in various health issues. Vitamin C, a potent antioxidant, is known for its ability to neutralize free radicals and support overall cellular health. Despite numerous studies on the protective effects of vitamin C, the molecular details of its interaction with GPX remain unclear. In this study, we employ computational methods, including molecular docking and dynamics simulations, to predict and visualize the molecular-level interaction between vitamin C and GPX. Our results reveal a favorable binding affinity, supported by negative free energy values, suggesting strong interactions. Detailed analyses of various parameters provide insights into the structural flexibility of the ligand, vibrational dynamics, and clustering characteristics. Overall, this study enhances our understanding of the molecular mechanisms underlying the beneficial effects of vitamin C in combating oxidative stress, with potential implications for therapeutic interventions.

Keywords: Molecular Interaction; Vitamin C (Ascorbic Acid); Glutathione Peroxidase (GPX); Computational Study; Antioxidant Defense System

Introduction

Antioxidants are compounds that play a crucial role in protecting cells from the damaging effects of oxidative stress [1-5]. Oxidative stress occurs when there is an imbalance between the production of reactive oxygen species (ROS) and the body's ability to neutralize them. ROS, including free radicals, can cause damage to cellular structures such as proteins, lipids, and DNA, contributing to various health issues and the aging process [6]. Antioxidants work by neutralizing ROS, preventing them from causing harm to cells. They do this by donating electrons or hydrogen atoms, stabilizing the free radicals and reducing their reactivity. There are several types of antioxidants, including enzymes produced by the body and antioxidants obtained from the diet [3,4,7-9].

Vitamin C, also known as ascorbic acid ($C_6H_8O_6$), is a water-soluble vitamin that is well-known for its antioxidant properties that can donate electrons (e^-) to neutralize free radicals and reactive oxygen species like singlet oxygen (1O_2), like superoxide ($O_2^{\cdot-}$), hydroxyl radical (OH^{\cdot}) etc. By doing so, it helps prevent cellular damage caused by oxidative stress [10,11]. Vitamin C works both in the aqueous (water-soluble) and lipid (fat-soluble) phases of cells, making it effective in various cellular compartments. Vitamin C can regenerate other antioxidants, such as vitamin E. After vitamin E donates electrons (e^-) to neutralize free radicals, it becomes a radical itself. Vitamin C can help regenerate vitamin E, allowing it to continue its antioxidant function. This interplay between vitamins C and E enhances the overall antioxidant defense in the body [12]. Vitamin C has the ability to chelate (bind to and remove) metal ions, such as iron and copper, which can contribute to the generation of free radicals. By chelating these ions, vitamin C helps prevent the formation of additional reactive oxygen species [13,14]. Vitamin C is essential for the synthesis of collagen, a structural protein that is crucial for the health of connective tissues, skin, blood vessels, and bones, and collagen provides structural support and helps prevent oxidative damage to tissues [15,16]. Vitamin C supports the immune system by enhancing the function of white blood cells, which play a key role in immune response. During times of infection or inflammation, the demand for vitamin C may increase, highlighting its importance in maintaining a healthy immune system [17].

Vitamin C has been the subject of numerous research studies investigating its effects on oxidative stress and various health conditions. Researchers often explore the potential benefits of vitamin C due to its well-known antioxidant properties [18]. Some studies have investigated the effects of vitamin C supplementation on exercise-induced oxidative stress. Intense physical activity can lead to increased

production of free radicals, and researchers have explored whether vitamin C can help mitigate the oxidative stress associated with exercise [19]. In different research studies of arsenic induced myocardial damage also vitamin C has used as a positive control for its protective effects against oxidative damage of cardiac tissue [3,4,20,21]. Glutathione peroxidase (GPX) is an enzyme that plays a key role in the enzymatic antioxidant defense system. It is involved in the reduction of hydrogen peroxide and organic hydroperoxides, which are harmful byproducts of cellular metabolism. The level of this enzyme is reduced due to oxidative stress but it is increased in presence of vitamin C to reduce oxidative damage [3,4,21]. Though there are so many studies conducted on the activity of GPX in presence of vitamin C, but the process of molecular interaction of them is not cleared till now as per the literature study. So, the present study is designed to explore how does vitamin C is molecularly interacted with GPX.

Methods and Materials

Complement experimental approaches with computational methods such as molecular docking and molecular dynamics simulations are used to predict and visualize the interaction at the molecular level of vitamin C and GPX enzyme. For the smooth conduction of the study, we employed highly configured computer system with Autodock4, a freely available software tool for academic users, to conduct molecular docking. In performing these docking procedures, we specifically selected glutathione peroxidase enzyme as proteins from organs documented to be influenced by oxidative stress and ascorbic acid (vitamin C) as a ligand. The Figure 1 shows the name and the structure of the collected structural protein from RCSB Protein Data Bank and Figure 2 shows the ligand name and its structure obtained from PubChem. The steps involved in detailing the molecular docking processes [22] with some modifications are shown below:

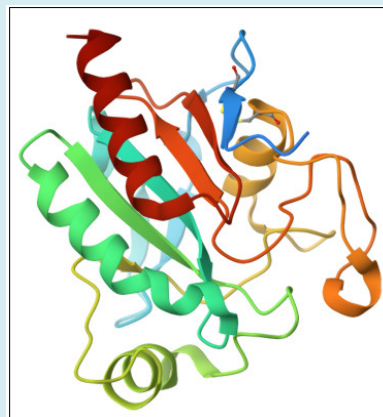
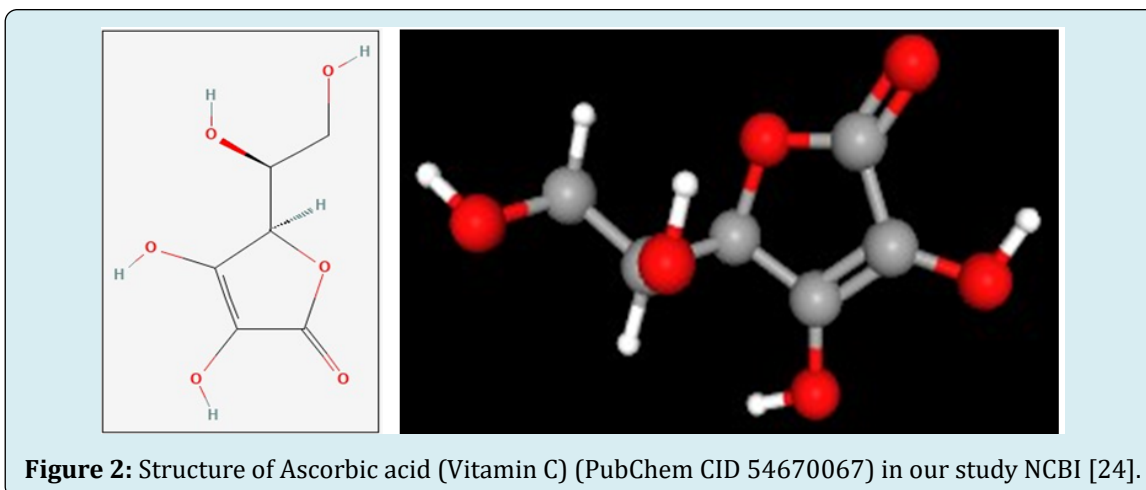


Figure 1: Structure of Glutathione peroxidase (PDB ID 7FC2) in our study [23].



1. The PDB and SDF files for the protein (macromolecule) and ligand were acquired from the Protein Data Bank and PubChem respectively.
2. Preparing the protein PDB files involved addressing the presence of additional waters. The files were loaded into the ADT GUI, where water molecules were identified as HOH* from a string and subsequently removed following a warning.
3. Macromolecular file preparation included the addition of polar hydrogens without bond order. Subsequently, charges were introduced using ADT, with default Kollman charges being applied (ADT automatically adds Kollman charges for a peptide).
4. In the concluding step of protein preparation, parameters were incorporated, and the files were saved as a 7fc2.pdbqt.
5. Ligand is then converted into PBD format by using OpenBable2.3.2a software.
6. Ligand, ascorbic acid is then loaded in the running ADT and parameters are prepared as per the direction and are saved as VitC.pdbqt.
7. Setting up the grid and generating the grid parameter file is crucial. To calculate docking interaction energy, a 3D box (grid) is created, enclosing the protein molecule. The grid volume must be sufficiently spacious to permit unrestricted rotation of the ligand, even in its most extended conformation. The parameters essential for constructing this grid are stored in the grid parameter file, named molecule.gpf.
8. Now a new file is created by naming 7fc2.gpf and saved in the docking folder.
9. Following this, Autogrid4 was executed to generate a map for each atom type in the ligand and produce the corresponding macromolecular file with the extension 7fc2.glg during the Run.
10. Creating the Docking Parameter File involved reading the macromolecular pdbqs and ligand.out.pdbq files. AutoDock offers various search methods, including the

annealing method, the genetic algorithm, local search, and the hybrid genetic algorithm with local search. The chosen algorithm for the analysis was the Lamarckian genetic algorithm, where offspring can inherit the local search adaptations of their parents. The docking task is initiated from the 'Run' command.

11. The .dlg files are then accessed through a terminal, and the final docked energy, Gibbs free energy, and inhibition constant for each run are recorded. For the most valuable result we have determined 500 numbers of runs.

Result and Discussion

The total charge on a molecule is the sum of the charges on its constituent atoms, taking into account the number of electrons and protons. In this study we have found that the overall electric charge associated with the ligand molecule which is vitamin C is -3.001 e. A negative charge indicates an excess of electrons compared to protons, suggesting that the ligand is anionic (it has gained electrons) [25]. A rotatable bond is a single bond (sigma bond) between two non-terminal heavy atoms. Heavy atoms are those that are not hydrogen. Rotatable bonds represent the connections in a molecule that can rotate freely around their axis, allowing for different conformations or spatial arrangements of the atoms. The more rotatable bonds a molecule has, the more potential conformations it can access [26]. In Table 1, we have found that its value is 9 torsions generally indicates a moderate to high level of structural flexibility. Number of atoms in ligand is it is providing information about the molecular composition of a ligand. In chemistry, a ligand is a molecule or ion that can form a coordination complex by binding to a central metal atom. The ligand usually donates electrons to the metal, forming a coordination bond [27]. Table 1 indicates that the ligand under consideration consists of 17 atoms. These atoms could be a combination of different elements, and their arrangement and connectivity determine the structure of the ligand. Non-hydrogen atoms in ligand

provide the information about the molecular composition of a ligand, specifically indicating the number of non-hydrogen atoms in the ligand [28]. The non-hydrogen atoms in ligand of this experiment shows that it's value is 13 (Table 1). These non-hydrogen atoms could be a combination of different elements, and their arrangement and connectivity determine the structure of the ligand. Knowing the count of non-hydrogen atoms is essential for understanding the size, complexity, and potential reactivity of the ligand [28]. In Table 1, the number of vibrational degrees of freedom of ligand is 45," it indicates that the ligand molecule has a total of 45 distinct ways in which its atoms can undergo vibrational motion. This is a significant amount of vibrational flexibility and suggests that the ligand is likely to have a complex and dynamic structure [29]. Torsional degrees of freedom refer to the ability of parts of a molecule to rotate around single bonds. Each single bond connecting two non-terminal atoms introduces a torsional degree of freedom, representing a way in which the atoms on either side of the bond can rotate relative to each other [30]. In this experiment the number of torsional degrees of freedom is found 9 in Table 1 which indicates that the molecule has nine torsional or rotational degrees of freedom. So, the molecule is relatively flexible, and its structure can vary due to rotations around these specific bonds. This flexibility can have implications for the molecule's behavior in different environments or when interacting with other molecules.

Total charge on ligand	-3.001 e
Number of Rotatable Bonds in Small Molecule	9 torsions
Number of atoms in ligand	17
Number of non-hydrogen atoms in ligand	13
Number of vibrational degrees of freedom of ligand	45
Number of torsional degrees of freedom	9
Estimated Free Energy of Binding	-2.74 kcal/mol
Information entropy for clustering	0.36 (rmstol = 2.00 Angstrom)
Estimated loss of torsional free energy upon binding	+2.6847 kcal/mol

Table 1: Information of different parameters of the molecular docking.

A negative free energy of binding indicates that the binding process is energetically favorable. In other words, the binding of the ligand to the target is predicted to release energy. Gibbs Free Energy and Binding Energy are crucial parameters studied using AutoDock, as discussed earlier. The

output results, represented by ΔG , provide essential insights into a closed system. AutoDock furnishes the minimum value of Gibbs free energy (ΔG) for each conformer of the ligand when docked to the protein. Additionally, it facilitates the calculation of the equilibrium binding constant (K) in each case, with these two parameters linked by the straightforward relation $\Delta G = -RT \ln K$ [31]. In Table 1 we have found that the estimated free energy of binding is -2.74 kcal/mol refers to a calculated value that represents the change in free energy associated with the binding of the vitamin C to the target protein glutathione peroxidase in a biological system suggest stronger binding interactions. Here in Figure 3 we can see the interaction of vitamin C with protein in the same way.

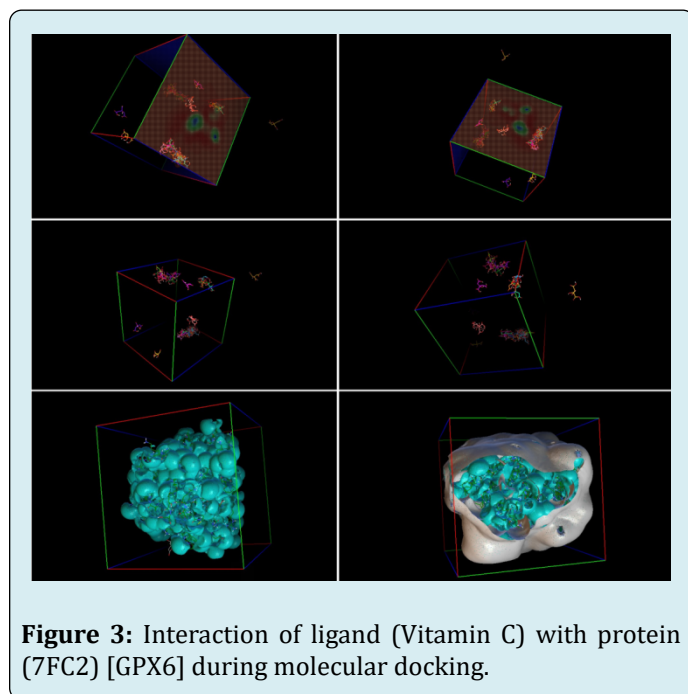


Figure 3: Interaction of ligand (Vitamin C) with protein (7FC2) [GPX6] during molecular docking.

"Entropy for clustering" likely refers to the entropy associated with the clustering of molecular conformations generated during the docking process. Molecular docking is a computational method used to predict the preferred orientation of one molecule (the ligand) when it binds to another molecule (the target or receptor) [32]. The combination of an entropy value of 0.36 and an RMSD tolerance of 2.00 Angstroms of Table 1 of this study suggests that the clustering process is yielding relatively homogeneous conformations, and the structural diversity within each cluster is limited to deviations within the specified RMSD tolerance.

A positive value indicates an increase in energy [33]. In this experiment the value of loss of torsional free energy upon binding is +2.6847 kcal/mol (Table 1) suggests that the binding process is associated with an increase in the energy required for the torsional rotation of certain bonds within

the molecules. The positive value here indicates that the binding process is associated with a higher energy cost for the torsional rotations within the molecules.

“CLUSTERING HISTOGRAM” Table 2 section describes the characteristics of a specific cluster of conformations at Cluster Rank 35 in the molecular docking simulation. The lowest binding energy Figure 4, mean binding energy, and the number of conformations in the cluster provide insights into the energetics and diversity of conformations within this particular cluster. Lower binding energies and a higher number of conformations generally indicate a more

favorable and diverse set of docking poses in the cluster which is located in the Figure 5.

Cluster Rank 35	1
Lowest Binding Energy	-4.04
Run	378
Mean Binding Energy	-2.74
Num in Clus	216

Table 2: Clustering Histogram of the molecular docking.

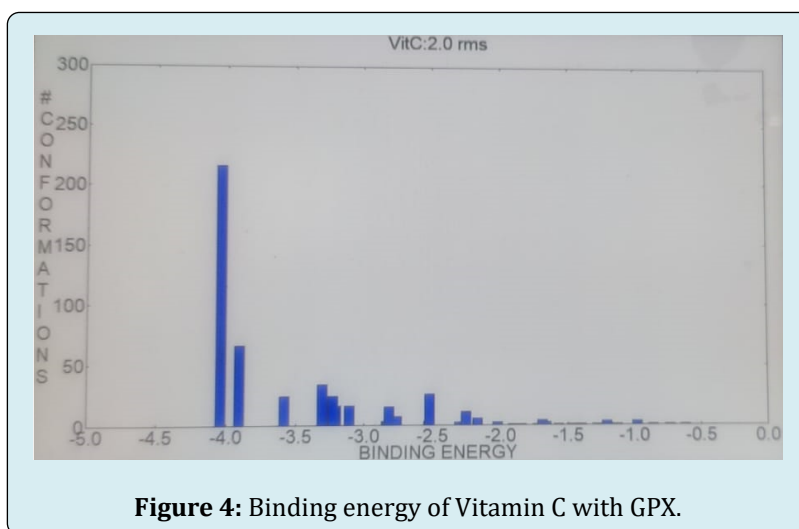


Figure 4: Binding energy of Vitamin C with GPX.

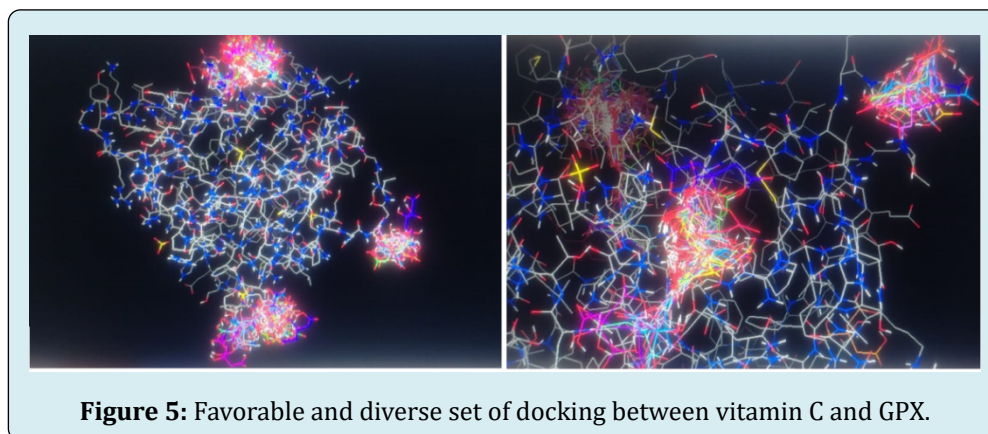


Figure 5: Favorable and diverse set of docking between vitamin C and GPX.

In summary, the presented results provide a comprehensive overview of various parameters and aspects related to the molecular docking of vitamin C with the target protein (GPX6). Here the negative charge on the ligand suggests that the ligand (vitamin C) is anionic, indicating an excess of electrons compared to protons. This information is crucial for understanding the overall charge distribution in the ligand. The presence of 9 rotatable bonds indicates a moderate to high level of structural flexibility for the ligand. This flexibility can be important for the ligand to

adapt to the binding site of the target protein, allowing for different conformations. The ligand is composed of 17 atoms, providing insight into its molecular size and complexity. The arrangement and types of atoms influence the ligand's interactions with the target. The information about 13 non-hydrogen atoms gives a more specific view of the ligand's composition, excluding hydrogen atoms. This is crucial for understanding the core structure of the ligand. The high number of vibrational degrees of freedom (45) indicates a significant degree of vibrational flexibility in the ligand. This

can influence its behavior in different chemical environments. The presence of 9 torsional degrees of freedom suggests that the ligand is relatively flexible, and its structure can vary due to rotations around specific bonds. The negative value indicates that the binding of the ligand to the protein is energetically favorable. A lower value suggests a stronger binding interaction. The entropy value of 0.36, with an RMSD tolerance of 2.00 Angstroms, suggests that the clustering process has yielded relatively homogeneous conformations. This information is vital for understanding the diversity and reliability of the docking results. Estimated Loss of Torsional Free Energy upon Binding (+2.6847 kcal/mol) which is a positive value suggests an increase in the energy required for the torsional rotation of bonds upon binding. This information provides insights into the structural changes associated with the binding process. The information presented in the clustering histogram provides details about a specific cluster at rank 35. The lowest binding energy, mean binding energy, and the number of conformations in the cluster give a detailed view of the energetics and diversity within this cluster.

Conclusion

The current comprehensive computational study sheds light on the molecular interaction between vitamin C (ascorbic acid) and glutathione peroxidase (GPX), a crucial enzyme in the antioxidant defense system. The negative free energy values obtained from molecular docking signify a favorable binding affinity, indicating strong interactions between vitamin C and GPX. The detailed analyses of various parameters, including the ligand's structural flexibility, vibrational dynamics, and clustering characteristics, enhance our understanding of this interaction at the molecular level.

Vitamin C's ability to neutralize free radicals and support cellular health is well-established, and our study provides molecular insights into its interaction with GPX. The presented results offer a nuanced understanding of the structural features and dynamics associated with the binding process. Furthermore, the study highlights the potential implications of this interaction for therapeutic interventions aimed at combating oxidative stress-induced damage, a factor implicated in various health issues.

This research contributes valuable information to the existing body of knowledge regarding the molecular mechanisms underlying the protective effects of vitamin C. The findings not only advance our understanding of the antioxidant defense system but also pave the way for future studies and therapeutic developments in the realm of oxidative stress-related conditions. Overall, our computational study serves as a significant step forward in unraveling the intricate details of the molecular interplay

between vitamin C and GPX.

Statement and Declaration

Conflicts of interest

Authors do not have any conflict of interest.

Funding

Not applicable.

Acknowledgements

I am thankful to all the participants and authors for their cooperation, continued support and hard work for the successful completion of this study.

Data Availability Statement

Raw data may be available upon request.

References

1. Kunitomo M (2007) Oxidative stress and atherosclerosis. *Journal of the Pharmaceutical Society of Japan* 127(12): 1997-2014.
2. Bhattacharjee S, Sarkar C, Pal S (2013) Additive beneficial effect of folic acid and vitamin B12 co-administration on arsenic-induced oxidative damage in cardiac tissue in vivo. *Asian journal of pharmaceutical and clinical research* 6(1): 64-69.
3. Bhattacharjee S, Pal S (2014) Additive protective effects of selenium and vitamin E against arsenic induced lipidemic and cardiotoxic effects in mice. *International journal of pharmacy and pharmaceutical sciences* 6(5): 406-413.
4. Bhattacharjee S, Pal S (2014) Antilipidemic and cardioprotective effects of vitamin B12 and folic acid against arsenic toxicity. *International journal of pharmaceutical, chemical and biological sciences* 4(2): 353-360.
5. Yang X, Dong WB, Li QP, Kang L, Lei XP, et al. (2016) Resveratrol increases sirtuin 1 expression in peripheral blood mononuclear cells of premature infants and inhibits the oxidative stress induced by hyperoxia in vivo. *Chinese journal of contemporary pediatrics* 18(1): 72-77.
6. Zeber-Lubecka N, Ciebiera M, Hennig EE (2023) Polycystic Ovary Syndrome and Oxidative Stress-From

- Bench to Bedside. *International journal of molecular sciences* 24(18): 14126.
7. Barzegar A (2012) Proton-coupled electron-transfer mechanism for the radical scavenging activity of cardiovascular drug dipyridamole. *PloS one* 7(6): e39660.
 8. Chen J, Yang J, Ma L, Li J, Shahzad N, et al. (2020) Structure-antioxidant activity relationship of methoxy, phenolic hydroxyl, and carboxylic acid groups of phenolic acids. *Scientific reports* 10(1): 2611.
 9. Thbayh DK, Reizer E, Kahaly MU, Viskolcz B, Fiser B (2022) Antioxidant Potential of Santowhite as Synthetic and Ascorbic Acid as Natural Polymer Additives. *Polymers* 14(17): 3518.
 10. Akorede GJ (2020) Protective effect of vitamin C on chronic carbamazepine-induced reproductive toxicity in male wistar rats. *Toxicology reports* 7: 269-276.
 11. Ludke A, Akolkar G, Ayyappan P, Sharma AK, Singal PK (2017) Time course of changes in oxidative stress and stress-induced proteins in cardiomyocytes exposed to doxorubicin and prevention by vitamin C. *PloS one* 12(7): e0179452.
 12. Traber MG, Stevens JF (2011) Vitamins C and E: beneficial effects from a mechanistic perspective. *Free radical biology & medicine* 51(5): 1000-1013.
 13. Kontoghiorghes GJ, Kolnagou A, Kontoghiorghes CN, Mourouzidis L, Timoshnikov VA, et al. (2020) Trying to Solve the Puzzle of the Interaction of Ascorbic Acid and Iron: Redox, Chelation and Therapeutic Implications. *Medicines* 7(8): 45.
 14. Shen J, Griffiths PT, Campbell SJ, Uttinger B, Kalberer M, et al. (2021) Ascorbate oxidation by iron, copper and reactive oxygen species: review, model development, and derivation of key rate constants. *Scientific reports* 11: 7417.
 15. Chambial S, Dwivedi S, Shukla KK, John PJ, Sharma P (2013) Vitamin C in disease prevention and cure: an overview. *Indian journal of clinical biochemistry* 28(4): 314-328.
 16. DePhillipo NN, Aman ZS, Kennedy MI, Begley JP, Moatshe G, et al. (2018) Efficacy of Vitamin C Supplementation on Collagen Synthesis and Oxidative Stress After Musculoskeletal Injuries: A Systematic Review. *Orthopaedic journal of sports medicine* 6(10).
 17. Carr AC, Maggini S (2017) Vitamin C and Immune Function. *Nutrients* 9(11).
 18. Lee EY, Lee MY, Hong SW, Chung CH, Hong SY (2007) Blockade of oxidative stress by vitamin C ameliorates albuminuria and renal sclerosis in experimental diabetic rats. *Yonsei medical journal* 48(5): 847-855.
 19. Ristow M, Zarse K, Oberbach A, Klötting N, Birringer M, et al. (2009) Antioxidants prevent health-promoting effects of physical exercise in humans. *Proceedings of the National Academy of Sciences of the United States of America* 106(21): 8665-8670.
 20. Nabavi SF, Nabavi SM, Mirzaei M, Moghaddam AH (2012) Protective effect of quercetin against sodium fluoride induced oxidative stress in rat's heart. *Food & function* 3(4): 437-441.
 21. Manna P, Sinha M, Sil PC (2008) Arsenic-induced oxidative myocardial injury: protective role of arjunolic acid. *Archives of toxicology* 82(3): 137-149.
 22. Huey R, Morris G (2008) Using autodock 4 with autodock tools: a tutorial by the Scripps Research Institute.
 23. Sun J (2022) Crystal Structure of GPX6.
 24. National Center for Biotechnology Information [NCBI] (2023) Ascorbic Acid.
 25. Taakili R, Canac Y (2020) NHC Core Pincer Ligands Exhibiting Two Anionic Coordinating Extremities. *Molecules (Basel, Switzerland)* 25(9): 2231.
 26. Seidel T, Permann C, Wieder O, Kohlbacher SM, Langer T (2023) High-Quality Conformer Generation with CONFORGE: Algorithm and Performance Assessment. *Journal of chemical information and modeling* 63(17): 5549-5570.
 27. Goodman H, Mei L, Gianetti TL (2019) Molecular Orbital Insights of Transition Metal-Stabilized Carbocations. *Frontiers in chemistry* 7: 365.
 28. Smith RD, Engdahl AL, Dunbar JB, Carlson HA (2012). Biophysical limits of protein-ligand binding. *Journal of chemical information and modeling* 52(8): 2098-2106.
 29. Tuffery P, Derreumaux P (2012) Flexibility and binding affinity in protein-ligand, protein-protein and multi-component protein interactions: limitations of current computational approaches. *Journal of the Royal Society, Interface* 9(66): 20-33.
 30. Bodmer NK, Havranek JJ (2018) Efficient minimization of multipole electrostatic potentials in torsion space. *PloS one* 13(4): e0195578.
 31. Majumder D, Mukherjee S (2013) Molecular Docking

- Assessment of Efficacy of Different Clinically Used Arsenic Chelator Drugs. *Journal of Computational Medicine*, pp: 1-8.
32. Meng XY, Zhang HX, Mezei M, Cui M (2011) Molecular docking: a powerful approach for structure-based drug discovery. *Current computer-aided drug design* 7(2): 146-157.
33. Deng Y, Roux B (2009) Computations of standard binding free energies with molecular dynamics simulations. *The journal of physical chemistry B* 113(8): 2234-2246.



Novel Insight into the Cellular and Molecular Signaling Pathways of *Costus speciosus* in the Treatment of COVID-19: A Review

Debasree Lodh¹ and Arijit Chakraborty^{2*} 

¹Department of Botany, Holy Cross College, Agartala, Tripura, India; ²Department of Sports Physiology and Nutrition, National Sports University (A Central University), Imphal, Manipur, India

*Correspondence to: Arijit Chakraborty, Department of Sports Physiology and Nutrition, National Sports University, Imphal 795001, Manipur, India. ORCID: <https://orcid.org/0000-0003-2975-7333>. Tel: +91-9874321916, E-mail: say.arijit22@gmail.com or arijitphysiology@gmail.com

Citation of this article: Lodh D, Chakraborty A. Novel Insight into the Cellular and Molecular Signaling Pathways of *Costus speciosus* in the Treatment of COVID-19: A Review. *Nat Cell Sci* 2024;2(1):42–58. doi: 10.61474/ncs.2023.00026.

Abstract

The latest pandemic of coronavirus disease 2019 (COVID-19), caused by the infection of severe acute respiratory syndrome coronavirus 2 (SARS-CoV-2), has brought upon the world an unparalleled challenge. Since its inception, scientists and researchers have come together to develop various forms of vaccines and efficient therapeutic agents. In addition, plant products have been considered safe, cost-effective, and reliable molecules capable of neutralizing various microorganisms, including viruses. In this review, research articles on natural products related to antiviral effects were searched from various databases, such as the Web of Science, Google Scholar, Medline, Scopus, and PubMed, until August 2021, using English keywords. Moreover, the effectiveness of a locally available plant called *Costus speciosus* and its natural extracts on SARS-CoV-2 is discussed, while also providing insight into the cellular and molecular pathways of its active components that are involved in viral suppression. However, the lack of information regarding the safety profile and dosage for diverse diseases is one of the limitations of *Costus speciosus* as a natural medicine that can also interfere with COVID-19 pathogenesis by inhibiting SARS-CoV-2 replication and entry into host cells. We also highlight the use of plants as possible therapeutic agents in the prevention and management of COVID-19.

Keywords: SARS-CoV-2; COVID-19; Pandemic; Secondary metabolism; Antiviral agents; Natural products.

Introduction

Coronavirus disease 2019 (COVID-19) is an infectious disease caused by severe acute respiratory syndrome coronavirus 2 (SARS-CoV-2), a single-stranded positive-sense RNA virus that is very contagious and has quickly spread globally; this disease results in severe mortality and has no specific cure.¹ The effective management of COVID-19 is still not in control and is not feasible with the recurrent mutations of SARS-CoV-2, even after applying continuous vaccination drives and treatment with drugs that are available in the market.² To discover a potential and appropriate drug for COVID-19, scientists have been working hard; however, to date, no effective methods for the prevention and therapeutic management of COVID-19 infection have been reported. Owing to the scarcity and unavailability of effective vaccines, antiviral drugs, effective prophylactic therapies, and remedies are still required to prevent SARS-CoV-2 infection; thus, the burden of the COVID-19 pandemic shined a light on the need to develop alternative preventive and treatment options.

Nowadays, the World Health Organization focuses on developing effective treatments and welcomes innovative therapies giving more emphasis to traditional medicines as tradi-

tional medicinal plants are the largest reservoir of biologically active secondary metabolites, which play an important role in curing different diseases including diseases caused by viruses from ancient times.³ Ayurveda, Unani, and Siddha are the most ancient indigenous systems of medicine of human civilization used to treat various disorders for many centuries using a variety of medicinal plants with their preventive, curative, and rehabilitative properties.

Costus, from the family Costaceae and order Zingiberales, is a large genus comprising over ~150 species that has a long ethno-medicinal account in India and has been used in traditional systems of medicine—Ayurveda, Unani, and Siddha—since ancient times. According to the Ayurvedic Pharmacopoeia of India (2008),⁴ *Costus* is referred to as “kebuka” and has properties like rasa, guna, virya, vipaka, and karma; it is used in formulations like krmighna, kvatha, andurna against agnimandya, slipada, arsa, grahani, jvara, kamala, kasa, kusta, raktavikara, krimiroga, and kaphaja, among others.

Costus speciosus (*C. speciosus*) Koen. ex Retz. is a perennial herb with a tuberous horizontal rhizome and spirally arranged simple leaves with bisexual flowers.⁵ It exhibits multiple cytotypes, occurs worldwide,⁶ and grows wild in shady places of mixed deciduous forests in India.⁷ Rhizomes

Received: October 12, 2023 | Revised: December 15, 2023 | Accepted: February 27, 2024 | Published online: March 30, 2024

contain high amounts of diosgenin.⁸ The active ingredients include diosgenin, dioscin, β -sitosterol, glucoside, gracillin, saponin, quinine, α -tocopherol, tricontanoic acids, curcumin, tricontanol, aliphatic hydroxyl ketones, triterpenes, abscisic acid, starch mucilage, oxa-acids, fatty acids, corticosteroids, and tigogenin. Traditionally, the plant has been used as an astringent, depurative, purgative, febrifuge, expectorant, and muscle relaxant. In addition, it has been used for the treatment of pneumonia, rheumatism, urinary diseases, fever, jaundice, mental disorders, fever, and dysentery (Fig. 1).⁹ The phytochemicals presented in *C. speciosus* possess a number of activities, such as antiviral, antibacterial, antifungal, antioxidant, immunomodulatory activity, antipyretic, antidiabetic, adaptogenic, anthelmintic, antistress, hepatoprotective, anti-inflammatory, and many other biological activities,⁹ demonstrating its potential for the prevention and therapeutic usefulness in the treatment of COVID-19.

In this current scenario, as there is no registered medicine to treat COVID-19,¹ *C. speciosus* could be a promising antiviral component to prevent and cure SARS-CoV-2 infection without any harmful side effects. This review compiles all of the information regarding the potential of *C. speciosus* as an effective therapeutic agent to fulfill the global demand to prevent or treat COVID-19 and can serve as a guide for further research for the early development of new drugs and clinical applications to combat this deadly disease.

Distribution

The plant *C. speciosus* is widely distributed in the humid tropical and subtropical regions on both sides of the equatorial plane.^{5,10} It is exclusively distributed throughout the globe, especially in the tropical regions of Asia, Africa, and the Americas.^{11,12} *C. speciosus* is region-specific and native to the Malay Peninsula of Southeast Asia,¹³ India, Indonesia, Sri Lanka, and Malaysia; however, it has been naturalized in some other tropical areas, including Hawaii.¹¹ Within India, it grows from the central and eastern Himalayas to southern India and is also located in the Andaman and Nicobar Islands.¹⁴ *C. speciosus* is generally distributed below an altitude of 1,500 m in tropical forests throughout the Indian subcontinent,¹⁵ mostly in moist, warm, and hot evergreen forests. The geospatial distribution in the country ranges throughout to the foothills of the Himalayas from Himachal Pradesh to Assam; the Vindhya Satpura Hills in central India; the Eastern Ghats of Andhra Pradesh; the Western Ghats of Maharashtra, Karnataka, Tamil Nadu, Kerala, Meghalaya, Bihar, and Khasi; as well as the Jaintia Hills, Uttarakhand, Orissa, MP, North Bengal, West Bengal, and Himalayan tracts,¹¹ excluding the arid and semi-arid areas of Punjab, Haryana, Rajasthan, Gujarat, and the Peninsular India (Table 1).^{9–28} This plant thrives well on rich moist soil in shady localities under deciduous forests; hence, it is located wild in the soggy wet-lands, particularly in the streams and river banks.¹⁶ It grows well in a climate with high humidity¹⁶ and is found in road-side ditches and low-lying areas¹⁰ in the marshy and shady places¹⁷ of forest plantation. In many regions, this plant is also cultivated for its ethno-medicinal and ornamental purposes.^{9,11,16}

Morphology of *C. speciosus*

C. speciosus Smith belongs to the family Costaceae and

is an ornamental, perennial, rhizomatous, erect, succulent, herbaceous, and monocotyledonous plant; it grows up to 2.7 m in height, arising from a horizontal rhizome.⁹ Tuberous rhizomes clothed with sheaths are found in the lower parts, whereas the upwards parts are leafy.²⁹ The upper surface of the rhizome is marked with circular nodal scars with remnants of leaf bases; on the other hand, the lower and lateral surfaces exhibit small circular scars of roots or a few wiry fractured yellowish-brown rootlets.³⁰ The stem is sub-woody at the base.¹⁴ The leaves are simple, dark green in color, elliptical to oblong or oblong to lanceolate, thick, sessile, and silky pubescent beneath, and spirally arranged on the stems; the leaf sheaths are coriaceous. The flowers are bisexual, large, and white, and they occur in cone-like terminal dense spikes, with bright red bracts and a lip with a yellowish throat.³¹ The flowers look like crape paper; thus, the common name of the plant is “Crape ginger.” Flowering generally occurs during the months of July to October.³² The attractive red cone-shaped bracts remain attached to the inflorescence, even after the flowers fade away. The fruits are capsular, globose trigonous, and red in color. The seeds are black, with white aril. The style is filiform, the stigma generally has a semilunar ciliated depression, and the ovary is generally three-celled. The ovules are many and superposed.^{5,9,18,33} A detailed overview of all of the probable mechanistic details of *C. speciosus* as well as salient findings is also provided in Table 2.^{11,12,15,17,19–23,34–50}

Various pharmacological activities of *C. speciosus*

Anti-inflammatory activity

The term inflammation is classically defined as a complex biological response in which areas become reddened, hot, swollen, and often painful, especially as a reaction to injury or infection *per se*.⁵¹ It is well known that SARS-CoV-2 replication triggers the inflammatory response in the host cellular milieu.⁵² Acute lung injury during SARS-CoV-2 infection is due to aggressive inflammation initiated by viral replication and allied factors.⁵³ When inflammation is overwhelming, it may lead to serious unfavorable outcomes or even death, as seen during the COVID-19 pandemic.⁵⁴ Inflammation also plays a key role in the development and severity of COVID-19 when it occurs with other diseases (i.e., comorbidity).⁵⁵ Thus, controlling or preventing the inflammatory response may be an effective way of preventing the life-threatening condition in patients with COVID-19. One of the keys to successfully manage the disease is to effectively control the inflammation rapidly with the appropriate anti-inflammatory drugs.⁵⁶

Clinical evidence has shown that during COVID, uncontrolled inflammation turns into hyperinflammation and becomes chronic, which inhibits the adaptive immune responses and ultimately causes multiple organ dysfunction. Such dysregulated inflammation results in a “cytokine storm” that is manifested due to the release of high levels of pro-inflammatory cytokines, such as interleukin (IL) 1 β , IL6, granulocyte colony-stimulating factor, interferon gamma-induced protein 10, monocyte chemoattractant protein 1, macrophage inflammatory protein-1 alpha, tumor necrosis factor-alpha, IL10, IL7, and IL2, as well as chemokines by respiratory epithelial cells, dendritic cells, and macrophag-

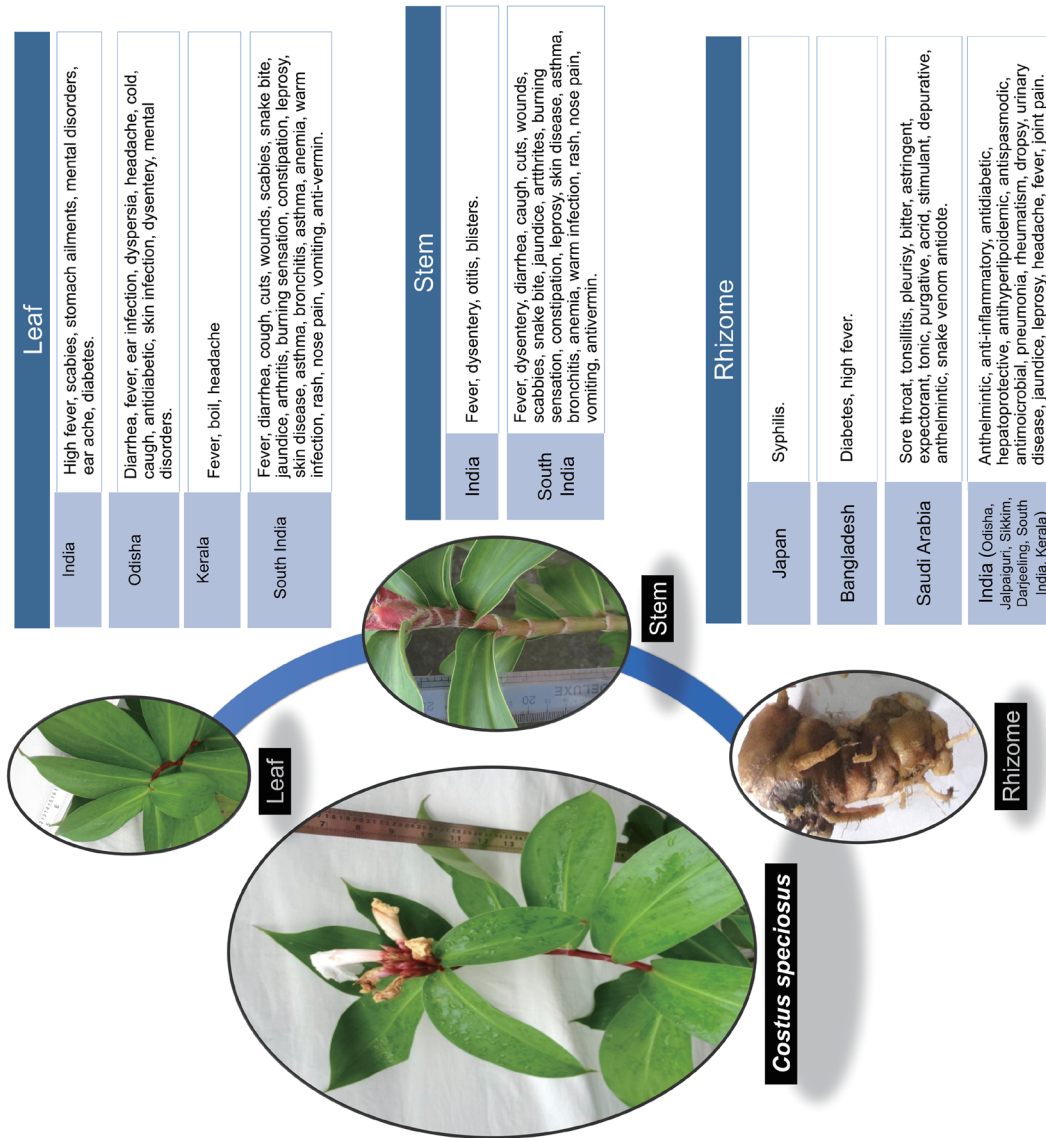


Fig. 1. Parts of *Costus speciosus* and their uses.

Table 1. Mode of uses in different parts of *Costus speciosus* in various regions of the world

Location	Parts used	Mode of use	References
Japan	Rhizome	Rhizome extract is used for controlling syphilis.	13,22
Malaysia	Whole plant	The plant is used for small pox.	9, 15
Indonesia	Whole plant	This plant is commonly used to treat insect bite, to inhibit male fertility, skin diseases, wounds, dysentery, diarrhoea, fever, backache, sore eyes and also used as a traditional male contraception in some areas.	16
Bangladesh	Rhizome	The rhizome is used for diabetes and high fever.	25
Saudi Arabia	Rhizome	In Saudi folk medicine, the rhizome is used for the treatment of sore throat, tonsillitis, and pleurisy. This plant is also traditionally used as a bitter, astringent, expectorant, tonic, purgative, acrid, stimulant, depurative, anthelmintic, and expectorant. <i>C. speciosus</i> is one of the most effective traditional medicinal plants in Islamic medicine. <i>Costus</i> has been mentioned in the Prophet's medicine for treating pharyngitis and tonsillitis in children, pleurisy, and as an antidote for snake venom.	12,23
India	Leaf; Stem; Root; Rhizome	<i>C. speciosus</i> is one of the constituents of the indigenous drug "amber mezhugu," which is useful in treating rheumatism. Bruised leaves are used for bathing or topically applied to reduce fever in patients with high fevers. The leaves are also used to treat scabies, stomach ailments, mental disorders, and earaches. Diabetic people in India eat one leaf daily to keep their blood glucose levels low. The decoction of the stem is used to control fever and dysentery. The juice of the freshly burned stem is used as an ear drop to heal otitis. The stems are ground into a paste and applied to blisters. In Indian traditional medicine, the rhizomes and roots of <i>C. speciosus</i> are believed to have antihelmintic, anti-inflammatory, antidiabetic, hepatoprotective, antihyperlipidemic, antispasmodic, and antimicrobial activities. Rhizomes are given in pneumonia, rheumatism, dropsy, urinary diseases, jaundice, and diabetes. The juice of the rhizome is traditionally given with sugar to treat leprosy, worm infestations, abortion, and applied to the head for cooling and relief from headaches. The decoction of the rhizome is used for crushing kidney and bladder stones. The plant is used in traditional medicine to treat burning sensation during urination, inflammation, flatulence, constipation, helminthiasis, leprosy, skin diseases, fever, persistent cough, asthma, rheumatism, bronchitis, inflammation, and anemia. Internally, the plant is used for eye and ear infections, diarrhea (sap from leaves, young stems), colds, catarrhal fever, cough, dyspepsia, and treating boils. It is also used as an ingredient in cosmetics to enhance sexual attractiveness, as mentioned in KamaSutra. In India, herbal preparations of <i>C. speciosus</i> are currently used by local people in tea bags (herbal-chai), supplements, beverages, and food items that regulate body sugar and cholesterol levels. It is also used locally for diabetes and jaundice.	9,12–15, 17,20
Odisha	Rhizome; Leaf	The rural and tribal people of Odisha use the rhizome of <i>C. speciosus</i> as a raw vegetable or as a cooked vegetable, and it is highly nutritious with a high content of carbohydrates, starch, amylase, protein, and lipids/oil. The tribal communities of the state used the rhizome to cure joint pain, skin infections, and consumed it as a nutraceutical. Rhizomes are also given in diseases such as pneumonia, expectorant, for curing asthma, fever, bronchitis, leprosy, skin diseases, rheumatism, dropsy, skin diseases, snake bites, urinary diseases, jaundice, among others. The rural and tribal people use the leaves against diarrhea, fever, ear infections, dyspepsia, headache, cold, and cough. The leaves are reported to possess antidiabetic properties and are used against skin infections, dysentery, and to aid in mental disorders, etc. It is not only used as therapeutic medicine but for other socio-cultural purposes, such as wrapping indigenous food items, mat making, and treatment of evil repellents.	18

(continued)

Table 1. (continued)

Location	Parts used	Mode of use	References
West Bengal	Rhizome; Stem	Rhizome is used to treat red urine, dyspepsia, and diabetes. The peeled stem is chewed to relieve thirst in the jungle.	11,24,26
Darjeeling	Rhizome	The rhizome decoction is used by the tribes of Darjeeling.	11,27
Kerala	Leaf, Rhizome	The fresh juice of the plant leaf and rhizome is used in Kerala.	28
Eastern Himalayan	Whole plant	<i>C. speciosus</i> is one such plant used by the locals of the regions of eastern Himalayan belt.	19
Sikkim hills	Rhizome	Rhizome decoction is used by the tribes of Sikkim hills.	27
Eastern Hima layan	Whole plant	<i>C. speciosus</i> is one such plant used by the locals of the regions of eastern Himalayan belt.	19
South India	Stem; Leaves; Rhizome	This plant is used as food and medicine by the Kannikars, the primitive hill tribes of South India. The juice of the rhizome is applied to the head for cooling and relief from headaches. A decoction of the stem is used for fever and dysentery. Bruised leaves are applied during a fever. Patients with high fever mostly use leaf infusion or decoction as a sudorific or in a bath. The sap from leaves and young stems is used against diarrhea, coughs, cuts, wounds, scabies, snake bites, jaundice, arthritis, burning sensations, constipation, leprosy, skin diseases, asthma, bronchitis, inflammations, anemia, worm infections, rashes, nose pain, to stop vomiting, and as an anti-vermin and for abortion.	10,21

Costus speciosus, *C. speciosus*.

Table 2. The detailed overview of all the probable mechanistic details of *Costis speciosus* with their salient findings

SI No.	Plant related activity	Reference	Duration of the study	Years of literature reviews	Salient findings	Inclusion & exclusion criteria
1.	Anti-inflammatory activity	12	2013–2014	1973 to 2017	The methanolic extract of <i>C. speciosus</i> demonstrated potent anti-inflammatory effects in vitro studies by inhibiting pro-inflammatory mediators in murine BV-2 cells. The aqueous solution of <i>C. speciosus</i> is also used as nasal drops to improve acute symptoms of pharyngitis and tonsillitis, highlighting its potential as a promising strategy for various inflammatory disorders.	Patients with acute pharyngitis and tonsillitis were included.
		34	–	1956 to 2014	Ethanol leaf extracts of <i>C. speciosus</i> revealed the presence of alkaloids, tannins, saponins, steroids, terpenoids, flavonoids, and total phenols, indicating potential for anti-inflammatory activities.	–
		35	–	1955 to 1997	Ethanol extract of <i>C. speciosus</i> demonstrated significant anti-inflammatory effects, particularly in carrageenan-induced edema and cotton pellet-induced granuloma formation.	–
		36	–	1962 to 2011	The anti-inflammatory activity of methanol extracts from <i>C. speciosus</i> aerial parts was evaluated using the carrageenan-induced paw edema test in rats.	–

(continued)

Table 2. (continued)

SI No.	Plant related activity	Reference	Duration of the study	Years of literature reviews	Salient findings	Inclusion & exclusion criteria
19			–	1974 to 2014	The heat-induced haemolytic assay was conducted by incubating methanol extract of <i>C. speciosus</i> leaves at various concentrations with the RBC suspension. The percentage of haemolysis and membrane stabilization were calculated, indicating the concentration-dependent anti-inflammatory activity of the extract.	–
37			–	1932 to 2013	The denaturation of proteins, a known cause of inflammation, was assessed by subjecting the leaf extracts of <i>C. speciosus</i> in different concentrations and evaluating their ability to protect against protein denaturation and membrane stabilizing activity was determined by assessing the extracts' impact on erythrocyte membrane stability.	–
38			–	1968 to 2014	The anti-inflammatory activity was assessed through <i>in vitro</i> studies such as membrane stability testing, hypotonicity-impelled HRBC hemolysis, protein denaturation inhibition and <i>in vivo</i> tests such as formalin-induced writhing test and tail immersion test using methanol extract of <i>C. speciosus</i> on selected healthy male rats.	–
2.	Adaptogenic activity	39	Albino rats were treated for 16 days.	1968 to 2008	The study investigated the antistress activity of ethanolic extracts from <i>C. speciosus</i> rhizomes on albino rats subjected to cold immobilization stress using Soxhlet extraction. The extracts prevented neurotransmitter depletion, particularly norepinephrine and dopamine, and modulated MAO activity suggesting adaptogenic potential of the plant.	–
12			–	1973 to 2017	The study suggested that extracts from <i>C. speciosus</i> reduce stress-induced elevations of 5-HT and 5-HIAA levels, indicating a potential antidepressant effect.	–
40			–	1966 to 1983	The study investigated the impact of immobilization stress on the release of 5-hydroxyindoles (specifically 5-HT or serotonin) in the rat hippocampus using <i>in vivo</i> voltammetry.	–
3.	Anti-diabetic activity	11	–	1972 to 2016	Ethanolic extracts of <i>C. speciosus</i> rhizome have shown effectiveness in reducing blood glucose levels and improving lipid profiles in rats.	–

(continued)

Table 2. (continued)

SI No.	Plant related activity	Reference	Duration of the study	Years of literature reviews	Salient findings	Inclusion & exclusion criteria
37			–	1932 to 2013	The anti-diabetic activity assessment involved extracting compounds from <i>C. speciosus</i> leaves using ethanol. The compounds were identified through silica column chromatography and spectroscopic analysis. The study concluded by highlighting the potential of the identified compounds in treating diabetes.	–
20			–	1956 to 2012	The study focused on quantifying diosgenin, a steroidal saponin and major bioactive compound in <i>C. speciosus</i> using HPLC analysis. Diosgenin extraction involved hydrolysis and hexane extraction. HPLC was conducted on leaves and rhizomes, revealing variation in diosgenin content among species and plant parts.	–
41			The experimental period lasted for 30 days.	1951 to 2008	<i>C. speciosus</i> roots were extracted with hexane to isolate costunolide, which was administered to streptozotocin-induced diabetic rats. Costunolide demonstrated significant normoglycemic and hypolipidemic effects, suggesting its potential as a drug for managing diabetes.	Male Wistar rats weighing about 190–200 g were included. Diabetic rats were included based on a fasting plasma glucose range. Rats outside the specified weight range and those not meeting the criteria for STZ-induced diabetes were excluded.
21			The experimental period three weeks. The rats were treated twice daily with the extracts.	1974 to 2016	Petroleum ether extract, ethanol extract and water extract of <i>C. speciosus</i> leaves were orally administered to streptozotocin-induced diabetic rats. Ethanolic extract exhibited significant antidiabetic effects in streptozotocin-induced diabetic rats.	Inclusion criteria involved the selection of streptozotocin-induced diabetic rats.
42			The experimental period lasted for 15 days, during which the rats were treated daily.	1969 to 2008	The ethanolic extract of <i>C. speciosus</i> rhizome was investigated using Soxhlet apparatus and demonstrated significant antidiabetic effects in alloxan-induced diabetic rats.	Inclusion: Wistar Albino rats weighing 150–180 g. Exclusion: Rats not developing hyperglycemia 48 hours after alloxan injection were excluded and replaced with new animals.

(continued)

Table 2. (continued)

SI No.	Plant related activity	Reference	Duration of the study	Years of literature reviews	Salient findings	Inclusion & exclusion criteria
22			–	1970 to 2009	Aqueous, methanolic and hexane extracts of <i>C. speciosus</i> demonstrated efficacy in reducing serum glucose and improving other biochemical parameters in diabetic rats. Additionally, the leaves exhibit hypoglycemic properties and enhance insulin action.	–
43			–	1954 to 2016	Diosgenin quantification through HPTLC, and in vitro assessments including starch–iodine assay for antidiabetic activity, were performed with methanolic extract of <i>C. speciosus</i> .	–
4.	Antimicrobial Activity	34	–	1956 to 2014	The ethanolic leaf extract revealed the presence of potential bioactivities, validating its traditional medicinal use and highlighting its potential in drug discovery.	–
44			–	1972 to 2018	Ethanolic extracts of <i>C. speciosus</i> rhizomes, particularly in high concentrations and obtained through both hot and cold methods, demonstrated significant antibacterial and antifungal activities against diverse pathogenic microorganisms. Aqueous extract on hot displayed antibacterial activity, with no antifungal activity. Aqueous extract on cold did not exhibit antibacterial effects against any tested microorganisms.	–
45			–	1987 to 2007	The study focused on the phytochemical screening, HPTLC separation, and antimicrobial screening of <i>C. speciosus</i> . Methanolic and aqueous extracts exhibited antibacterial activity against <i>Staphylococcus aureus</i> , with the traditional use of boiling in water supporting this finding. However, methanolic extract showed no inhibitory activity against other bacteria.	–
46			–	1980 to 2012	The study investigated the antimicrobial properties of <i>C. speciosus</i> roots, employing steam distillation for essential oil extraction, cold percolation for plant extracts, and epoxidation of diosgenin. Results demonstrated significant inhibitory effects on fungi and bacteria.	–
47			–	1966 to 2011	The essential oil extracted from the rhizome of <i>C. speciosus</i> was analyzed using GC-FID and GC-MS. The antibacterial screening demonstrated significant activity against both gram-positive and gram-negative bacteria.	–

(continued)

Table 2. (continued)

SI No.	Plant related activity	Reference	Duration of the study	Years of literature reviews	Salient findings	Inclusion & exclusion criteria
		17	–	1973 to 2019	The findings suggested the potential of antimicrobial activity was the leaves of <i>C. speciosus</i> . The agar well diffusion assay revealed significant antimicrobial effects, with the highest activity observed against <i>E. coli</i> .	–
5.	Anthelmintic Activity	48	–	1970 to 2010	The article was a review that consolidates information on the phytochemical and pharmacological properties of <i>C. speciosus</i> . The methodology involves the study and investigation of available literature related to the plant.	–
		15	–	1970 to 2015	<i>Pheretima posthuma</i> were employed as experimental worms. The anthelmintic activity of <i>C. speciosus</i> was assessed using methanolic and aqueous extracts of the aerial parts. The anthelmintic activity of the extracts was compared with a standard drug, albendazole (20 mg/ml).	–
6.	Estrogenic Activity	23	–	1972 to 2020	The methanolic extract of <i>C. speciosus</i> rhizome used to examine the uterine weight of adult female rats.	–
		49	–	1940 to 2010	The study presented data suggesting a significant stimulation of uterine activity by <i>C. speciosus</i> rhizome extract, with a focus on the role of its constituent, b-sitosterol, acting via a non-estrogen receptor-mediated mechanism.	–
		50	–	1970 to 2004	The study provided information about the chemical composition of <i>C. speciosus</i> by different experimental methods such as-Liebermann-Burchardt test, HPLC, UV spectrum analysis, IR spectrum analysis, thin layer chromatography.	–
7.	Antipyretic Activity	35	Drug administration occurred 10 hours after yeast administration.	1955 to 1994	Antipyretic properties were studied in yeast-induced pyrexia in rats. Only male albino rats were used for the antipyretic study, and rectal temperature was recorded. The ethanolic extract of the <i>C. speciosus</i> rhizome demonstrated significant anti-pyretic properties.	–

Costus speciosus, *C. speciosus*.

es.⁵⁷ According to recent reports, cytokine storm and severe inflammation are highly correlated for the progression of SARS-CoV-2 infection.⁵⁸ It has been observed that lung epithelial cells play a crucial role in the release of several pro-inflammatory cytokines, including IL6 and IL8.⁵⁹ Various inflammatory markers such as high levels of C-reactive protein, ferritin, and D-dimers as well as the neutrophil-to-lymphocyte ratio and serum levels of several inflammatory cytokines and chemokines are associated with the disease severity and death of COVID-19 patients.⁶⁰ In addition, it has been observed that aberrant pathogenic T cells and inflammatory monocytes are rapidly activated, producing a huge number of cytokines and inducing an inflammatory storm.⁶¹

Nonsteroidal anti-inflammatory drugs (such as aspirin, ibuprofen, celecoxib, and indomethacin) are widely prescribed for the relief of pain and inflammation during COVID-19.⁶² These drugs alleviate inflammation through effectively blocking the production of prostaglandins via inhibition of cyclooxygenase enzymes.⁶³ Anti-inflammatory therapeutics, such as colchicine, are used to treat COVID-19-associated excessive inflammation⁶⁴ that acts by interacting with the Nod-like receptor protein 3 inflammasome protein complex, suppressing the release of the cytokines IL1 β , IL18, and IL6.⁶⁵ Colchicine also can bind to free tubulin dimers and block microtubule polymerization; therefore, it interrupts inflammatory cell activities and cytokine release.⁶⁶ Moreover, colchicine is used to control the white blood cell-mediated inflammatory activities, thus inhibiting the production of superoxides and the release of numerous cytokines and pyrogens from the white blood cells.⁶⁷ Quercetin and Ivermectin also have been suggested as anti-inflammatory drugs for the treatment of COVID-19 because they work by reducing the production of tumor necrosis factor- α , IL1, and IL6 as well as suppressing lipopolysaccharide-induced translocation of nuclear factor kappa-light-chain-enhancer of activated B cells.⁶⁸ The signaling pathway of the anti-inflammatory effects occurs through the inhibition of enzymes like cyclooxygenases and lipoxygenases, which are responsible for eicosanoid generation. This in turn reduces the concentrations of inflammatory mediators such as prostaglandins and leukotrienes. Also, they prevent the activation of nuclear factor kappa-light-chain-enhancer of activated B cell target genes, such as those for the cytokines IL1 α , IL1 β , IL6, IL8, and tumor necrosis factor- α , which are considered potential markers for inflammation.⁵⁸ Experimental studies indicate that *C. speciosus* has potent anti-inflammatory effects due to the presence of the active compounds costunolide and diosgenin, which have been isolated from the plant.¹² The flavonoids and terpenoids present in the ethanolic leaf extract of *C. speciosus* also exhibit anti-inflammatory properties.³⁴ To investigate the traditional uses of *C. speciosus* for the treatment of inflammation, numerous experimental studies have been conducted. The ethanolic extract of the *C. speciosus* rhizome has shown anti-inflammatory properties in carrageenan-induced edema formation in rats.³⁵ In addition, the methanolic extract of the *C. speciosus* aerial parts has demonstrated anti-inflammatory activities in adult albino rats and Swiss albino mice.³⁶ Likewise, the methanolic extract of *C. speciosus* leaves has shown anti-inflammatory activity by inhibiting the heat-induced hemolysis of red blood cells.¹⁹ The denaturation of proteins is one of the main causes of inflammatory disease. *In-vitro* studies have demonstrated

that the ethanolic extract of *C. speciosus* leaves inhibits protein denaturation in inflammatory disease by controlling auto-antigen production.³⁷ Moreover, the methanolic extract of *C. speciosus* seeds has shown significant anti-inflammatory activity by inhibiting hypotonic lysis of the erythrocyte membrane in a red blood cell membrane stabilization study. It also has been noticed that the methanolic extract exhibits anti-inflammatory activity by blocking cyclooxygenase activity followed by the inhibition of prostaglandin synthesis.³⁸ Despite enormous efforts for the development of new drugs for the treatment of COVID-19, to date, no clinical trial has shown a validated significant effect. Therefore, there is still a lack of specific efficacious clinically proven drugs, vaccines, as well as other antiviral medications and therapies to control the virus that causes COVID-19.⁶⁹ Based on the above-mentioned antiviral, anti-inflammatory, and immunoregulatory activity, *C. speciosus* might be a promising safe, natural candidate for the treatment and prevention of COVID-19 in the future.

Adaptogenic activity

Adaptogens are classical stress-protective compounds that help organisms to acclimatize under different forms of stress as well as to increase adaptability, resilience, and hence survival by activating certain adaptive signaling pathways of the cellular and organismal defense systems.⁷⁰ Adaptogens also stimulate the cellular defense mechanisms and increase non-specific resistance and adaptation to stress by expressing stress-activated proteins and activating the extra- and intracellular signaling pathways. Likewise, adaptogens coordinate to alleviate stress-induced mental and behavioral disorders.⁷¹ *C. speciosus* rhizome extracts act as an effective adaptogenic agent when administered in stress-induced experimental albino rats. The extract showed antistress and adaptogenic activity in brain neurotransmitter profiles and in monoamine oxidase enzyme levels by normalizing norepinephrine, dopamine, 5-hydroxy tryptamine, and 5-hydroxy indole acetic acid against cold immobilization.³⁹ This plant extract also has been used in the formulation of an effective antistress and antidepressant drug against central nervous system disorders,¹² since the extract significantly reduced the stress-induced increase of 5-hydroxy tryptamine and 5-hydroxy indole acetic acid levels in brain tissues by preventing the alarm reaction, which causes a significant increase in 5-hydroxy indole acetic acid and 5-hydroxy tryptamine levels.⁴⁰

Adaptogens play a potentially significant role at all stages of viral infections. They can decrease the duration of the acute phase of illness by affecting the neuroendocrine-immune system. Adaptogens likely combat infection through their specific and nonspecific antiviral properties, attenuate escalating inflammation through their potent anti-inflammatory effects, repair oxidative stress-induced injuries in compromised cells and tissues, and provide baseline support through their immunomodulatory, immunostimulatory, and anti-oxidant effects. In COVID-19 patients, the effects of adaptogens mainly occur during their convalescence. Adaptogens are primarily preferred for the treatment of viral infections as they modulate innate and adaptive immunity as well as anti-inflammatory activity, detoxify and repair the oxidative stress-induced damage in the cells, and direct antiviral effects by inhibiting viral docking or replication; thus, they can improve the quality of life of patients during convales-

cence. Recent data from clinical experimental studies have shown that melatonin, a novel therapeutic agent against SARS-CoV-2, helps to bolster the immune system, which is activated by adaptogens through the melatonin signaling pathway.⁷² Melatonin as an adaptive hormone⁷³ also plays an important role in the regulation of homeostasis,⁷⁴ which in turn can be activated using novel *C. speciosus* plant extracts.

Safe and nontoxic psychotropic medications that do not aggravate the psychiatric condition are a prerequisite for the treatment of COVID-19 patients.⁷⁵ Therefore, considering the urgent need to find a specific pharmacotherapy for COVID-19 patients, the rhizomic extract of *C. speciosus* may be recommended as an easily available, affordable, nontoxic, and safe adaptogenic agent for the treatment of COVID-19 patients.

Antidiabetic activity

Diabetes mellitus is a chronic metabolic disorder caused either by the failure of requisite insulin production due to the loss of beta cells present in the pancreas (as in type 1 diabetes), or when the sensitivity of those cells is diminished due to insulin resistance (as in type 2 diabetes).⁷⁶ Hyperglycemia occurs when an excessive amount of glucose circulates in the blood plasma; on the other hand, hypoglycemia ensues when the blood glucose level decreases. Both hyperglycemia and hypoglycemia may disrupt an already malfunctioning innate immune system in patients with diabetes, increasing their susceptibility to infections.⁷⁷ Uncontrolled diabetes is associated with macro- and microvascular complications affecting the health and survival of patients.⁷⁸

C. speciosus has been demonstrated to have immense antidiabetic properties as it regulates the secretion of insulin from pre-existing beta cells of the islets of Langerhans.¹¹ This appears through induction of the expression of the insulin gene in pancreatic cells and insulin receptor-A in hepatic cells, and increasing the serum insulin levels consequently increases glucose uptake through induction of glucose transporter 2 gene expression. The hypoglycemic effect of various active constituents is exerted through potentiation of insulin synthesis and release from the existing beta cells as well as increasing the tissue sensitivity of insulin to glucose uptake. The leaves and rhizomes of *C. speciosus* have shown antidiabetic activity due to the presence of phytochemical flavonoids³⁷ and diosgenin, a steroidal saponin.²⁰ Additionally, costunolide, extracted from *C. speciosus*, significantly reduced the plasma glucose level when administered to streptozotocin-induced diabetic male Wistar rats at different doses⁴¹ by inhibiting the expression of nitric oxide synthase.⁷⁹ Similarly, the administration of aqueous and methanolic rhizome extracts showed a reduction in the blood glucose level in streptozotocin-induced diabetic rats. The ethanolic extract of *C. speciosus* leaves was found to significantly reduce the blood glucose level when administered orally to diabetic experimental animal models.²¹ The ethanolic extract of *C. speciosus* rhizomes also showed a significant antidiabetic effect in alloxan-induced diabetic rats.⁴² In diabetic rats, the hexane crude extract of *C. speciosus* rhizomes was effective in bringing down and normalizing the serum glucose level.²² The *in-vitro* antidiabetic potential of *C. speciosus* was also assessed by a starch-iodine color assay.⁴³

Most of the available clinical studies have shown that

diabetes mellitus is one of the most common and prevalent comorbidities in COVID-19 patients that is causing considerable morbidity and mortality rates globally.⁸⁰ Therefore, as *C. speciosus* is a potent antidiabetogenic agent, it should be considered as one of the first lines of defense. Patients with diabetes tend to have more severe disease vulnerability with poor glycemic control, which has a negative impact on the immunological system and may lead to a high risk of infections and serious life-threatening chronic complications with worse outcomes when they test positive for COVID-19.⁸¹ *In-vitro* animal studies have shown that when angiotensin-converting enzyme 2 (ACE2), the main receptor responsible for COVID-19, binds with SARS-CoV-2, this biological mechanism reduces adequate insulin secretion by damaging the function of the beta cells of pancreatic islets.⁸² On the other hand, infection secondary to diabetic complications is also accompanied by a huge production of cytokines, causing cytokine storms, which may induce insulin resistance.⁸³ Both altered insulin secretion and insulin resistance are responsible for uncontrolled blood sugar levels, which are generally noticed in patients infected with SARS-CoV-2; therefore, acute and chronic diabetes significantly affect both the innate and the adaptive immune system⁸⁴ and are linked to poor white blood cell function, including impaired phagocytosis by neutrophils, neutrophil chemotaxis, macrophage and monocyte function, and innate cell-mediated immunity.⁸⁵ Patients with diabetes (type 1 or type 2) have been identified as being at an increased risk for respiratory tract infections and serious illness from COVID-19 relative to the healthy general population⁸⁶ because there is a defect in the innate immunity, which aggravates phagocytosis, neutrophil chemotaxis, and/or cell-mediated immunity.⁸⁷

The mortality rate of COVID-19 patients with diabetes was significantly higher (~42.3%) than that of COVID-19 patients without diabetes.⁷⁸ Numerous recent studies have indicated that SARS-COV-2 infection can lead to multi-organ injuries with a worsening clinical status and composite adverse outcomes in individuals with pre-existing diabetes.⁸⁸ In light of the currently available data, people with diabetes are at risk for developing severe and critical forms of COVID-19 and seem to be more susceptible and vulnerable; thus, they need special care.⁸⁹ However, it is very obvious that patients with diabetes need to continuously control and regularly monitor their blood glucose levels, which requires careful clinical management, with extra precautions and special attention to prevent COVID-19. Therefore, it is urgently needed to develop novel antidiabetic medications, which will play a distinctive role in protecting people from infection and could reduce the risk of morbidity and mortality in patients with uncontrolled glycemia. Antidiabetic drugs (e.g., insulin, dipeptidyl peptidase 4 inhibitors, sodium-glucose cotransporter 2 inhibitors, glucagon-like peptide 1 receptor agonists, thiazolidinediones, metformin, sulfonylureas, pioglitazone, liraglutide, hydroxychloroquine, etc.) have been used in COVID-19 patients to manage their diabetes;⁹⁰ however, they show various complications for lowering persistent high blood glucose levels. Therefore, in order to protect these patients, the administration of a drug formulated from naturally occurring *C. speciosus* may be prescribed as a future preventative therapy for patients with diabetes, as good glycemic control is the key to reduce the probability of contracting COVID-19 and will help to overcome the detrimental adverse effects

of this disease. Due to its low cost, widespread availability, and good tolerability, *C. speciosus* plant extract is definitely a potential candidate and an appropriate add-on drug that could safely be prescribed as a sustainable, nontoxic, effective herbal antidiabetic drug therapy for treating and controlling the insulin levels of diabetic patients in order to decrease complications due to COVID-19.³³

Antimicrobial activity

Co-infections, also known as dual-infections, secondary infections, or superinfections caused by multiple pathogens of viral, bacterial, or fungal origin, are a common complication causing severe illness among COVID-19 patients and result in a major risk of unfavorable outcomes, which may prolong the acute phase of COVID-19 and are also associated with increased rates of morbidity and mortality.⁹¹ Published clinical data show that COVID-19 patients are vulnerable to co-infections caused by bacterial and/or fungal pathogens.⁹² These bacterial and/or fungal secondary infections by multiple pathogens interfere with the immune status, which is a big threat to patients during COVID-19.⁹³

Opportunistic infections by other microorganisms develop in patients diagnosed with COVID-19 during or after the initial infection with a virus, and they are associated with worse adverse outcomes than that of either infection on its own.⁹⁴ Sometimes, due to the combined effects of the microbial pathogens, patients may be exposed to severe disease conditions leading to fatal clinical complications. The most common bacteria reported during co-infections in COVID-19 patients mainly include *Staphylococcus aureus*, *Streptococcus pneumoniae*, *Haemophilus influenzae*, *Pseudomonas aeruginosa*, *Klebsiella pneumoniae*, *Acinetobacter baumannii*, and *Mycoplasma pneumoniae*.⁹⁵ Secondary fungal co-infections (e.g., candidiasis, aspergillosis, cryptococcosis, pneumocystosis, and histoplasmosis) also have been identified in patients with COVID-19,⁹⁶ including *Aspergillus flavus*, *Aspergillus fumigatus*, *Candida glabrata*, and *Candida albicans*, among others.⁹⁷ Mucormycosis, also known as the black fungus, is another serious fungal infection that produces life-threatening complications detected among COVID-19 patients.⁹⁸

To overcome severe disease, various antibacterial, antifungal, and antiviral drugs are administered to COVID-19 patients.⁹⁶ The use of antimicrobial drugs is one of the principal methods in medicine that is widely employed to help reduce and prevent different infectious diseases, either bacterial or fungal.⁹⁹ The most frequently prescribed antibiotics that are used to prevent the occurrence of secondary bacterial infections in COVID-19 patients include ceftriaxone/cefotaxime, ampicillin/amoxicillin, quinolones, imipenem, ceftriaxone, fluoroquinolone, azithromycin, quercetin, rapamycin, doxycycline, fluoroquinolones, macrolides, cephalosporins, azithromycin, moxifloxacin, ceftriaxone, vancomycin, and cefepime.¹⁰⁰ Meanwhile, the drugs used to treat fungal infections in COVID-19 patients include amphotericin B, itraconazole, caspofungin, fluconazole, and voriconazole.¹⁰¹

Some of the alternative antiviral drugs that are used in the management of COVID-19 target specific steps within the life cycle of SARS-CoV-2, such as darunavir, atazanavir, saquinavir (protease inhibitors); umifenovir (fusion inhibitor); remdesivir, favipiravir (inhibitors of viral RNA polymerase/RNA synthesis); lopinavir/ritonavir (inhibitors of viral protein

synthesis); ivermectin (inhibitor of viral replication); hydroxychloroquine, chloroquine (viral entry inhibitors); oseltamivir (viral release inhibitor); nitazoxanide (immunomodulator); ribavirin, sofosbuvir (nucleotide reverse transcriptase inhibitor); emtricitabine, and azvudine (nucleoside reverse transcriptase inhibitor).¹⁰² As viral-bacterial-fungal co-infections are one of the largest medical concerns resulting in increased mortality rates, it is imperative to pay attention to these co-infections in critical patients positive for COVID-19.⁹⁵ In most cases, patients are treated with broad-spectrum antimicrobial drugs with unknown efficacy¹⁰³ for the suspected bacterial or fungal co-infections,¹⁰⁴ but they are not very effective for the treatment of COVID-19 and also suppress the immune system.¹⁰¹ Based on the recent clinical data, serious adverse side effects have been reported in patients when treated with the above-mentioned antimicrobial drugs,⁹² since no specific drug has been approved and shown to be effective until now;⁹³ whereas a newer drug development regime is time consuming¹⁰⁷ for the prevention and treatment of human coronavirus infections.¹⁰⁸ Therefore, immediate efforts and effective treatment strategies are needed to reduce the risk of transmission and to manage future pandemics.¹⁰² This critical reality demands urgency for a special focus on developing novel, effective, and safe antimicrobial drugs with more promising clinical development to combat invasive microbes.

From the thorough phytochemical studies and investigations of the available literature on *C. speciosus*, it has been clearly found that the *C. speciosus* plant extract possesses plethoric secondary metabolites (e.g., flavonoids, phenols, tannins, alkaloids, steroids, terpenoids, etc.), which act as an effective antimicrobial substance against a wide range of microorganisms.³⁴ Hexane and ethanolic extracts of *C. speciosus* leaves and rhizomes exhibit promising antibacterial and antifungal activities against various pathogenic microorganisms.⁴⁴ Moreover, the aqueous extract shows antibacterial activity against *S. aureus*,⁴⁵ which is one of the causative agents for co-infection in COVID-19. In addition, it has been noted that the epoxidation of diosgenin extracted from the rhizome of *Costus* shows antifungal activity⁴⁶ and that components of the essential oil (e.g., α -humulene and zerumbone) extracted from the rhizomes of *C. speciosus* possess considerable antibacterial activity.⁴⁷

It also has been noticed that sometimes the use of synthetic antibiotic drugs increases the risk of death during secondary infections in COVID-19 patients.¹⁰⁹ Furthermore, antibiotic overuse is associated with subsequent harm, which leads to resistance against the microorganisms,¹¹⁰ and these antibiotic-resistant infections are a significant threat to COVID-19 patients. On the other hand, it is very challenging to distinguish between severe COVID-19 and bacterial and fungal secondary infections.¹⁰³

Therefore, the experimental results suggest that since the *C. speciosus* plant extract acts as an effective antimicrobial agent, it possibly could be used as a safe and effective antimicrobial medicine¹⁷ for invasive secondary bacterial and/or fungal co-infections, which are more life-threatening than the initial viral infection during COVID-19.

Anthelmintic activity

Anthelmintics are a class of generic drugs that are used to destroy parasitic worms without causing any significant harm to

the host cell. Some reports of substantial anthelmintic activity of the methanolic and aqueous extracts of the aerial parts of *C. speciosus* against earthworms are present in the existing literature as they have been used widely for the primary evaluation of anthelmintic compounds *in vitro* because they mimic intestinal worms in their reaction to helminthiasis,⁴⁸ suggesting that the plant can be used as a promising anthelmintic agent to cure the disease.¹⁵ There are plethoric anthelmintic medicines, viz. niclosamide, ivermectin, and nitazoxanides, in the market that are employed to symptomatically treat and cure COVID-19 patients.¹¹¹ It has been reported that potential helminth co-infections exacerbate the immune systems susceptible to newer contagions.¹¹² It also has been noted that helminth parasites have symbiotically adapted to their specific hosts during the long evolutionary process, thus resulting in chronic diseases of the host; however, the mortality rate is low. There are several modulations in the host surface that are brought about by these parasites; the immune system is one of them. In general, the parasites induce a hyporesponsive state of the host's immune system, and, in situations like the COVID-19 pandemic, such attributes may worsen the situation *per se*. Therefore, the current situation demands the launch of newer therapeutic drugs and treatment options that are widely and easily available as well as affordable, effective, and safe, without causing any systemic side effects. As the *C. speciosus* plant extract has potent anthelmintic activity, it may be a potent addition to prevent SARS-CoV-2 viral replication and may be recommended for symptomatic treatment for further clinical evaluation and development of new drugs to cure and treat COVID-19.

Estrogenic activity

Estrogen, a primary female sex hormone that actively regulates the cellular and molecular processes, is involved in the development of the female reproductive system along with the maintenance of secondary sexual characteristics. Both ethanolic and methanolic extracts of *C. speciosus* rhizomes have been shown to exert an effective estrogenic effect in animal models.^{23,49} Additionally, uterine stimulant properties were observed when rhizome extracts of *C. speciosus* were administered on spontaneous phasic uterine contractions, which were mainly due to nonestrogenic effects with a consequent increase in uterotonic contractions induced via calcium entry on L-type calcium channels and sarcoplasmic reticulum calcium release.⁴⁹ There are several reports explaining that the saponins present in the *C. speciosus* extract induced a profound estrogenic activity in sprayed rats, significantly increased uterine weight and uterine glycogen concentration, and produced proliferative changes in the uterus.⁵⁰

Recently, estrogenic activity has been linked with the repair of infected respiratory tissues, which provide protection from developing a severe infection by SARS-CoV-2 in females and thus act as a strong immune-regulatory agent in both the innate and adaptive immune systems.¹¹³ It has been well speculated that the SARS-CoV-2 spike protein binds to ACE2 receptors and that estrogens play an important role in the interactions between the SARS-CoV-2 spike protein and the human ACE2 receptor that protects the human lung during infection caused by SARS-CoV-2.¹¹⁴ Derivatives of estrogen molecules (17 β -diol and S-equol) modulate the ACE2-dependent membrane fusion protein and reduce the entry of the SARS-CoV-2 spike protein into lung cells. Es-

trogen also affects cardiac ACE2 levels and activity through its receptors estrogen receptor alpha and G protein-coupled estrogen receptor, by regulating ACE2 shedding via disintegrin and metalloprotease 17 and transmembrane serine protease 2. This linear correlation of ACE2 gene transcripts with estrogen receptor alpha and G protein-coupled estrogen receptor mRNAs is associated with higher values of ACE2 gene expression.¹¹⁵ Estrogens stimulate the immune system by modulating the function of B cells and thus improve T-helper 2 cell activity. They stimulate the nasal immune system by increasing the activity of phagocytes, dendritic cells, and natural killer cells.¹¹⁶ Estrogens are elevated during *C. speciosus* administration, which also exhibits anti-inflammatory and immuno-modulatory effects against COVID-19, thus reducing SARS-CoV-2 infectivity through modulation of pro-inflammatory signaling pathways.¹¹⁷

These observations strongly indicate the potential protective effect of *C. speciosus* via modulating estrogenic activity; therefore, it could be recommended for future therapeutic strategies against COVID-19 (Fig. 2).

Antipyretic activity

Cumulatively, antipyretics are a group of drugs that reduce fever during pyrexia or conditions leading to an increase in the core body temperature. The ethanolic rhizome extract of *C. speciosus* has been shown to exhibit an antipyretic effect in yeast-induced pyrexia in an animal model by acting through inhibition of the production of prostaglandins in the hypothalamus.³⁵ An uncontrolled increase in body temperature leading to fever is one of the most common initial symptoms of COVID-19 in approximately 80% of patients,¹¹⁸ so it is considered that there is a close connection between pyrexia and the onset of the disease. Under these circumstances, it is mandatory to control and reduce fever with artificial antipyretics, which is beneficial for COVID-19 patients.¹¹⁹ Recent COVID-19 treatment guidelines by the World Health Organization have recommended the use of antipyretics²⁴ as a first line of defense. Several synthetic antipyretics (e.g., ibuprofen, paracetamol, among others) are readily available in the market as over-the-counter medications; however, consuming them may lead to severe irreversible side effects.¹²⁰ Therefore, the administration of *C. speciosus* extract or its derivatives for its natural antipyretic activity may be an effective option as a safe and nontoxic herbal antipyretic medicine for the symptomatic treatment of COVID-19 patients.

Conclusions

The therapeutic potential of *C. speciosus* extract or its derivatives against COVID-19 is significant, given their diverse modes of action and their ability to impact different cellular and molecular pathways that are related to the pathophysiology of the disease. The present review emphasizes the need for comprehensive studies to entirely understand the efficacy, safety, and mechanism of action of these natural compounds derived from *C. speciosus*. As the global scientific community continues to search for effective treatments for COVID-19, natural products offer a valuable resource for discovering novel antiviral agents.

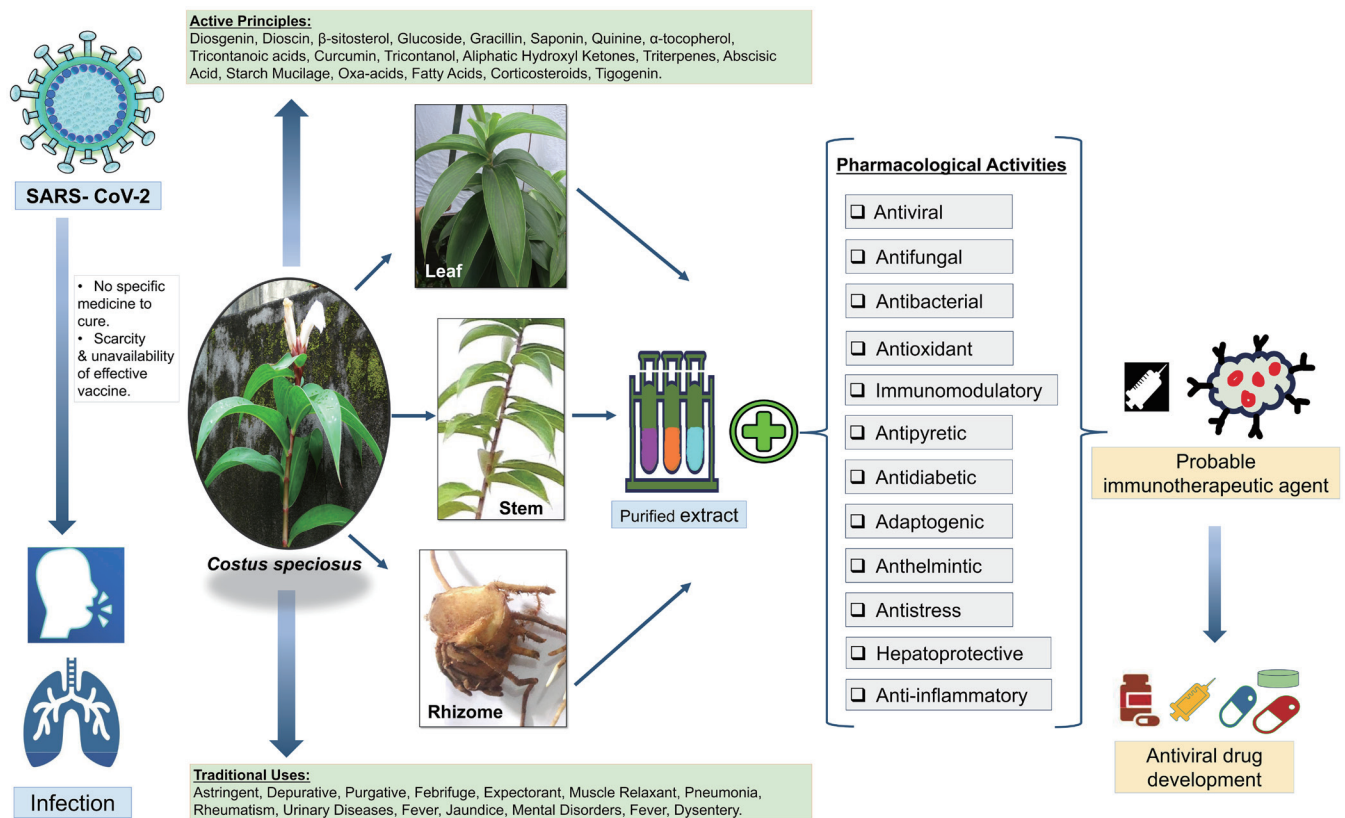


Fig. 2. Overview of cellular and molecular mechanisms of *Costus speciosus* and COVID-19.

In conclusion, the role of *C. speciosus* in combating COVID-19 is an area of great interest and potential. Continued research and clinical trials are essential to validate the efficacy of these compounds and to potentially integrate them into the broader strategy for managing and treating COVID-19. The exploration of natural products not only offers hope for new therapeutic options but also highlights the importance of biodiversity and natural resources in addressing global health challenges.

Acknowledgments

None.

Funding

This study received no specific grant from any funding agency in the public, commercial, or not-for-profit sector.

Conflict of interest

The authors have no conflict of interest related to this publication.

Author contributions

Conceptualization: AC; study design: DL; analysis and in-

terpretation of data: DL; manuscript writing: DL, AC; statistical analysis: DL; administration: DL, AC; critical revision AC; technical or material support: DL; overall supervision: AC.

Abbreviations

ACE2, angiotensin-converting enzyme 2; *C. speciosus*, *Costus speciosus*; COVID-19, coronavirus disease 2019; IL, interleukin; SARS-CoV-2, severe acute respiratory syndrome coronavirus 2.

References

- [1] Malarkannan SP, Dharumarajan P, Hariyohesh MK. A clinical study of Siddha herbal preparation – M V Kashayam for the treatment, control, and management of COVID-19. *Asian J Pharmaceut Clin Res* 2021;14(6):104–107. doi:10.22159/ajpcr.2021.v14i6.41582.
- [2] Khuntia BK, Sharma V, Qazi S, Das S, Sharma S, Raza K, et al. Ayurvedic medicinal plants against COVID-19: an in silico analysis. *Nat Prod Commun* 2021;16(11):1–9. doi:10.1177/1934578X211056753.
- [3] Kumar S, Dobos GJ, Rampp T. The Significance of Ayurvedic Medicinal Plants. *J Evid Based Complementary Altern Med* 2017;22(3):494–501. doi:10.1177/2156587216671392, PMID:27707902.
- [4] Ministry of Health and Family Welfare. The Ayurvedic Pharmacopoeia of India. Ministry of Health and Family Welfare. vol- I (III, IV, V). New Delhi: Department of AYUSH; 2008.
- [5] Deb DB. The flora of Tripura state. Vol-I, II. Dehli: Today and Tomorrows' Printers and Publishers; 1981.
- [6] Kumar V, Subramaniam B. Chromosome Atlas of flowering plants of the Indian subcontinent. vol- I, II. Dehli: Bot Surv Ind; 1986.

- [7] Hoker JD. The flora of British India. 6th edition. London: Reeve and Co. Ltd; 1894.
- [8] Tyagi BR, Gupta MM. Ploidy status and diosgenin content in *Costus speciosus* (Koen.) Sm. *Cytologia* 1987;52:41–46. doi:10.1508/cytologia.52.41.
- [9] Singh P, Khosa RL, Srivastava S, Mishra G, Jha KK, Srivastava S, et al. Pharmacognostical study and establishment of quality parameters of aerial parts of *Costus speciosus*-a well known tropical folklore medicine. *Asian Pac J Trop Biomed* 2014;4(6):486–491. doi:10.12980/APJTB.4.2014C1103, PMID:25182951.
- [10] Ariharan VN, Devi VNM, Rajakokhila M, Prasad PN. Antibacterial activity of *Costus speciosus* rhizome extract on some pathogenic bacteria. *Int J Adv Life Sci* 2012;4:24–27.
- [11] Choudhury J, Sarma BP. A review on antidiabetic property of *Costus speciosus* (Kemuka). *Int J of Allied Med Sci Clin Res* 2016;4(3):601–606. doi:10.61096/ijamscr.v4.iss3.2016.601-606.
- [12] El Far AH, Shaheen HM, Alsenosy AW, El Sayed YS, Jaouni SKA, Mousa SA. *Costus speciosus*: traditional uses, phytochemistry, and therapeutic potentials. *Pharmacogn Rev* 2018;12(23):120–127. doi:10.4103/phrev.phrev_29_17.
- [13] Al-Attas AA, El-Shaer NS, Mohamed GA, Ibrahim SR, Esmat A. Anti-inflammatory sesquiterpenes from *Costus speciosus* rhizomes. *J Ethnopharmacol* 2015;176:365–374. doi:10.1016/j.jep.2015.11.026, PMID:26593213.
- [14] Bhuyan B, Zaman K. Evaluation of hepatoprotective activity of rhizomes of *Costus speciosus* (J. Konig) Smith. *Pharmacologyonline* 2008;3:119–126.
- [15] Malabadi RB, Chalannavar RK, Meti NT, Gani RS, Vijayakumar S, Mulgund GS, et al. Insulin Plant, *Costus speciosus*: ethnobotany and pharmacological updates. *Int J Curr Res Biosci Plant Biol* 2016;3(7):151–161. doi:10.20546/ijcrbp.2016.307.021.
- [16] Sari IP, Nurrochmad A, Rahayu S. Evaluation of anti-fertility effect of aqueous extract of *Costus speciosus* (Koen.) J.E. Smith rhizome in mice. *Int J Pharmaceut Clin Res* 2016;8(5):440–444.
- [17] Vaidya M, Shingadia H. Antimicrobial activity of *Costus speciosus*. (J. Koieng) Sm. *World J Pharmaceut Res* 2020;9(2):959–963. doi:10.20959/wjpr20202-16672.
- [18] Behera A, Devi RS, Pradhan S, Biswal S, Jena PK, Biswal SK, et al. Phytochemical analysis and antioxidant potential of *Costus speciosus* L. *European J Med Plants*. 2020;31(10):64–72. doi:10.9734/EJMP/2020/v31i1030284.
- [19] Sanadhya I, Durve A, Bhot M, Varghese J, Chandra N. Evaluation of medicinal activities of *Costus speciosus*. *World J Pharm Res* 2014;3(4):623–633. doi:10.13140/RG.2.2.34278.24646.
- [20] Sulakshana G, Rani S. HPLC analysis of diosgenin in three species of *Costus*. *Int J Pharma Sci Res* 2014;5(11):747–749.
- [21] Agrawal S, Chandewar A, Tiwle R, Kochar N. Study of antidiabetic effects of different extracts from *Costus speciosus* (Koen) leaves. *IOSR J Pharma Biol Sci* 2020;15(2-III):58–66.
- [22] Swati S, Agarwal P. *Kebuka (Costus speciosus)*: a critical review. *World J Pharm Pharmaceut Sci* 2015;4(10):421–429.
- [23] Bahshwan SM, Aljehany BM. A review on the therapeutic and medicinal activities of *Costus speciosus*. *Pharmacophore* 2020;11(3):124–129.
- [24] Alhazzani W, Møller MH, Arabi YM, Loeb M, Gong MN, Fan E, et al. Surviving Sepsis Campaign: guidelines on the management of critically ill adults with Coronavirus Disease 2019 (COVID-19). *Intensive Care Med* 2020;46(5):854–887. doi:10.1007/s00134-020-06022-5, PMID:32222812.
- [25] Mohiuddin M, Alam MK, Basak SR, Hossain MK. Ethno-medico botanical study among the four indigenous communities of Bandarban, Bangladesh. *Bangladesh J Plant Taxon* 2012;19(1):45–53. doi:10.3329/bjpt.v19i1.10941.
- [26] Chaudhuri RHN, Molla HA, Pal DC, Roy B. Plants used in traditional medicine by some tribals of Jalpaiguri District, West Bengal. *Bull Bot Surv Ind* 1982;24(1-4):87–90.
- [27] Chhetri DR, Parajuli P, Subba GC. Antidiabetic plants used by Sikkim and Darjeeling Himalayan tribes, India. *J Ethnopharmacol* 2005;99(2):199–202. doi:10.1016/j.jep.2005.01.058, PMID:15894127.
- [28] Benny M. Insulin plants in garden. *Nat Prod Rad* 2004;3(5):349–350.
- [29] Nahak G, Sahu RK. Free radical scavenging activity of rhizome of *CCos-tus speciosus* (Koen) J.E. SM. *Int J Inst Pharm Life Sci* 2011;1(3):62–69.
- [30] Gupta AK, Tondon N, Sharma M. Quality Standards of Indian Medicinal Plants. VII: 48. New Delhi: Medicinal Plants Unit, Published by Ind Council Med Res; 2008.
- [31] Billore KV, Yelne MB, Dennis TJ, Choudhuri BG. Database on medicinal plants used in Ayurveda. New Delhi: Central Council for Research in Ayurveda & Siddha, Department of ISM & H, Ministry of Health & Family Welfare, Govt. of India; 2005.
- [32] Sarin YK, Bedi KL, Atal CK. *Costus speciosus* rhizome as source of diosgenin. *Curr Sci* 1974;43:569–570. doi:10.1016/j.sajb.2015.01.012.
- [33] Jayawardena N, Watawana MI, Jayathilaka RT, Waisundara VY. The Antioxidant and Starch Hydrolase Inhibitory Activity of Ten Spices in an In Vitro Model of Digestion: Bioaccessibility of Anthocyanins and Carotenoids. *Evid Based Complement Alternat Med* 2015;2015:764238. doi:10.1155/2015/764238, PMID:26693245.
- [34] Ramya R, Dharmotharan R. Qualitative and quantitative analysis of phytochemicals of *Costus speciosus*. *Int J Health Sci Res* 2015;5(12):170–176. doi:10.13140/RG.2.2.34278.24646.
- [35] Binny K, Kumar SG, Dennis T. Anti-inflammatory and antipyretic properties of the rhizome of *Costus speciosus* (Koen.) sm. *J Basic Clin Pharm* 2010;1(3):177–181. PMID:24825984.
- [36] Srivastava S, Singh P, Jha KK, Mishra G, Srivastava S, Khosa RL. Anti-inflammatory, Analgesic and Antipyretic Activities of Aerial Parts of *Costus speciosus* Koen. *Indian J Pharm Sci* 2013;75(1):83–88. doi:10.4103/0250-474X.113532, PMID:23901165.
- [37] Khan MF, Ramu A. Spectral characterization of bioactive compounds from *Costus pictus* and *Costus speciosus*. *Int J ChemTech Res* 2018;11(09):353–363. doi:10.20902/IJCTR.2018.110941.
- [38] Azam S, Ansari P, Jalil S, Ibrahim AH, Sultana N, Hossain MM, et al. Antinociceptive activity investigation of the methanolic crude extract of *Costus speciosus* in Mice. *Progr Nutri* 2016;18(4):436–442.
- [39] Verma N, Khosa RL. Effect of *Costus speciosus* and *Wedelia chinensis* on brain neurotransmitters and enzyme monoamine oxidase following cold immobilization stress. *J Pharm Sci Res* 2009;1(2):22–25.
- [40] Joseph MH, Kennett GA. Stress-induced release of 5-HT in the hippocampus and its dependence on increased tryptophan availability: an in vivo electrochemical study. *Brain Res* 1983;270(2):251–257. doi:10.1016/0006-8993(83)90598-x, PMID:6224532.
- [41] Eliza J, Daisy P, Ignacimuthu S, Duraipandian V. Normo-glycemic and hypolipidemic effect of costunolide isolated from *Costus speciosus* (Koen ex. Retz.) Sm. in streptozotocin-induced diabetic rats. *Chem Biol Interact* 2009;179(2-3):329–334. doi:10.1016/j.cbi.2008.10.017, PMID:19007766.
- [42] Revathy J, Sangamithira SP, Abdulla SS, Kumar PS. An experimental evaluation of the antidiabetic and antioxidant effect of *Costus speciosus* rhizome extract in alloxan induced albino rats. *Biosci Biotech Res Asia* 2011;8(2):789–793. doi:10.13005/bbra/936.
- [43] Kumar M, Misra A, Srivastava A, Shukla PK, Tewari LM, Srivastava S. Comparative pharmacognostical and pharmacological evaluation of *Costus speciosus* (Koen) J.E. Sm. germplasm collected from eastern ghats of India. *Pharmacog J* 2020;12(1):150–156. doi:10.5530/pj.2020.12.22.
- [44] Saraf A. Phytochemical and antimicrobial studies of medicinal plant *Costus speciosus* (Koen.) phytochemical and antimicrobial studies. *E J Chem* 2010;7(S1):S405–S413. doi:10.1155/2010/605735.
- [45] Lin P, Wang M, Wei Y, Kim T, Wei X. Coronavirus in human diseases: Mechanisms and advances in clinical treatment. *Med Comm* 2020;1(3):270–301. doi:10.1002/mco2.26, PMID:33173860.
- [46] Al-Kattan MO, Khayyat SA. Antimicrobial activity and chemical analyses of oil constituents of medicinal plant *Costus speciosus* (Koen.). *Biomed Res* 2017;28(2):734–739.
- [47] Thambi M, Shafi MP. Rhizome essential oil composition of *Costus speciosus* and its antimicrobial properties. *Int J Pharmaceut Res Allied Sci* 2015;4(1):28–32.
- [48] Srivastava S, Singh P, Jha KK, Mishra G, Srivastava S, Khosa RL. Anthelmintic activity of aerial parts of *Costus speciosus*. *Int J Green Pharm* 2011;5:325–328. doi:10.4103/0973-8258.94356.
- [49] Lijuan W, Kupittayanant P, Chudapongse N, Wray S, Kupittayanant S. The effects of wild ginger (*Costus speciosus* (Koen) Smith) rhizome extract and diosgenin on rat uterine contractions. *Reprod Sci* 2011;18(6):516–524. doi:10.1177/1933719110391278, PMID:21566

- 246.
- [50] Jahfar M, Abdul Rahim AK, Jincy A, Unnikrishnan KP. Assay of steroidal sapogenin in *Costus speciosus* rhizomes. *Asian J Chem* 2008;20(2):1382–1388.
- [51] Ferrero-Miliani L, Nielsen OH, Andersen PS, Girardin SE. Chronic inflammation: importance of NOD2 and NALP3 in interleukin-1beta generation. *Clin Exp Immunol* 2007;147(2):227–235. doi:10.1111/j.1365-2249.2006.03261.x, PMID:17223962.
- [52] Ricciotti E, Laudanski K, FitzGerald GA. Nonsteroidal anti-inflammatory drugs and glucocorticoids in COVID-19. *Adv Biol Regul* 2021;81:100818. doi:10.1016/j.jbior.2021.100818, PMID:34303107.
- [53] Bruce E, Barlow-Pay F, Short R, Vilches-Moraga A, Price A, McGovern A, et al. Prior Routine Use of Non-Steroidal Anti-Inflammatory Drugs (NSAIDs) and Important Outcomes in Hospitalised Patients with COVID-19. *J Clin Med* 2020;9(8):2586. doi:10.3390/jcm9082586, PMID:32785086.
- [54] Wong RSY. Inflammation in COVID-19: From pathogenesis to treatment. *Int J Clin Exp Pathol* 2021;14(7):831–844. PMID:34367415.
- [55] Saghazadeh A, Rezaei N. Immune-epidemiological parameters of the novel coronavirus - a perspective. *Expert Rev Clin Immunol* 2020;16(5):465–470. doi:10.1080/1744666X.2020.1750954, PMID:32237901.
- [56] Gilzad-Kohan H, Jamali F. Anti-Inflammatory Properties of Drugs Used to Control COVID-19 and their Effects on the Renin-Angiotensin System and Angiotensin-Converting Enzyme-2. *J Pharm Pharm Sci* 2020;23:259–277. doi:10.18433/jpps31346, PMID:32735768.
- [57] Bonaz B, Sinniger V, Pellissier S. Targeting the cholinergic anti-inflammatory pathway with vagus nerve stimulation in patients with Covid-19? *Bioelectron Med* 2020;6:15. doi:10.1186/s42234-020-00051-7, PMID:32743022.
- [58] Saeedi-Boroujeni A, Mahmoudian-Sani MR. Anti-inflammatory potential of Quercetin in COVID-19 treatment. *J Inflamm (Lond)* 2021;18(1):3. doi:10.1186/s12950-021-00268-6, PMID:33509217.
- [59] Gao Y, Li T, Han M, Li X, Wu D, Xu Y. Diagnostic utility of clinical laboratory data determinations for patients with the severe COVID-19. *J Med Virol* 2020;92(7):791–796. doi:10.1002/jmv.25770, PMID:32181911.
- [60] Merad M, Martin JC. Author Correction: Pathological inflammation in patients with COVID-19: a key role for monocytes and macrophages. *Nat Rev Immunol* 2020;20(7):448. doi:10.1038/s41577-020-0353-y, PMID:32488203.
- [61] Zhou Y, Fu B, Zheng X, Wang D, Zhao C, qi Y. Aberrant pathogenic GM-CSF+ T cells and inflammatory CD14+CD16+ monocytes in severe pulmonary syndrome patients of a new coronavirus. *BioRxiv* 2020. doi:10.1101/2020.02.12.945576.
- [62] Wong AY, MacKenna B, Morton CE, Schultze A, Walker AJ, Bhaskaran K, et al. Use of non-steroidal anti-inflammatory drugs and risk of death from COVID-19: an OpenSAFELY cohort analysis based on two cohorts. *Ann Rheum Dis* 2021;80(7):943–951. doi:10.1136/annrheumdis-2020-219517, PMID:33478953.
- [63] Robb CT, Goepp M, Rossi AG, Yao C. Non-steroidal anti-inflammatory drugs, prostaglandins, and COVID-19. *Br J Pharmacol* 2020;177(21):4899–4920. doi:10.1111/bph.15206, PMID:32700336.
- [64] Reyes AZ, Hu KA, Teperman J, Wampler Muskardin TL, Tardif JC, et al. Anti-inflammatory therapy for COVID-19 infection: the case for colchicine. *Ann Rheum Dis* 2021;80(5):550–557. doi:10.1136/annrheumdis-2020-219174, PMID:33293273.
- [65] Martinon F, Pétrilli V, Mayor A, Tardivel A, Tschopp J. Gout-associated uric acid crystals activate the NALP3 inflammasome. *Nature* 2006;440(7081):237–241. doi:10.1038/nature04516, PMID:16407889.
- [66] Dalbeth N, Lauterio TJ, Wolfe HR. Mechanism of action of colchicine in the treatment of gout. *Clin Ther* 2014;36(10):1465–1479. doi:10.1016/j.clinthera.2014.07.017, PMID:25151572.
- [67] Chia EW, Grainger R, Harper JL. Colchicine suppresses neutrophil superoxide production in a murine model of gouty arthritis: A rationale for use of low-dose colchicine. *Br J Pharmacol* 2008;153(6):1288–1295. doi:10.1038/bjp.2008.20, PMID:18264123.
- [68] Mittal N, Mittal R. Inhaled route and anti-inflammatory action of ivermectin: Do they hold promise in fighting against COVID-19? *Med Hypotheses* 2021;146:110364. doi:10.1016/j.mehy.2020.110364, PMID:33246694.
- [69] Xia L, Shi Y, Su J, Friedemann T, Tao Z, Lu Y, et al. Shufeng Jiedu, a promising herbal therapy for moderate COVID-19: antiviral and anti-inflammatory properties, pathways of bioactive compounds, and a clinical real-world pragmatic study. *Phytomed* 2021;85(153390):1–10.
- [70] Panossian AG, Efferth T, Shikov AN, Pozharitskaya ON, Kuchta K, Mukherjee PK, et al. Evolution of the adaptogenic concept from traditional use to medical systems: Pharmacology of stress- and aging-related diseases. *Med Res Rev* 2021;41(1):630–703. doi:10.1002/med.21743, PMID:33103257.
- [71] Panossian AG. Adaptogens in mental and behavioral disorders. *Psychiatr Clin North Am* 2013;36(1):49–64. doi:10.1016/j.psc.2012.12.005, PMID:23538076.
- [72] Panossian A, Brendler T. The Role of Adaptogens in Prophylaxis and Treatment of Viral Respiratory Infections. *Pharmaceuticals (Basel)* 2020;13(9):236. doi:10.3390/ph13090236, PMID:32911682.
- [73] Arushanian EB, Beier EV. Pineal hormone melatonin is an universal adaptogenic agent. *Usp Fiziol Nauk* 2012;43(3):82–100. PMID:23101381.
- [74] Panossian A, Seo EJ, Efferth T. Novel molecular mechanisms for the adaptogenic effects of herbal extracts on isolated brain cells using systems biology. *Phytomedicine* 2018;50:257–284. doi:10.1016/j.phymed.2018.09.204, PMID:30466987.
- [75] Ostuzzi G, Papola D, Gastaldon C, Schoretsanitis G, Bertolini F, Amadeo F, et al. Safety of Psychotropic Medications in People With COVID-19: Evidence Review and Practical Recommendations. *Focus (Am Psychiatr Publ)* 2020;18(4):466–481. doi:10.1176/appi.focus.18308, PMID:33343260.
- [76] Ugwueze CV, Ezeokpo BC, Nnolim BI, Agim EA, Anikpo NC, Onyekachi KE. COVID-19 and diabetes mellitus: the link and clinical implications. *Dubai Diabet Endocrinol J* 2020;26:69–77. doi:10.1159/000511354.
- [77] Calder PC, Dimitriadis G, Newsholme P. Glucose metabolism in lymphoid and inflammatory cells and tissues. *Curr Opin Clin Nutr Metab Care* 2007;10(4):531–540. doi:10.1097/MCO.0b013e3281e72ad4, PMID:17563475.
- [78] Sara AR, Shehata EM, Raslan M, Sabri NA. Management protocols deviation of COVID-19 in diabetic patients. Is it applicable? *Acta Sci Pharmaceut Sci* 2021;5(2):57–66. doi:10.31080/ASPS.2021.05.0747.
- [79] Gupta R, Bajpai KG, Johri S, Saxena AM. An overview of Indian novel traditional medicinal plants with antidiabetic potentials. *Afr J Tradit Complement Altern Med* 2008;5(1):1–17.
- [80] Luo SK, Hu WH, Lu ZJ, Li C, Fan YM, Chen QJ, et al. Diabetes patients with comorbidities had unfavorable outcomes following COVID-19: a retrospective study. *World J Diabet* 2021;12(10):1789–1808. doi:10.4239/wjcd.v12.i10.1789.
- [81] Sadera R, Youssef J, Ramadan A, Ahmed MH. What are the changes and burden associated with COVID-19 in diabetes management and delivery of the diabetes services? *J Endocrinol Metab* 2020;10(6):155–161. doi:10.14740/jem699.
- [82] Yang JK, Lin SS, Ji XJ, Guo LM. Binding of SARS coronavirus to its receptor damages islets and causes acute diabetes. *Acta Diabetol* 2010;47(3):193–199. doi:10.1007/s00592-009-0109-4, PMID:19333547.
- [83] Ceriello A, De Nigris V, Praticchizzo F. Why is hyperglycaemia worsening COVID-19 and its prognosis? *Diabetes Obes Metab* 2020;22(10):1951–1952. doi:10.1111/dom.14098, PMID:32463166.
- [84] Jafar N, Edriss H, Nugent K. The Effect of Short-Term Hyperglycemia on the Innate Immune System. *Am J Med Sci* 2016;351(2):201–211. doi:10.1016/j.amjms.2015.11.011, PMID:26897277.
- [85] McDonald HI, Nitsch D, Millett ER, Sinclair A, Thomas SL. New estimates of the burden of acute community-acquired infections among older people with diabetes mellitus: a retrospective cohort study using linked electronic health records. *Diabet Med* 2014;31(5):606–614. doi:10.1111/dme.12384, PMID:24341529.
- [86] Hasan SS, Kow CS, Bain A, Kavanagh S, Merchant HA, Hadi MA. Pharmacotherapeutic considerations for the management of diabetes mellitus among hospitalized COVID-19 patients. *Expert Opin Pharmacother* 2021;22(2):229–240. doi:10.1080/14656566.2020.1837114, PMID:33054481.
- [87] Bornstein SR, Rubino F, Khunti K, Mingrone G, Hopkins D, Birkenfeld AL, et al. Practical recommendations for the management of diabetes in patients with COVID-19. *Lancet Diabetes Endocrinol* 2020;8:546–550. doi:10.1016/S2213-8587(20)30152-2.

- [88] Yu B, Li C, Sun Y, Wang DW. Insulin treatment is associated with increased mortality in patients with COVID-19 and type 2 diabetes. *Cell Metabol* 2021;33:65–77. doi:10.1016/j.cmet.2020.11.014, PMID:33248471.
- [89] Ferrara F, Zavaleta E, Vitiello A, Villalobos JA, Zovi A, Langella R, et al. Retrospective observational study on the impact of the Covid-19 pandemic on the prescription of medications for the treatment of Attention Deficit/Hyperactivity Disorder. Comparison of a European and an American cohort. *Riv Psichiatr* 2023;58(6):284–292. doi:10.1708/4143.41408, PMID:38032032.
- [90] Singh AK, Khunti K. Assessment of risk, severity, mortality, glycemic control and antidiabetic agents in patients with diabetes and COVID-19: A narrative review. *Diabetes Res Clin Pract* 2020;165:108266. doi:10.1016/j.diabres.2020.108266, PMID:32533989.
- [91] Lin L, Lu L, Cao W, Li T. Hypothesis for potential pathogenesis of SARS-CoV-2 infection—a review of immune changes in patients with viral pneumonia. *Emerg Microbes Infect* 2020;9(1):727–732. doi:10.1080/22221751.2020.1746199, PMID:32196410.
- [92] Zhu X, Ge Y, Wu T, Zhao K, Chen Y, Wu B, et al. Co-infection with respiratory pathogens among COVID-2019 cases. *Virus Res* 2020;285(2020):1–6. doi:10.1016/j.virusres.2020.198005, PMID:32408156.
- [93] Mustapha A, Nikau J, Isa T. COVID-19 and antibiotic resistance: parallel pandemics and different intercessions. *Microb Infect Dis* 2021;2(1):15–24.
- [94] Feldman C, Anderson R. The role of co-infections and secondary infections in patients with COVID-19. *Pneumonia (Nathan)* 2021;13(1):5. doi:10.1186/s41479-021-00083-w, PMID:33894790.
- [95] Sharifipour E, Shams S, Esmkhani M, Khodadadi J, Fotouhi-Ardakani R, Koohepaei A, et al. Evaluation of bacterial co-infections of the respiratory tract in COVID-19 patients admitted to ICU. *BMC Infect Dis* 2020;20(646):1–7. doi:10.1186/s12879-020-05374-z, PMID:32873235.
- [96] Silva LN, Mello TP, Ramos LS, Branquinha MH, Roudbary M, Santos ALS. Fungal infections in COVID-19-positive patients: A lack of optimal treatment options. *Curr Topics Med Chem* 2020;20(22):1951–1957. doi:10.2174/15680266202200917110102, PMID:33040728.
- [97] Yang X, Yu Y, Xu J, Shu H, Xia J, Liu H, et al. Clinical course and outcomes of critically ill patients with SARS-CoV-2 pneumonia in Wuhan, China: a single-centered, retrospective, observational study. *Lancet Respir Med* 2020;8(5):475–481. doi:10.1016/S2213-2600(20)30079-5.
- [98] Kameshwaran S, Sriram N, Darla R, Manimekalai P, Dhanalakshmi M. Symptoms and treatment strategy of black fungus in COVID-19 patients. *Int J Pharm Clin Res* 2021;5(2):59–62.
- [99] Raslan M, Eslam MS, Sara AR, Nagwa AS. Antimicrobial resistance and second wave of COVID-19: will it impose management protocols deviation? *Ann Pharmacol Toxicol* 2020;1(1:1001):1–3.
- [100] Mustafa L, Tolaj I, Baftiu N, Fejza H. Use of antibiotics in COVID-19 ICU patients. *J Infect Dev Ctries* 2021;15(4):501–505. doi:10.3855/jidc.14404, PMID:33956649.
- [101] Mehta P, Chakraborty A, Andrabi S. W. et al. COVID-19 vaccination does not affect male sexual functions. *Reprod Biol Endocrinol* 2023;21:3. doi:10.1186/s12958-022-01052-8.
- [102] Yavuz SS, Ünal S. Antiviral treatment of COVID-19. *Turk J Med Sci* 2020;50:611–619. doi:10.3906/sag-2004-145, PMID:32293834.
- [103] Sieswerda E, Boer MGJ, Bonten MMJ, Boersma WG, Jonkers RE, Aleva RM, et al. Recommendations for antibacterial therapy in adults with COVID-19—An evidence based guideline. *Clin Microbiol Infect* 2021;27:61–66. doi:10.1016/j.cmi.2020.09.041, PMID:33010444.
- [104] Rawson TM, Moore LSP, Zhu N, Ranganathan N, Skolimowska K, Gilchrist M, et al. Bacterial and fungal coinfection in individuals with Coronavirus: a rapid review to support COVID-19 antimicrobial prescribing. *Clin Infect Dis* 2020;71(9):2459–2468. doi:10.1093/cid/ciaa530.
- [105] Instiaty, Darmayani IGAAPS, Marzuki JE, Angelia F, William, Siame A, et al. Antiviral treatment of COVID-19: a clinical pharmacology narrative review. *Med J Indones* 2020;29:332–345. doi:10.13181/mji.rev.204652.
- [106] Sanders JM, Monogue ML, Jodlowski TZ, Cutrell JB. Pharmacologic Treatments for Coronavirus Disease 2019 (COVID-19): A Review. *JAMA* 2020;323(18):1824–1836. doi:10.1001/jama.2020.6019, PMID:32282022.
- [107] Ashburn TT, Thor KB. Drug repositioning: identifying and developing new uses for existing drugs. *Nat Rev Drug Discov* 2004;3(8):673–683. doi:10.1038/nrd1468, PMID:15286734.
- [108] Salim FA, Diab HA, Hmedan AK, Dhidah HNED, Baayo RE, Hussain MS. A study of anti-bacterial, anti-fungal activities of ethanolic and aqueous extracts of *Costus speciosus*. *Pharmaceut Chem J* 2019;6(1):11–18.
- [109] Hsu J. How covid-19 is accelerating the threat of antimicrobial resistance. *BMJ* 2020;369:m1983. doi:10.1136/bmj.m1983, PMID:32423901.
- [110] Langford BJ, So M, Raybardhan S, Leung V, Westwood D, MacFadden DR, et al. Bacterial co-infection and secondary infection in patients with COVID-19: a living rapid review and meta-analysis. *Clin Microbiol Infect* 2020;26:1622–1629.
- [111] Tarighi P, Eftekhari S, Chizari M, Sabernavaei M, Jafari D, Mirza-beigi P. A review of potential suggested drugs for coronavirus disease (COVID-19) treatment. *Eur J Pharmacol* 2021;895:173890. doi:10.1016/j.ejphar.2021.173890, PMID:33482181.
- [112] Siles-Lucas M, González-Miguel J, Geller R, Sanjuan R, Pérez-Arévalo J, Martínez-Moreno Á. Potential Influence of Helminth Molecules on COVID-19 Pathology. *Trends Parasitol* 2021;37(1):11–14. doi:10.1016/j.pt.2020.10.002, PMID:33153921.
- [113] Suba Z. Prevention and therapy of COVID-19 via exogenous estrogen treatment for both male and female patients. *J Pharm Pharm Sci* 2020;23(1):75–85. doi:10.18433/jpps31069, PMID:32324533.
- [114] Stelzig KE, Canepa-Escaro F, Schilliro M, Berdnikovs S, Prakash YS, Chiarella SE. Estrogen regulates the expression of SARS-CoV-2 receptor ACE2 in differentiated airway epithelial cells. *Am J Physiol Lung Cell Mol Physiol* 2020;318(6):L1280–L1281. doi:10.1152/ajplung.00153.2020, PMID:32432918.
- [115] Wang H, Sun X, VonCannon JL, Kon ND, Ferrario CM, Groban L. Estrogen receptors are linked to angiotensin-converting enzyme 2 (ACE2), ADAM metalloproteinase domain 17 (ADAM-17), and transmembrane protease serine 2 (TMPRSS2) expression in the human atrium: insights into COVID-19. *Hypertension Res* 2021;44:882–884. doi:10.1038/s41440-021-00626-0, PMID:33536584.
- [116] Stadio AD, Volpe AD, Ralli M, Ricci G. Gender differences in COVID-19 infection. The estrogen effect on upper and lower airways. Can it help to figure out a treatment? *Eur Rev Med Pharmacol Sci* 2020;24:5195–5196.
- [117] Al-kuraishy HM, Al-Gareeb AI, Faidah H, Al-Maiahy TJ, Cruz-Martins N, Batiha GES. The looming effects of estrogen in COVID-19: A rocky rollout. *Front Nutri* 2021;8:1–8. doi:10.3389/fnut.2021.649128, PMID:33816542.
- [118] Zhu J, Ji P, Pang J, Pang J, Zhong Z, Li H, He C, et al. Clinical characteristics of 3062 COVID-19 patients: a meta-analysis. *J Med Virol* 2020;92(10):1902–1914. doi:10.1002/jmv.25884, PMID:32293716.
- [119] Steiner AA. Should we let fever run its course in the early stages of COVID-19? *J R Soc Med* 2020;113(10):407–409. doi:10.1177/0141076820951544, PMID:32930066.
- [120] Ma LL, Liu HM, Luo CH, He YN, Wang F, Huang HZ, et al. Fever and antipyretic supported by traditional chinese medicine: A multi-pathway regulation. *Frontiers Pharmacol* 2021;12(583279):1–21. doi:10.3389/fphar.2021.583279, PMID:33828481.



Potentiality of Resveratrol in Mitigating Exercise-Induced Inflammation - A Bioinformatic Study on Interleukin-6 (IL-6) in Athletes

Arijit Chakraborty¹, Debasree Lodh² and Surajit Bhattacharjee^{3*}

¹Department of Sports Physiology and Nutrition, National Sports University, India

²Department of Botany, Holy Cross College, India

³Department of Biological Sciences, Prachya Bharati Higher Secondary School, India

*Corresponding author: Surajit Bhattacharjee, Department of Biological Sciences, Prachya Bharati Higher Secondary School, Agartala, Tripura, India-799007; email:surajit.hptu@gmail.com, ORCID: 0000-0003-3877-3044

Research Article

Volume 2 Issue 1

Received Date: March 14, 2024

Published Date: April 02, 2024

DOI: 10.23880/oajksm-16000111

Abstract

Background: Athletes, engaging in vigorous exercise, confront elevated reactive oxygen species (ROS) and inflammation. Dietary antioxidants, abundant in diverse foods, offer protection. Resveratrol, a potent polyphenol from grapes and berries, explores its anti-inflammatory potential and mechanism through in-silico analysis in athletes.

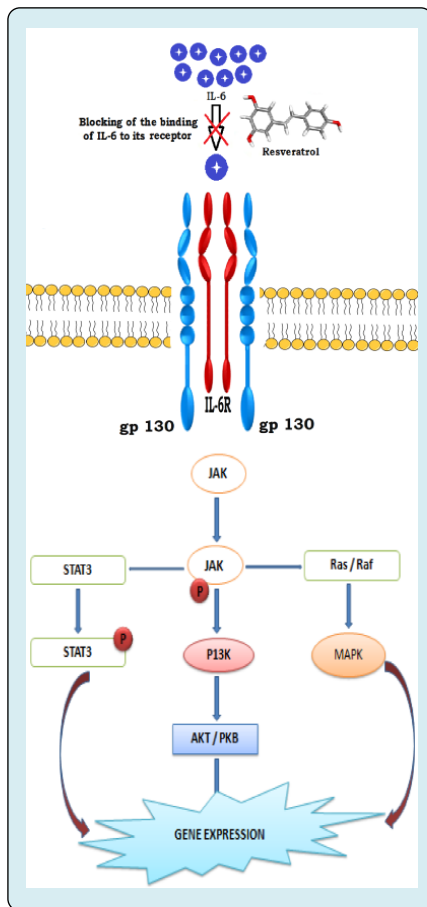
Method: Initial steps involved IL-6 data retrieval (PDB ID 1alu), receptor preparation, and ligand selection (Resveratrol, CID 445154). IL-6 receptor binding site identification utilized literature and PyMol. Molecular docking was facilitated by AutoDock, validated through re-docking and overlay methods. Lead molecule selection in in silico virtual screening was based on binding energy (-5 to -15 kcal/mol). The evaluation concluded with interaction assessment and binding affinity calculation.

Result and Discussion: The study utilized IL-6 from the Protein Data Bank. Resveratrol was prepared for molecular docking. Docking outcomes showed optimal fit and interaction of resveratrol with IL-6, forming three bonds and exhibiting a low binding energy of -5.2 kcal/mol. The research addressed exercise-induced inflammation, emphasizing IL-6's role. Bioinformatics and molecular docking provided insights into IL-6 binding. Resveratrol demonstrated a potential inhibitory effect on IL-6 action, presenting a promising avenue for anti-inflammatory intervention in athletes.

Conclusion: Exploring resveratrol's anti-inflammatory potential on IL-6, our study used molecular docking, suggesting its protective effects in athletes. Ongoing research is vital for validation and broader implications.

Keywords: Exercise; Inflammation; Resveratrol; Interleukin-6 (IL-6); Bioinformatics

Graphical Abstract



Abbreviations: PDB: Protein Data Bank; ROS: Reactive Oxygen Species.

Introduction

Vigorous participation in intense physical activity makes athletes more susceptible to heightened levels of circulating reactive oxygen species (ROS) in the body and is contingent on the mode, intensity, and duration of exercise [1]. A solitary session of intense exercise is sufficient to generate substantial amounts of ROS, leading to increased levels of inflammatory markers. Inflammation is considered as a complex biological response of body tissues to harmful stimuli, such as pathogens, damaged cells, or irritants. It is a protective mechanism that involves immune cells, blood vessels, and molecular mediators. The purpose of inflammation is to eliminate the initial cause of cell injury, clear out damaged cells and tissues, and initiate tissue repair. Exercise, especially intense or prolonged physical activity, can cause micro-damage to muscle fibers, leading to inflammation. While this is a natural part of the muscle repair and strengthening process, excessive inflammation can delay recovery, leading to prolonged soreness and

reduced muscle function and proper management helps in faster recovery and repair of these tissues. While exercising, active muscle fibers exhibit oxygen consumption rates 200 times higher than during periods of rest, resulting in the production of inflammatory markers [2,3]. Various potential explanations exist for the diverse outcomes observed in relation to exercise and its effects on proinflammatory and inflammation-responsive cytokines and there has been reported an elevation in interleukin-6 (IL-6) concentration of 50-folds after the end of a marathon run in the participants [4]. Earlier findings have shown a connection between dietary interventions, such as the consumption of antioxidant-rich foods, and decreased levels of inflammatory mediators in athletes, both during periods of rest and after exercise [5]. This discovery motivated scientists to explore alternative foods that enhance athletes' oxidative stress and diminish their inflammatory markers.

Antioxidants, abundant in diverse foods, act as vital defenders against oxidative stress caused by free radicals [6-8]. Fruits like berries and citrus, alongside vegetables such as spinach and kale, are rich sources. Nuts, seeds, and oils, coupled with beverages like green tea, offer additional avenues to bolster antioxidant intake [9]. Various plant products, vitamins and antioxidants show different mitigating roles of various complications [10-12]. For athletes, the anti-inflammatory effects of antioxidants hold particular significance. Strenuous physical activity elevates oxidative stress, leading to inflammation. Antioxidants play a crucial role in mitigating this inflammatory response, supporting athletes in recovery and injury prevention [13]. By incorporating antioxidant-rich foods, athletes may experience reduced inflammatory markers, promoting overall health. Beyond their anti-inflammatory impact, antioxidants contribute to cardiovascular well-being, fostering heart health through improved blood flow and oxidative damage reduction [14]. This dual benefit is especially pertinent for athletes aiming to optimize performance and recovery. While a balanced diet is the primary means of antioxidant intake, targeted consumption of these compounds emerges as a strategic approach for athletes seeking to enhance their athletic capabilities and mitigate the inflammatory effects associated with intense training.

Resveratrol, a potent polyphenol, is found in certain foods like grapes, red wine, and berries. Known for its antioxidant properties, resveratrol has gained attention for potential health benefits [15]. It demonstrates anti-inflammatory effects, contributing to cardiovascular health by improving blood flow and reducing oxidative stress. Additionally, studies suggest its potential in supporting longevity and cognitive function [16]. While available in supplement form, obtaining resveratrol through a balanced diet remains ideal for maximizing its positive impact on

overall health. Moreover, numerous interventions have utilized these dietary components to explore their influence on inflammatory markers. To date, there has been no research investigating the anti-inflammatory potential of resveratrol and its mechanism of interaction in athletes. Hence, the present study seeks to assess the impact of resveratrol on IL-6 in athletes through an in-silico analysis, exploring its mechanism of action.

Materials and Methods

Sequence Retrieval

The sequence and structure of IL-6 were obtained from the Protein Data Bank (PDB) with the PDB ID 1alu. The receptor protein was readied by eliminating the ligand and water from the active site and introducing polar hydrogens [17].

Compound Preparation

3D conformer of resveratrol (C₁₄H₁₂O³), PubChem CID 445154 was downloaded and used as a ligand in this study.

Identification of Binding Site

Exploring scientific literature, researching articles, and utilizing databases are common methods for identifying the ligand binding site of the human IL-6 protein. The IL-6 receptor binding site was discerned through the utilization of PyMol, protein visualization software [18].

Molecular docking

Following the methodology established in our previous work i.e. Bhattacharjee S, et al. [19] molecular docking was undertaken using IL-6 (PDB ID 1alu). The macromolecular file preparation involved adding polar hydrogens and introducing charges via ADT with default Kollman charges, automatically incorporating Kollman charges for a peptide. Protein parameters were integrated, saving files as 1alu.pdbqt. The ligand, resveratrol (PubChem CID 445154), was converted to PDB format using Open Babel 2.3.2a, loaded into ADT, and configured as instructed, resulting in ligand.pdbqt. Creating a grid with sufficient space for unrestricted ligand rotation Wang S, et al. [18], parameters were stored in molecule.gpf, and a new file, 1alu.gpf, was saved. Autogrid4 generated maps, producing 1alu.glg during the Run. Docking Parameter File creation involved reading macromolecular pdbqs and ligand.out.pdbq files. AutoDock, using the Lamarckian genetic algorithm, initiated the docking task. Terminal access to .dlg files recorded final docked energy, Gibbs free energy, and inhibition constant for each of the 500 runs, ensuring optimal results.

Validation of Docking Approach

The diverse docking parameters were confirmed through individual re-docking of a crystallized ligand molecule against the IL-6 receptor. Validation of the molecular docking simulation technique was conducted using the overlay method and chemical similarity assessment [20].

Computer-Based Screening

After validating the docking approach, an *in silico* virtual screening was carried out through molecular docking simulations.

Evaluation of Virtual Screening Results

After conducting molecular docking simulations, lead molecules were selected based on the lowest binding energy within the specified range of -5 to -15 kcal/mol. The assessment of results emphasized hydrophilic and lipophilic interactions among binding residues within the active ligand binding site of the protein and the ligand. The calculation of the ligand's binding affinity for a specific target was performed as illustrated in the following equation:

$$K_i = e[\Delta G/RT]$$

Here, ΔG represents the change in free energy upon binding, R denotes the gas constant, and T signifies the temperature in Kelvin.

Results

Chosen and Prepped Macromolecule

The human IL-6 (PDB ID: 1alu), obtained from the Protein Data Bank, comprises a single protein chain consisting of 157 amino acids. The three-dimensional structure model of IL-6 is depicted in Figure 1. After the end of the processing of the protein molecule, it was saved in *.pdbqt format using AutoDock software.

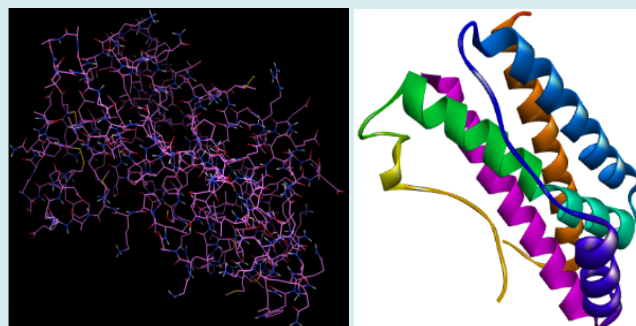
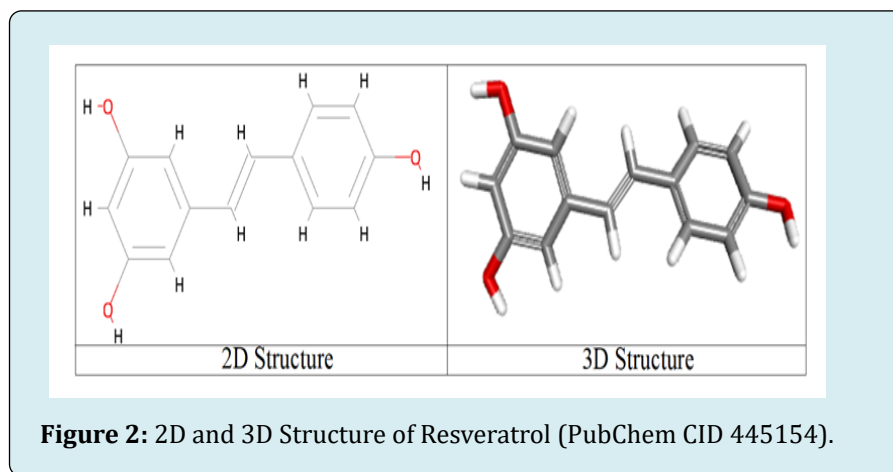


Figure 1: Three-dimensional (3D) structure model of IL-6 (1-alu) acquired from the RCSB Protein Data Bank.

The Ligand Primed For Molecular Docking

The ligand molecule contained three rotatable bonds, all of which were maintained in their rotatable state.

Subsequently, the prepared ligand was stored in *.pdbqt format. In Figure 2 it is shown that the resveratrol molecule contains 12 atoms of hydrogen with 3 atoms of oxygen.

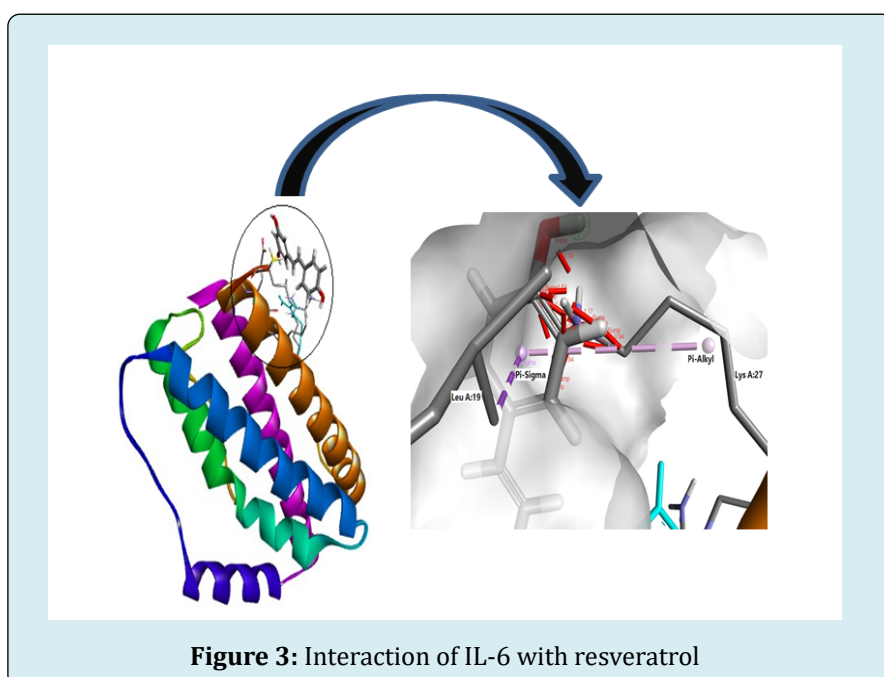


Protein	x-D	y-D	z-D	x center	y center	z center
1-alu	122.89	102.65	43.69	40.096	40.079	40.038

Table 1: Coordinates utilized for the preparation of the grid box.

Protein	Ligand	Interacting residues	Types of Bonds	Binding energy (kcal/mol)
1-alu	Resveratrol	Glu A:23	van der Waals	-5.2
		Leu A:19	Pi-Sigma	
		Lys A:27	Pi-Alkyl	

Table 2: Docking Outcomes of the Ligand Bound to the Human IL-6 Receptor.



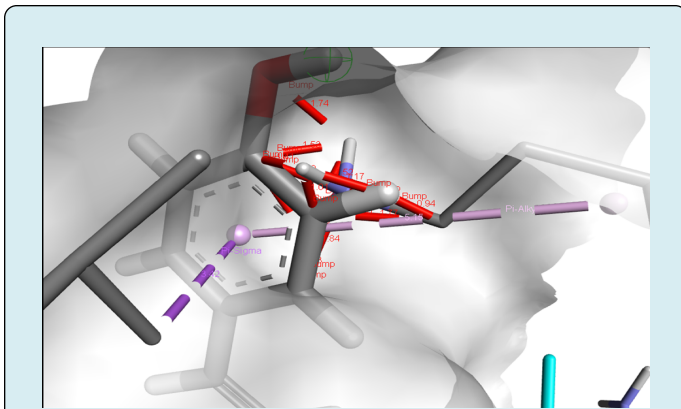


Figure 4: Types of bonds formed with their distance in IL-6 protein with resveratrol.

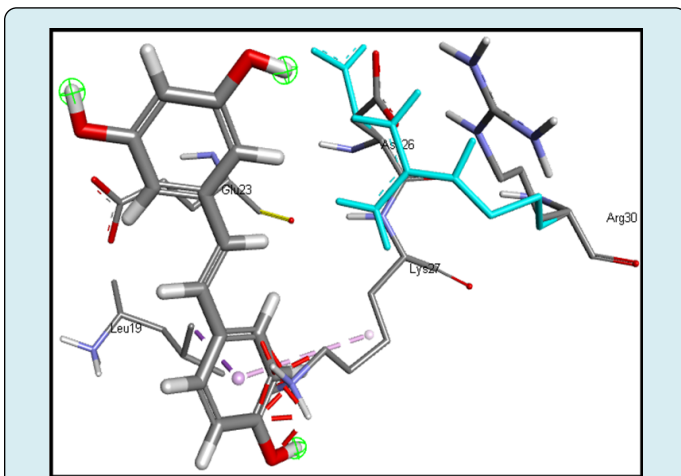


Figure 5: Interaction of the amino acids and their number with resveratrol.

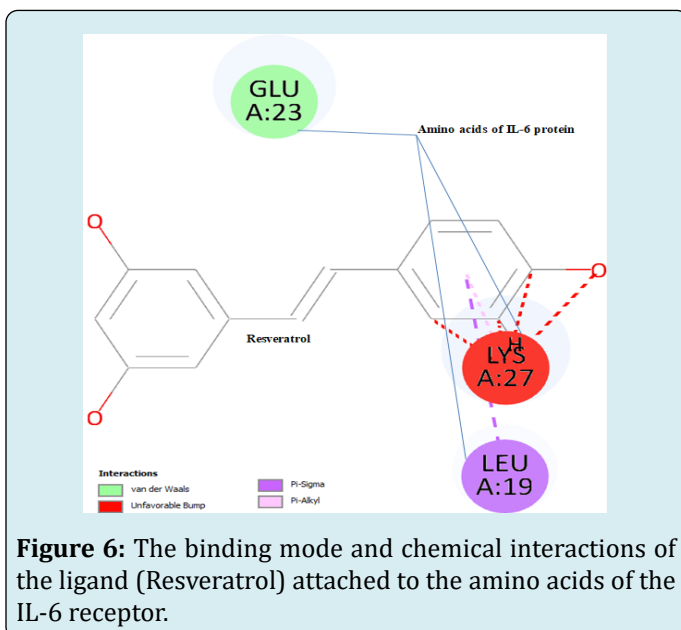


Figure 6: The binding mode and chemical interactions of the ligand (Resveratrol) attached to the amino acids of the IL-6 receptor.

Discussion

Heavy exercise has long been associated with numerous health benefits, including improved cardiovascular health and enhanced physical fitness. However, recent research has shed light on a potential downside to intense physical activity - the increased levels of Interleukin-6 (IL-6) among sports persons. IL-6 is a cytokine that plays a crucial role in the body's inflammatory response [21]. While moderate exercise is known to have anti-inflammatory effects, heavy exercise can lead to an upsurge in IL-6 levels, contributing to inflammatory problems [22]. The paradox of exercise-induced inflammation lies in the delicate balance between the positive effects of moderate exercise and the potential drawbacks of excessive physical exertion [23]. High levels of IL-6 can trigger an inflammatory response that may manifest as muscle soreness, joint pain, and even systemic inflammation [24]. This has significant implications for athletes and fitness enthusiasts, as chronic inflammation is associated with various health issues, including an increased risk of chronic diseases [25,26]. When there is an excessive increase in cytokine production, it leads to a phenomenon known as a cytokine storm. This heightened inflammatory reaction may contribute to the development of multiple organ dysfunction syndrome as well as inflammatory response syndrome [27,28]. In response to this emerging challenge, the scientific community has turned to innovative approaches, particularly bioinformatic applications, to unravel the complex interplay between exercise, IL-6, and inflammation. Bioinformatics leverages computational tools and techniques to analyze vast amounts of biological data, facilitating a deeper understanding of molecular pathways and interactions [29,30]. Researchers are now using bioinformatics to explore the intricate mechanisms through which heavy exercise influences IL-6 levels and subsequent inflammatory responses [29,31]. This multidisciplinary approach enables the identification of potential targets for intervention, paving the way for the development of anti-inflammatory drugs tailored to mitigate the negative consequences of intense physical activity.

The integration of bioinformatics in sports medicine and pharmaceutical research represents a promising avenue for precision medicine [32]. The preeminent computational method for probing protein active sites and ligand conformation within the targeted protein's active pocket is molecular docking. The scrutinized docked complexes, stemming from these studies, were evaluated for binding affinities (Kcal/mol), molecular interactions, and bonding interactions. The lowest binding energy value serves as a key indicator of the ideal conformational position of the ligand within the active region of the targeted protein IL-6 [33]. By deciphering the molecular intricacies of exercise-induced inflammation, scientists aim to develop personalized

interventions that optimize the health benefits of exercise while minimizing the associated inflammatory risks. This holistic approach not only benefits athletes striving for peak performance but also contributes to our broader understanding of the intricate relationship between physical activity, inflammation, and overall health. As we delve deeper into the realms of bioinformatics, the quest for anti-inflammatory drugs tailored to the needs of sports persons takes on a more informed and targeted trajectory.

In our study we have found that, resveratrol exhibited a perfect fit within the IL-6 binding site, demonstrating the lowest binding energy of -5.2 kcal/mol in the results after (Table 2). According to Figures 5, 6 and Table 2, resveratrol forms 3 bonds namely, van der Waals, Pi-sigma and Pi-Alkyl bonds with Glu A:23, Leu A:19 and Lys A:27 respectively. So, it could be possible mechanisms for the inhibition of IL-6 action the ligand compound. A study has shown that quercetin could demonstrably bind to the IL-6R by partially (30%-35%) blocking IL-6 binding. It has been reported that the lys and glu residues provoke a complete loss of ligand binding to the IL-6R. Hence, the interplay among quercetin, catechin, gallic acid, and IL-6R is expected to impede IL-6 ligand binding to the receptor through modifications in receptor affinity or protein conformation. According to Chu M, et al. [34,35] found that resveratrol is potentially effective in diminishing or regulating elevated IL-6 levels linked to physical activity. However, its impact on IL-6 changes related to factors like age might be limited. The data presented suggests that resveratrol exhibits anti-inflammatory and protective effects during exercise by reducing IL-6 levels. Nevertheless, further studies in the future are necessary to validate this hypothesis. The results of the current study propose that disrupting interactions within IL-6 signaling pathways or the IL-6R could interrupt the signaling associated with inflammatory diseases triggered by increased IL-6 expression. Additionally, this study shares similarity with the findings of Ezaouine A, et al. [29]. This mechanism could provide a potential therapeutic approach for addressing inflammatory bowel diseases.

Conclusion

Our study delved into the potential anti-inflammatory impact of resveratrol on IL-6 in athletes through in-silico analysis. Molecular docking revealed resveratrol's optimal fit within the IL-6 binding site, forming three key bonds. Resveratrol may mitigate IL-6 levels during exercise, suggesting protective effects. Ongoing investigations are crucial for validating and expanding on these insights, contributing to bioinformatics in sports medicine for inflammation management in intense physical activity.

Conflict Of Interest Declaration: The authors declare no

conflicts of interest.

Funding: Nil.

References

1. Gomez Cabrera MC, Viña J, Ji LL (2016) Role of Redox Signaling and Inflammation in Skeletal Muscle Adaptations to Training. *Antioxidants* 5(4): 48.
2. Deaton CM, Marlin DJ (2003) Exercise-associated Oxidative Stress. *Clini. Tech. Equine Prac* 2(3): 278-291.
3. Mazani M, Nemati A, Amani M, Haedari K, Mogadam RA, and et al. (2018) The effect of probiotic yoghurt consumption on oxidative stress and inflammatory factors in young females after exhaustive exercise. *J Pak Med Assoc* 6(12): 1748-1754.
4. Pedersen BK, Hoffman-Goetz L (2000) Exercise and the immune system: regulation, integration, and adaptation. *Physiological reviews* 8(3): 1055-1081.
5. Koivisto AE, Olsen T, Paur I, Paulsen G, Bastani NE et al. (2019) Effects of antioxidant-rich foods on altitude-induced oxidative stress and inflammation in elite endurance athletes: A randomized controlled trial. *PLoS one* 1(6): e0217895.
6. Sarkar C, Bhattacharjee S, Pal S (2013) Mitigating role of folic acid and vitamin B12 against sodium arsenite induced oxidative stress in rat testis. *Journal of Applied Bioscience* 39(1):16-23.
7. Bhattacharjee S, Pal S (2014) Antilipidemic and cardioprotective effects of vitamin B12 and folic acid against arsenic toxicity. *IJPCBS* 4(2): 353-360.
8. Abdali D, Samson SE, Grover AK (2015) How effective are antioxidant supplements in obesity and diabetes? *Medical principles and practice.* 24(3): 201-215.
9. Lobo V, Patil A, Phatak A, Chandra N (2010) Free radicals, antioxidants and functional foods: Impact on human health. *Pharmacognosy reviews* 8(4): 118-126.
10. Bhattacharjee S, Pal S (2022) Arsenic- induced oxidative stress in cardiac tissue of rats: synergistic effects of folic acid and vitamin B12. *Challenges and Advances in Pharmaceutical Research* 8: 49-63.
11. Bhattacharjee S (2023) Applications of Laportea interrupta as a traditional therapeutic agent by the tribes of Tripura and it's potentiality in pharmaceuticals. *International Journal of Pharmaceutical Sciences and Research* 14(8): 3728-3741.

12. Yasmin R, Gogai S, Bora J, Chakraborty A, Dey S, et al. (2023) Nobel insight into the cellular and molecular signalling pathways of Hibiscus sabdariffa on cancer prevention: a review. *Journal of Cancer Prevention* 28(2): 77-92.
13. Clemente-Suárez VJ, Bustamante-Sanchez Á, Mielgo-Ayuso J, Martínez-Guardado I, Martín-Rodríguez, A et al. (2023) Antioxidants and Sports Performance. *Nutrients*, 15(10): 2371.
14. Bojarczuk A, Dzitkowska-Zabielska M (2022) Polyphenol Supplementation and Antioxidant Status in Athletes: A Narrative Review. *Nutrients* 15(1):158.
15. Koushki M, Amiri-Dashatan N, Ahmadi N, Abbaszadeh HA, Rezaei-Tavirani M (2018) Resveratrol: A miraculous natural compound for diseases treatment. *Food science & nutrition* 6(8): 2473-2490.
16. Csiszar A (2011) Anti-inflammatory effects of resveratrol: possible role in prevention of age-related cardiovascular disease. *Annals of the New York Academy of Sciences* 1215(1): 117-122.
17. Somers W, Stahl M, Seehra JS (1997) 1.9 A crystal structure of interleukin 6: implications for a novel mode of receptor dimerization and signaling. *The EMBO journal*, 16(5): 989-997.
18. Wang S, Shi M, Fang L, Xu S, Wang C, et al. (2019) Design of dual inhibitors of human TNF- α and IL-6 with potentials for the treatment of rheumatoid arthritis. *Tropical Journal of Pharmaceutical Research* 18(11): 2305-2312.
19. Bhattacharjee S, Chakraborty S, Sharma A, Chakraborty A, Das PK, et al. (2024) Molecular Insights into the Interaction of Vitamin C (Ascorbic Acid) with Glutathione Peroxidase: A Comprehensive Computational Study. *Med Anal Chem Int J* 8(1): 000188.
20. Mujwar S, Pardasani KR (2015) Prediction of riboswitch as a potential drug target and design of its optimal inhibitors for Mycobacterium tuberculosis. *Int J Comput Biol Drug Des* 8(4): 326-347.
21. Docherty S, Harley R, McAuley JJ, Crowe LAN, Pedret C, Kirwan, et al. (2022). The effect of exercise on cytokines: implications for musculoskeletal health: a narrative review. *BMC sports science, medicine & rehabilitation* 14(1): 5.
22. Cerqueira É, Marinho DA, Neiva HP, Lourenço O (2020) Inflammatory Effects of High and Moderate Intensity Exercise-A Systematic Review. *Frontiers in physiology* 10: 1550.
23. El Assar M, Álvarez-Bustos A, Sosa P, Angulo J, Rodríguez-Mañas L (2022) Effect of Physical Activity/Exercise on Oxidative Stress and Inflammation in Muscle and Vascular Aging. *International journal of molecular sciences* 23(15): 8713.
24. Sebba A (2021) Pain: A Review of Interleukin-6 and Its Roles in the Pain of Rheumatoid Arthritis. *Open access rheumatology : research and reviews* 13: 31-43.
25. Nash D, Hughes MG, Butcher L, Aicheler R, Smith, et al. (2023) IL-6 signaling in acute exercise and chronic training: Potential consequences for health and athletic performance. *Scandinavian journal of medicine & science in sports*, 33(1), 4-19.
26. Tanaka T, Narazaki M, Kishimoto T (2014) IL-6 in inflammation, immunity, and disease. *Cold Spring Harbor perspectives in biology* 6(10): a016295.
27. Kellum JA, Kong L, Fink MP, Weissfeld LA, Yealy DM, et al. (2007) Understanding the inflammatory cytokine response in pneumonia and sepsis: results of the Genetic and Inflammatory Markers of Sepsis (GenIMS) Study. *Archives of internal medicine* 167(15): 1655-1663.
28. Jaffer U, Wade RG, Gourlay T (2010) Cytokines in the systemic inflammatory response syndrome: a review. *HSR proceedings in intensive care & cardiovascular anesthesia* 2(3): 161-175.
29. Ezaouine A, Salam MR, Nouadi B, Anachad O, Messal ME, et al. (2022) In Silico Prediction of the Bioactive Profile and Metabolites of Satureja nepeta in Diseases Related to the Excessive Production of Interleukin-6. *Bioinformatics and biology insights* 16.
30. Rakhecha B, Agnihotri P, Dakal TC, Saquib M, Monu, et al. (2022) Anti-inflammatory activity of nicotine isolated from Brassica oleracea in rheumatoid arthritis. *Bioscience reports* 42(4): BSR20211392.
31. Morettini M, Palumbo MC, Bottiglione A, Danieli A, Del Giudice S, et al. (2024) Glucagon-like peptide-1 and interleukin-6 interaction in response to physical exercise: An in-silico model in the framework of immunometabolism. *Computer methods and programs in biomedicine* 245: 108018.
32. Marques L, Costa B, Pereira M, Silva A, Santos J, et al. (2024) Advancing Precision Medicine: A Review of Innovative In Silico Approaches for Drug Development, Clinical Pharmacology and Personalized Healthcare. *Pharmaceutics* 16(3): 332.
33. Malik A, Naz A, Ahmad S, Hafeez M, Awan FM, et al. (2021)

Inhibitory Potential of Phytochemicals on Interleukin-6-Mediated T-Cell Reduction in COVID-19 Patients: A Computational Approach. *Bioinformatics and biology insights* 15: 11779322211021430.

34. Chu M, Tsang MS, He R, Lam CW, Quan ZB, et al. (2020) The Active Compounds and Therapeutic Mechanisms of Pentaherbs Formula for Oral and Topical Treatment

of Atopic Dermatitis Based on Network Pharmacology. *Plants (Basel, Switzerland)* 9(9): 1166.

35. Vafae R, Hatamabadi H, Soori H, Hedayati M (2019) The Impact of Resveratrol Supplementation on Inflammation Induced by Acute Exercise in Rats: Il6 Responses to Exercise. *Iranian journal of pharmaceutical research: IJPR* 18(2): 772-784.



China Petroleum Processing and Petrochemical Technology

[HOME](#) [ABOUT](#) [LOGIN](#) [SEARCH](#) [CURRENT](#) [ARCHIVES](#) [ANNOUNCEMENTS](#) [SUBMISSION](#)

Home > Archives > Volume 23, Issue 2, July December-2023

Volume 23, Issue 2, July December-2023

Table of Contents

Articles

ASSESSING THE IMPACTS OF CLIMATE CHANGE ON HYDROPOWER GENERATION AND THE POWER SECTOR IN NIGERIA

George Mmadubueze Okoye, Yousef Kassem, Hüseyin Gökçekuş

PDF

EVALUATION OF MECHANICAL PROPERTIES OF POLYMER COMPOSITES PROCESSED BY 3D PRINTING

Deepak Kumar B N1, Mahesh Dutt K2

PDF

IMPACT OF BRAND AMBASSADOR ON BRANDING TOWARDS THE INTEREST OF CUSTOMERS IN INDIAN RETAILS: VALIDATION OF FACTORS

Mr. Subhajit Paul, Dr. Anirban Dutta, Dr. Prosenjit Ghosh

PDF

IMPACT OF REUSING TTDM WATER IN PAINT PRODUCTION

Dharshini S1, Srimathi H2, Krishnamoorthy A3

PDF

UNDERSTANDING THE SERVICE QUALITY AND CUSTOMER SATISFACTION OF MOBILE BANKING: A STUDY IN DEHRADUN

Dr. Som Aditya Juyal, Dr. Amit Nautiyal

PDF

 **Clarivat Analytics**



Scopus

SJR SCImago Journal & Country Rank

 Compendex on Engineering Village

EBSCO Research Databases

China Petroleum Processing and Petrochemical Technology

Q3 Energy Engineering and Power Technology

SJR 2022
0.23

powered by scimagojr

JOURNAL CONTENT

Browse

- » By Issue
- » By Author
- » By Title

FONT SIZE

NOTIFICATIONS

- » View
- » Subscribe

[JOURNAL HELP](#)

China Petroleum Processing and Petrochemical Technology
REGIONAL ENERGY RESOURCES INFORMATION CENTER
P.O.Box 4, Klong Luang, Pathumthani 12120, China



China Petroleum Processing and Petrochemical Technology

HOME ABOUT LOGIN SEARCH CURRENT ARCHIVES ANNOUNCEMENTS SUBMISSION

Home > Volume 23, Issue 2, July December-2023 >

IMPACT OF BRAND AMBASSADOR ON BRANDING TOWARDS THE INTEREST OF CUSTOMERS IN INDIAN RETAILS: VALIDATION OF FACTORS

Mr. Subhajit Paul, Dr. Anirban Dutta, Dr. Prosenjit Ghosh

Abstract

The retail industry has changed dramatically and hence the battle to recruit and maintain customers has intensified dramatically. The marketing semiotic elements features were crucial in framing the strategies in this case. The primary goal of this research is to identify and validate the characteristics connected to brand ambassadors as a component of marketing semiotics that is responsible for generating customer attention in Indian retails. The technique used in this study is descriptive in nature, and primary data was acquired from 962 valid respondents via a structured questionnaire. Following the completion of the data analysis (using Amos version 20), six factors were identified using confirmatory factor analysis (CFA), which are considered to be the factors responsible for generating customer interest in Indian retails and have been validated using convergent and discriminant validity. The conclusions of this study have a strong implication on how an organisation's communication strategy should be developed.

Keywords

marketing semiotics, brand ambassador, CFA, convergent validity, discriminant validity, Indian retail.

Full Text:

PDF

 Clarivat
Analytics



Scopus[®]

 SJRI SCImago
Journal & Coun
Rank

 Compendex on
Engineering Villag[®]

 EBSCO
HOST Research
Databases

China Petroleum Proces:
and Petrochemical...

 Q3 Energy Enginee
and Power
Technology
Best Qual

SJR 2022
0.23
powered by scimagojr.

JOURNAL CONTENT

Browse

- » By Issue
- » By Author
- » By Title

FONT SIZE

NOTIFICATIONS

- » View
- » Subscribe



The Indian Economic Journal

JOURNAL OF THE INDIAN ECONOMIC ASSOCIATION

Volume - 5 • Special Issue • December 2023

**PRODUCTIVITY AND
GROWTH IN THE
INDIAN
MANUFACTURING**





CONTENTS

- | | |
|--|--|
| <p>1. Importance of MSMEs in the success of 'Make in India' initiative
DEEPAK PAL
ANUP KUMAR 01</p> | <p>9. Impact of Intellectual Capital (IC) on the financial performance of firms in India
T. SITA RAMAIAH
SOMA MAHESH KUMAR
RADHA MOHAN CHEBOLU 86</p> |
| <p>2. Comparative analysis of performance of Micro, Small and Medium Enterprises (MSMEs) In India: Pre and Post-Liberalisation Period
SETAKA PALAKA
DHANALAXMI PATTNAIK 11</p> | <p>10. Investigation of Association between Financial Development and Performance of Industrial Sector with Unit Level Data
SUPRAN KUMAR SHARMA 96</p> |
| <p>3. Growth of Indian Public Sector Defence Companies during Make in India Regime (2014-2023)
SAGER REDDY ADAVELLI
RAMA KRISHNA YELAMANCHILI 21</p> | <p>11. Growth of Manufacturing Sector in India – An empirical study
MUTYALA VENKATESWARA RAO 115</p> |
| <p>4. India striving towards a \$5 Trillion Economy
ANITA DAS 29</p> | <p>12. A Critical Analysis of the role of Loan and Advances from Public Sector Banks in the Growth of MSMEs
ARCHIT RAI
KRISHNA BHUSHAN PADMADEO 122</p> |
| <p>5. A study on Consumer buying intention towards Green Beauty Cosmetics: An exploration of factors
ABHISHEK KUMAR
APARNA BHARDWAJ
NIRMALYA DEBNATH
SHARMILI CHAKRABORTY 40</p> | <p>13. Drivers of International Competitiveness of Indian Clothing and Textile Industry – Examining the Diamond Model
P KALYANI
SWATI MATHUR
Y RAMAKRISHNA 127</p> |
| <p>6. An Empirical analysis of Manufacturing Sector in India - During 1998 -2018
M. VENKATESWARA RAO
PERARAPU LAKSHMI NARAYANA
MOKA BALA SWAMY 52</p> | <p>14. Issues and Challenges of Small Scale Industries in India
K. MADHU BABU 135</p> |
| <p>7. Mudra Yojana: A New Engine of Growth, Employment creation and evaluation in India
PARAMESHWARA NAIK 62</p> | <p>15. Industrial Landscape of Bihar: A comparative analysis with India (2011-20)
SWETA
RAJESH KUMAR SUMAN 139</p> |
| <p>8. Myth and Reality of Small-Scale Industries in Indian Economy: An ANALYSIS
BUDHEN KUMAR SAIKIA
TEEKAPPA M 76</p> | <p>16. Performance of Industrial Sector with special reference to Manufacturing Industries in India
K. RAJA 152</p> |
| | <p>17. Role of MSME in Economic Development of Rural India
P. CHENNAKRISHNAN 160</p> |

A study on Consumer buying intention towards Green Beauty Cosmetics: An exploration of factors

Abhishek Kumar*
Aparna Bhardwaj**
Nirmalya Debnath***
Sharmili Chakraborty****

Abstract

Environmental deterioration is a critical issue for contemporary society since it influences consumer behaviour to shift towards environmentally friendly purchases. A detailed literature research on green purchasing behaviour was done in order to comprehend the decision-making process for buying green products. An innovation in the marketing industry is the creation of eco-friendly products. Many people are turning away from chemical-based cosmetics in favour of ecological ones. Because they contain toxic ingredients like triphenyl phosphate and petroleum, chemical-based cosmetics and beauty products are neither healthful nor safe for anyone, male or female. For this reason, several cosmetic items are also prohibited. In order to reduce the negative effects on health and the environment, it is crucial to adopt green buying behaviour (GPB), as opposed to conventional purchasing practises. Different businesses are now demonstrating increased concern for their waste management, pesticide use, and packaging materials. The reason for responsible environmental behaviour has become so popular is because it has long-term advantages for both the person and for all countries. Organisations are now incorporating ecological principles into their daily operations, including trash management.

Therefore, the altered attitude has had a significant impact on several industries, particularly consumer beauty items; the manufacturing and cosmetics sector has also taken the lead in implementing ethical production techniques to minimise the effects on the environment.

Businesses are forced by this ethical activity to comprehend the intentions behind their ethical purchases, and it also supports their long-term market viability. There isn't much discussion of this in recent literature, particularly when it comes to the uses of green cosmetics. As a result, in order to advance the literature in this area, this work aims to develop a predictive sustainable model by conducting an empirical study to look at the relationships between various variables, including attitude, social norms, perceived behaviour control, environmental consciousness, health consciousness, appearance consciousness, exposure to green advertising, and consumer purchase intention for eco-friendly cosmetics.

As a result, this research report has shed light on the subject and attempted to ascertain consumer buying habit regarding green cosmetics as well as the purchasing patterns of customers in Tripura. The study concentrated on how consumers choose products based on how they view green beauty products. Exploratory factor analysis (EFA) was used to examine the data from 412 respondents. The results support the notion that Indian consumers are aware of green cosmetics, have a positive attitude towards them, and intend to make environmentally conscious purchases. The survey will help the company to develop policies and marketing plans that take into account how consumers feel about green cosmetic products. This study is helpful for anyone who plans to investigate consumer behaviour in the future in regard to green products or cosmetics.

*Associate Professor, School of Management, KIIT Deemed to be University, An Institution of Eminence, Bhubaneswar
**Postdoctoral Fellow, Magadh University, Bodh Gaya, Bihar
***Assistant Professor, Department of Business Management, Tripura University, Agartala, Tripura
****Research Scholar, Department of Business Management, Tripura University, Agartala, Tripura

The Indian Economic Journal
(Under UGC CARE List - Group I)

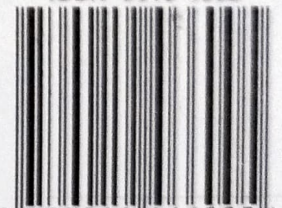
REGISTERED WITH THE REGISTRAR
OF NEWSPAPER FOR INDIA
RNI Regn.No. 46913/87

SUPPORTED BY :

Indian Economic
Association Trust
for Research &
Development



ISSN 0019-4662



9 770019 466005 >